Investigation and manipulation of SOD1 mutant misfolding, aggregation and seeding

Wen-wen Li

A Thesis submitted for the degree of

Doctor of Philosophy

University College London

Institute of Ophthalmology

2016

Declaration

I, Wenwen Li (李雯雯), confirm that the work presented in this thesis is my own. Where information has been derived from other sources, I confirm that this has been indicated in the thesis.

Signed By

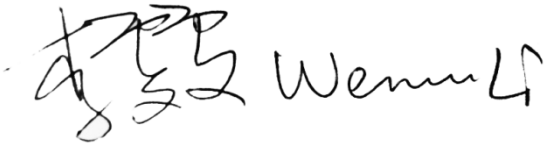

Abstract

The presence of ubiquitylated protein aggregates in neurons and surrounding cells is considered one of the hallmarks of neurodegenerative disorders, such as amyotrophic lateral sclerosis (ALS). Since the identification of *SOD1* as the first causative gene in 1993, extensive research has been carried out to investigate the role Cu/Zn superoxide dismutase-1 (SOD1) aggregation plays in ALS pathogenesis. Recently, it has been reported that SOD1 inclusions could propagate in a prion-like manner, by seeding the aggregation of soluble functional proteins and transmitting aggregation to neighbouring cells. HSJ1 (DnaJB2) is a chaperone that can reduce protein aggregation in several neurodegenerative disease models; such as, Huntington's disease and Parkinson's disease. HSJ1a overexpression has also been shown to improve motor neuron survival in an animal model of SOD1-ALS.

In this study, I tested the hypothesis that HSJ1 could alter SOD1-aggregation and seeding *in vitro* and in cell models. I developed an *in vitro* system with purified proteins to explore the tendency of SOD1 wild type ($SOD1^{WT}$) and mutants ($SOD1^{MT}$) to aggregate and seed further aggregation. The results showed that $SOD1^{WT}$ is resistant to seeding unless the protein is destabilized and partially unfolded. Purified HSJ1 could reduce SOD1 aggregation. I then developed transient and inducible cell models to investigate the effects of HSJ1 on SOD1 aggregate formation and expansion. In cells, HSJ1 interacted preferentially with $SOD1^{MT}$, and could reduce SOD1 inclusion formation, and disassembled pre-existing SOD1 inclusions. Using an inducible stable cell line expressing HSJ1a, unfolded protein response (UPR) markers were modestly reduced after ER stress, suggesting HSJ1a expression could potentially reduce disease-related intracellular stress. Collectively, these findings shed light on HSJ1 as a potential candidate targeting misfolded and aggregated SOD1 for future investigation.

Acknowledgements

I would like to thank my supervisor Prof. Mike Cheetham for offering me the Ph.D position, for his continuing guidance over the past four years and for his support when I met problems. I would also like to thank Prof. Alison Hardcastle for her generous help and solid advice on this project. Special thanks go to Ms Naheed Kanuga for patiently taking good care of the entire group. Thanks to all the members in our lab who have helped me all along this way, especially Dr. Sergey Novoselov, Dr. Jim Bellingham, Dr. Nele Schwarz, Dr. Sek-shir Cheong and Dr. Cerys Evans, for sharing the techniques, protocols, reagents and experience with me. I will miss working in the lab with you together. I would also love to thank members from my previous group, who provided me help with relevant bioinformatics work.

This Ph.D project is financially supported by China Scholarship Council (CSC) affiliated with the Chinese Ministry of Education.

Finally, I would love to thank all my family members, friends, and colleagues around the world for supporting me, encouraging me and putting faith in me from the very start.

Publications Arising from This Study

Journal papers:

Smith HL, **Li W**, Cheetham ME*. Molecular chaperones and neuronal proteostasis. *Semin Cell Dev Biol* 2015;40:142–52. (cover figure).

Ottaviani D, Marin O, Arrigoni G, Franchin C, Vilardell J, Sandre M, **Li W**, Parfitt DA, Pinna LA, Cheetham ME*, Ruzzene M*. Protein kinase CK2 modulates HSJ1 function through phosphorylation of the UIM2 domain. *Hum Mol Genet* 2016 ddw420. doi: 10.1093/hmg/ddw420.

Table of Contents

List of Figures

List of Tables

List of Abbreviations

Abbreviations	Full Name
ACD	α-crystallin
ADP	adenosine diphosphate
ALS	amyotrophic lateral sclerosis
ALS2	alsin
AMAP	α-amino-3-hydroxy-5-methyl-4-isoxazole propionic acid
AMPK	adenosine monophosphate-activated protein kinase
Amp	ampicillin
ANG	angiogenin
ANOVA	analysis of variance
ANS	1-anilinonaphthalene-8-sulfonate
ARE	antioxidant-response element
ASK1	apoptosis signal-regulating kinase 1
ATF6	activating transcription factor 6
ATG	autophagy-related genes
ATP	adenosine triphosphate
ATXN2	ataxin 2
BSA	bovine serum albumin
BCA	bicinchoninic acid
Bcl-2	B-cell lymphoma 2
Bcl-xS	BCL-2 like 1
Bcl-xL	B-cell lymphoma-extra large
BNIP3L	BCL-2/adenovirus E1B 19kDa interacting protein 3-like
Bsd	blasticidin
C9orf72	chromosome 9 open reading frame 72
CaBP	Ca^{2+} binding proteins
Cam	chloramphenicol
CaMK	Ca^{2+}/calmodulin-dependent protein kinase
CBD	cleint binding domain
CDF4	cyclin-dependent kinase 4
CFP	cyan fluorescent protein
Cg	chromogranine
CHCHD10	coiled-coil-helix-coiled-coil-helix domain containing 10
CHMP2B	chromatin modifying protein 2B
CMA	chaperone mediated autophagy
CMT2	Charcot-Marie-Tooth type 2
CNS	central nervous system
Co-IP	co-immunoprecipitation
CPK	creatine phospho kinase
CTE	C-terminal extension
cyto c	cytochrome c
DAO	D-amino acid oxidase
DAPI	4,6-diamidino-2-phenylindole
DCTN1	dynactin
ddH_2O	distilled water
dHMN	distal hereditary motor neuronopathies

DMEM	Dulbecco's modified eagle medium
DMF	N,N-dimethylformamide
DMSO	dimethylsulphoxide
DNA	deoxyribonucleic acid
DNAJB	DnaJ homolog subfamily B
EAAT2	excitatory amino acid transporter 2
E. coli	Escherichia coli
EDEM	ER degradation-enhancing alpha-mannosidase-like lectins
ELP3	elongation protein 3 homolog
ER	endoplasmic reticulum
ERAD	ER-associated degradation
ESCRT	endosomal sorting complex required for transport
EtoH	ethanol
fALS	familial amyotrophic lateral sclerosis
FBS	fetal bovine serum
FCCP	carbonyl cyanide 4- (trifluoromethoxy) phenylhydrazone
FIG4	polyphosphoinositide phosphatase
FTD	frontotemporal dementia
FUS	fused in sarcoma
G418	geneticin
GADD34	growth arrest and DNA damage-inducible protein 34
GFP	green fluorescent protein
GLT-1	glutamate transporter 1
GOI	gene of interest
HBSS	Hank's balanced salt solution
hnRNP	heterogeneous nuclear ribonucleo-protein
HRP	horseradish peroxidise
HSJ1	homo sapiens DnaJ 1
HSP	heat shock protein
Hyg	hygromycin
IFNγ	Interferon γ
IgG	immunoglobulin G
IKK	IκB kinase
IL	interleukin
IP	immunoprecipitation
IPTG	isopropyl β-D-1-thiogalactopyranoside
IRE1	inositol-requiring enzyme 1
IRES	internal ribosome entry site
JNK	stress-activated/c-Jun N-terminal kinase
Kan	kanamycin
KBBP	kappa B-motif binding phosphoprotein
kDa	kilo Dalton
KI	knock-in
KO	knock-out
LAMP	lysosome-associated membrane protein
LC3	microtubule-associated protein 1 light chain 3 alpha
LDH	lactate dehydrogenase
LET	lactate enflux transporters
LIR	LC3II-interacting region
MAPT	microtubule-associated protein tau
MBR	metal-binding region

MCP-1	monocyte chemoattractant protein 1
MCS	multiple cloning site
MCU	mitochondrial calcium uniporter
M-CSF	macrophage colony stimulating factor
MG132	carbobenzoxy-Leu-Leu-leucinal
MICU1	mitochondrial calcium uptake 1
mTOR	mammalian target of rapamycin
mNCE	mitochondrial Na^{+}/Ca^{2+} exchanger
MND	motor neuron disease
MVB	multivesicular body
mPTP	mitochondrial permeability transition pore
mUP	mitochondrial uniporter
NEFH	Neurofilament, heavy polypeptide
Neo	neomycin
NF-kB	nuclear factor kappa-B
NGF	nerve growth factor
NGFR	nerve growth factor receptor
NMDA	N-methyl-d-aspartic acid
NO	nitric oxide
NOX	nicotinamide adenine dinucleotide phosphate-oxidase
NP-40	nonyl phenoxypolyethoxylethanol
NRF2	NF-E2-related factor 2
ONPG	ortho-Nitrophenyl-β-galactoside
OPTN	optineurin
PBS	phosphate buffered saline
PC	phospho creatine
PCR	polymerase chain reaction
PDI	protein-disulphide isomerase
PE	phosphatidylethanolamine
PEG	polyethylene glycol
PEG2	prostaglandin E2
PKR	the double-stranded RNA activated protein kinase
PERK	PKR-like ER kinase
PFA	paraformaldehyde
PHF	paired helical filaments
PI	phosphatidylinositol
PI3K	phosphatidylinositol 3-phosphate kinase
PI3P	phosphatidylinositol-3-phosphate
PIC	proteinase inhibitor cocktail
PIS	penicillin and streptomycin
PMCA	plasmalemmal Ca2+-ATPase
pNCE	plasmalemmal Na+/Ca2+ exchanger
PNS	peripheral nervous system
PP1	protein phosphatase 1
PPI	protein-protein interaction
PRPH	peripherin
RAN	repeat associated non-ATG
ROS	reactive oxygen species
RNA	ribonucleic acid
RNS	reactive nitrogen species
RyR	ryanodine receptors

S1P/S2P	site-1 and site-2 proteases
sALS	sporadic amyotrophic lateral sclerosis
SB	sodium butyrate
SBD	substrate binding domain
SDS	sodium dodecyl sulphate
SDS-PAGE	sodium dodecyl sulphate polyacrylamide gel electrophoresis
SEDI	SOD1 exposed dimer interface
SERCA	sarco/ER Ca^{2+} ATPase
SETX	senataxin
SMA	spinal muscular atrophy
SMN	survival motor neuron
smHSP	small HSP
SNP	single nucleotide polymorphism
SOD1	Cu/Zn superoxide dismutase
SPCA	secretory pathway Ca^{2+}-ATPase
TAE	Tris acetate EDTA
TBS	tris-buffered saline
TBK1	TANK1 binding kinase 1
TDP-43	TAR DNA binding protein-43
Tet	tetracycline
$TetO_2$	2-fold Tet operators
TetR	tetracycline repressor
TFE	2,2,2-trifluoroethanol
Tm	melting temperature
TNF	tumor necrosis factor
TRAF2	TNF receptor-associated factor 2
TUB4A	tubulin 4A
WT	wild type
WTL	wild type-like
UBQLN2	ubiquilin-2
UBR	ubiquitin protein ligase E3 component n-recognin
UIM	ubiquitin interacting motif
UPR	unfolded protein response
UPS	ubiquitin proteasome system
UV	ultra-violet
VAPB	vesicle-associated membrane protein-associated protein B
VCP	valosin-containing protein
VDAC	voltage-dependent anion channel
VGCC	voltage-gated Ca^{2+} channels
XBP1	X-box binding protein 1
X-gal	5-bromo-4-chloro-3-indolyl-β-D-galactoside
XIAP	X-linked inhibitor of apoptosis protein
YIF1A	Yip1-interacting factor homologue A
YFP	yellow fluorescent protein
Zeo	zeocin

Chapter 1

Introduction

Part of this chapter has been published in

Smith HL, Li W, Cheetham ME. Molecular chaperones and neuronal proteostasis. Semin Cell Dev Biol 2015;40:142–52.

1.1 Neuronal proteostasis challenges

1.1.1 Nervous structure and function

The human nervous system is a vital connectome that links and coordinates the organs and the rest of body, functioning to detect, interpret and respond to internal and external stimuli. Structurally, the nervous system is divided into ① central nervous system (CNS) (Tuladhar et al. 2015) and ② peripheral nervous system (PNS) (Cuevas 2015). The CNS mainly consists of the brain, retina and spinal cord, whilst PNS encompasses motor and sensory neurons extended from CNS and connects to muscles and other organs. Functionally, the nervous system can be classified into ① the somatic system that connect the brain and spinal cord with muscles and sensory receptors, and ② the autonomic system that regulates the body processes that function without consciousness.

The neural network is composed of highly specialized cells: neurons, which usually consist of soma, dendrites, axons and synaptic terminals. Neurons are highly differentiated with various morphologies and functions (Hammond & Hammond 2015), including ① sensory neurons that transduce physical stimuli into neural signals; ② motor neurons that transmit neural signals from brain and spinal cord into muscle contractions and glandular outputs; and ③ interneurons that connect neurons within nervous system. In addition, the non-neuronal cells named glia also play important roles in supporting, nutrition, homeostasis, myelin formation and signal transmission in nervous system.

Motor neurons are further categorized into upper motor neurons and lower motor neurons, depending upon their locations. Upper motor neurons originate in the cerebral cortex, and their axons project out of precentral gyrus, form corticospinal and corticobulbar tracts, descending to the spinal cord and brainstem, where they activate lower motor neurons (de Lahunta et al. 2009b). The lower motor neurons, mainly located in the spinal cord and brainstem, innervate intrafusal and/or extrafusal muscle fibers via axonal terminals (de Lahunta et al. 2009a). Upper motor neuron lesions occurring above the anterior horn of the spinal cord can result from stroke, multiple sclerosis, spinal cord injury or other acquired brain injury (Tshala-Katumbay & Spencer 2007). In contrast, damage to lower motor neurons cause muscle atrophy, decreased strength and decreased reflexes in affected areas (Borasio & Appel 2003; Ramahi et al. 2014).

1.1.2 Motor neuron vulnerability

Motor neurons are particularly susceptible to injury especially in neurodegenerative diseases. The reason for this is not clear as yet; however, the features of motor neurons may provide some clues.

Motor neuron is a group of large-volume cells with long axonal compartments, which demands robust cytoskeletal support, stable axonal transport, optimal mitochondrial function, high level of energy metabolism as well as a delicate balance between protein synthesis and degradation. These features of motor neurons make them vulnerable to intrinsic and extrinsic stress: unlike other neurons, motor neurons are highly dependent on cellular signaling via reactive oxygen species (ROS) and reactive nitrogen species (RNS) (Wang & Michaelis 2010), resulting in high levels of intrinsic free radicals; In addition, high expression of unedited calcium permeable α-amino-3-hydroxy-5-methyl-4-isoxazole propionic acid (AMPA) receptors, high glutamatergic input, and low expression of calcium-buffering proteins lead to sensitivity towards excitotoxicity (further discussion in section 1.3.7) (Kwak et al. 2010).

Motor neurons also seem to have a high threshold for inducing a protective heat shock response as well as possibly reduced proteasome capacity to degrade the damaged proteins (van Oosten-Hawle & Morimoto 2014), thus creating additional challenges for motor neurons to cope with physiological burdens.

1.2 Amyotrophic lateral sclerosis

1.2.1 Clinical phenotypes of ALS

Motor neuron diseases (MND) are a class of neurodegenerative disorders, in which the motor neurons that control voluntary muscle activity selectively dysfunction, causing severe disability, progressive paralysis and death (Olby 2004; Polymenidou & Cleveland 2008), including ① amyotrophic lateral sclerosis (ALS), ② primary lateral sclerosis, ③ progressive muscular atrophy, ④ progressive bulbar palsy and ⑤ pseudobulbar palsy. Nowadays, the majority of studies on MND have focused on ALS, as it accounts for ~75% of MND cases.

Initially described in 1869 by the French neurobiologist and physician Jean-Martin Charcot, ALS was firstly known as Charcot's sclerosis (Charcot & Joffroy 1869). ALS is now familiarly known in the United States as Lou Gehrig's disease in honour of a baseball player who developed the disease in the 1930s. ALS is characterized by progressive loss of upper motor neurons in the motor cortex and lower motor neurons in brainstem and spinal cord with consequently atrophy of associated muscles and supporting cells (Boillee et al. 2006). The clinical symptoms of ALS commonly include muscle weakness and atrophy, leading to respiratory compromise, and eventually death (Lima & Nucci 2011; Hardiman et al. 2011; Gordon 2013; Sabatelli et al. 2013). Traditionally regarded as pure motor neuron disorder, ALS recently has been reported to affect sensory neurons, spinocerebellar pathways as well as the neuronal groups within the substantia nigra and the hippocampal dentate granule layer in patients, therefore it can be reconsidered as a multisystem disease in which motor neurons tend to degenerate earliest and most severely (Ferraiuolo et al. 2011) . Among ALS patients, only 5-10% of cases are familial (Sabatelli et al. 2013), the remaining cases arise sporadically. The worldwide pathogenic incidence is approximately 0.3-2.5 per 100,000 individuals with a mean age-onset between 47-52 years old for familial ALS (fALS) patients and 58-62 years old for sporadic ALS (sALS) patients (Wood-Allum & Shaw 2010). ALS patients usually die in 2-5 years after symptom onset due to respiratory failure, only ~10% are reported to survive longer than 10 years.

1.2.2 Genes implicated in ALS

The identification of *SOD1* as the first causative ALS gene in 1993 triggered the first major wave of genetic research in ALS (Rosen et al. 1993), *SOD1* mutations account for approximately 20% of fALS cases. Since then, high-throughput, genome-wide mapping has become the primary strategy to identify unknown causative genes, which helped to discover rare fALS-related variants in alsin (*ALS2*) (Yang et al. 2001), senataxin (*SETX*) (Chen et al. 2004), dynactin (*DCTN1*) (Münch et al. 2004), vesicle-associated membrane protein-associated protein B (*VAPB*) (Nishimura et al. 2004). However, the next milestone did not come until 2006 with identification of TAR DNA binding protein-43 (*TDP-43*) causative mutations (Neumann et al. 2006), which are causal in 5% of familial patients and some apparent sALS patients, followed by discovery of fused in sarcoma (*FUS*) (Kwiatkowski et al. 2009; Vance et al. 2009), and identification of intronic hexanucleotide expansion of chromosome 9 open reading frame 72 (*C9ORF72*) in 2011 (Renton et al. 2011; DeJesus-Hernandez et al. 2011), mutation of which is the most common genetic defect (~35%) in ALS patients.

Although the aetiology of ALS has not been fully determined at present, identification of fALS-associated genes (Table 1.1) has great significance, as those genetic variants and their gene products are highly applicable not only to fALS cases but also in sALS cases, which provide us insights into the potential cellular mechanisms underlying pathogenesis (Figure 1.1) (Ferraiuolo et al. 2011), including RNA dysregulation, mitochondrial dysfunction, oxidative stress, protein aggregation, dysregulated endosomal trafficking, endoplasmic reticulum (ER) stress, excitotoxicity, neuroinflammation, and impaired axonal transport. Genes that have not been consistently replicated in different populations or validated in additional independent populations are excluded from Table 1.1. A number of association studies have identified genetic variants that could increase the risk of developing sALS (Table 1.2); however, many of these are not well understood.

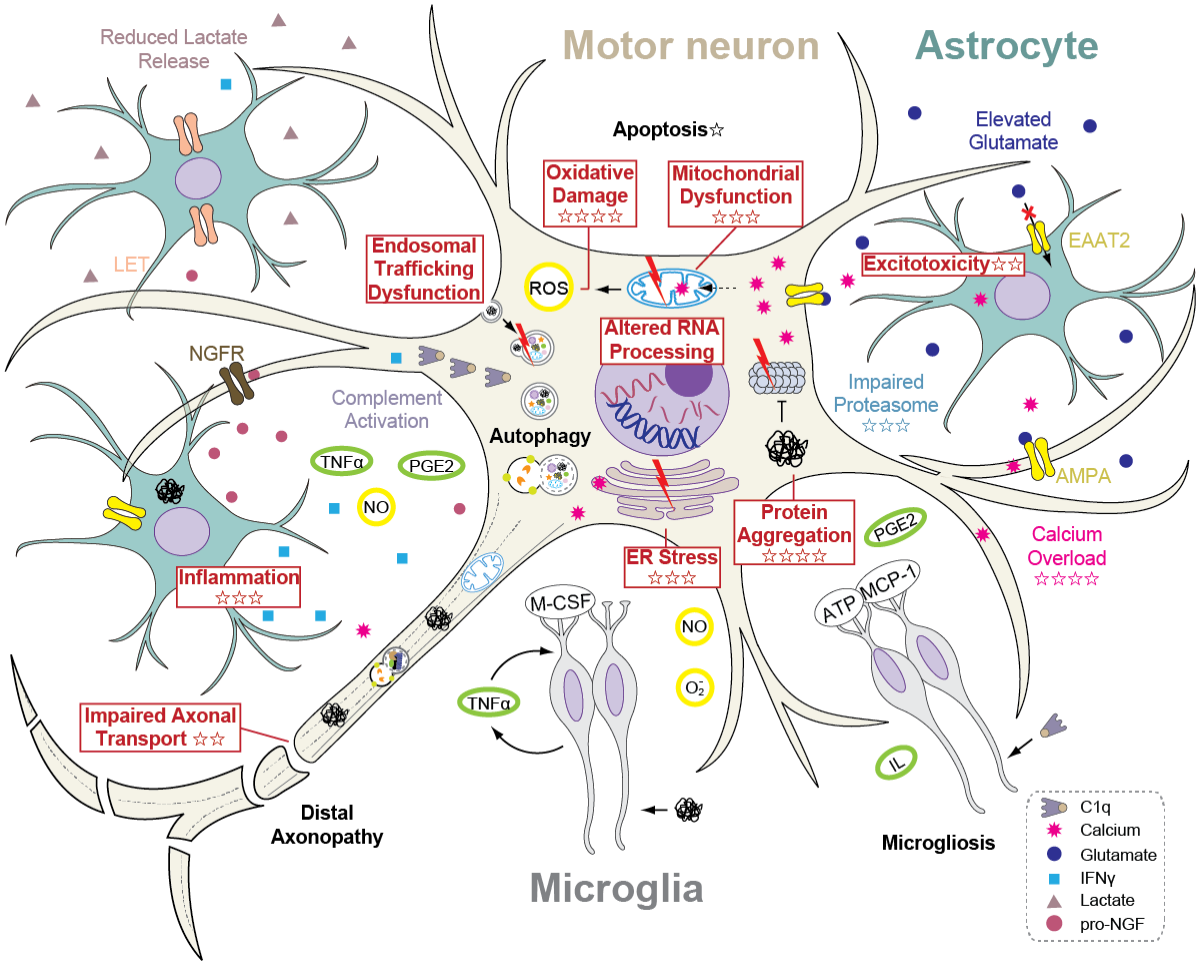

Figure 1.1 Molecular mechanisms of ALS pathogenesis. ALS is a complex disorder involving disrupted homeostasis as well as abnormal interactions with neighbouring cells. Motor neurons can undergo dysregulated RNA processing, together with mitochondrial dysfunction, oxidative damage, calcium overload, protein aggregation, impaired proteasome function and ER stress, which contribute to activation of apoptotic or autophagic cascades. Impaired axonal transport causes energy deficit in distal axon. Motor neurons are able to produce complement subunits as stress signals to neighbouring cells. Astrocytes contribute to neuron injury by inflammatory mediators (e.g., NO and TNFα), reduced glutamate uptake by inhibition of EAAT2, reduced lactate release, etc. Microglia are subsequently activated, initiating a major inflammatory cascade, which further contributed to disease progression via secreted factors. *Abbreviations:* EAAT2, excitatory amino acid transporter 2; IFNγ, Interferon γ; IL, interleukin; LET, lactate enflux transporters; MCP-1, monocyte chemoattractant protein 1; M-CSF, macrophage colony stimulating factor; NGF, nerve growth factor; NGFR, NGF receptor; NO, nitric oxide; PGE2, prostaglandin E2; ROS, reactive oxygen species. Pathogenic events directly implicated as being caused by SOD1 mutants in ALS pathology are scored (0-5 stars). *Figure is redrawn based on Ferraiuolo et al (2011).*

Gene subtype	Chromosomal locus	Pathogenic proteins (Gene)	Inheritance (Incidence)	A
Oxidative stress				
ALS1	21q22.11	Cu/Zn superoxide dismutase 1 (*SOD1*)	AD 20%*	+
RNA processing				
ALS4	9q34.13	Senataxin (*SETX*)	AD 5%	
ALS6	16p11.2	Fused in sarcoma (*FUS*)	AD 5%*	+
ALS9	14q11.1	Angiogenin (*ANG*)	AD 1%	
ALS10	1p36.22	TAR DNA binding protein-43 (*TARDBP*)	AD 5%	+
ALS13	12q23-q24.1	Ataxin-2 (*ATNX2*)	Ud (R)	+
ALS20	12q13.1	Heterogeneous nuclear ribonucleo-protein A1 (*HNRNPA1*)	AD (R)	
ALS21	5q31.2	Matrin 3 *(MATR3*)	AD (R)	
	7q15.2	Heterogeneous nuclear ribonucleo-protein A2/B1 (*HNRNPA2B1*)	AD (R)	
	17q11.1-q11.2	TATA-binding protein-associated factor (*TAF15*)	Ud (R)	
Endosomal trafficking and cell signalling				
ALS2	2q33.2	Alsin (*ALS2*)	AR 1%	
ALS8	20q13.33	Vesicle-associated membrane protein -associated protein B (*VAPB*)	AD (R)	+
ALS11	6q21	Polyphosphoinositide phosphatase (*FIG4*)	AD (R)	
ALS12	10p13	Optineurin (*OPTN*)	AR (R)*	+
ALS17	3p11.2	Chromatin modifying protein 2B (*CHMP2B*)	AD (R)	
ALS19	2q33.3-q34	Receptor tyrosine-protein kinase erbB-4 (*ERBB4*)	AD (R)	
Glutamate excitotoxicity				
	12q24.11	σ-amino-acid oxidase (*DAO*)	AD (R)	
Protein degradation				
ALS14	9p13.3	Valosin-containing protein (*VCP*)	AD 1%	+
ALSX	Xp11.21	Ubiquilin-2 (*UBQLN2*)	XD (R)	+
ALS-FTD 3	5q35.3	Sequestosome 1 (*SQSTM1*)	AD 1%	+
Cytoskeleton				
ALS18	17p13.3	Profilin 1 (*PFN1*)	AD (R)	
ALS dementia-	17q.21	Microtubule-associated protein tau (*MAPT*)	AD (R)	
	2p22.3	Spastin (*SPAST*)	AD (R)	
Axonal transportation				
ALS5	15p14	Spatacsin (*SPG11*)	AR (R)*	
	2p13.1	Dynactin (*DCTN1*)	AD (R)	
	22q12.1-	Neurofilament, heavy polypeptide (*NEFH*)	AD 1%	+
Other				
ALS16	9p13.3	σ-non-opioid receptor 1 (*SIGMAR1*)	AR (R)	
ALS-FTD 1	9p21.2	Chromosome 9 open reading frame 72 (*C9orf72*)	AD 35%	+
ALS-FTD 2	22q11.23	Coiled-coil-helix-coiled-coil-helix domain containing 10 (*CHCHD10*)	AD (R)	
ALS-FTD 4	12q14.2	TANK-binding kinase 1 (*TBK1*)	AD (R)	
	12q13.12	Peripherin (*PRPH*)	Ud (R)	+
Unknown				
ALS3	18q21	Unknown (*ALS3*)	AD (R)	
ALS7	20p13	Unknown (*ALS7*)	AD (R)	

Table 1.1 Genes implicated in familial ALS. Genes associated with fALS with inherited incidence were presented. Gene products reported to be immunopositive in aggregates (A) in ALS patients are marked as (+). Rare (R) indicated an incidence lower than 1%. *Abbreviations*: AD, autosomal dominant; AR, autosomal recessive; R, rare; Ud, undefined. *Table was adapted from* http://alsod.iop.kcl.ac.uk.

Chromosomal locus	Risk factors (Gene)
14q11.2	Apurinic Endonuclease DNA repair enzyme (*APEX*)
7q36.2	dipeptidyl-peptidase 6 (*DPP6*)
8p21.1	Elongation protein 3 homolog (*ELP3*)
2q36.1	Ephrin type A receptor 4 (*EPHA4*)
1p32.1	FGGY carbohydrate kinase domain containing (*FGGY*)
6p22.2	Haemochromatosis (*HFE*)
12p11.23	Inositol 1,4,5-trisphosphate receptor type 2 (*ITPR2*)
1q24.2	Kinesin-Associated Protein 3 (*KIFAP3*)
17q21.31	Progranulin (*PGRN*)
7q21.3	Paraoxonase (*PON1-3*)
5q12.2-q13.3	Survival Motor Neuron (*SMN1-2*)
19p13.12	unc-13 homolog A (*UNC13A*)
6p21	Vascular Endothelial Growth Factor (*VEGF*)
20q13.33	Zinc finger protein 512B (*ZNF512B*)

Table 1.2 Genes associated with sporadic ALS. The genes associated with increased risk of sALS are presented even through the cause of sALS remained unclear. Gene variants, such as the single nucleotide polymorphism (SNP), abnormal copy number, modifier, or mutation (e.g. insertion, substitution, deletion) are discovered in sALS cases, based on GWAS analysis.

1.2.3 Cu/Zn Superoxide dismutase-1

1.2.3.1 Cu/Zn SOD1 wild-type

Cu/Zn superoxide dismutase 1 (SOD1) was first characterized as erythocuprein in 1969 (McCord & Fridovich 1969); it is encoded by *SOD1* gene that maps to chromosome 21q22.11 (Siddique T, Figlewicz DA, Pericak-Vance MA, Haines JL, Rouleau G, Jeffers AJ, Sapp P, Hung WY, Bebout J, McKenna-Yasek D 1991). Wild-type SOD1 ($SOD1^{WT}$) monomer is composed of an eight-stranded β-barrel motif (Table 1.3) (Rakhit & Chakrabartty 2006). Each subunit is acetylated and binds to a solvent-exposed catalytic Cu^{2+} ion and a buried Zn^{2+} ion that stabilizes the conformation. Cu^{2+} and Zn^{2+} ions are directly linked by a bridging His-63, and indirectly linked by interactions between His-46 and His-71 via Asp-124, forming an extended secondary bridge. Physiologically SOD1 functions as a non-disulfide-linked homo-dimer via ditryptophan cross-link at Trp-33 (Figure 1.2).

	Feature	Site	Function
Sites	Metal binding	H46	Copper ion
		H48	
		H63	
		H63	Zinc ion
		H71	
		H80	
		D83	
		H120	Copper ion
Amino Acid Modifications	Modified residue	A1	N-acetylalanine
		K70	N6-acetyllysine
		S98	Phosphoserine
		K122	N6-acetyllysine
	Disulphide bond	C57 +C146	S-S disulfide bond
	Cross-link	W32	1-(tryptophan-3-yl)-tryptophan (W-W) (interchain)

Table 1.3 Metal binding sites and amino acid modifications of SOD1.

SOD1 (EC=1.15.1.1) is a metalloenzyme that catalyzes the oxidation/reduction conversion of the superoxide radicals, which are normally produced during the oxidative phosphorylation in mitochondria, into molecular oxygen and hydrogen peroxide (Zelko et al. 2002). Hydrogen peroxide can be converted into water by glutathione peroxidase later.

$$SOD1\text{-}Cu^{2+} + {}^{\bullet}O_2^- \rightarrow SOD1\text{-}Cu^{+} + O_2$$

$$SOD1\text{-}Cu^{+} + {}^{\bullet}O_2^- + 2H^{+} \rightarrow SOD1\text{-}Cu^{2+} + H_2O_2 \xrightarrow[\text{Catalase}]{\text{Glutathione Peroxidase}} H_2O$$

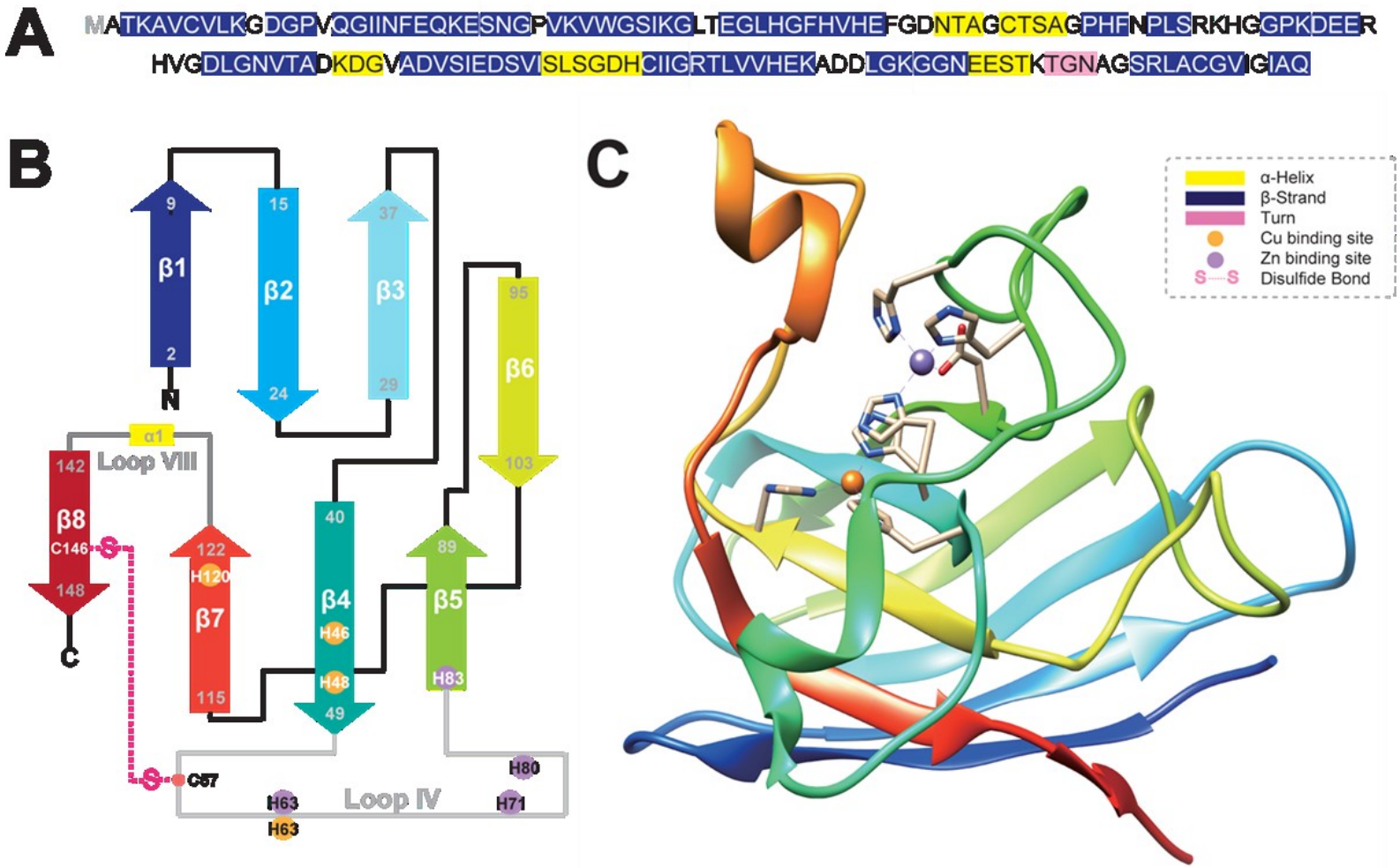

Figure 1.2 The primary, secondary and tertiary structures of wild-type SOD1. (A) The primary sequence of monomer $SOD1^{WT}$ is shown with **(B)** the secondary structure (uniprot No. P00441). $SOD1^{WT}$ contains 8 β-sheets (blue), links (green), 1 α-helix (yellow), with 1 Cu^{2+} (orange) and 1 Zn^{2+} (purple) per subunit. The disulphide bond (pink) loops (black& grey) and the Cu^{2+}/Zn^{2+} binding sites are highlighted. **(C)** The tertiary structure of $SOD1^{WT}$ (PDB No.4FF9) from N-terminus (dark blue) to C-terminus (red) with metal ions and modifications is represented in a 3D model.

SOD1 primarily localizes in the cytoplasm, mitochondria, nuclei and membranous organelles, presumably peroxisomes (Pardo et al. 1995; Zelko et al. 2002; Lin & Lai 2013). SOD1 is an abundant enzyme ubiquitously expressed in the brain (especially cerebral cortex), endocrine tissues (especially adrenal gland), lung, liver, gallbladder, pancreas, stomach and skin (Uhlen et al. 2015). Besides liver, SOD1 is also highly expressed in interneurons and motor neurons in human spinal cord (Pardo et al. 1995), where SOD1 is concentrated in perikarya, dendrites, and axons.

1.2.3.2 Cu/Zn SOD1 mutations

To date, more than 170 mutations in SOD1 have been characterized, almost all of which result in ALS phenotypes. Mutated residues are uniformly distributed throughout the 154AA polypeptide (Figure 1.3), including the residues located at/near the pole of β-barrel, the dimer interface, the active sites, the C terminus of charged loop that guides O^{2-} binding, along with the Cu^{2+} and/or Zn^{2+} ion binding sites. SOD1 mutations can be further divided into insertions, C-terminal truncations, frame-shift, deletions, and the most frequent: missense amino acid substitutions.

Based on metal-binding affinity, SOD1 mutations can be categorized into two subfamilies (Hayward et al. 2002; Tiwari & Hayward 2005; Munch & Bertolotti 2010) : wild type-like (WTL) mutations and metal-binding region (MBR) mutations. WTL mutations retain the ability to bind Cu^{2+}/Zn^{2+} ions and exhibit relatively normal enzymatic activity, indicating subtle changes to the native backbone structure. The WTL subfamily is mainly located at the dimer interface, β-barrel and charged loop, including A4V, G37R, L38V, G41S, H43R, G72S, D76Y, L84V, D90A, G93A, E100G, I113T, E133-1e, E133-2e, N139K, L144F. In contrast, MBR mutations are deficient in Cu^{2+}/Zn^{2+} ion content, and exhibit severe thermal and structural disorders. The mutations at, or near the Cu^{2+}/Zn^{2+} binding sites, active sites, O^{2-} guiding sites belong to the MBR subfamily, including H46R, H48Q, G85R, D124V, D125H, S134N, and C146R.

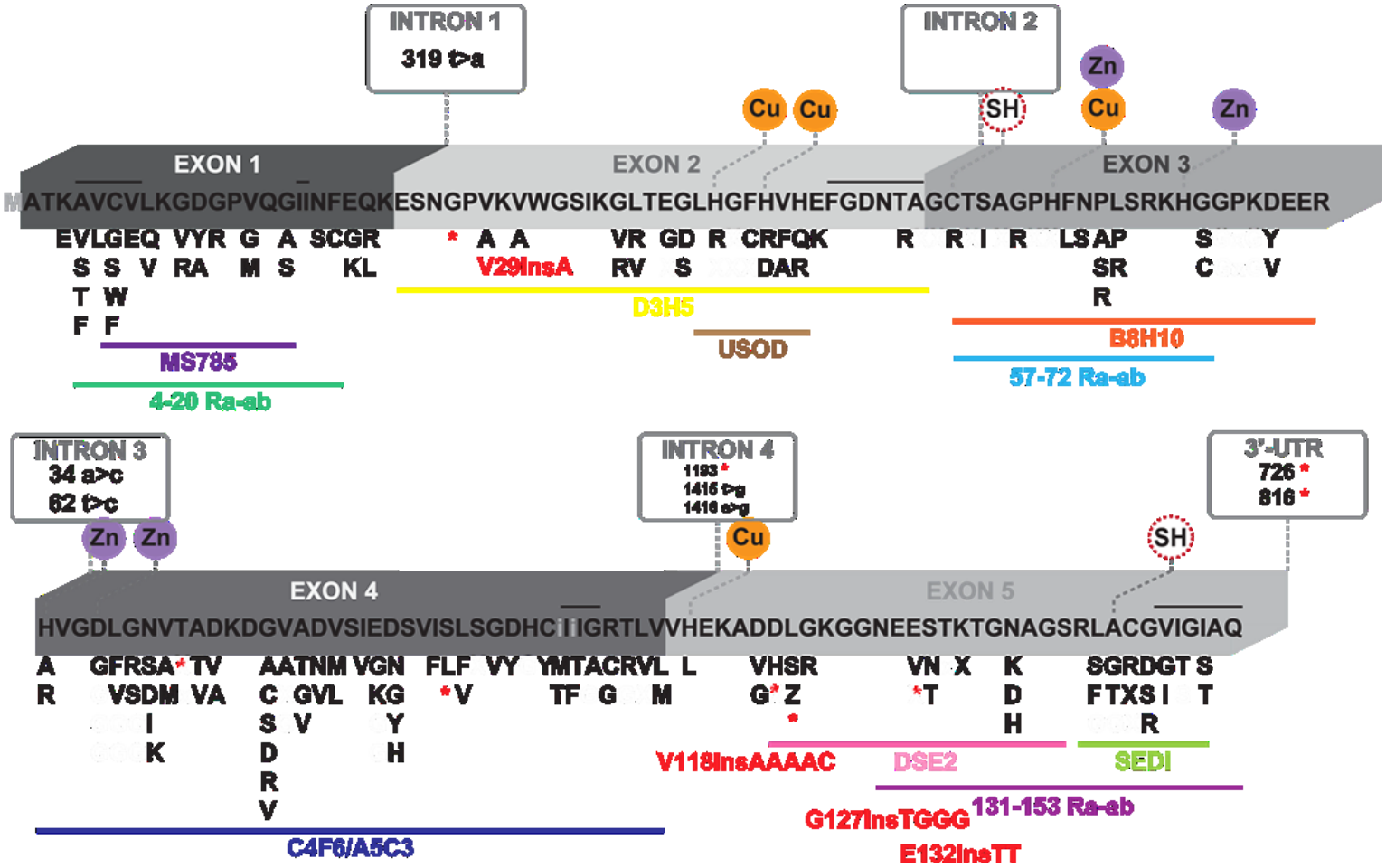

Figure 1.3 Pathogenic mutation sites in SOD1 with epitopes for conformation specific antibodies highlighting regions exposed in SOD1 upon misfolding. The primary structure of wild-type SOD1 with the positions of mutations displayed below. Insertions were highlighted below the sequence in red. Substitutions were illustrated in detail under the specific amino acid of the wild-type. Deletions are indicated by the asterisk (*) in red. The line above the sequence represented the amino acids at the dimer interface, the mutations of that led to the monomerization of SOD1. The binding regions of conformational specific antibodies for misfolded SOD1 were depicted below.

Extensive hydrogen bonding interactions and the overall loop ordering of $SOD1^{WT}$ and metallated SOD1 WTL mutants are similar (Hart et al. 1998; Cardoso et al. 2002; DiDonato et al. 2003; Hough et al. 2004). However, subtle but significant changes were observed in local packing, backbone dynamics and flexibility of specific regions, for example, $SOD1^{G93A}$ exhibited different backbone mobility in a solution NMR as compared with $SOD1^{WT}$ (Shipp et al. 2003). SOD1 WTL mutants show difference from $SOD1^{WT}$ along dimer interface (Hayward et al. 2002). In contrast to WTL mutants, crystal analysis reveals that MBR mutants exhibit significant conformational shifts on the electrostatic loop and Zn^{2+}-binding loop while leaving the dimer interface and β-barrier unaltered (Valentine & Hart 2003). MBR mutants are different from $SOD1^{WT}$ and WTL mutants in metal ion binding content (Hayward et al. 2002), thermal stability (Tiwari & Hayward 2006), superoxide activity and visible absorption spectra (Yiwari et al. 2009).

The mutations discussed above mainly affect SOD1 protein structure and its functions. SOD1 mutants can lose or gain function (section 1.2.3.3), both types of mutations give rise to a series of consequences biophysically, such as the reduction of the repulsive charge and net surface charge (Sandelin et al. 2007; Shi et al. 2014), tendency to monomerize, looser more flexible conformation, increase of hydrophobicity (Munch & Bertolotti 2010) or reduction of Tm (Tiwari & Hayward 2006).

1.2.3.3 Cytotoxicity of SOD1 mutant in ALS

Mutated SOD1 proteins ($SOD1^{MT}$) are reported to account for ~20% of fALS and ~3-5% of sALS cases (Andersen et al. 2003). SOD1-associated fALS is mainly autosomal dominant. An exception is $SOD1^{D90A}$ which can be inherited in either dominant or recessive manner (Al-Chalabi et al. 1998). Since Rosen *et al*'s work in 1993, a vast amount of research has been carried out to investigate the deleterious effects of SOD1 mutants on neuronal tissues, but the exact pathogenic mechanisms have not been fully elucidated yet. So far, there are two hypotheses that dominate the potential cytotoxicity generated by mutated SOD1 (Valentine & Hart 2003): ① oxidative damage (section 1.3.3) and ② oligomerization and/or aggregation-mediated damage (section 1.2.3.3.2-3). Both of theories initiate with unfolding and/or misfolding processes.

1.2.3.3.1 SOD1 unfolding

Given that both metal occupancy and disulphide status are suggested to be determinants of SOD1 mutant cytotoxicity, it is important to characterize the different unfolded states of SOD1 (Ip et al. 2011). Hence, SOD1 could be further classified into disulphide reduced (2SH), disulphide oxidized (S-S), fully metallated (holo) and metal-free (apo) states, all the theoretical combinations are presented in Figure 1.4.

SOD1 in tissue lysate equilibrates between active metallated dimer and inactive Cu^{2+}-free dimer (Bartnikas & Gitlin 2003). ① Cu^{2+} deficient $SOD1^{S\text{-}S}$ is reported to exhibit a compact conformation and structural similarity to holo-SOD1 (Doucette et al. 2004). Amongst SOD1 mutants, Zn^{2+} binding alone is sufficient to maintain the loop (Banci et al. 2003; Banci et al. 2002). However, $SOD1^{H46R}$ as an exception binds Zn^{2+} but shows severe disorder of electrostatic and zinc loops (Antonyuk et al. 2005; Elam et al. 2003). ② Moreover, Cu^{2+}-deficient $SOD1^{SH}$ exhibits a looser conformation, which lacks one or both cysteines required for disulphide formation. For instance, Cu^{2+}-deficient $SOD1^{S\text{-}S\ C57S}$ exhibits the increased flexibility of the disulphide loop, compared to Cu^{2+}-deficient $SOD1^{S\text{-}S\ WT}$ (Doucette et al. 2004). ③ In addition, metal-free $SOD1^{S\text{-}S}$ showed the disorder of the Zn^{2+} and electrostatic loops, and a lose conformation (Strange et al. 2003). The MBR mutants favour this Cu/Zn-free state, this loop disorder exposes buried interaction motifs (Elam et al. 2003; Strange et al. 2003; Antonyuk et al. 2005), increases the hydrophobicity of SOD1 and facilitates aggregate formation in solution (Tiwari et al. 2005). ④ Furthermore, metal-free $SOD1^{SH}$, the metal-free, disulphide reduced enzyme, accumulates and interacts aberrantly within cells, such as BCL-2 (Pedrini et al. 2010), Derlin-1 (Nishitoh et al. 2008), Dorfin (Niwa et al. 2002) and GLT1 (Trotti et al. 2001). Metal-free $SOD1^{SH\ A4V}$ in the C6A/C111S background is reported to form aggregates in solution, but metal-free $SOD1^{SH\ WT}$ in the C6A/C111S background forms monomer without aggregate (Furukawa & O'Halloran 2005). Collectively, loss of post-translational modifications can significantly destabilize SOD1; cause various unfolding conformations, therefore increasing potential misfolding opportunities during ALS pathogenesis.

$SOD1^{WT}$ exhibits high thermochemical and conformational stability (Roe et al. 1988; Forman & Fridovich 1973); however, SOD1 mutants perturb structural stability. Amongst SOD1 mutants, even the well-folded WTL mutants are rather vulnerable to disulphide reduction and impaired metal binding. This susceptibility to partial unfolding at physiological pH and temperature is a shared feature of all SOD1 mutants. Structural disorder may result in aberrant self-interaction or localized dysfunction in specific cellular compartments, which would be further discussed in section 1.4.3.

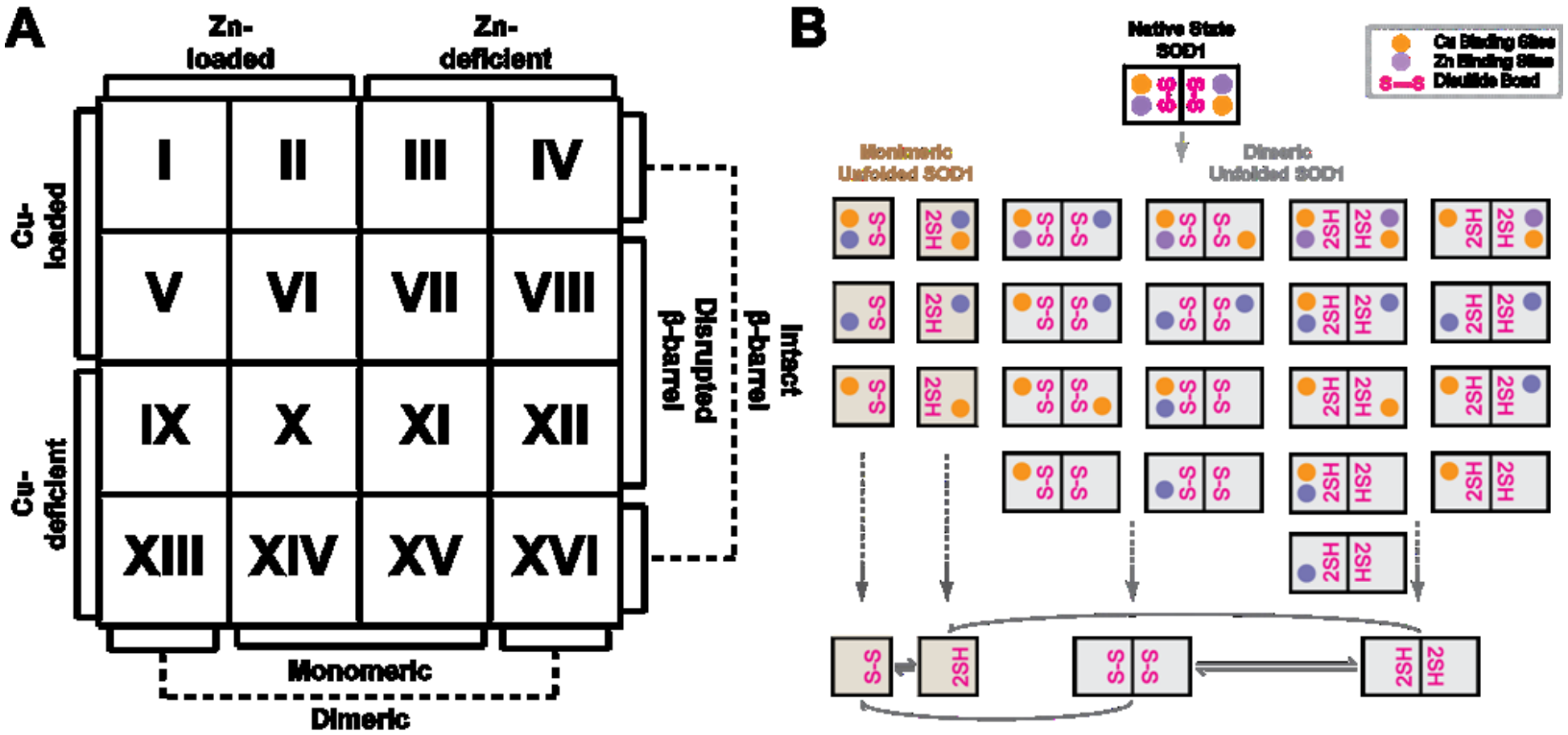

Figure 1.4 Sixteen-state model of unfolded SOD1. (A) Schematic of the unfolding states of SOD1. $SOD1^{WT}$ was reported to unfold via a Cu-loaded Zn-deficient monomeric intermediate. $SOD1^{G93A}$ was confirmed to unfold through a Cu-deficient Zn-loaded dimeric intermediate with a disrupted core structure. $SOD1^{G85R}$ unfolded via a Cu-deficient Zn-loaded monomeric intermediate with a disrupted core structure. **(B)** Schematic of potential SOD1 unfolding process.

1.2.3.3.2 Loss of function or gain of toxicity?

An interesting debate is whether $SOD1^{MT}$ associated fALS is a result of gain of toxic properties, or a loss of dismutase function?

Current studies favour gain of function theory based on the evidence: ① a lack of ALS phenotype was observed in SOD1 knock-out mice (Reaume et al. 1996). In addition, deletion of endogenous mouse SOD1 in transgenic mice expressing human $SOD1^{G85R}$ showed no effects on disease course (Bruijn et al. 1998); ② an increased SOD1 dismutase activity was observed in $SOD1^{G93A}$ transgenic mice that developed a loss of motor neurons (Joyce et al. 2011); ③ a lack of correlation between SOD1 enzymic activity and the aggressiveness of clinical phenotypes in ALS patients (Ratovitski et al. 1999). However, data from *Sod1*$^{-/-}$ mice suggested that loss of function also contributes to oxidative stress, glutamate toxicity, distal neuron axonopathy, and finally neuronal susceptibility (Yoshida et al. 2000; Ho et al. 1998; Matzuk et al. 1998; Huang et al. 1997; Reaume et al. 1996). In addition, reduction of enzymatic activity is reported to facilitate the monomerization of dimeric SOD1 through glutathionylation and oxidation, which might promote SOD1 unfolding as well (Redler et al. 2011). In conclusion, it is generally believed that SOD1 associated ALS is a result of gain of function, instead of loss of function.

It is worth mentioning that SOD1 mRNA is reported to form ribonucleic complex to increase protein half-life. However, this process is disrupted if the transcripts contain mutations (Lu et al. 2007), which might explain the specific increased sensitivity of RNA processing in neuronal tissues in ALS patients.

There are three major hypotheses about the mechanisms of aberrant redox biochemistry resulted from mutated SOD1: ① peroxidation; ② tyrosine nitration; ③ reverse catalysis. It is reported that mutations in SOD1 enhance its reactivity towards abnormal substrates. Wild type SOD1 catalyses dismutation of O_2^-, but SOD1 mutants could reverse this reaction. Wiedau-Pazos *et al* (1996) reported mutated SOD1 used H_2O_2 as substrates, produced abnormal free radical $^{\bullet}OH$ and $^{\bullet}O_2^-$ as follows (Wiedau-Pazos et al. 1996):

$$SOD1\text{-}Cu^{+} + H_2O_2 \rightleftharpoons SOD1\text{-}Cu^{2+} + OH^{-} + {}^{\bullet}OH$$

$$① \quad SOD1\text{-}Cu^{2+} + H_2O_2 \rightleftharpoons SOD1\text{-}Cu^{+} + 2H^{+} + {}^{\bullet}O_2^{-}$$

Similarly, Backman *et al* (1993) reported mutated SOD1 aberrantly used peroxynitrite (H-Tyr-P) as substrates, promoting the nitration of proteins, especially neuro-filaments and receptor tyrosine kinases (Beckman et al. 1993).

$$^{\bullet}O_2^- + NO^{\bullet} \rightarrow NO_3^-$$

$$\text{②}\quad NO_3^- + \text{H-Tyr-P} \overset{\text{SOD1-Cu}^+}{\rightleftharpoons} OH^- + NO_2\text{-Tyr-P}$$

In addition, some SOD1 mutants show a decreased Zn^{2+} binding affinity (e.g., A4V and I113T), Crow *et al* (1997) reported such Zn^{2+}-deficient SOD1 mutants also favoured tyrosine nitration and induced apoptosis via peroxynitrite, even the Zn^{2+}-deficient $SOD1^{WT}$ exhibited similar cytotoxicity (Crow et al. 1997), suggesting loss of Zn^{2+} might be a shared feature in the SOD1 fALS patients.

$$(Zn^-)SOD1\text{-}Cu^+ + O_2 \rightarrow (Zn^-)SOD1\text{-}Cu^{2+} + O_2^-$$

$$NO^- + O_2 \overset{(Zn^-)SOD1\text{-}Cu^+}{\rightleftharpoons} NO_3^-$$

$$\text{③}\quad NO_3^- + \text{H-Tyr-P} \overset{(Zn^-)SOD1\text{-}Cu^+}{\rightleftharpoons} OH^- + NO_2\text{-Tyr-P}$$

The importance of peroxynitrite synthesis remains controversial in ALS pathogenesis. If it is central to the gained toxic property, reduction of NO within neurons would reduce toxicity of $SOD1^{MT}$. However, inhibition of NO synthase shows little effects on survival on $SOD1^{G93A}$ mice (Facchinetti et al. 1999).

Given all the evidence collectively, there are several theories about the deleterious properties of mutated SOD1 gain of function (Cleveland & Rothstein 2001), such as pro-apoptosis via caspase activation, altered gene expression, Cu-mediated oxidative damage; superoxide-generation because of Zn-deficiencies; aberrant protein interaction and aggregation. The theory of Cu^{2+}-mediated oxidative damage suggests aberrant harmful products and intermediates would accumulate during the process of aging, cause damage to cellular components, resulting in gradual loss of viability and finally, death of motor neurons, the increased oxidative damage within ALS background was verified in vast amount of research (further discussion in section 1.3.3). The appearance of pronounced mitochondrial vacuolation at early stage of disease onset seems to be consistent with oxidative damage. However, Subramaniam *et al* (2002) reported a *Ccs*$^{-/-}$ background shows no effects on survival of $SOD1^{G93A}$ $SOD1^{G37R}$ and $SOD1^{G85R}$ transgenic mice (Subramaniam et al. 2002). Similarly, mutations on H46, H48, H63, and H120 that abolish the Cu^{2+} binding site, thus producing enzymatically inactive protein, were still able to develop ALS symptoms in a transgenic mouse (Wang et al. 2007). In addition, multiple anti-oxidant drug therapies (such as vitamin E, N-acetylcysteine, creatine, glutathione and dexpramipexole) only show modest effects on ALS mice, these findings are at odds with theory that oxidative damage is the primary cause of cytotoxicity.

1.2.3.3.3 SOD1 aggregation

As discussed above, mutated SOD1 shows decreased metal ion content and disulphide bonds. Upon stress, structural flexibility and aberrant redox biochemistry reactions would contribute to aggregation formation. For instance, compared to fully metallated $SOD1^{WT}$, Zn-deficient $SOD1^{WT}$ and SOD1 mutants are prone to aggregate (Martyshkin et al. 2003; Roberts et al. 2007). In the context of ALS, as a consequence of looser or flexible conformations, mutated SOD1 initiates either local subtle misfolding or global unfolding/misfolding, hence promoting the abnormal dimerization and/or oligomerization. SOD1 oligomers would gradually increase in size and ultimately form proteinaceous inclusions, as observed in ALS patients.

In the aggregation formation process, SOD1 oligomers are believed to be selectively toxic to motor neurons (Brotherton et al. 2013); SOD1 exhibits a higher expression level in liver cells compared to that in brain yet shows little toxicity (Pasinelli et al. 2004). It has been suggested that oligomers might be the most toxic species of mutated SOD1, and further aggregation could be a defence system to sequester the oligomers and prevent them interacting with other cellular components aberrantly (Sherman & Goldberg 2001), which could activate cell death. High molecular weight oligomerized species of SOD1 are observed in the spinal cords of $SOD1^{G93A}$ mice before disease onset. An ALS-associated epitope identified on SOD1 oligomers using C4F6 supported this hypothesis (Redler et al. 2014). However, the exact stoichiometry and SOD1 oligomer species have never been validated. These hypotheses involving oligomers raises the questions, are SOD1 aggregates central to ALS pathogenesis, are they just harmless byproducts or defence response to sequestrate aberrant cellular components?

Instead of oligomers, research has focused on the consequences of SOD1 aggregation, as aggregates are ubiquitously present in almost all fALS, sALS patients as well as mouse models regardless the genetic backgrounds. In contrast to TDP-43, SOD1 is detected as a component of aggregates only in fALS1 cases and not the other familial cases. SOD1 aggregates *in vivo* structurally appear amorphous or pore-shaped, co-localized with ubiquitin, p62, OPTN (controversial results), UBQLIN2, but not RNA granule markers (Blokhuis et al. 2013). These insoluble inclusion bodies are observed in the brainstem and spinal, coincident with disease on-set and accumulate progressively.

However, what are the specific mechanisms of the $SOD1^{MT}$ aggregation-mediated damages to neuron tissues? The consequences of these aggregates could provide us clues. ① First of all, SOD1 aggregates might randomly sequester or co-aggregate other vital components required to maintain neuron survival (Prause et al. 2013). ② Additionally, $SOD1^{MT}$ as well as SOD1 aggregates are reported to aberrantly interact

with proteins that wild type SOD1 is not able to, which disrupt functional protein-protein interaction (PPI) network, leading to global elevated stress signals (Jain et al. 2008). ③ Aggregates that are difficult to refold and/or degrade (Kriegenburg et al. 2012; Olzmann et al. 2008), cause dysfunction of multiple organelles as well as the transport pathways in between. As proof of that, SOD1 aggregates are reported to interfere with energy metabolism reactions in the mitochondrial innermembrane (referred to section 1.3.2), increase unfolded protein stress within ER (referred to section 1.3.6), block transport of ER-Golgi intermediated compartment (referred to section 1.3.5) (Soo et al. 2015), and engender destabilization of microtubules (Pandey et al. 2007). ④ As SOD1 aggregates cannot be easily dissociated; the balance between protein synthesis and degradation could shift. SOD1 aggregates inhibit proteasomal activity by modification of subunits and 'clogging' the UPS system (Kabashi & Durham 2006; Mulligan & Chakrabartty 2013; Cheroni et al. 2005; Tashiro et al. 2012), which also impair autophagosome clearance by inhibiting dynein/dynactin functions (Maday et al. 2012). Low protein degradation capacity is insufficient for global protein turnover, giving rise to the accumulation of damaged cellular components even injured organelles. In addition, partial inhibition of UPS provokes larger aggregate formation even in the non-neuronal cells, which could further affect the viability of neurons. ⑤ The decreased chaperone activity and high threshold of heat shock response are equally important (van Oosten-Hawle & Morimoto 2014). Abnormal SOD1, including misfolded, oligomerzied as well as aggregated SOD1 protein, specifically recruit the chaperone machinery, sequester or suppress heat shock proteins (HSP), resulting in global reduction of folding activity. The decreased expression levels of various chaperones are observed in $SOD1^{G93A}$ as well as $SOD1^{G85R}$ mice (Jain et al. 2008). Heat shock response impairment would make things even worse (Batulan et al. 2003): under thermal stress, glial cells not motor neurons, exhibit upregulation of HSPs. Therefore, motor neurons are unable to cope with burden of misfolded proteins, further promoting aggregation.

1.2.3.3.4 SOD1 mutants in motor neurons and neighbouring cells

Other than the debate about the primary pathways mediated by gained toxicity, another basic question has not been resolved yet: are the motor neurons the direct targets of SOD1 toxicity? To answer this question, it is vital to characterize whether the toxicity induced by SOD1 is autonomous or non-autonomous.

To investigate the roles of different cell types in the progression of ALS, SOD1 mutants were selectively expressed in motor neurons or microglia in chimeric mice, or in primary or stem cell-based models. $SOD1^{G37R}$ mice received transplantation of bone marrow from $MyD88^{-/-}$ mice exhibited a significantly earlier disease onset and shorter lifespan (Kang & Rivest 2007). Wang *et al* (2008) also reported that transgenic mice

with expression of $SOD1^{G93A}$ restricted to spinal motor neurons and interneurons showed similar pathological and immunohistochemical abnormalities (Wang et al. 2008). Furthermore, non-neuronal cells expressing $SOD1^{WT}$ with motor neurons postponed the disease onset and extended the survival of $SOD1^{G37R}$ mice (Clement et al. 2003). A decreased expression of $SOD1^{G93A}$ in motor neurons of transgenic mice showed a modest effect on duration but significantly delayed the symptom onset (Wang et al. 2008). Combined with evidence described in section 1.3.2-1.3.8 as well as section 1.2.3.3.2-.1.2.3.3.5, it is suggested that expression of SOD1 mutant-induced neuron degeneration is cell-autonomous, or at least partial autonomous in the early stage.

Besides motor neurons, the surrounding cells such as microglia, peripheral macrophages, and astrocytes also play a role in disease progression via neuroinflammation. Neuroinflammation is an immune response to neuronal cues. In ALS, astrocytes are activated after injury, shift their morphology, become proliferative, secrete pro-inflammatory cytokines and growth factors, as well as produce nitric oxide, hence greatly affecting the local environment (Julien 2007). Astrocytes cause direct toxic damage to motor neurons by releasing interferon gamma (IFNγ) (Aebischer et al. 2011) and nerve growth factor (NGF) (Pehar et al. 2004). Activated astrocytes abolish EAAT2 expression (Trotti et al. 1999; Trotti et al. 2001; Rothstein et al. 1995; Couratier et al. 1993; Su et al. 2003), which results in inability to clear glutamate, prolonging motor neuron excitotoxicity. Haidet-Phillips *et al* (2011) confirmed astrocyte-mediated motor neuron death in the post-mortem tissues of SOD1 causative ALS patients (Haidet-Phillips et al. 2011). Knockdown of $SOD1^{MT}$ in astrocytes prolonged survival by delaying disease onset in $SOD1^{G85R}$ mice.

Among other factors released by astrocytes, macrophage-colony stimulating factor (M-CSF) (Imai & Kohsaka 2002; Gowing et al. 2009) and monocyte chemoattractant protein-1 (MCP-1) (Sargsyan et al. 2009) and tumor necrosis factor-α (TNFα) (Y. Liu et al. 2009) activate microglia cells, increasing proliferation and migration. Reactive microglia produce ROS, pro-inflammatory cytokines [such as interleukins (IL)], TNFα as well as prostaglandins (PGE2) (Glass et al. 2010). Extracellular ATP coming from damaged neurons is reported to bind to microglia (Apolloni et al. 2013), therefore contributing to activation. Motor neurons participate in microglial activation by releasing $SOD1^{MT}$ co-secreted with chromogranin (Cg) (Urushitani et al. 2006). In ALS patients or mouse models, microglia are also shown to be reactive in the spinal cord. Inhibition of $SOD1^{G93A}$ or $SOD1^{G37R}$ expression in microglia and peripheral macrophages in chimeric mice delayed progression late in disease (Kang & Rivest 2007), yet showed little effects on early progression or age-of-onset. Microglia expressing $SOD1^{MT}$ in cell

models showed toxicity towards motor neurons in co-culture. Compared to $SOD1^{WT}$ control (Xiao et al. 2007), microglia expressing $SOD1^{G93A}$ exhibited increased superoxide and nitric oxide production *in vitro*, which was also toxic to primary motor neurons (Di Giorgio et al. 2007). Interestingly, $PU.1^{-/-}$ mice that received bone marrow transplants from $SOD1^{G93A}$ mice were unable to develop ALS-like phenotype (Beers et al. 2006), suggesting activated microglia alone are not enough to induce motor neuron injury *in vivo*. Emerging findings suggest a toxic non-autonomous effect of microglia contributes to progression, instead of disease onset.

Given all the evidence gathered above, these findings suggest $SOD1^{MT}$ in motor neurons affects disease onset and early progression, whereas $SOD1^{MT}$ in microglia, peripheral macrophages and astrocytes contributes to the progression of disease at late stage.

1.2.3.3.5 Seeding and transmission of PrP-like SOD1 aggregates

Recent findings have suggested that SOD1 aggregation in ALS can self-propagate and spread in a prion-like mechanism. In the infectious prion disease, prions propagate by inducing a conformational change in PrP^{C} to form PrP^{SC} aggregates. Therefore, the term 'prion-like' in neurodegenerative disorders is used to describe a similar infectious process, self-assembly and spread. Similarly, the disease spreads in a characteristic pattern in ALS patients, from an initial site of onset to the surrounding neuroanatomy. According to the seeding model, $SOD1^{MT}$ propagates by converting $SOD1^{WT}$ into aberrant conformation and co-aggregation. Aggregates are continuously formed and taken up by neighbouring cells, initiating a vicious cycle: penetration of aggregates into intracellular compartment, seeding, and transmission.

Emerging evidence have reported the seeding and transmission in the cell models as well as animal models. Grad *et al* (2011) reported a pathogenic conformational change of endogenous $SOD1^{WT}$ induced by SOD1 aggregates using conformational specific antibodies (3H1 and 10C12) (Grad et al. 2011). Münch *et al* (2011) observed that exogenous $SOD1^{H46R}$ aggregates were internalized in an ATP-, actin-, lipid raft-, macropinocytosis-dependent and a clathrin-, dynamin-, and caveolin-independent manner. Additionally, these recombinant SOD1 seeds further seeded aggregation of intracellular SOD1, which could be further released and trasmitted between neighbouring cells (Münch et al. 2011).

Glia-to-neuron interactions have also been implicated in prion-like mechanism. The toxic effects of glia cells expressing $SOD1^{MT}$ on motor neurons in chimeric mice or co-culture have been discussed in section 1.2.3.3.4. Interestingly, Basso *et al* (2013) reported the $SOD1^{MT}$ altered secretion and exosome release in astrocytes. This

astrocyte-derived exosome transferred SOD1 aggregates to spinal motor neurons and selectively induced cell death (Basso et al. 2013). Sábado *et al* (2014) reported a prion-like mechanism for trans-synaptic propagation of SOD1 misfolding from ventral horn motor neurons to dorsal root ganglion sensory neurons (Sabado et al. 2014).

Collectively, increasing studies suggest that aggregated SOD1 is transmissible through a seeding mechanism and between cells. This seeded aggregation is regarded as potentially a key event in the progression of SOD1-related ALS disease.

1.3 Pathogenic mechanisms underlying ALS

1.3.1 Dysregulated RNA processing

RNA processing is a tightly regulated, highly complex pathway, including transcription, pre-mRNA splicing, editing, transportation, translation and degradation. Emerging evidence suggests dysfunctional RNA metabolism is a common pathway in ALS pathogenesis. To date, six major proteins, angiogenin (ANG), FUS, TDP-43 and senataxin (SETX) in fALS, elongator protein 3 (ELP3) and SMN in sALS have been associated with dysregulated RNA processing in ALS pathology.

Dysregulated RNA processing was firstly implicated in motor neuron degeneration by identification of SMN1 in spinal muscular atrophy (SMA) (Lefebvre et al. 1995). Identification of DNA-RNA helicase SETX in juvenile-onset fALS in 2004 provided further evidences (Chen et al. 2004). SETX protein is a component of ribonucleoprotein complexes. But the precise mechanism of SETX-associated ALS remains unclear.

Identification of fALS mutations in TDP-43 (Neumann et al. 2006) and FUS (Kwiatkowski et al. 2009; Vance et al. 2009) drew further attention to dysregulated RNA metabolism as a pathway in ALS. TDP-43 and FUS are RNA-DNA binding proteins implicated in multiple aspects of RNA processing. TDP-43 contains 2 RNA recognition domains (Kuo et al. 2009), whose targets involve RNA transcripts of disease-associated genes, such as TARDBP itself, FUS, VCP or many other genes, e.g., ACRV1, APOA2 (Sephton et al. 2011). Similarly, FUS contains RNA recognition domains (Wang et al. 2015), and functions as a transcriptional activator in oncogenic fusions, or regulator of protein expression, such as nuclear factor kappa-B (NF-κB) (Uranishi et al. 2001), or transcription factor PU.1 (Hallier et al. 1998). Interestingly, most of pathogenic mutations on TDP-43 are located in exon 6 that encodes glycine-rich domain (Ou et al. 1995; Wang et al. 2004), and mutations on FUS are mainly located in exon 13-15 that encode RGG-rich region (Iko et al. 2004; Morohoshi et al. 1998), both these regions contain a nuclear localization signal (Zakaryan & Gehring 2006), therefore, mutated TDP-43 and FUS continuously shuttle between nucleus and cytoplasm in a transcription-dependent manner. Importantly, TDP-43 is a common component of cytoplasmic inclusions in ALS pathogenesis independent of the presence of mutation. Furthermore, mutations in TDP-43 or FUS appear to lead to protein aggregation.

1.3.2 Mitochondrial dysfunction

Mitochondria play the central role in energy production and calcium homeostasis. Early studies on post-mortem tissues of ALS patients reported structural and morphological

abnormalities of mitochondria (Menzies et al. 2002; Sasaki & Iwata 1999; Hirano et al. 1984). Interestingly, multiple mouse models [SOD1, TDP-43 (Shan et al. 2010; Xu et al. 2010; Wang et al. 2013), and FUS (Huang et al. 2011; Tradewell et al. 2012)] and patients exhibit mitochondrial vacuolation or fragmented mitochondrial network before disease onset, indicating mitochondrial dysfunction is not only an early event but also a potentially vital process in the cascade of ALS. Recently, variants in a novel gene named coiled-coil-helix-coiled-coil-helix domain containing 10 (*CHCHD10*) were identified in frontotemporal dementia (FTD)-ALS (Bannwarth et al. 2014; Chaussenot et al. 2014; Genin et al. 2015), and reported to cause respiratory chain deficiency, fragmentation of mitochondrial network, and defects in cristae maintenance in fALS patients.

Mitochondrial dysfunction can be mediated by mutated SOD1. The degenerative vacuolated mitochondria are bound by $SOD1^{MT}$ (Higgins et al. 2003), which forms aggregates in the mitochondrial intermembrane space (Ahtoniemi et al. 2008), accumulate on the outer membrane in transgenic mice in an age-dependent way (Chiu et al. 1995). *In vitro*, isolated mitochondria exposed to purified $SOD1^{G93A}$ and $SOD1^{G37R}$ show structural damage as well as increased sensitivity upon oxidative stress, ultimately leading to release of cytochrome c (*cyto c*) (Pickles et al. 2013). Specifically, SOD1 mutants or iperoxidized $SOD1^{WT}$ abnormally bind to B-cell lymphoma 2 (BCL-2) in the mitochondrial outer membrane (Pedrini et al. 2010; Pasinelli et al. 2004), where SOD1 switches the bioenergetics states in affected motor neurons by favouring glycolysis and inhibiting mitochondrial respiration, contributing to dysregulated energy and/or oxidative metabolism in the long term. $SOD1^{MT}$-BCL-2 interaction altered the voltage-dependent anion channels (VDAC) conducting states (Pedrini et al. 2010), giving rise to insufficient ATP production, abnormal free radical formation, increased mitochondrial membrane potential, dysregulated calcium signalling, and reduced electron transport chain activity. In 2010, *in vivo* work observed $SOD1^{G93A}$ directly inhibited VDAC1 conductance by aberrant interaction and co-aggregation (Israelson et al. 2010), indicating VDAC1 is a candidate affected by $SOD1^{MT}$ directly and indirectly.

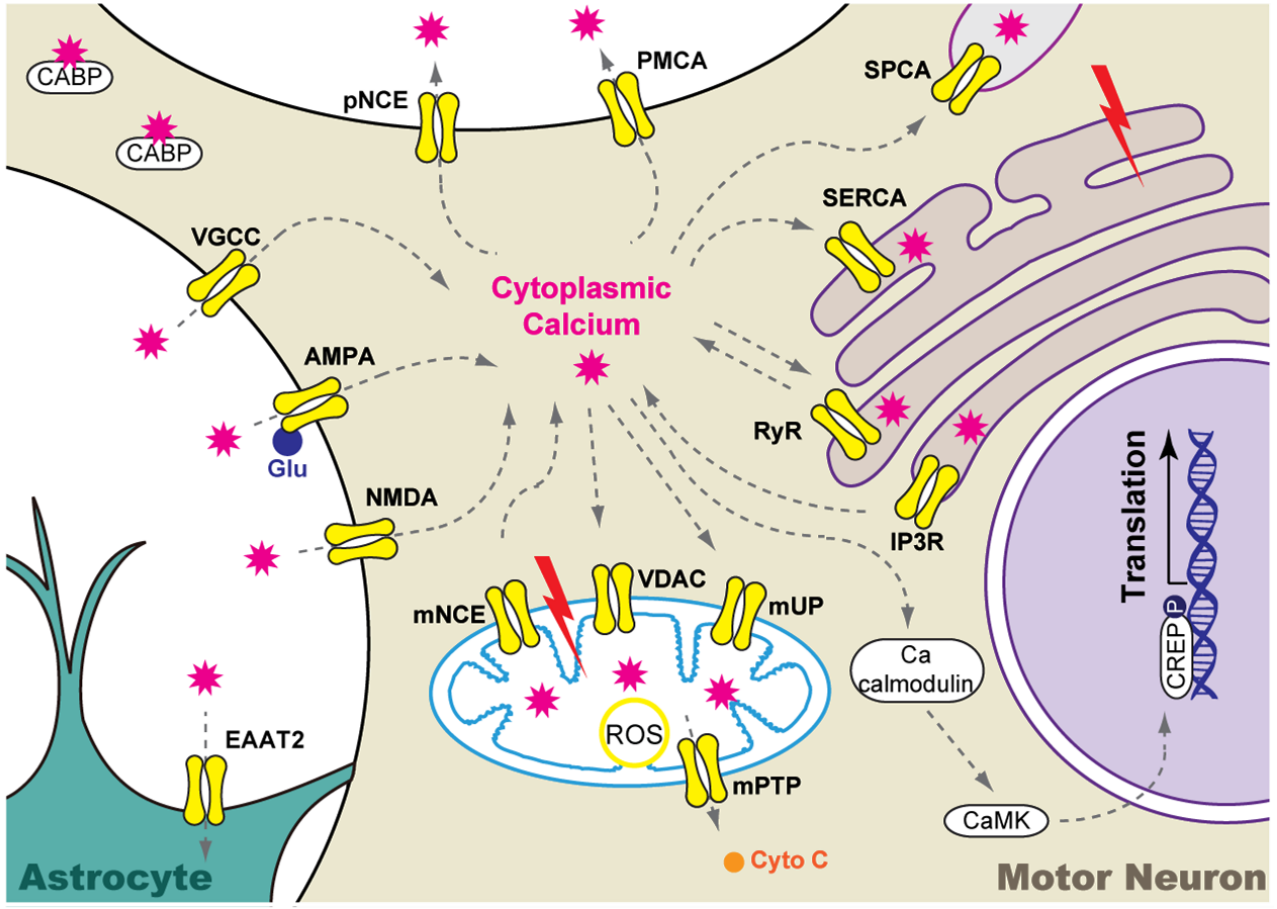

Figure 1.5 Calcium signalling in ALS. Calcium enters into motor neurons via VGCC, NMDA and unedited AMPA. Increased cytoplasmic Ca^{2+} triggers a leak of Ca^{2+} from ER via RyR, which is taken up by mitochondria via mUP rapidly or VDAC slowly. Mitochondria slowly release Ca^{2+} via mNCE. The calcium cycle between the ER and mitochondria is mediated via VDAC-IP3R. Cytoplasm Ca^{2+} outflows through pNCE or PMCA. Excess Ca^{2+} causes ER stress and increased production of ROS, promoting release of cyto *c* via mPTP, thus triggering apoptosis. Ca^{2+} also activates several CaMK signaling cascades, results in CREB activation and phosphorylation. *Abbreviation:* CaBP, Ca^{2+} binding proteins; CaMK, Ca^{2+}/calmodulin-dependent protein kinase. mNCE, mitochondrial Na^{+}/Ca^{2+} exchanger; mPTP, mitochondrial permeability transition pore; mUP, mitochondrial uniporter; PMCA, plasmalemmal Ca^{2+}-ATPase, pNCE, plasmalemmal Na^{+}/Ca^{2+} exchanger; RyR, ryanodine receptor; SERCA, sarco/ER Ca^{2} ATPase; SPCA, secretory pathway Ca^{2+}-ATPase; VGCC, voltage-gated Ca^{2+} channel. Figure is redrawn based on Tadic *et al* (2014).

Calcium homeostasis between mitochondria and ER is also observed to be disrupted in different ALS subtypes (Figure 1.5) (Guatteo et al. 2007). Calcium as a ubiquitous second messenger participates in various signaling pathways, which is essential for homeostasis. Elevated Ca^{2+} level is detected in spinal cord in ALS patients (Siklós et al. 1996) as well as animal models (Carriedo et al. 2000; Damiano et al. 2006; Jaiswal & Keller 2009). $SOD1^{G93A}$ mice exhibit depressed mitochondrial calcium uniporter (MCU) and mitochondrial calcium uptake 1 (MICU1) in spinal cord (Parone et al. 2013), leading to the reduced calcium buffering capacity. Defects in calcium buffering have been detected in animal models in presymptomatic stage (Damiano et al. 2006). Moreover, high levels of calcium are possibly overloaded to the ER and mitochondria, affecting neuron survival by favouring pro-death factors. Upregulation of apoptotic factors is observed in $SOD1^{G93A}$ transgenic mice in the early stage of disease progression. It is reported that in $SOD1^{G93A}$, $SOD1^{G85R}$ as well as $SOD1^{G37R}$ mice, pro-apoptotic factors are upregulated [e.g., Bad (BCL-2-associated death promoter) and Bax (BCL-2-associated X protein)] and anti-apoptotic proteins are downregulated [e.g., BCL-2, BCL-XL (B-cell lymphoma-extra large) and XIAP (X-linked inhibitor of apoptosis protein)] (Ishigaki et al. 2002; Vukosavic et al. 1999; Damiano et al. 2006), leading to reduction of mitochondrial membrane potential, hence triggering cyto *c* release (Takeuchi, Kobayashi, Ishigaki, et al. 2002; Kirkinezos et al. 2005). Caspases are subsequently activated. Overexpression of BCL-2 (Kostic et al. 1997), drug treatments using minocycline (cyto *c* inhibitor) (Gordon et al. 2007), or zVAD-fmk (spectrum caspase inhibitor) (Li et al. 2000) exhibited modest inhibition effects of disease progression in animal models.

1.3.3 Oxidative stress

Oxidative stress arises from imbalance between production of free radicals and the defense systems that neutralize the reactive intermediates or repair the resulting damages. Oxidative stress in ALS occurs either as results of mitochondrial dysfunction, or can contribute to mitochondrial dysfunction. Samples collected from ALS patients show biomarkers of free radical damages within ventral horn neurons. Specifically, oxidized DNA and RNA (8-OHdG) (Ferrante et al. 1997), proteins (3-nitrotyrosine) (Beal et al. 1997) and lipids (4-hydroxynonenal) (Smith et al. 1998) have been identified using relevant biomarkers in post-mortem tissues from sALS, fALS cases and $SOD1^{G93A}$ mice (Turner et al. 2009). Sources of oxidative stress in ALS have been thoroughly characterized mostly in SOD1 animal models, demonstrating $SOD1^{MT}$ mediates several aberrant oxidative reactions therefore producing various free radicals (discussed in section 1.2.3.3.2). But is that the major source for increased oxidative stress considering all those abnormal reactions required a copper ion loaded onto

$SOD1^{MT}$? Depletion of copper loading showed little effects on disease onset, progression or pathology of those SOD1 transgenic mice (Subramaniam et al. 2002), indicating SOD1 mutant induced oxidative stress via pathways beyond its enzymatic activity. Traditionally SOD1 was regarded as the major factor; however, emerging findings demonstrate that TDP-43 is also capable of inducing oxidative stress in cultured motor neurons (Walker et al. 2013; Dewey et al. 2011).

Apart from generation of abnormal free radicals, defects in defense system also contribute to increased oxidative stress in ALS. Microarray analysis of motor neurons expressing SOD1 mutants suggest downregulation of antioxidant response involved genes (Kirby et al. 2005), such as transcription factor nuclear erythroid 2-related factor 2 (NRF2). The activated form of NRF2 translocates from cytoplasm to nucleus, binds antioxidant-response element (ARE) enhancer sequence (Kraft et al. 2007), hence upregulating antioxidant defense system. Animal models reveal a significant reduction of NFR2 mRNA in comparison with control mice (Kirby et al. 2005).

A novel pathway of SOD1 mutant-mediated motor neuron degeneration via microglia has been reported (discussed in section 1.2.3.3.4). It is worth mentioning that $SOD1^{MT}$ increases the nicotinamide adenine dinucleotide phosphate-oxidase (NOX)-mediated superoxide production by interacting and locking Rac1 into its active state (Kanekura et al. 2005; Harraz et al. 2008), resulting in prolongation of ROS production in microglia. Knock out (KO) of either NOX1 or NOX2 is shown to extend lifespan of $SOD1^{G93A}$ mice significantly (Marden et al. 2007; Carter et al. 2009).

1.3.4 Protein aggregation

One of the central hallmarks of ALS is the presence of cytoplasmic ubiquitylated protein aggregates in neurons and surrounding oligodendrocytes. Intracellular inclusions consist of different components in distinct fALS subtypes, proteins presented as compositions of aggregates in post-mortem tissues are marked as '+' in Table 1.1.

Mutations in SOD1 were the first associated with protein aggregation in fALS (Rosen et al. 1993). Research aimed at verifying the physiological effects of protein aggregation mainly focused on SOD1 until 2004, when VAPB mutants were identified as components of inclusions in fALS patients.

Following the identification of SOD1 aggregates (discussed in section 1.2.3.3.2-1.2.3.3.5), a breakthrough was achieved in 2006 by identification of TDP-43 (Neumann et al. 2006) and then FUS in 2009 (Vance et al. 2009; Kwiatkowski et al. 2009) as major components of ubiquitylated inclusions in ALS cases. Interestingly, non-mutated TDP-43 is discovered in aggregates in spinal cord, hippocampal, and frontal cortex in

almost all sALS and majority of SOD1-negative fALS patients, but not observed in SOD1-associated fALS patients (Tan et al. 2007). Overexpression of hyperphosphorylated TDP-43^{WT} exhibits a deleterious effect with nuclear localization in cultured neurons (Barmada et al. 2010) or animal model (Xu et al. 2010). The effects become more prominent when TDP-43^{MT} is overexpressed, which shifts from nucleus to cytoplasm (Winton et al. 2008). Various TDP-43 mutants are prone to misfold, aggregate, and form cytoplasmic inclusions along with the disease progression. Similar to TDP-43, FUS is also present in the inclusions in majority sALS and fALS cases except for SOD1 causative fALS cases (Mackenzie et al. 2007). Mutated FUS relocalises from the nucleus to cytoplasm, forming pathogenic aggregate-like granules via either RNA-dependent or RNA-independent pathways (Shelkovnikova et al. 2014). It is noted that this cytoplasmic relocalization is observed in some but not all FUS animal models (Barmada et al. 2010; Bosco et al. 2010; Huang et al. 2011; Wang et al. 2011; Daigle et al. 2013). Recently, C9orf72 has been characterized as the most prevalent cause of ALS (DeJesus-Hernandez et al. 2011; Renton et al. 2011). Expanded-repeat C9orf72 dipeptides produced by repeat associated non-ATG (RAN) dependent translation (i.e. polyGA, polyGP, polyGR, polyPR and polyPA) (Ash et al. 2013) have been identified as components of TDP-43-negative, p62-/UBQLN2-positive cytoplasmic and/or nuclear inclusions in the hippocampus, frontotemporal neocortex and cerebellum (Brettschneider et al. 2012; Al-Sarraj et al. 2011). These C9orf72 dipeptides distinguish patients from non-expanded repeat carriers.

In addition, spinal cord tissue from sALS cases shows accumulation of ATXN2 aggregates (Elden et al. 2010), a protein that functions in mRNA polyadenylation, stress granule formation, polyribosome assembly and miRNA synthesis. ATXN2 with 27-33 polyQ repeats is associated with ALS, whereas a repeat number greater than 34 leads to SCA (Van Langenhove et al. 2012). Several other relatively less studied genes are also associated with protein aggregation (Blokhuis et al. 2013; Wood et al. 2003). Collectively, a large number of studies provide evidence that protein aggregation is an important pathway in ALS.

1.3.5 Aberrant endosomal trafficking

Endocytosis is a process by which extracellular substances or surface membrane proteins are engulfed and transported into correct intracellular compartments via vesicles (Grant & Donaldson 2009). In functional neurons, early endosomes fuse with internalized vesicles, undergo stepwise maturation, including Rab-switching, phosphatidylinositol (PI) conversion, endosomal sorting complex required for transport (ESCRT) machinery, as well as lumenal acidification, thus forming late endosomes. Mature cargos are subsequently delivered to cell body in dynein-dependent

transportation along the axon (Parton & Dotti 1993). Dysfunctional endosomal networks have been observed in several subtypes of fALS, including ALS2, ALS8, ALS11, ALS12, ALS14 and ALS-FTD3.

Physiologically, alsin acts as a guanine nucleotide exchange factor in membranous compartments that activates key factors for vesicle fusion and endosome maturation (Yang et al. 2001). Alsin is also co-localized with LC3/p62-positive autophagosomes (Hadano et al. 2010). Conversely, Alsin mutants (C157Y, G540E) caused failure of relocalization, leading to accumulation of immature early endosomes (Otomo et al. 2011). VCP-RH mutations (RH9 or RH12) impair maturation of endosome and/or autophagosomes in cultured neurons (Ritz et al. 2011). In the later steps of maturation, missense FIG4 (KIAA0274) causes insufficient PI conversion (Chow et al. 2007). FIG4 KO mice show accumulated LC3-II, p62 and LAMP-2 in neurons and astrocytes with a shorter lifespan (Ferguson et al. 2009). CHMP2B encodes charged multivesicular body (MVB) protein 2B, a component of ESCRT-III complex. Loss of ESCRT-III causes autophagosome accumulation with p62-positive aggregates (Filimonenko et al. 2007), leading to dendritic retraction prior to disease on-set (Lee et al. 2007).

ALS associated-mutations also interfere with ER-Golgi trafficking in soma (Kuijpers et al. 2013; Moustaqim-barrette et al. 2014). Inhibition of VAPB using antibody gives rise to accumulated COP I-coated vesicles (cis-Golgi to ER transports) (Duden 2003). In addition, VABP interacts with transmembrane regions of Yip1-interacting factor homologue A (YIF1A) that is required for membrane trafficking into dendrites (Kuijpers et al. 2013). In the presence of $VAPB^{P56S}$, YIF1A is recruited to the VABP aggregates along with other important factors (Mórotz et al. 2012; Kuijpers et al. 2013), and then loses its ERGIC localization, leading to abnormal dendrite morphology in the early stage in mouse model.

1.3.6 ER stress

The endoplasmic reticulum compartment is a specialised organelle where secreted or membrane proteins are synthesized, folded and processed with the assistance from a large network of chaperones, foldases as well as cofactors (Voeltz et al. 2002). The ER also plays an important role in calcium storage (Lautenschlaeger et al. 2012) and lipid synthesis (Zhou & Liu 2014). If the homeostasis of ER is disrupted, proteins are misfolded and accumulate within ER lumen, a condition termed as ‘ER stress’ (Naidoo 2009).

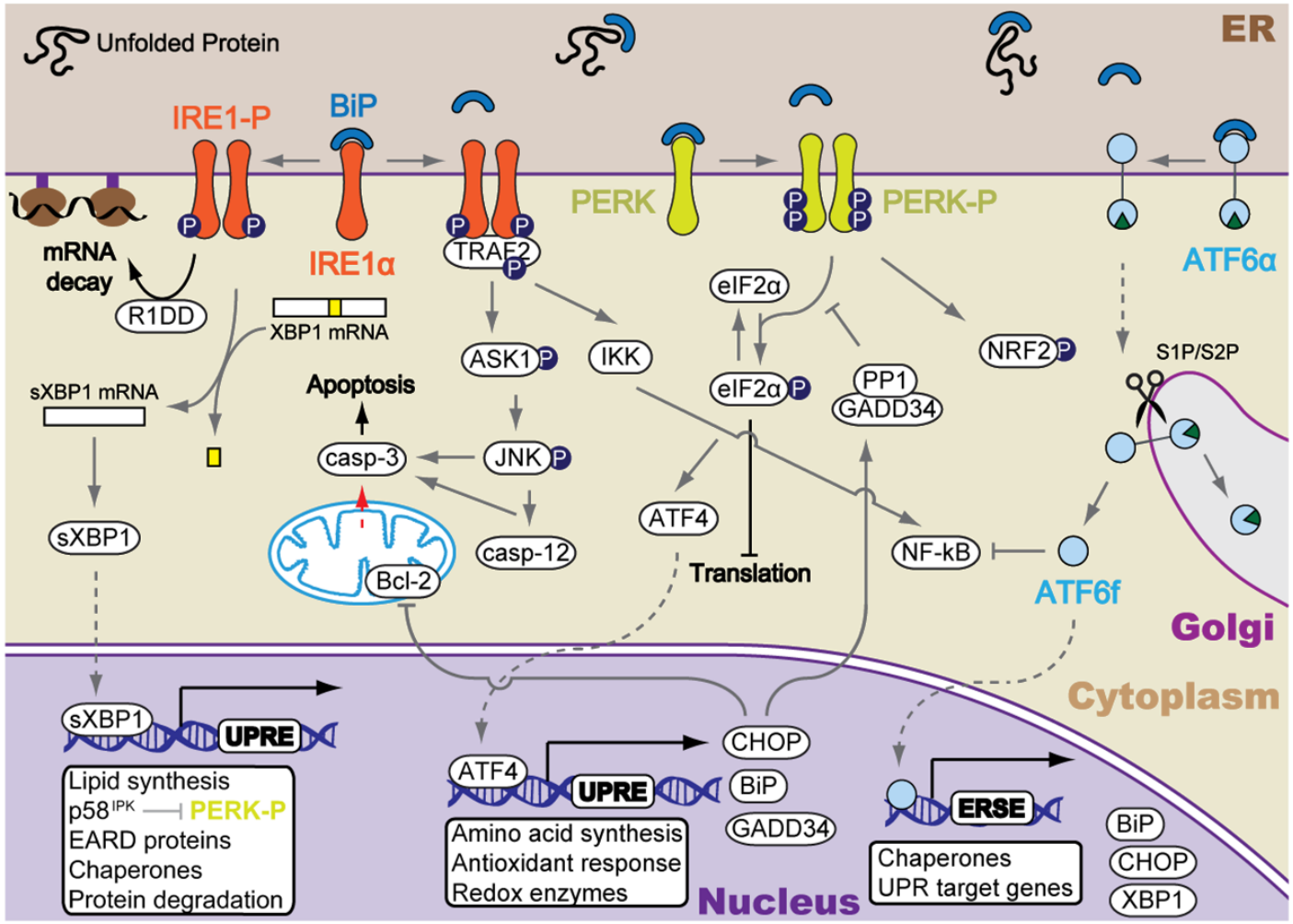

Figure 1.6 ER stress. Upon ER stress, BiP dissociated from UPR sensors (e.g., IRE1, PERK and ATF6) leading to their activation. p-IRE1 splices XBP1 mRNA. p-PERK phosphorylates eIF2α, thereby down-regulating protein synthesis. Meanwhile, p-eIF2α activates ATF4. ATF6 is transported to Golgi, where it is cleaved by S1P/S2P. Then spliced XBP1, ATF4 and fragmented ATF6 translocate into nucleus, upregulating UPR related genes. Once the damage is irreversible, apoptotic factors or pathways (e.g. CHOP, caspases, AKT-JNK, IKK-NF-kB) are activated, resulting in programmed cell death. Abbreviation: ASK1, apoptosis signal-regulating kinase 1; GADD34, growth arrest and DNA damage-inducible protein 34; IKK, IκB kinase; JNK, stress-activated/c-Jun N-terminal kinase; NRF2, NF-E2-related factor 2; PP1, protein phosphatase 1; S1P/S2P, site-1 and site-2 proteases; TRAF2, TNF receptor-associated factor 2.

ER stress engages an integrated signal transduction system which aims to re-establish homeostasis by reducing demand, increasing protein folding capacity and quality control, which is known as unfolded protein response (UPR) (Hetz 2012).The accumulation of unfolded or misfolded proteins is detected by ER stress sensor proteins, such as the inositol-requiring enzyme 1 (IRE1) (Plongthongkum et al. 2007; Pincus et al. 2010), the double-stranded RNA activated protein kinase (PKR) like ER kinase (PERK) (Sou et al. 2012; Huber et al. 2013), as well as the activating transcription factor 6 (ATF6) (Wang et al. 2000; Yoshida et al. 2001). ER stress sensors are bound to chaperone BiP (GRP78, HSPA5). However, in the presence of unfolded proteins, BiP dissociates from sensor proteins and binds to unfolded/misfolded proteins (Bertolotti et al. 2000), thereby activating UPR pathways (Figure 1.6).

Several lines of evidences indicate ER stress is an early event in ALS pathogenesis (Saxena et al. 2009; Saxena & Caroni 2011). Upregulation of IRE1 is reported in sALS cases as well as SOD1^{G93A} mice (Kikuchi et al. 2006; Atkin et al. 2006; Atkin et al. 2008; Saxena & Caroni 2011). Elevated IRE1 is detected before disease on-set in the SOD1^{G93A} mouse model. Accordingly, the amount of spliced XBP-1 (sXBP-1) mRNA is increased in these symptomatic SOD1^{G93A} mice (Kikuchi et al. 2006). In addition, transgenic mice crossbred from SOD1^{G86R} and XBP-1Nes$^{-/-}$ background with XBP-1 deletion in nervous system (Hetz et al. 2008), have a modestly prolonged lifespan compared to SOD1^{G86R} mice alone. Similarly, an upregulation of PERK is observed in SOD1^{G93A} mice (Atkin et al. 2006). Phosphorylated PERK and phosphorylated eIF2α are observed in the spinal cord of these SOD1 mice in the pre-symptomatic stage (Nagata et al. 2007). Drug treatment of SOD1^{G93A} mice using salubrinal, an inhibitor of dephosphorylation of p-eIF2α, improves the muscle force and prolongs lifespan (Boyce et al. 2005). In addition, increased ATF6 is also reported in sALS samples and SOD1^{G93A} mice (Atkin et al. 2008; Atkin et al. 2006). Cleaved ATF6 is elevated in symptomatic or end-stage SOD1^{G93A} and SOD1^{G85R} mice (Kikuchi et al. 2006), whereas the level of full-length ATF6 remained unchanged. Knockdown of ATF6 increases inclusion incidence in cells transiently expressing SOD1^{MT} (Hetz et al. 2009). In addition to ER stress sensors, ER-resident chaperones, such as Grp78, Grp58, protein-disulphide isomerase (PDI), calnexin and calreticulin, are also detected as UPR makers in ALS patients as well as SOD1 transgenic mice (Lautenschlaeger et al. 2012). Increased amounts of PDI are observed in symptomatic as well as in presymptomatic mice (Atkin et al. 2008; Hetz et al. 2009), and PDI colocalized with SOD1 aggregates. Besides SOD1, TDP-43 mutants (Suzuki et al. 2011) and VAPB^{P56S} (Teuling et al. 2007; Gkogkas et al. 2008) are also reported to interact with UPR upstream signalling proteins, therefore enhancing the damage caused by ER stress.

If the restoration of ER homeostasis fails, prolonged activation of UPR can trigger apoptosis even though these mechanisms are cytoprotective (Sano & Reed 2013; Sovolyova et al. 2014). In ALS patients as well as transgenic animal models, once the damage to the cells became irreversible, pro-apoptotic factors are upregulated [BCl-2-like 1 (BCl-xS), Bax, Bad, p53 upregulated modulator of apoptosis (Puma), Chop] and anti-apoptotic proteins (BCl-2, BCl-xL) are down-regulated (Hetz 2012; Sano & Reed 2013; Sovolyova et al. 2014), hence activating caspases.

Aberrant SOD1 mutant-mediated interactions also contribute to disrupted ER homeostasis. Several $SOD1^{MT}$ (A4V, G85R, G93A) specifically interacted with Derlin-1 (Nishitoh et al. 2008), attenuate the retro-translocation of substrates for ER associated degradation (ERAD), subsequently activate IRE1–TRAF2–ASK1 pathway and ultimately lead to cell death. Conversely, overexpression of Derlin-1 ameliorated $SOD1^{G93A}$ or $SOD1^{G85R}$-induced ER stress by reducing misfolded protein accumulation in a cell model (Mori et al. 2011).

1.3.7 Excitotoxicity

In the human CNS, glutamate functions as the main excitatory neurotransmitter. In a fully functional synapse, glutamate binds to postsynaptic receptors. Excitatory signals are terminated by glutamate uptake transporters on surrounding astrocytes or neighboring neurons (Foran & Trotti 2009). Glutamatergic receptors are categorized into ① ion channel-coupled or receptors, e.g. N-methyl-d-aspartic acid (NMDA), AMPA and kainate, and ② G protein-coupled receptors. Classically, a demarcation exists between calcium-permeable NMDA receptors and calcium-impermeable AMPA and kainate receptors. However, AMPA receptors expressed in motor neurons lack the GluR2 subunit, a component normally post-translationally edited at Q/R site in the 2^{nd} transmembrane domain that determines its calcium impermeability (Takuma et al. 1999; Kawahara et al. 2003; Kwak & Kawahara 2005), which renders motor neurons vulnerable towards excitotoxicity.

In ALS patients, excitotoxicity is induced by the excessive activation of glutamate receptors, altered glutamine synthetase or impaired glutamate uptake, giving rise to elevated level of glutamate. Excitotoxicity results in subsequent imbalance between calcium influx-efflux, activation of catabolic enzymes, perturbation of energy production, and ultimately cell death (le Verche et al. 2011). The first hypothesis for increased glutamate levels in ALS patients emerged when transport of glutamate was shown to be selectively decreased in synaptosomes due to loss of excitatory amino acid transporters 2 (EAAT2) (Rothstein et al. 1992). In mouse astrocytes, kappa B-motif binding phosphoprotein (KBBP) is reported to bind to promoter of glutamate transporter

1 (GLT1) (homologous to human EAAT2), reducing KBBP expression and transcriptional dysfunction of GLT-1 (Yang et al. 2009). Specific reduction of the expression of GLT-1 only in affected regions is observed in late-stage $SOD1^{G93A}$ and $SOD1^{G85R}$ mice as well as $SOD1^{G93A}$ rats (Bruijn et al. 1997; Canton et al. 1998; Dunlop et al. 2003), but no significant changes in early-symptomatic stage (Bendotti et al. 2001). In addition, overexpression of GLT-1 in $SOD1^{G93A}$ mice partially rescues excitotoxicity and prolongs lifespan (Kong et al. 2012), indicating loss of EAAT2 might not be a primary event for ALS pathogenesis. Recently, another ALS-linked causative gene involving excitotoxicity has been identified, which encodes D-amino acid oxidase (DAO), an enzyme that metabolizes D-serine (Sasabe et al. 2012). D-serine is a co-agonist and activator of NMDA. DAO^{R199W} potentially contributes to protein aggregation and excitotoxicity via NMDA receptor (Paul & De Belleroche 2014), which induce apoptotic and/or autophagic cell death ultimately.

1.3.8 Neuroinflammation

Neuroinflammation in ALS is normally characterized by activated astrocytes, microglia and infiltrating lymphocytes (Komine & Yamanaka 2015), an immune response could also contribute to ALS progression, which has been discussed in section 1.2.3.3.4.

1.3.9 Impaired axonal transport

Axonal transport is also important in ALS pathophysiology, as motor neurons are highly polarized group of cells with long axons that require robust transport of essential materials to the axon. The transport machinery usually composed of ① microtubule-dependent kinesin-mediated anterograde transport towards the neuromuscular junction and ② cytoplasmic dynein-dynactin mediated retrograde transport towards the cell body (Hirokawa et al. 2009; Bowman & Goldstein 2009). Defects in either supply or clearance within an axon potentially lead to neuronal death.

Inhibition of kinesin-based fast transportation by $SOD1^{MT}$ is detected in both fALS and sALS cases (De vos et al. 2007), however, no interaction between $SOD1^{MT}$ and kinesin-family members has been characterized in $SOD1^{G93A}$ mice. Conversely, defective dynein-dynactin is more directly linked to neurodegenerative diseases. Mutations of DCTN1, which encodes $p150^{Glued}$ subunit of dynactin, cause human distal hereditary motor neuropathy (Münch et al. 2004). Overexpression of $p150^{Glued}$ mutant causes a dissociation of dynactin complex (Vaughan et al. 2002; Watson & Stephens 2006; Lloyd et al. 2012), resulting in defects in vesicular transport, axonal swelling, axon-terminal degeneration as well as autophagic death. Besides the causative or contributive variants, other cellular events underlying pathogenic processes are also involved. For instance, ① impaired mitochondrial fission/fusion as well as defects of

axonal transport result in low mitochondrial contents in distal axons, leading to global defective transport due to insufficient energy supplement (Dupuis et al. 2009). ② Increased glutamate, an important transmitter mediated excitotoxicity reduces transportation of neurofilament via phosphorylation (Ackerley et al. 2000). The p38 MAPK is observed to be activated in $SOD1^{G93A}$ mice as well, which also phosphorylates neurofilaments. (Ackerley et al. 2004) ③ The damaged cargos could aberrantly bind to, or release from motors, disrupting global stoichiometry and causing axonopathy (Fischer et al. 2004), resulting in the typical 'dying-back' phenomenon observed in ALS patients.

1.4 Therapeutics strategies in ALS

1.4.1 ALS animal models

Shortly after the discovery of SOD1 mutations in fALS cases, a transgenic mouse model expressing 20-24 copies of human $SOD1^{G93A}$ under human SOD1 (hSOD1) promotor was developed (Gurney et al. 1994). Since then, many SOD1 transgenic animal models have been created, including *C. elegans*, *Drosophila*, zebrafish, chicken, mouse and rat. In addition, endogenous SOD1 variants were also reported in dog and chimpanzee. Amongst different species, rodents are widely utilized as the primary model for ALS research.

$SOD1^{MT}$ transgenic rodent models recapitulate clinical features of ALS patients, including mitochondrial vacuolation, distal axonopathy, neuromuscular dysfunction, gliosis and most importantly, loss of motor neurons (McGoldrick et al. 2013). Instead of universal hSOD1 promoter, specific promoters to express SOD1 in nervous system, astrocytes or microglia have also been utilized to investigate cell autonomous or non-cell autonomous effects in ALS (Van Den Bosch 2011; McGoldrick et al. 2013; Turner & Talbot 2008). SOD1 transgenic rodents exhibit variable ages of symptom onset and rates of disease progression. Developments of ALS-like symptoms are highly dependent on 4 factors: SOD1 mutation, copy number, gender and genetic background. Studies using SOD1 rodent models lay the foundation for our understanding of the mechanisms underlying pathophysiology of ALS. To date, several transgenic rodent models expressing ALS pathogenic genes have been developed, including SOD1, ALS2, TDP-43, FUS, SETX, VAPB, FIG4, OPTN, VCP, UBQLN2, CHMP2B, ERBB4, C9orf72, DCTN1, DAO, NEF-L, PRPH, VEGF and MAPT.

1.4.2 Therapeutics strategies targeting ALS

Over the past three decades, there have been a large number of double-blind, placebo-controlled clinical trials carried out, targeting the potential pathogenic mechanisms underlying ALS (Table 1.6). Respiratory and nutritional treatments could improve overall survival (Goyal & Mozaffar 2014), but only a few successes have been achieved in pharmacological human trials (Mitsumoto et al. 2014), even though many agents were shown to be effective in animal models. These challenges need to be overcome for successful therapy to reach clinics.

Targets	Clinical trials	Presumed mechanisms
Mitochondrial dysfunction	Creatine, acetyl-L-carnitine, olesoxime, dexpramipexole.	Stabilizes mitochondrial membrane permeability.
Oxidative stress	CoQ10,N- acetylcysteine, glutathione, vitamin E, *edaravone*, selegiline. dexpramipexole	Increases anti-oxidative property, free radical scavenge.
Proteinopathy	Arimoclomol.	Facilitates degradation of aggregates.
Excitotoxicity	Branched-chain aminoacids, lamotrigine, *riluzole*, gabapentin, nimodipine, dextromethorphane, memantine, topiramate, mexiletine, ceftriaxone, talampanel.	Reduces glutamate release, Ca^{2+}channel blocker, reduces glutamate, NMDA receptor blocker, AMPA receptor blocker, antagonists, GABA-analog, increases EAAT2 activity.
Neuro inflammation	Plasma exchange, total lymphoid irradiation, glatiramer acetate, cerecoxib, minocycline, masitinib NP001, cyclosporine.	Humoral factors, T-cell, microglial suppressor, anti-inflammatory, vaccination theory, T-helper cells.
Apoptosis	Pentoxyfilline, TCH346, minocycline.	Inhibits TNFα linked apoptosis, Inhibits GAPDH-linked apoptosis.
Autophagy	Lithium carbonate, pioglitazone.	Facilitates degradation of aggregates.
Astrocytes	Ono-2506	Blocks gliosis.
Neurotrophic factors	CNFT, *IGF-1*, BDNF, GDNF, xaliprodene, GCSF.	Pleotropic neurotropic receptors, retrograde transport from the muscle axonal terminals, serotonin agonist.
Growth factors	Cholinesterase inhibitors, growth hormone, erythropoietin, octacosanor, gangliosides, thyrotropine releasing hormone.	Myotrophic effects, systemic trophic factors, ergotropic effects.
Genetic defects	Phenylbutirate, valproic acid, antisense SOD1 oligonucleotides	Histone deacetylase inhibitor, blocks production SOD1.
Stem cells	hSCNSC, aMSC, hNSC, aBMSC.	Replacement of lost or degenerating neurons.
Viral infection	Transfer factor, tilorone, indinavir	Antiviral

Table 1.4 Drug treatments tested in clinical trials targeting ALS. *Table 1.6 adapted from Mitsumoto et al (2014).*

Nearly 50 randomised controlled trials have been undertaken since 1980, riluzole is the only FDA and EMA approved disease-specific medication for ALS (Gibson & Bromberg 2012). After riluzole and IGF-1, FDA accepted another new drug application in 2016, therefore, edaravone becomes the third potential ALS drug in history. Currently, there are several candidate drugs are being tested in phase III (masitinib combined with riluzole, edaravone, creatine, vitamin E, IGF-1, MCI-186, ceftriaxone and minocycline), together with candidates that get out of phase II (arimoclomol, mecobalamin, mexiletine, tauroursodeoxycholic acid, co-enzyme Q10 and cannabis sativa) (Turner et al. 2009; Bruijn & Cudkowicz 2006; Gibson & Bromberg 2012; Mitsumoto et al. 2014; Ittner et al. 2015). In addition, to treat the muscle cramps caused by ALS, mexiletine was also tested for off label use (Stephens et al. 2017).

Development of ALS drugs is at a pivotal point as most of the human clinical trials are reported to be negative and no effective disease-modifying strategies have been introduced to clinic since riluzole. It is plausible that ALS is a complex disorder with heterogenous causes; therefore, a single drug is unlikely to have a significant effect on disease progression. Paradoxically, the agents tested on sALS patients in clinical trials were pre-tested in SOD1 animals, but the majority of sALS cases show no defects of SOD1. Furthermore, drug treatments on transgenic animals are normally carried out at pre-symptomatic stage, yet patients in clinical trials were often treated at post-symptomatic stage, which might partially explain why drug developments targeting ALS achieved so little in the past 30 years. Among distinct potential strategies aiming at restoring proteostasis, molecular chaperones have shown significant importance in protein quality control in ALS pathogenesis.

1.5 Protein quality control

In crowded intracellular compartments, stochastic fluctuations, the presence of destabilising sequence variants, environmental stress, or metabolic challenges can cause proteins with exposed hydrophobic domains to misfolding. Therefore, elaborate intrinsic networks of protein quality control have evolved to monitor and maintain the integrity of protein homeostasis (proteostasis). Cellular protein quality control depends on three interconnected pathways, i.e. ubiquitin proteasome system (UPS), autophagy, and molecular chaperones, whereby misfolded proteins either be refolded, degraded or be sequestrated.

1.5.1 Ubiquitin proteasome system

Most soluble, short-lived misfolded or damaged proteins are cleared via UPS, a rapid, precise and timely processing protein degradation pathway implicated in several cellular processes, for instance, maintenance of protein quality control, DNA repair, proliferation, signal transduction and cell stress response (Nandi et al. 2006). E1/E2/E3 ubiquitin ligases labelling substrates with polyubiquitin allowing them to be recognized and then degraded by 26S proteasomes (Myung et al. 2001).

The 26S proteasome is a 2.5MDa complex composed of a 20S proteolytic core and 19S regulatory cap (Gallastegui & Groll 2010). The 20S core consists of four heptameric staggered rings, including 2 outer α-rings guarding the proteasome chamber and 2 inner β-rings harbouring proteolytic activities. The 19S regulatory cap is composed of a base as well as a lid. Both the base and the lid contain subunits that bind to polyubiquitin chains. Once the substrates are bound to the 19S subunit, the ubiquitin chains are cleaved by the metalloisopeptidase Rpn11 subunit from the lid complex, and subsequently unfolded by the AAA-ATPase subunits on the base (Verma et al. 2002). Then the unfolded peptides proceed to proteolytic 20S chamber, where the substrates are broken down into peptide fragments. The cross-talk between UPS and chaperone machinery has not been fully characterized, but several E3 ligase family members are known to ubiquitylate substrates in an Hsp70-dependent way (Demand et al. 2001; Esser et al. 2004), including carboxy-terminal Hsp70 interacting protein (CHIP).

Misfolded proteins in ER lumen or membrane are cleared by ERAD (Meusser et al. 2005). Misfolded proteins are recognized by ER chaperones, e.g. the Hsp70 protein BiP, ER degradation-enhancing alpha-mannosidase-like lectins (EDEM), PDI, calnexin and calreticulin (Araki & Nagata 2011). Powered by energy derived from ATP hydrolysis, the retrotranslocation machinery composed of p97/VCP complex drives the polypeptides across ER membrane transport channels to the cytosol (Zhong et al. 2004;

Lim et al. 2009), where the substrates are modified by E3 ligases in an ATP-dependent manner. Subsequently, the substrates with polyubiquitin chain are recognized and degraded by UPS in cytosol. Upon extreme cellular stress, ERAD functions as the final defence strategy for ER homeostasis.

1.5.2 Autophagy

Misfolded or aggregated proteins can also be cleared via the lysosome-autophagy system, which targets long-lived macromolecular complex as well as organelles (Glick et al. 2010). Executed by autophagy-related genes (ATG), autophagy is an evolutionarily conserved mechanism for degradation and renovation, functioning in housekeeping, differentiation, growth control, defence, metabolic regulation, tissue remodelling and acclimatization. Autophagy is classified into three subtypes, i.e., macroautophagy (Feng et al. 2014), microautophagy (Li et al. 2012), and chaperone-mediated autophagy (CMA) (Majeski & Fred Dice 2004).

Stress signals (e.g., oxygen shortage, growth factor deprivation, starvation, DNA damages, etc.) induce the autophagic regulator protein kinase, mammalian target of rapamycin complex (mTORC1) as well as adenosine monophosphate-activated protein kinase (AMPK) dephosphorylate ULK1 (ATG1 orthologs) complex that subsequently activate the Beclin-1 class III phosphatidylinositol 3-phosphate kinase (PI3K)-Vps34 core complex These complexes function to produce phosphatidylinositol-3-phosphate (PI3P) (He & Klionsky 2009), initiating the assembly of isolation membranes. The crescent-shaped isolation membrane elongates and closes via two ATG7-dependent ubiquitin-like conjunction systems: ① ATG7 (E1-like) and ATG10 (E2-like) conjugate ATG5 to ATG12, ATG5-ATG12 conjugation complex then binds ATG16L in a non-covalent way (Hanada et al. 2007).② pro-LC3 (ATG8 orthologs) is converted to LC3-I by ATG4 cleavage (Geng & Klionsky 2008), then linked with phosphatidylethanolamine (PE) to form LC3II and subsequently introduced to the membrane of phagophore, by ATG7, ATG3 (E2-like) as well as ATG5-ATG12-ATG16L complex (E3-like). After maturation, autophagosomes containing sequestrated cytosolic substrates are docked to and fused with lysosome (Ganley 2013), allowing the digestion of cargos by acidic hydrolases. In addition, microautophagy involves direct engulfment of cytoplasmic cargos at a lysosomal membrane by tubes, which mediate invagination and vesicle scission into the lysosomal lumen (Uttenweiler et al. 2007). In CMA, proteins containing a pentapeptide KFEQR motif are recognized by Hsc70 then targeted to lysosome for degradation via lysosome-associated membrane protein 2 (LAMP2a) (Cuervo & Wong 2014). Other than non-selective autophagy, emerging findings indicate that selective autophagy is observed in mammalian cells, including mitophagy, perophagy, reticulophagy, crinophagy, aggrephagy, xenophagy and ribophagy.

The need for proteostasis requires both functional degradative pathways. The UPS and autophagy are tightly controlled and coordinated. A number of studies demonstrate a close cross-talk between UPS and autophagy (Korolchuk et al. 2010). Impairment of the UPS would trigger compensatory autophagy (Pandey et al. 2007). Conversely, knockdown of ATGs leads to accumulation of ubiquitylated substrates (Komatsu et al. 2006). UPS and autophagy used to be considered as independent; however, recent findings suggest that ubiquitylation targets shared substrates in both mechanisms. In support of this, Johansen et al (2011) reported that autophagic adaptors such as p62, the neighbour of BRCA1 gene 1 (NBR1) and BCL-2/adenovirus E1B 19kDa interacting protein 3-like (BNIP3L), function as bridges between polyubiquitylation and autophagy (Kraft et al. 2010; Johansen & Lamark 2011; Shaid et al. 2012). Autophagic adaptor proteins contain an LC3-II-interacting region (LIR) and an ubiquitin binding domain. Once bound to the ubiquitylated substrates, adaptor targets the client proteins to autophagosome by binding to LC3-II via LIR.

1.5.3 Molecular chaperone machinery

Molecular chaperones are defined as a group of proteins that interact with, stabilize, or assist other polypeptide to gain their native or functionally active conformation without being present in the final structure (Ellis 1987). Physiologically, chaperones are normally associated with protein synthesis, implicated in translation and translocation machinery as well as assisting folding. Upon stress, heat shock proteins (Hsps) serve to protect cells from damage (Lindquist & Craig 1988). Cells possess different classes of chaperones, generally categorized initially based on their molecular mass, i.e., Hsp110, Hsp90, Hsp70, Hsp60, Hsp40 as well as small Hsp (smHsp).

1.5.3.1 HSPC family

Hsp90 is an ATP-dependent chaperone that functions in activation and stabilization of client proteins, including protein kinases, transcriptional factors, cell surface receptors, cell cycle regulators as well as structural proteins (Pearl & Prodromou 2006). Hsp90 engages with various adaptors (co-chaperones) that simultaneously interact with client proteins and Hsp90. In eukaryotic cells, Hsp90 exists as a compact dimer, with an ATP-binding domain (N-domain), substrate-binding domain (M-domain) and a dimerization domain (C-domain) (Li & Buchner 2012). During the substrate delivery process, ATP binds to N domain, which seals the nucleotide binding pocket, inducing a conformational shift. N-domain then dimerizes, enhances ATP hydrolysis (Panaretou et al. 2002), subsequently promoting the dissociation of Hsp90-co-chaperone complex as well as the release of substrates.

1.5.3.2 HSPA family

The Hsp70 subfamily is central to the molecular chaperone network. Hsp70 consists of a N-terminal ATPase domain (NBD) and a C-terminal substrate binding domain (SBD), connected by a linker that enables the NBD to allosterically control conformational changes of the SBD (Mayer & Bukau 2005). The Hsp70 family in human is composed of at least 11 members, including *HSP70*, *HSC70 (HSPA8)*, *GRP75*, *BiP (HSPA5)*, etc.

Hsp70 proteins assist the folding process by transient interaction with exposed hydrophobic segments client proteins and then undergo an ATP hydrolysis-dependent cycle of substrate binding-release steps regulated by co-chaperones (Erbse et al. 2004), such as DnaJ family. DnaJ chaperones bind to the substrate, deliver the client protein to the SBD of an ATP-bound state Hsp70, with binding pocket and lid open. DnaJ simulates the ATPase activity of Hsp70, promoting high affinity substrate binding by promoting lid closure (Laufen et al. 1999). Nucleotide exchange factors such as GrpE and Bag-1 induce the dissociation of ADP as well as rebinding of ATP, triggering the opening of the lid and the release of substrate (Erbse et al. 2004). There are two rate limiting steps in Hsp70 binding-release cycle, i.e. ATP hydrolysis and ADP dissociation. Therefore, co-chaperones as well as other co-factors are required for the cycling between ATP-ADP bound states (Szabo et al. 1994).

As one of the most highly conserved classes of HSPs, Hsp70 plays an indispensable role in proteostasis: Hsp70 is reported to assist folding of nascent proteins, assist precursors assemble into oligomers in the cytosol, ER as well as mitochondria, refold misfolded polypeptides to functionally native state, promote the trans-membrane protein transport, and disassemble preformed aggregates.

1.5.3.3 DNAJ family

The DnaJ family is the main driver as well as regulator of Hsp70 machinery. DnaJ proteins share a highly conserved J-domain that composed of 4 α-helices that is crucial for lowering the activation energy of ATP hydrolysis (Greene et al. 1998). Ranging from 10 to 254kDa in molecular mass, DnaJ chaperones are further classified into 3 subtypes depending on domain composition (A, B and C) (Cheetham & Caplan 1998) . The DnaJA subfamily shares all the domains presented in *E. coli* DnaJ, including an N-terminal J-domain, a Gly/Phe (G/F)-rich region, a zinc-finger motif and a C-terminal client binding region (CBD). DnaJB family contain an N-terminal J-domain, a Gly/Phe (G/F)-rich region, whereas DnaJCs contain a J-domain that is not necessarily located at the N-terminus.

DnaJ proteins function as co-chaperones in a chaperone network with Hsp70. The J-domain facilitates interaction with Hsp70 by binding to NBD domain, thereby simulating its ATPase activity as well as recruiting substrates (Gssler et al. 1998). Additionally, DNAJ proteins bind to C-terminal EEVD-motif of Hsp70 via CBD domain (Suzuki et al. 2010). In conjunction with Hsp70, DNAJ family members are further implicated in the Hsp90 network (Cintron & Toft 2006), folding/refolding within ER compartment (DnaJB11/ERdj3), stress signal response (DnaJC3/p58IPK in the UPR), translation (Sis1, DnaJC2/Mpp1), protein translocation (DnaJC1/ERdj1, DnaJC23/ERdj2 and DnaJC13/Rem-8), protein degradation (DnaJA1/Hdj2, DnaJB2/HSJ1).

1.5.3.4 HSPB family

Small Hsp family is a group of ATP-independent chaperones with molecular weight in the range of 15-30kDa (Garrido et al. 2012), including Hsp25 (HSPB1), MKBP (HSPB2), Hsp27 (HSPB3), αA-crystallin (HSPB4), αB-crystallin (HSPB5), Hsp20 (HSPB6), cvHsp (HSPB7) and Hsp22 (HSPB8). Small Hsp chaperones share a conserved α-crystallin (ACD) domain in C-terminal region that is flanked by variable N-terminal domain (NTD) and C-terminal extension (CTE) (Sun & MacRae 2005). The CTE mediates substrates recognition and promotes the formation of oligomers (Mogk et al. 2003). Many small Hsps are able to bind to unfolded or misfolded proteins, keep substrates in a folding-competent state, thereby preventing aggregation and assisting refolding or degradation of substrates in concert with other ATP-dependent chaperones (Lee et al. 1997). In addition, by undergoing transient phosphorylation, small Hsp also play a role in signal transduction (Calderwood et al. 2010).

1.5.4 *Homo sapiens* DnaJ protein 1

In 1992, Cheetham *et al* reported the identification of *Homo sapiens* DnaJ 1 (HSJ1) from an Alzheimer's disease patient human brain frontal cortex expression cDNA library using an antibody against paired helical filaments (PHF) (Cheetham et al. 1992). HSJ1 shared high sequence similarity with the *E.coli* DnaJ protein J domain and was the first human DnaJ protein identified.

Encoded by a gene located at chromosome 2q32-q34 (Chapple et al. 1999), HSJ1 is a type II DnaJB protein that is alternatively spliced into two isoforms, HSJ1a and HSJ1b (Cheetham et al. 1992). Both of isoforms consist of ① a J domain, ② a G/F rich region, ③ a client binding domain (CBD) and ④ two ubiquitin-interaction motifs (UIMs) (Figure 1.7). Interestingly, UIM domains are unique to HSJ1 amongst the DnaJ subfamily (Westhoff et al. 2005). The two isoforms only differ at their C-terminus: HSJ1a contain a DVF domain but HSJ1b contains a terminal extension with a terminal CAAX box than enables prenylation. HSJ1 is preferentially expressed in neurons yet there are distinct

localizations between isoforms (Chapple & Cheetham 2003): HSJ1a is present in the nucleus and cytoplasm, whereas HSJ1b localises to the cytosolic face of ER via the prenyl geranyl-geranyl moiety added to the C-terminus.

HSJ1 can function to target substrates to proteasome for degradation in neurons. HSJ1 is reported to directly interact with non-ubiquitylated client proteins, and stimulate substrate loading onto Hsp70 via its J-domain (Westhoff et al. 2005). Alternatively, HSJ1 can recognize ubiquitylated substrates with ubiquitin chains of more than 4 moieties through its UIMs. Once the substrate is bound to Hsc70, CHIP/Ubc5 machinery ubiquitylates the HSJ1-client conjugation complex. Hence, HSJ1 can act as an escort factor, accompanying ubiquitylated client proteins for degradation. Upon nucleotide exchange, if the chaperone-client complex dissociates, the UIMs binding to ubiquitin chains could protect the client proteins from ubiquitin hydrolases, thereby ensuring the proteasomal signal remains intact. Westhoff *et al* (2005) reported that HSJ1a docked to the proteasome via UIMs. In addition, HSJ1b can target unfolded/misfolded ER membrane proteins for ubiquitylation and degradation via ERAD pathway (Chapple & Cheetham 2003; Westhoff et al. 2005), for instance, cystic fibrosis transmembrane conductance regulator (CFTR) and G-protein coupled receptor melanocortin-4 receptor (Meimaridou et al. 2011).

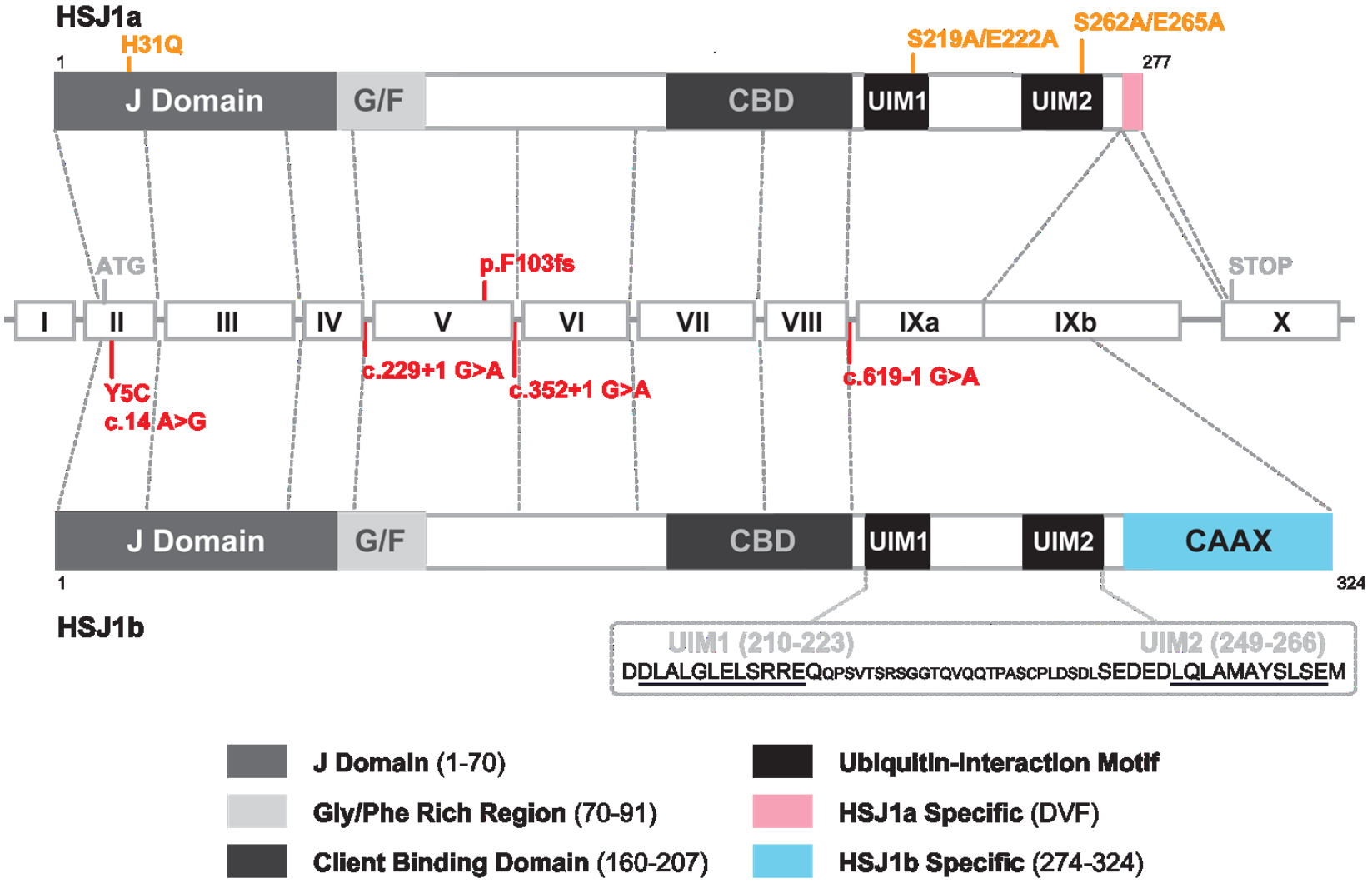

Figure 1.7 Domains and mutations in the two HSJ1 isoforms. HSJ1 is alternative spliced into 2 isoforms at C-terminus, HSJ1a and HSJ1b. Both isoforms contain a J-domain, G/F rich region, client binding domain and two UIMs. Mutations labelled in red indicate the disease mutations discovered in human patients. Mutations labelled in orange are generated via mutagenesis in the Cheetham lab to investigate HSJ1 function.

In 2012, Blumen *et al* reported the first case of autosomal recessive distal hereditary motor neuropathy (dHMN) caused by a mutation in *DNAJB2* in a consanguineous Jewish family (Blumen et al. 2012). Since then, four additional mutations have been discovered in familial cases (Figure 1.6). Amongst these five mutations, four are splicing mutations that result in premature stop codon and loss of expression. In 2014, Gess *et al* reported a missense substitution mutation HSJ1^{Y5C} in a family presenting a phenotype of dHMN and Charcot-Marie-Tooth type 2 (CMT2) (Gess et al. 2014). Teive *et al* (2016) reported that a dHMN Brazilian patients carrying HSJ1 mutation presented a phenotype of peripheral motor neuropathy, associated to parkinsonism and cerebellar ataxia (Teive et al. 2016). Sanchez *et al* (2016) identified a deletion of exon 2-4 (3.8kB) in a family presented phenotypes of SMA and Parkinsonism (Sanchez et al. 2016). Unpublished work in Cheetham lab (Heather Smith PhD thesis) has confirmed that Y5C leads to destabilization of HSJ1 and reduced expression by 95%. Collectively, these genetic data demonstrate HSJ1 is an important factor implicated in motor neuron survival.

1.6 Chaperones and neuronal homeostasis

1.6.1 Failure of protein quality control in ALS

Proteomic studies on the brain and spinal cord tissue obtained from transgenic rodent ALS animal models indicate that failure of protein quality control is a common event in pre-symptomatic stage or at the early stages of symptom on-set (de Oliveira et al. 2013; De Oliveira et al. 2014). These studies revealed reduced capacity of chaperones, impaired UPS as well as altered autophagic markers. Furthermore, dominant genetic variants encoding for components of the protein quality control machinery related to vesicle transport, autophagy, ER homeostasis and UPS, including p62, optineurin, VCP, VAPB and ubiquilin-2 are associated with ALS, indicating protein quality control is important in ALS pathogenesis.

In SOD1^{G93A} and SOD1^{G85R} mice, chaperone capacity is reduced in spinal cord prior to symptom onset (Bruening et al. 1999; Tummala et al. 2005). Several chaperones are detected in the inclusions formed within transgenic mice spinal cord, including Hsp25, αB-crystallin, Hsc70 and CHIP (Jain et al. 2008). It has been suggested that increased levels of misfolded proteins are loaded onto unchanged levels of the chaperone machinery, thus resulting in diminished chaperone activity.

Global reduced proteasomal activity is observed in affected neurons in the late pre-symptomatic or early symptomatic stage of SOD1^{G93A} mice (Kabashi & Durham 2006). Kabashi *et al* (2004) discovered that in these transgenic mice, a reduction in 20S β-

subunits resulted in dysfunction of UPS (Kabashi et al. 2004). Meanwhile, experimental evidence shows that partially ubiquitylated SOD1 are co-aggregated with CCS (Kato et al. 2001), 20S subunits, ubiquitin and several Hsps (Prause et al. 2013), further supporting the theory that UPS is clogged and impaired in ALS pathogenesis (Cheroni et al. 2005; Kabashi et al. 2004).

Autophagy induction has been observed in $SOD1^{G93A}$ and $SOD1^{H46R}$ mice, supported by elevated level of autophagic marker LC3-II detected in the early stages of disease onset (Morimoto et al. 2007; Li et al. 2008; Zhang et al. 2011). Autophagosome accumulation was observed in late stage transgenic mice as well as the post-mortem tissues from sALS patients (Tokuda et al. 2016; Zhang et al. 2011), indicating a vesicle trafficking dysfunction, which might further contribute to disease progression by inducing autophagic cell death. Interestingly, knock out of neuronal autophagic machinery component (ATG7) did not cause ALS-phenotypes in transgenic mice (Tashiro et al. 2012), but in the same study, ablation of UPS component RPT3 in motor neurons induced ALS-like symptoms.

1.6.2 Up-regulation of molecular chaperone is neuroprotective

Given the potential neuroprotective effects of chaperones in protein quality control as well as the high threshold for induction of heat shock response in motor neurons, upregulation of one single chaperone or group of chaperones could be used as therapeutic approaches to combat neurodegeneration. Increasing evidence show that the chaperone machinery is protective in various neurodegenerative models (Table 1.7) (Smith et al. 2015).

Family	Member	Disease/ protein	Highlights
HSP110	HSPH2	**ALS/SOD1**	Improved vesicle transport deficit in SOD1^{G85R} squid axoplasm; with DNAJB1 suppressed polyQ toxicity in flies.
		HD/Htt	
	HSPH1	AD/Tau	HSP105 knock out mouse had increased p-tau and Aβ; suppressed aggregation of SOD1^{G93A} in cells.
		ALS/SOD1	
HSP90	HSPC1	AD/ Aβ	Reduced Aβ aggregation *in vitro*; with Hsp60 and Hsp70 Aβ mitochondrial dysfunction in cells.
HSP70	HSPA5	AD/ Aβ	Bound APP and reduced Aβ secretion; reduced polyQ aggregation and toxicity in cells; reduced α-syn toxicity in rats; reduced P23H rhodopsin aggregation and photoreceptor cell death.
		HD/Htt	
		PD/α-syn	
		RP/Rho	
	HSPA8	AD/Tau	Bound tau and facilitates microtubule polymerization reducing insoluble tau; QBP1 fusion reduced polyQ aggregation and toxicity in cells and mice, ATPase mutant reduced large polyQ aggregates but no effect on defect in polyQ fly; binds α-syn and reduced toxicity of binding to mutant SOD1.
		HD/Htt	
		PD/α-syn	
		ALS/SOD1	
	HSPA1 A*	AD/ Aβ	Reduced Aβ aggregation in vitro and in transgenic mice; modest effect on R6/2 Htt mice but increased aggregation on knock-down in HD flies; suppression of α-syn toxicity in flies cells and mice, but another report found no effect in mice; reduced mutant SOD1 aggregation in cells but had no effect in mice;
		AD/Tau	
		HD/Htt	
		PD/α-syn	
		ALS/SOD1	
		ALS/TDP43	
HSP40	DnaJA1	AD/Tau	Antagonized protective effect of Hsp70 on Tau; increased polyQ aggregation in some cell models; increase binding of Hsp70 to α-syn.
		HD/Htt	
		PD/α-syn	
	DnaJB1	AD/ Aβ	Reduced Aβ aggregation in vitro with Hsp70; suppressed Htt inclusion formation but did not affect toxicity in cells, but protective with Hsp110 in flies;
		HD/Htt	
		PD/α-syn	
	DnaJB2	AD/Tau	Reduced polyQ aggregation *in vitro*, in cells, in mice and rats; reduced mutant SOD1 aggregation in cells and mice; suppress mutant parkin aggregation and promote functional refolding in cells; refold and inhibit Tau aggregation in cells; refold p-TDP-43 in cells; reduced C9orf72 aggregation in cells.
		HD/Htt	
		PD/Parkin	
		ALS/SOD1	
		ALS/TDP43	
		ALS/C9orf7	
	DnaJB6	AD/ Aβ	Efficient block of Aβ aggregation in vitro; blocked polyQ aggregation and toxicity in cells and frogs.
		HD/Htt	
	DnaJB8	HD/Htt	Blocked polyQ aggregation and toxicity in frogs.
	DnaJC10	RP/Rho	Reduced P23H rhodopsin aggregation in cells.
small HSP	HSPB1	AD/ Aβ	Reduced Aβ aggregation in vitro and toxicity on cells and in mice; altered Tau dynamics in mice; reduced polyQ aggregation and toxicity in cells and by viral delivery in rats but not transgenic mice; reduced α-syn fibril formation *in vitro* and toxicity in cells; reduced SOD1 aggregation *in vitro* but small effects in mice.
		AD/Tau	
		HD/Htt	
		PD/α-syn	
		ALS/SOD1	
	HSPB8	HD/Htt	Reduced Aβ aggregation *in vitro* and toxicity on cells; reduced polyQ aggregation; Most effective small Hsp at reducing α-syn fibril formation *in vitro*; enhanced autophagic clearance of SOD1 and TDP-43.
		PD/α-syn	
		ALS/SOD1	
		ALS/TDP43	
	HSPB5	AD/ Aβ	Reduced Aβ aggregation in vitro and toxicity on cell; reduced toxicity of α-syn in cells; reduced α-syn fibril formation *in vitro*; SOD1 aggregation *in vitro* but does not protect in mice.
		PD/α-syn	
		ALS/SOD1	
		PD/α-syn	

Table 1.5 Chaperones that combat neurodegeneration-related protein misfolding. *Aberrations*: α-syn, α-synuclein; Aβ, amyloid beta; AD, Alzheimer's disease; ALS, Amyotrophic lateral sclerosis; HD, Huntington's disease; Htt, huntingtin; PD, Parkinson's disease; Rho, rhodopsin; RP, retinitis pigmentosa.

In ALS pathogenesis, several chaperones are reported to ameliorate the symptoms in cell and animal models. ① Urushitan *et al* (2004) reported that Hsc70 (HSPA8) bound to, and ubiquitylated $SOD1^{G93A}$, hence promoting the degradation of SOD1 aggregates with the assistance of CHIP in a cell model (Urushitani et al. 2004). Furthermore, CHIP was discovered to be expressed and presented in ubiquitylated inclusions in spinal cord of $SOD1^{G93A}$ mice. ② In 2005, another member of Hsp70 family, Hsp70 (HSPA1A*) was reported to enhance the UPS degradation pathway, thereby reducing $SOD1^{H46R}$ and $SOD1^{G93A}$ inclusions in COS-7 cells as well as primary neurons (Matsumoto et al. 2005; Koyama et al. 2006; Matsumoto et al. 2006). Overexpression of Hsp70 in *Drosophila* rescued the eye phenotypes due to TDP-43^{A315T} toxicity (Estes et al. 2011). Disappointedly, Liu *et al* (2005) observed that elevated Hsp70 expression had no effects on disease onset or survival of $SOD1^{G93A}$, $SOD1^{G85R}$ and $SOD1^{G37R}$ mice (Liu et al. 2005). ③ Patel *et al* (2005) reported the protective effects of Hsp27 against apoptosis and oxidative stress caused by SOD1 are reported *in vitro* as well as in neuronal cells stably expressing $SOD1^{G93A}$ or $SOD1^{G93R}$ (Patel et al. 2005). *In vitro* studies demonstrate Hsp27 directly interacts with $SOD1^{MT}$, inhibiting aggregation elongation, rather than inhibiting formation of aggregate nuclei (Yerbury et al. 2013). In 2008, $SOD1^{G93A}$/HSP27 double transgenic mice exhibited delayed dysfunction of muscle force, a significant improvement in functional motor neuron units, and increased neuron survival only in the early phase of disease (Sharp et al. 2008). There was no evidence of sustained protective effects of Hsp27. ④ Hsp22 forms a complex with Bag3/Hsc70/CHIP in a cell model (Crippa et al. 2010), and enhanced autophagic clearance of on $SOD1^{G93A}$ and TDP-43 aggregates when proteasome activity was blocked. ⑤ Song *et al* (2013) discovered Hsp110 rescued the vesicle transport deficit in $SOD1^{G85R}$ squid axoplasm (Song et al. 2013). ⑥ Xu *et al* (2014) reported transgenic expression of small Hsp αB-crystallin (HSPB5) at> 6-fold the normal level in spinal cords of $SOD1^{G93A}$ mice was insufficient to attenuate protein aggregation or delay the onset of paralysis (Xu et al. 2014), even though studies showed αB-crystallin inhibited $SOD1^{G93A}$ aggregation formation *in vitro* (Yerbury et al. 2013).

However, the genetic manipulation of chaperones, in particular Hsp70 and Hsp27, had limited benefit in combating ALS progression *in vivo*. Thereby, a novel strategy that modulates chaperone networks, instead of manipulation of single chaperone protein proved to be more effective in restoring proteostasis. ① Kieran *et al* (2004) reported that arimoclomol amplified Hsp expression by enhanced binding of HSF-1 to heat shock elements, subsequently upregulated expressions of Hsp90, Hsp70 and Hsp60, hence modifying the disease (Kieran et al. 2004). Treatment with arimoclomol at pre-symptomatic or early stage after disease onset delayed the disease progression.

SOD1^{G93A} mice showed decreased ubiquitylated inclusions, and improvements in muscle force and motor neuron survival. Arimoclomol treatment at late stage was still able to delay the disease progression with a 22% increase in lifespan and reduced protein aggregation in SOD1^{G93A} mice (Kalmar et al. 2014; Kalmar et al. 2008). ② Celastrol addition to the diet significantly improved weight loss, muscle performance, motor neuron survival and delayed the symptom on-set in SOD1^{G93A} mice (Kiaei et al. 2005). Celastrol can induce Hsps and can also act as anti-inflammatory agent that is reported to reduce TNF-α, CD40, GFAP expression and inhibit NO production in lumbar spinal cord of ALS mice. ③ Overexpression of HSF-1 in SOD1^{G93A} mice improved the bodyweight loss, delayed age-of-onset and progression, and benefits early survival (Lin et al. 2013). It is the first *in vivo* study demonstrated that HSF-1 activation is a validated strategy for ALS animal models. ④ An inhibitor of Hsp90, named NXD30001, induced expression of HSPA1/DNAJ following the activation of HSF-1, which exhibited protective effects on cultured motor neurons dissociated from SOD1^{G93A} mice (Cha et al. 2014). Unfortunately, drug treatment using NXD30001 showed no effects *in vivo*.

1.6.3 HSJ1 restores proteostasis in neurodegeneration

HSJ1 can act as a potential modulator to restore proteostasis in multiple neurodegenerative disorders.

Emerging evidence demonstrate that HSJ1a overexpression can significantly reduce Htt inclusions in cells as well as transgenic animals. Overexpression of HSJ1a as well as non-membrane associated HSJ1b (generated via mutagenesis on CAAX box) significantly reduced polyQ inclusion incidence (Westhoff et al. 2005; Borrell-Pagès et al. 2006). Westhoff *et al* (2005) reported that the activity of HSJ1 to modulate polyQ aggregation was J-domain and UIM dependent (Westhoff et al. 2005). In addition, Howarth *et al* (2009) reported that HSJ1a and HSJ1b increased the presence of ubiquitinated proteins in the insoluble fraction in the N2a cells expressing polyQ (Howarth et al. 2009). In HD cell model, UPS inhibition promoted polyQ inclusions formation, indicating HSJ1a targeted misfolded polyQ for proteasomal degradation. In contrast, in R6/2 mice, overexpression of HSJ1a significantly disassembled Htt aggregates in the brain tissue by binding to K63-linked ubiquitin chains, thus inhibiting insoluble Htt macromolecule from further nucleation of inclusion (Labbadia et al. 2012). Compared to R6/2 mouse control, overexpression of HSJ1a significantly improved the neurological behaviour at the late stage of disease and reduced Htt aggregation by over 30%.

Rose *et al* (2011) showed overexpression of HSJ1a in PD cell model reduced parkin mutant inclusion incidence in a J-domain dependent manner. HSJ1a was proposed to partially rescue the disease by refolding the parkin aggregates to a functionally active conformation and localize to the dysfunctional mitochondria and thereby enable parkin mediated mitophagy of damaged mitochondria (Rose et al. 2011).

Similarly, overexpression of HSJ1a reduced SOD1 inclusion incidence in an ALS cell model as well as transgenic mice (Novoselov et al. 2013). Novoselov *et al* (2013) reported that HSJ1a promoted the ubiquitylation and proteasomal degradation of $SOD1^{G93A}$ inclusions in a J-domain and UIMs dependent manner in cell model. Overexpression of HSJ1a ameliorated the disease progression in late stage of $SOD1^{G93A}$ mice with improved muscle performance, increased the motor unit number, and enhanced motor neuron survival. Additionally, Chen *et al* (2016) reported that HSJ1a reduced aggregation of TDP-43 more effectively than all the other chaperones tested (Chen et al. 2016). This was mediated by refolding of phosphorylated TDP-43 in a J-domain dependent manner. Furthermore unpublished data in the Cheetham lab (Christina Zarouchlioti MRes thesis) reported that HSJ1a could reduce C9ORF72 dipeptide polyGA inclusion formation in a cell model.

Moreover, unpublished data from the Cheetham lab show that HSJ1a overexpression can reduce the tau aggregation and hyperphosphorylation in both cell and animal models (Dr Sergey Novoselov unpublished data).

In addition, the Cheetham lab have observed loss of motor neurons in the HSJ1 KO mice (Wendy Mustill and Heather Smith Ph.D thesis), which is similar to the phenotypes observed in human patients with autosomal recessive dHMN and CMT2, further supporting the theory that HSJ1 is crucial for neuronal proteostasis.

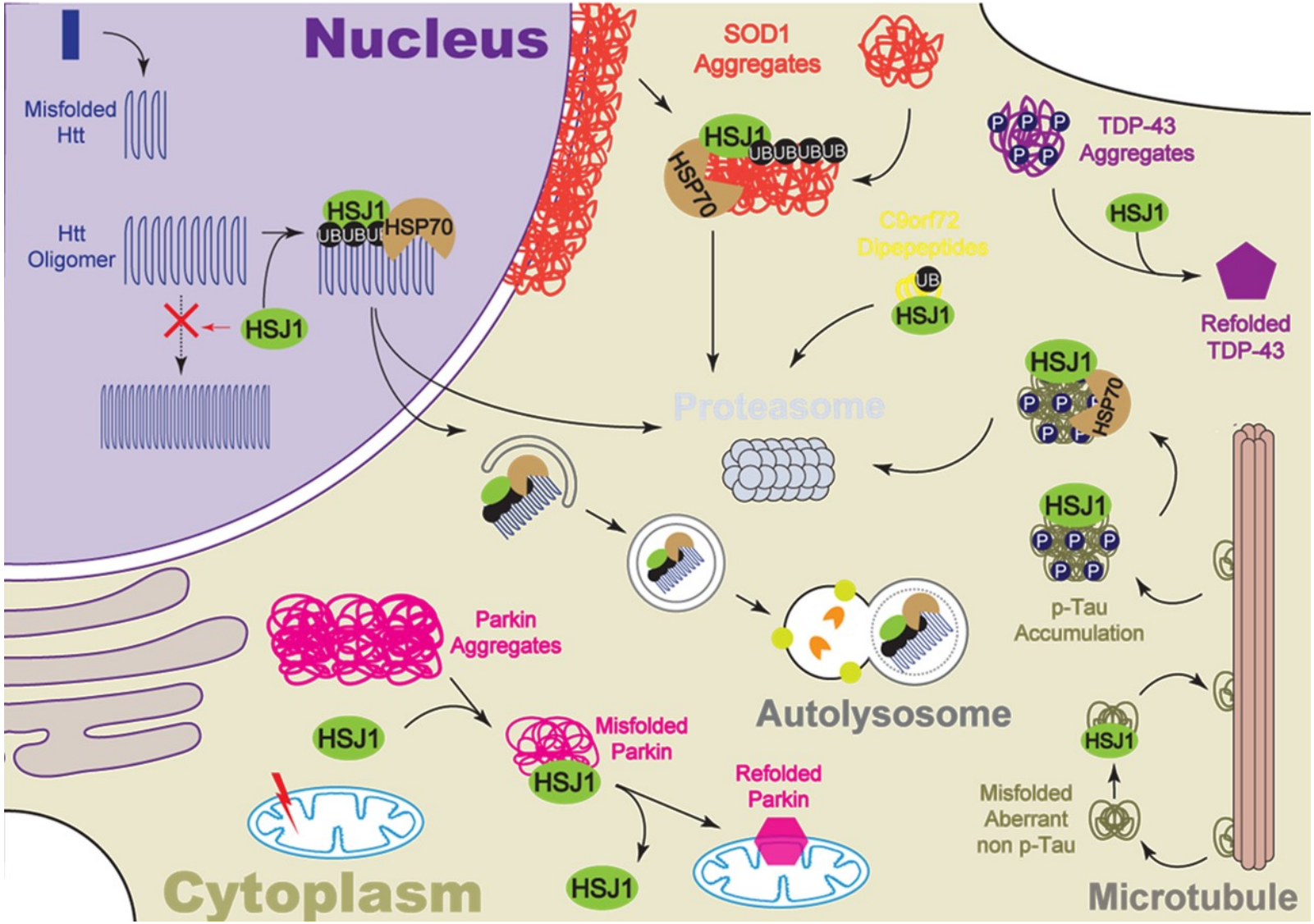

Figure 1.8 HSJ1 acts to restore proteostasis for several neurodegeneration proteins. Schematic illustrations show the anti-aggregation effects of HSJ1 on the neurodegenerative disorder-related proteins such as polyQ, SOD1, TDP-43, C9orf72, Parkin and Tau in cell model or *in vivo*.

1.7 Aim and Hypothesis

Although the ability of molecular chaperones and other factors to modify protein aggregation is well documented, neurodegeneration related protein seeding and the propagation of aggregation needs to be investigated. Interestingly, it is not known if seeding and propagation can be influenced by chaperones. At the start of this study SOD1 mutant proteins had been shown to seed and potentially transmit aggregation. Similarly, HSJ1 had recently been shown to influence Htt seeding. Therefore, this thesis describes an investigation into the mechanisms of SOD1-associated aggregation and potential seeding and if this could be influenced by molecular chaperones and in particular HSJ1. I also explored the potential mechanism by which HSJ1 rescues the SOD1 mutant-mediated cellular stress. My specific aims were:

① Establish an *in vitro* model of SOD1 aggregation and seeding using purified recombinant proteins.

② Investigate if purified HSJ1 proteins can affect SOD1 aggregation and seeding.

③ Develop a cell-based model of SOD1 aggregation and seeding.

④ Characterize the effects of potential inducers on SOD1 inclusion formation.

⑤ Investigate if HSJ1 inhibits the SOD1 aggregation at different stages, i.e., inhibiting SOD1 inclusion formation, disassembling preformed SOD1 inclusions, reducing recruitment effects of SOD1 inclusions, and inhibiting seeding & transmission.

⑥ Investigate if HSJ1 could rescue the failure of protein quality control.

Chapter 2

Materials and Methods

2.1 Molecular Biology and Biochemistry

2.1.1 Plasmid constructs

All the plasmids used or generated in this study are listed in Table 2.1.

2.1.2 Subcloning

The Cheetham lab subcloned the pCMV-HSJ1 and pEGFP-SOD1 previously, and received the pTRE-SOD1 from Prof. RI Morimoto, the inducible pcDNA5/FRT/TO-based chaperone plasmid library from Prof. HH Kampinga, and Gateway T-REX plasmids from Prof. A Hergovich as gifts.

The $SOD1^{WT}$, $SOD1^{G93A}$ and $SOD1^{G85R}$ inserts were amplified by polymerase chain reaction (PCR), and cloned into XhoI (NEB R1046S)-BamHI (NEB R0136) sites of pET-14b from pGEM-T easy vectors.

To generate mCherry-tagged SOD1, SOD1 fragments were released from pEGFP-SOD1 by double digestion with EcoRI (NEB R3101S) and BamHI, and ligated to the pre-cut pmCherry-C1.

To generate pcDNA5/FRT/TO-SOD1, SOD1 inserts released from pGEM-T easy vectors, and ligated onto BamHI-XhoI sites of pcDNA5/FRT/TO/V5 and pcDNA5/FRT/TO/eGFP empty vectors. Furthermore, the mCherry fragment was released from pGEM-T easy vectors and ligated to HindIII (NEB R3104)-BamHI sites of cut pcDNA5/FRT/TO/eGFP-$SOD1^{WT}$ plasmid to replace GFP.

To generate pT-Rex-DEST30-SOD1, SOD1 inserts were ligated to BamHI-XbaI (NEB R1045S) sites of the enter plasmid pENTR-3C-eGFP firstly, and then transferred to pT-Rex-DEST30 vector by the recombinase in Gateway LR reaction.

The fragment tetracycline repressor with internal ribosome entry site (IRES) was released from pMigR1_TetR plasmid, and cloned into pcDNA6/TetR plasmid via XbaI-NcoI (NEB R0193S) sites, thus generating pcDNA6/TetR_IRES_Bsd^R, this was performed by Prof. Hergovich's lab, UCL.

All the constructs generated in this study were confirmed by sequencing.

Backbones	Inserts	Tag	Resistance	Sources
pEGFP-C1	$SOD1^{WT}$ $SOD1^{G93A}$ $SOD1^{G85R}$	N-terminal GFP	Kanamycin	Prof. Cheetham
pmCherry-C1	$SOD1^{WT}$ $SOD1^{G93A}$ $SOD1^{G85R}$	N-terminal mCherry	Kanamycin	This Study
pTRE-2hyg	$SOD1^{WT}$ $SOD1^{G93A}$ $SOD1^{G85R}$	C-terminal CFP; YFP	Ampicillin Hygromycin	Prof. Morimoto
pET-14b	$SOD1^{WT}$ $SOD1^{G93A}$ $SOD1^{G85R}$	N-terminal 6*His	Ampicillin	This Study
	HSJ1a HSJ1b			Prof. Cheetham
pcDNA5/FRT/TO	$SOD1^{WT}$ $SOD1^{G93A}$ $SOD1^{G85R}$	N-terminal V5; eGFP; mCherry	Ampicillin Hygromycin	This Study
	BCL-2			
	HSJ1a HSJ1b			Prof. Kampinga
	Hsp110 Hsp105 Hsp70			
pT-Rex DEST30	$SOD1^{WT}$ $SOD1^{G93A}$ $SOD1^{G85R}$	N-terminal eGFP’	Ampicillin	This Study
pCMV-Tag3a	HSJ1a HSJ1b	N-terminal myc	Kanamycin	Prof. Cheetham
pCMV-Tag3	Ubiquitin	N-terminal myc	Ampicilin	Dr. Kopito
pcDNA3	CHIP	N-terminal myc	Ampicilin	Dr. Patterson
pFRT/lacZeo			Ampicillin Zeocin	Invitrogen
pcDNA6	TetR		Ampicillin Blasticidin	Invitrogen
	$TetR(IRES)Bsd^{R}$			Prof. Hergovich
pOG44	Flp recombinase		Ampicillin	Invitrogen

Table 2.1 Plasmids. Some plasmids listed in this table were used during this study, but the data were not shown in the thesis. Empty vectors were not presented in this table.

2.1.2.1 Polymerase chain reaction

Taking pEGFP-SOD1 as the template, the $SOD1^{WT}$, $SOD1^{G93A}$ and $SOD1^{G85R}$ DNA fragments are amplified using specific primers (Appendix 2.2) with GoTaq DNA polymerase (Promega M3008), engineered to introduce restriction endonuclease sites. Cycling conditions are described in Appendix 2.3.

2.1.2.2 Digestion

The inserts are released by the restriction enzyme digestion at 37ºC water bath for at least 1 hrs.

The backbones are also cut by suitable restriction enzymes at 37ºC water bath for 2 hrs. Then alkaline phosphatase (Promega M1821) was added into the reaction system for 30 mins and inactivated by heating at 65 ºC for 20 mins. The DNA products from digestion reaction were isolated and purified by either ethanol (EtoH) precipitation (Appendix 2.4) or gel electrophoresis.

2.1.2.3 Gel electrophoresis

DNA fragments were separated by agarose gel electrophoresis. DNA samples from PCR reactions were diluted in 6X loading dye (Appendix 2.5) to make the final concentration as 1X. Samples are loaded on agarose gel in the tris-acetate EDTA (TAE) buffer with red safe to visualise DNA (Appendix 2.6).

DNA was visualized and documented using an ultraviolet (UV) light of transilluminator system. The size of DNA was determined by relevant position compared to a standard DNA ladder (NEB N3231&N3232).

2.1.2.4 Gel purification

Followed the manufacture protocol, DNA bands from agarose gel electrophoresis were extracted and purified by a Qiaquick Gel Extraction kit (Qiagen 28706).

The gel was cut under the ultraviolet lamp, and 3 volumes (vol) of QG buffer was add after the gel slices were weighed. The mixture was incubated at 55ºC until the agarose gel melted. 1 vol of isopropanol was added to increase the yield. The samples were loaded to Qiaquick columns and centrifuged at 17000g for 1.5mins, washed with PE buffer and centrifuged to eliminate impurities. Another 1min centrifugation was applied to dry columns. Then the DNA was eluted in the ddH_2O.

Purified DNA samples were analyzed and quantified by agarose gel electrophoresis.

2.1.2.5 Ligation

The inserts were ligated to the purified backbones or pGEM-T Easy System (Promega A1360) by T4 ligase (NEB M0202S) (Appendix 2.7) following the manufacture protocol. The inserts and the vector were ligated at 20ºC for 1 hour or at 4ºC for 16hrs.

2.1.2.6 Transformation

After thawing on ice, the *E.coli* high efficiency competent bacterial cells (JM109 Promega L1001) (NEB 5-alpha NEB C2988J) are incubated with ligation products (100ng) or plasmid only (5ng) for 30 minutes.

Then the cells were heat shocked at 42ºC water bath for 45 seconds. Luria-Bertani Broth (LB) or Super Optimal broth with Catabolite repression (SOC) medium (Appendix 2.8) was added to the competent cells after 5 mins incubation on the ice for recovery. The transformation products were shaken at 37ºC for 1 hour before spreading them onto the LB agar plates (Appendix 2.9) with relevant antibiotics (Appendix 2.10) overnight, and if appropriate blue/white selection containing Isopropyl β-D-1-Thiogalactopyranoside (IPTG) (Sigma I6758), and 5-bromo-4-chloro-3-indolyl-β-D-galactoside (X-gal) (Invitrogen B1690) (Appendix 2.9). The white colonies indicate there is an insert in the vector.

2.1.3 Plasmid purification

2.1.3.1 Storage of bacteria

1vol of 100% pre-autoclaved glycerol (Sigma G5516) was mixed with 1vol of fresh bacterial culture in the stock vial. Then vials were transferred to -80 ºC for long-term storage.

2.1.3.2 Plasmid extraction (mini-prep)

Mini-prep was performed followed the manufacture's protocol via the Quicklyse Mini-prep kit (Qiagen 27405). A glycerol stock or one single colony picked from plates was cultured in LB medium with relevant selection antibiotics. After 37ºC overnight incubation with shaking, bacterial cells were harvested by centrifugation at 17000g for 1 minute.

QLL buffer containing the RNase and lysozyme and the following 1min-vortex were applied to lyse the cells. After 3min incubation, the sample was loaded to the Qiaquick column, and centrifuged at 17000g for 1.5 minutes. Columns were washed by buffer containing isopropanol and centrifuged to remove the impurities. Another 1.5min centrifugation was used to dry the columns. The plasmid was eluted in ddH_2O.

2.1.3.3 Plasmid extraction (midi-prep)

Midi-prep was performed according to the manufacture's protocol using the HiSpeed Plasmid Midi-prep Kit (Qiagen12643). A glycerol stock or one single colony picked from plates was incubated in LB medium with relevant selection antibiotics. After 37 ºC overnight incubation on the shaking platform, the cells were harvested by centrifugation at 17000g for 20 minutes at 4 ºC, resuspended the bacterial pellet in P1 buffer.

P2 buffer worked as the alkaline solution that lysed the bacterial cells for 5 minutes, then the P3 buffer containing acid was applied to neutralize. The lysate was transferred to a pre-equilibrated HiSpeed Midi Tip, washed with QC buffer and eluted by QF buffer, thus eliminating the majority of impurities, such as genomic DNA, RNA proteins, and lipid.

0.7 vol isopropanol was used to precipitate the 1 vol of plasmids. Samples were loaded to the QIAprecipitator Midi Module, washed by 70% ethanol and dried by the air, eluted in 1X Tris-EDTA buffer.

2.1.4 DNA quantification

The DNA concentration is quantified by measuring the absorbance at wavelength 260nm using the ND1000 spectrophotometer (NanoDrop Technologies).

2.1.5 Sequencing

The constructs are sequenced by the company named Source Bioscience to confirm that there were no mutations introduced by the PCR reaction (Appendix 2.11).

2.1.6 Bacterial expression

The expression vectors were transformed into expression *E.coli* stains to generate the recombinant protein. In this study, pET-14b plasmids were transformed into one-shot BL21(DE3)pLysS cells (Invitrogen C6060).

Bacterial cells were cultured in LB or M9 medium (Appendix 2.8) with ampicillin (Amp) (Sigma A9393) and chloramphenicol (Cam) (Sigma C0378) at 37ºC with shaking. Bacterial expression was inducted by 0.5mM IPTG, when the OD_{600} was 0.4-0.6. After 3-5h induction, cells were harvested by centrifugation at 17000g for 20min at 4ºC.

2.1.7 Protein purification

The recombinant 6XHis proteins expressed by bacteria were purified using the Ni-NTA superflow columns (Qiagen 30622).

2.1.7.1 Ni-NTA

E. coli bacterial cells were lysed by freeze/thawing and addition of 1mg/ml lysozyme (Sigma L7651) on the ice for 30mins. Samples were sonicated.in binding buffer with 1% PIC (Sigma P8849) and 1mM Mg^{2+}. 0.2% Trixon were added to the lysis buffer to stabilize and solubilize the proteins, and 1mM DTT was specially applied for 6XHis-tag DNAJB purification.

After centrifugation to remove the insoluble pellets, cell lysate was loaded onto the columns. 6XHis recombinant proteins were eluted after complete wash (Appendix 2.12). Ni-NTA columns can be regenerated according to manufacture protocol (Appendix 2.13).

2.1.7.2 Dialysis

The eluted purified protein products were dialyzed in the dialysis cassette (Thermo 66383/66003) at 4ºC for 4h in dialysis buffer (Appendix 2.14).

2.1.8 Protein quantification

The protein concentration was quantified using a bicinchoninic acid (BCA) protein quantitation kit (VWR 71285-3P).

Reagents A and B were mixed at a ratio of 50:1. 25µL of samples were pipette into a well of 96-well plate, and 200 µL of the A/B mix was added later. The plate was covered in aluminium foil and incubated at 37ºC for 30 mins.

The absorbance was measured at 562nm using a plate reader. Standard concentration curve is plotted based on the reading obtained from the serial dilutions of BSA stock. The concentration of the samples was determined based on the standard curve.

2.1.9 ATP regeneration system

Phosphocreatine (PC) (Sigma P7936) and creatine phosphor kinase (CPK) (Sigma C3755) can regenerate ATP from ADP thus keeping ATG concentration at a high level for ATP-dependent reactions.

$$PCK + PC + ADP = PCK + creatine + ATP$$

Based on the equilibrium, cell extract, 10X CPK (0.5mg/ml) stock, 10X energy mix buffer (Appendix 2.15) and the protein of interest constitute an ATP regeneration system at 30 ºC between 0-4 hrs.

2.1.10 Sedimentation assay

The soluble and insoluble fractions of the protein samples were separated by sedimentation at 17000g at 4ºC for 1 hour.

2.1.11 Protein labelling

Proteins in PBS buffer were labelled with fluorescent signals using the Texa protein labelling kit (Molecular Probes T10244) following the manufacture protocol.

Briefly, proteins were incubated with Texa dye at 20 ºC with sodium bicarbonate and DMSO for 1 hour. Then the samples were loaded onto the column containing resin that separated the labelled and unlabelled proteins into two bands. Under the hand-holding UV lamp to visualize fluorescence, the proteins then were eluted (Appendix 2.16).

2.1.12 Antibody purification

Sheep anti-HSJ1 polyclonal antibody was purified followed the manufacture's protocol using HiTrap NHS-activated chromatography column (Fisher 17-1408-01).

Ice-cold 1mM HCl was applied to wash the column. 10mg purified HSJ1a in 1XPBS buffer, was incubated with column at 20°C for 30min for ligand coupling. Then buffer A (500mM ethanolamine, 500mM NaCl, pH=8.3) and buffer B (100mM sodium acetate, 500mM NaCl, pH=4) was applied to deactivate excess active groups that have not coupled to the ligand and wash out the non-specifically bound ligands. 1X PBS was used as the washing buffer to adjust the pH back to neutral.

1ml serum was injected into the column, and incubated at 4°C for 1 hour. After washing 3 times, antibody was eluted by 2M glycine (pH=2.7). 1M Tris was added into the eluted samples afterwards to adjust pH back to 7.5 at the ratio of 1:25.

2.1.13 ANS fluorescent assay

The 1-anilinonaphthalene-8-sulfonate (ANS) (Sigma A1028) binding assay measures the changes of fluorescent intensity upon protein conformation shifted.

5mg/ml ANS in DMF was diluted in 200ul 1X PBS to make the final concentration as 150ug/ml. 5ug soluble protein sample was added in to the ANS working solution, incubated in the dark at 37°C for 30 minutes. The fluorescence emission spectra were measured by a plate reader from 400nm to 600nm using an excitation wavelength at 390nm. All the tests were performed in triplicate.

2.2. Cell Biology

2.2.1 Cell culture

2.2.1.1 Cell culture

Cell line	Species	Tissue	Sources
CHO	Hamster	Ovary	Cheetham lab
HEK-293T	Human	Kidney	Cheetham lab

Table 2.2 Cell lines.

Chinese hamster ovary (CHO) cells were cultured in Dulbecco's Modified Eagle Medium (DMEM) F12 with GlutaMAX™ supplemented with 10% (v/v) Fetal Bovine Serum (FBS), 100U penicillin and streptomycin (PIS), 0.25ug/ml fungizone (Invitrogen 15290018) at 37ºC in the 5% CO_2 humidified atmosphere.

Human embryonic kidney T (HEK293T) cell line was cultured in DMEM, supplemented with 10% (v/v) FBS and 100U PIS. The optimal growth condition for HEK293T cells was 37°C in 5% CO_2.

Cells were maintained in T75 culture flasks (Becton Dickinson) with 10ml completed medium and passaged every 3-4 days by 1ml 1X trypsin EDTA to dilute the cells in 1:10 ratio.

Cells for stable cell line selection were seeded at $2.5x10^4$ per well in a 96-well dish (VMR). Cells for visualisation of the fluorescently tagged proteins were seeded at $4x10^4$ per well in an 8-well permanox chamber slide (Nunc). Cells for western blot, southern blot and northern blot were seeded at $4x10^5$ per well in a 6-well dish (Corning).

2.2.1.2 Storage of cells

After trypsinizing and counting, cells were harvested at 1000 rpm for 10 minutes by centrifugation, resuspended in the pre-chilled cell freezing buffer [90% FBS, 10% dimethylsulfoxide (DMSO) (Sigma D4540)], then separated into 10^7/ml. Vials were transferred to the pre-chilled Mr. Frosty, then to the -80 freezer for 2 days, then to the liquid nitrogen for long-term storage.

Frozen cells were revived by thawing at 20ºC. Defrosted cells were transferred into a T25 flask containing fresh serum rich DMEM medium. Cells were incubated overnight at 37ºC and exchanged with fresh medium next day.

2.2.2 Transient transfection

24 hours post-plating, the transiently-transfection was performed via LipofectAmine and Plus regents (Invitrogen 18324) when the cells were about 70%-80% confluent with 100ng DNA for $5x10^4$ cells, or 1000ng DNA for $5x10^5$ cells.

The plasmid DNA was added to serum-free DMEM medium, co-incubated with the Plus reagent for 15mins at 20ºC, and then LipofectAmine reagent was added into the sample to incubate for another 15min, promoting the formation of lipid-DNA complexes (plus:lipo=2:1).

Transfection was carried out for 3hrs at 37ºC after adding the lipid-DNA complexes, which was stopped by DMEM medium supplemented with 20% FBS. Cells were incubated at 37 ºC overnight for further experiments.

2.2.3 RNA isolation

2.2.3.1 RNA extraction (mini-prep)

Mini-prep is performed followed the manufacture's protocol via the RNeasy mini-prep kit (Qiagen 74106), Qiashredder kit (Qiangen 79654) and RNase-free DNase set (Qiagen 79254). Mammalian cells from one well of 6-well or 12-well plate were washed twice with HBSS, tryplized and centrifuged at 1000rpm for 10min.

Cell pellets were thoroughly loosened by flicking, resuspended and vortexed in 350ul RLT buffer. Cell lysates were loaded onto a QIAshredder spin tube to homogenize. Discard the column. 350ul 70% ethanol was mixed with homogenized lysates.

700ul mixes were loaded onto RNeasy spin column, centrifuged for 15sec at 13000g. Discard the flow-through. 350ul RW1 buffer was applied to wash the column. To digest DNA, 10ul DNase I stock was mixed with 70ul RDD buffer, and incubated with the column at 20ºC for 15min, 350ul RW1 buffer was loaded onto the column to stop the reaction. The spin column was washed by 500ul RPE buffer and dried by air. The product RNA was eluted in 30ul RNase-free water.

2.2.4 Reverse transcription

Reverse transcription to transcript RNA into complement DNA (cDNA) was performed followed the manufacture's protocol via the Tetro cDNA Synthesis kit (Bioline bio-65043). Prepare the priming premix on ice in an RNase-free reaction tube:

RNA (<5ug)	nul
Primer (Oligo(dT)$_{18}$)	1ul
10mM dNTP mix	1ul
5X RT Buffer	4ul
RiboSafe RNase Inhibitor	1ul
Tetro Reverse Transcriptase (200U/ul)	1ul
DEPC-treated water	to 20ul

Table 2.3 Tetro cDNA synthesis reaction mix.

Incubate reaction mix at 45ºC for 1 hour. Terminate the reaction by heating at 85 ºC for 5mins. Samples were then chilled on ice. Store the cDNA at -20ºC freezer for long-term storage, or proceed to PCR immediately.

2.2.5 Immunocytochemistry

2.2.5.1 Visualization of fluorescent proteins

Cells transfected with fluorescently tagged plasmids were fixed in 4% (v/v) paraformaldehyde (PFA) (TAAB F017) in PBS at 20 ºC for 10min.

The nuclei were stained by 4',6-diamidino-2-phenylindole (DAPI) (Sigma D9564) at 2μg/ml for 5min. Then the mounting medium (DakoCytomation S3023) was applied to mount the slide. In all cases, after removal of solution, cells were washed twice with PBS. The excitation and emission of the fluorescent tags and fluorescent 2º Ab were illustrated in Table 2.2.

Fluorophore	Excitation (nm)	Emission (nm)
DAPI	345	458
GFP	489	509
mCherry	587	610
CFP	433	475
YFP	514	527
Cy2	492	510
Cy3	548	562
Cy5	649	670
Alexa 448	480	525
Alexa 594	590	617
Alexa 647	650	665

Table 2.4 Fluorescent tags & secondary antibodies and their excitation and emission channels. Some tags or secondary antibodies listed in this table were used during this study, but the data are not shown in the thesis.

2.2.5.2 Visualization of proteins by immune-cytochemistry (ICC)

Cells transfected plasmids were fixed in 4% (v/v) PFA in PBS at 20ºC for 10min. 0.5% (v/v) Triton-X 100 in the PBS was used for permeabilization for 10min.

Samples were incubated with relevant primary antibody at a specific concentration (v/v) in the blocking buffer for 1 hour after blocking by 3% bovine serum albumin (BSA) (Sigma A7906) and 10% serum in PBS for 30min. Primary antibody was detected by appropriate fluorescent secondary antibody at 20 ºC for 1h in the darkness. Then DAPI was applied to stain the nuclei at 20 ºC for 5min before mounting.

In all cases, after removal of solution, the cells were washed twice with PBS. The primary antibodies (pABs) used for ICC/Western blot in this study were demonstrated in the Table 2.4.

Antibodies	Sources	Suppliers	Applications		
			ICC	IB	IP
anti-V5	rabbit polyclonal	Sigma V8137	1:1000	1:2000	n/a
	mouse monoclonal	Sigma V8012	1:1000	1:1000	1:200
anti-His	mouse monoclonal	Sigma P1967	1:200	1:1000	n/a
anti-GFP	mouse monoclonal	Roche 11814460001	n/a	1:1000	1:100
	rabbit polyclonal	Abcam ab290	n/a	1:200	1:50
anti-c-myc	mouse monoclonal	Sigma M4439	1:1000	1:1000	1:200
anti-HA	mouse monoclonal	Sigma H3663	1:1000	1:1000	1:200
	rabbit polyclonal	Sigma H6908	1:1000	1:1000	1:200
anti-GAPDH	mouse monoclonal	Sigma G8795	n/a	1:3000	n/a
anti-β tubilin	mouse monoclonal	Sigma T8328	1:5000	1:3000	n/a
anti-SOD100	rabbit polyclonal	Stressgen ADI-SOD100	n/a	1:1000	1:100
anti-SEDI	rabbit polyclonal	Stressmaq	1:200	1:1000	1:200
anti-HSJ1	sheep polyclonal	Appendix 2.18	1:100	1:2000	1:200
anti-TetR02	mouse monoclonal	MoBiTec GmbH tetr02	n/a	1:1000	n/a
anti-BiP	rabbit polyclonal	Sigma G8918	1:100	1:3000	n/a
		Sigma SAB4501452	n/a	1:1000	n/a
anti IRE1α P	rabbit monoclonal	Novus 1102323	n/a	1:1000	n/a
anti-eIFα P	rabbit monoclonal	Sigma 117066	n/a	1:1000	n/a
anti-Perk P	rabbit monoclonal	Cell Signaling 3179S	n/a	1:1000	n/a
anti-ATF6α	mouse monoclonal	Abcam ab11909	n/a	1:1000	n/a

Table 2.5 Primary antibodies. Some pABs listed in this table were used during this study, but the data were not shown in the thesis. Abbreviations: ICC, immunocytochemistry; IB, immunoblotting; n/a not applicable.

2.2.6 Co-immunoprecipitation

2.2.6.1 Sample preparation

Cells of 6-well dishes were washed twice in 1X PBS buffer and lysed in 270µl co-immunoprecipitation (Co-IP) buffer (Appendix 2.19) containing 3% (v/v) protease inhibitor cocktail (PIC) (Sigma P8340) for 15 minutes on ice.

Cell lysates were scraped and sonicated, before centrifugation at 13000g for 10 minutes at 4ºC. 35µl of supernatant was collected for the input fraction. 200µl of supernatant were immunoprecipitated with a appropriate primary antibody at 4ºC for 4-6h or overnight on a rotating wheel. Then the 30ul of pre-washed protein G sepharose beads (Cat. No. 17-0618-01, GE Healthcare, Chalfont) were added into the each reaction, rotating at 4ºC for 2h.

Beads were washed twice using the Co-IP washing buffer (Appendix 2.19), then resuspended in 60µl 2x SDS-sample loading buffer. Both the inputs and precipitates were boiled at 95ºC for 15min, and then resolved by SDS-polyacrylamide gel (section 2.2.7).

2.2.7 SDS-PAGE &immunoblotting

2.2.7.1 Sample preparation

Bacterial cells were harvested by centrifugation and then sonicated. Centrifugation was aimed at separation of the supernatant and pellet at 13000g for 1min.

Mammalian cells from one well of the 6-well plate were washed twice by ice-cold PBS buffer, and then lysed in 200ul RIPA buffer (Appendix 2.19) with 3% PIC on ice for 15min. Lysates were harvested by scraping and then sonicated. Centrifugation was aimed at separation of the supernatant and pellet at 13000g for 1min.

The samples were diluted into Laemmli buffer (Appendix 2.20) to make the final concentration as 1X, and then heated at 95 ºC for 15min before loading.

2.2.7.2 Gel electrophoresis

The samples were loaded into the stacking gel and resolving gel (Appendix 2.21) with protein ladder (Fermentas SM1811) in 10-well gel or in 15-well gel. Samples were resolved at 160V, 400mA. Gel electrophoresis was performed via the BIO-RAD Protean II system with SDS running buffer.

2.2.7.3 SDS-PAGE

After gel electrophoresis, proteins from SDS-polyacrylamide gel were fixed and stained with the Coomassie staining buffer (Appendix 2.22) for 3h at room temperature or overnight, and then gel was destained by the Coomassie destaining buffer (Appendix 2.22). The results were documented by ChemiDoc™ XRS$^+$ System (BIO-RAD).

2.2.7.4 Western blot

After gel electrophoresis, proteins from SDS-polyacrylamide gel were transferred to nitrocellulose membrane rinsed by the transfer buffer (Appendix 2.23) in the semi-dry electro-transfer system under the condition of 15V/0.4A per piece of membrane for 20mins. Proteins were visualized on the membrane with Ponceau S staining solution (Appendix 3.24).

Membranes were incubated in 5% blocking buffer (Appendix 2.25) for 1h at room temperature or overnight at 4ºC to prevent non-specific binding. After PBS-Tween buffer wash twice, membranes were incubated with pAb in the blocking buffer for 1h at room temperature or 4ºC overnight, followed by another hour with appropriate secondary antibody (2ºAb)-horseradish peroxidase (HRP) incubation.

Enhanced chemiluminscence detection was performed by ECL Regent Kit (Thermo 80196), the mixture of regent A (500ul) and regent B (25ul) was used per membrane

for developing prior to film exposure. The results were documented by ChemiDoc™ XRS$^+$ System (BIO-RAD).

2.2.8 Stable cell line generation

To generate stable cell lines, different strategies were applied. Geneticin (G418) was used for selecting cells transfected with plasmids containing neomycin (Neo) resistance cassette (Figure 2.1). The inducible cell line named Flp-in T-REx was generated followed the manufacture's protocol (Figure 2.2), using zeocin, blasticidin (Bsd) and hygromycin (Hyg). Another inducible host cell line used in this study was generated by PhD student Rosalina Guarascio in Molecular and Cellular Neuroscience group in UCL Institute of Ophthalmology, the protocol of which is demonstrated in Figure 2.3.

The pEGFP-SOD1 and pmCherry-SOD1 plasmids were cut by the restriction enzyme DraIII (NEB R0129) at 37 ºC water bath for 2 hours. The pFRT/lacZeo was digested at 37ºC water bath for 2 hours by ScaI (NEB R3122S). A Qiagen Quick Gel Extraction kit was applied to purify the DNA as described above.

Drugs	Suppliers	Stoc	Mechanisms
Geneticin	Sigma (A1720)	700 mg/ml	Blocked the polypeptide synthesis by binding irreversibly to 80S ribosome, thus disrupting proof-reading.
Zeocin	Invitrogen (505255)	100 mg/ml	Suspected to degrade the DNA by intercalation into DNA planar bithiazole-containing moiety.
Blasticidin	Invitrogen (R210-01)	5 mg/ml	Inhibited protein synthesis by blocking peptide bound formation in the ribosome.
Hygromycin	Clontech (0020835)	50 mg/ml	Inhibited protein synthesis by interference with translocation to cause mistranslation at 70S ribosome.

Table 2.6 Antibiotics used for stable cell line generation.

2.2.8.1 Kill curves

G418 was added to cells in the 96-well dish at different concentrations to test the lowest killing concentration. The concentration varies from 50 to 2000ug/ml.

Zeocin, blasticidin or hygromycin was added to cells in the 96-well dish at different concentrations to test the lowest killing concentration separately. The concentration varies from 25 to 500 ug/ml.

2.2.8.2 G418 selection

Transfection was performed followed the manufacture's protocol by using LipofectAmine and Plus regents with 100ng/per $2.5*10^4$ CHO cells in the 96-well dish. 24h post-transfection, the cells were trypsinized and split into 6-well dishes. After the cells attached to the dish, G418 in DMEM completed medium was added into the well.

After 10-20 days selection, colonies were picking by the tips into the 96-well dishes. The selected cells were transferred to 48-well dish, 6-well dish, T25 flask and T75 flask. Cells stably expressing SOD1 were frozen down as described above.

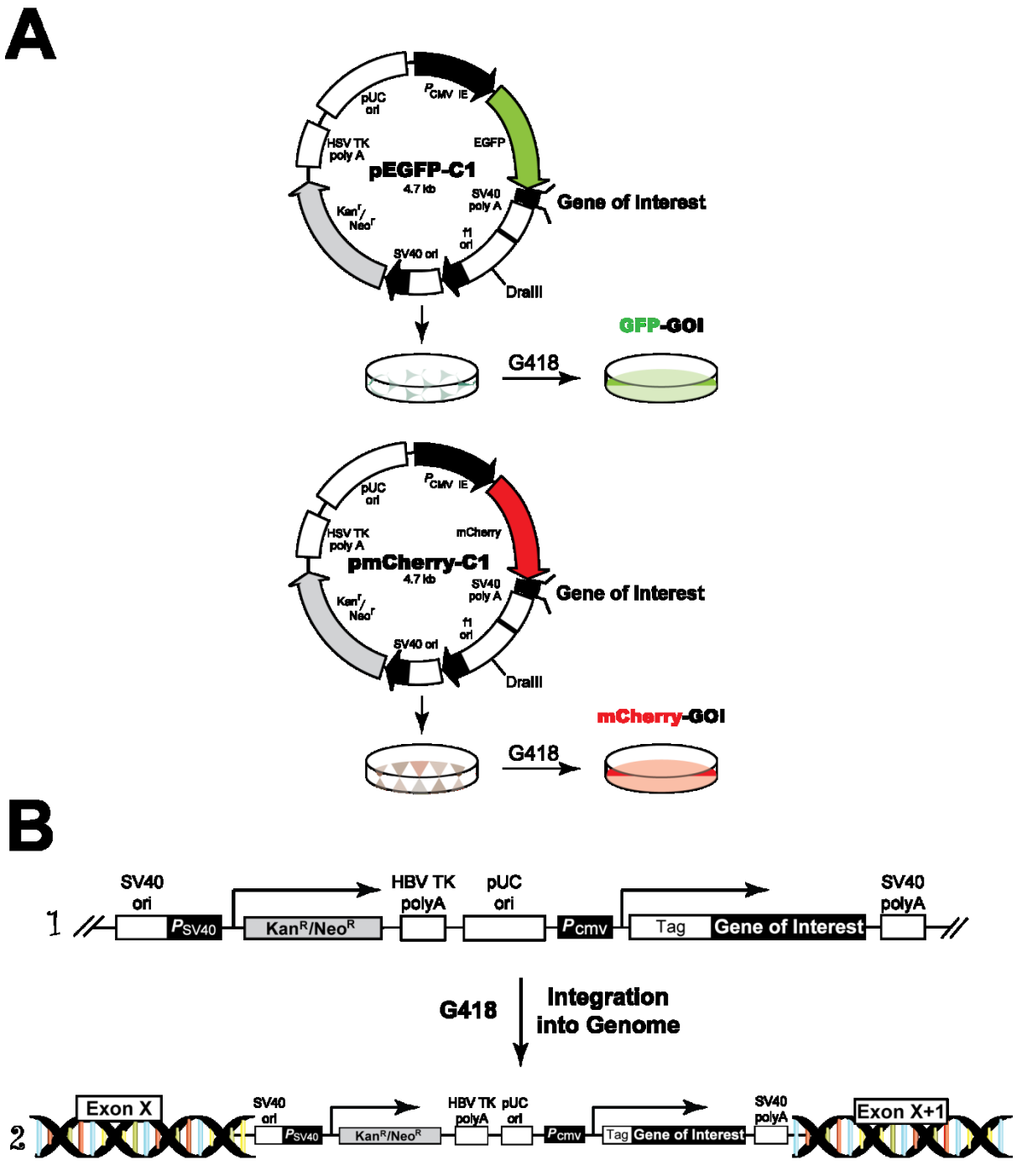

Figure 2.1 Constitutive cell line generation using G418. (A) Selection procedure of Neo-resistant stable cell lines; **(B)** Mechanism of integration and expression of G418 selected cells.

2.2.8.3. Zeocin selection

Transfection of linearized pFRT/lacZeo was performed followed the manufacture protocol by using LipofectAmine and Plus regents with 100ng/per $2.5*10^4$ CHO cells in the 96-well dish. Completed DMEM medium with zeocin was applied for selection.

2.2.8.4 β-galactosidase assay

Cells expressing β-gal-Zeo^R were trypsinized and harvested by centrifugation. Pellets were resuspended in the lysis buffer (Appendix 2.26) and frozen/thaw for several times. The soluble lysate was transferred to another tube.

Sample was added to 50ul 1X cleavage buffer (Appendix 2.26) with β-mercaptoethanol and 17 µl 4mg/ml ONPG, the mixtures were incubated at 37 ºC for 30mins, until the yellow colour developed. 125ul of the Stop buffer then was added to the reaction, to make the final volume as 202ul. A spectrophotometer was used to read the absorbance at 420nm, with untransfected cells used as blank.

2.2.8.5 Blasticidin selection

Transfection of pcDNA6/TR_IRES_Bsd^R was performed following the manufacture protocol by using LipofectAmine and Plus regents with 200ng/per $2.5*10^4$ CHO cells in the 96-well dish. Completed DMEM medium with zeocin and blasticidin was applied for selection.

2.2.8.6 Hygromycin selection

Co-transfection of pcDNA5/FRT/TO with gene of interest (GOI) and pOG44 was performed followed the manufacture protocol by using LipofectAmine and Plus regents with 100ng/per $2.5X10^4$ CHO cells in the 48-well dish. Completed DMEM medium with hygromycin and blasticidin was applied for selection.

The expression of GOI was induced by tetracycline (Tet) (Sigma 87128), and confirmed by western blot with appropriate pAB and 2ºAB.

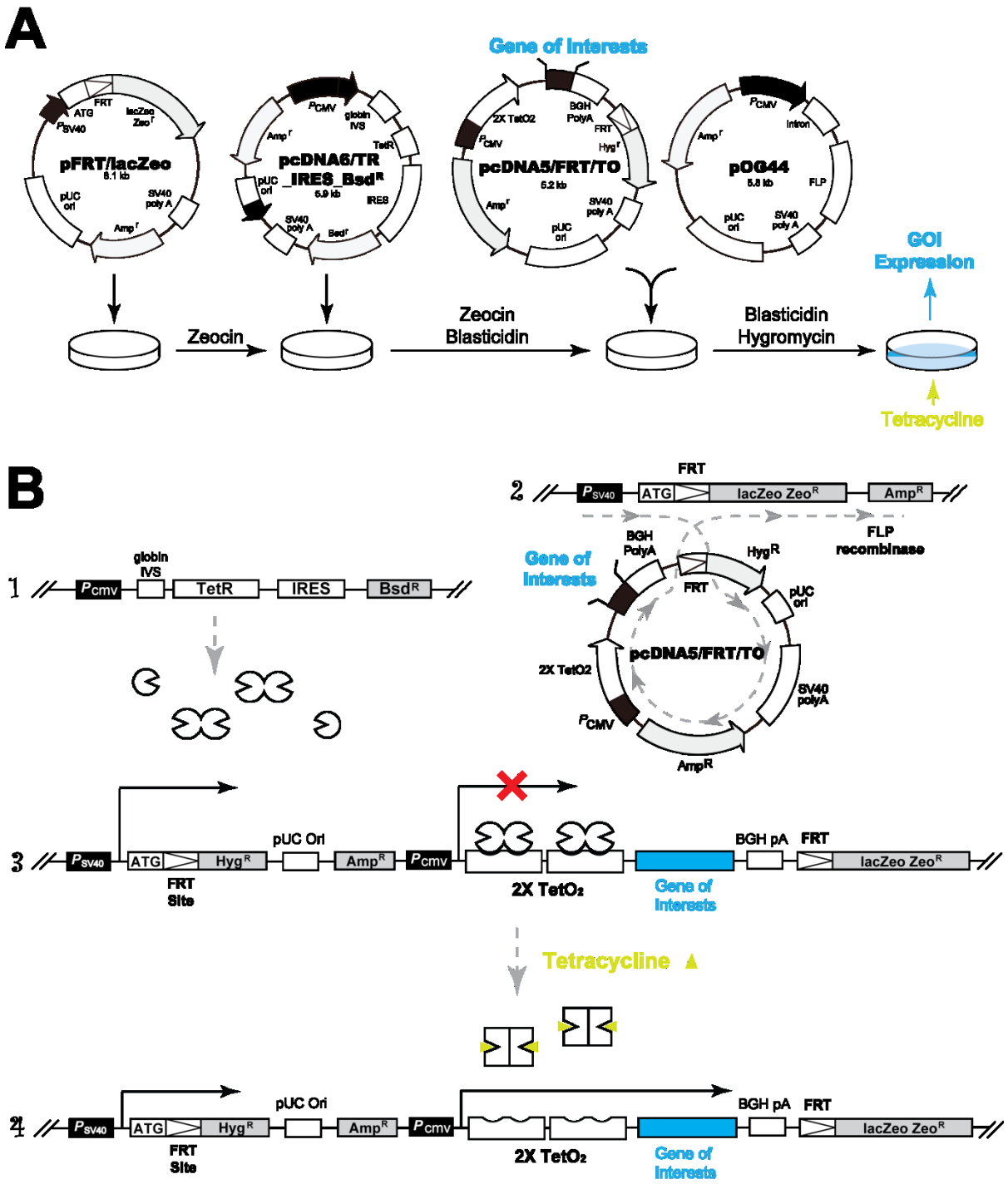

Figure 2.2 Flp-in T-Rex cell line generation using zeocin, Bsd and Hyg. (A) Selection procedure of flp-in T-Rex cell line; **(B)** Mechanism of tet-regulated expression of gene of interests.

2.2.9 Cell fusion

Cell fusion induced by polyethylene glycol (PEG) 1300-1500 (Sigma 202436) was performed followed the manufacture's protocol.

The CHO cells were seeded at $5*10^5$ per well in the 6-well dish or $2*10^5$ per well in the 24-well dishes. When the cells confluence was ~70-80%, transiently-transfection was performed by LipofectAmine and Plus reagents as described above. 24h post-transfection, cells expressing different proteins were trypsinized, mixed, and centrifuged at 1000 rpm for 5 minutes after wash by serum-free DMEM medium. The cell pellet was loosened by finger-flip before 50% pre-warmed PEG1300-1500 was added to the tubes to form cell slurry. The cell slurry was incubated at 37ºC for 5 minutes, then the cell fusion was stopped by adding the serum-free DMEM medium into the PEG-cell slurry. PEG was removed by centrifugation at 1000 rpm for 10 minutes. Then the cells were resuspended in DMEM completed medium, fixed and analyzed 16h post-fusion.

2.2.10 Drug Treatment

Drugs (Table 2.7) were diluted in serum-free medium and added to stable cell lines and transfected cells before cell fixation or lysis 24h post-transfection.

Drugs	Suppliers	Work	Effect
Thapsigargin	Sigma (T9033)	2-8uM	Blocked the transient increase in intracellular Ca^{2+} induced by angiostatin and endostatin. Induced apoptosis by disrupting intracellular free Ca^{2+} levels.
Ionomycin	Sigma (C7522)	2-5uM	Potentiated responses to NMDA, stimulated NO production by calmodulin-dependent constitutive NO synthase.
Kaempferol	Sigma (60010)	10uM	Activated the mitochondrial Ca^{2+} uniporter, and opened mPTP. Induced DNA degradation concurrent with lipid peroxidation. Inhibited the activity of fatty acid synthase.
FCCP	Sigma (C2920)	1uM	Depolarized plasma and mitochondrial membranes; stimulated Mg^{2+}-ATPase activity, mimiced the effect of selective glutamate NMDA on mitochondrial superoxide production.
Sodium Butyrate	Sigma (B5887)	0.5-5mM	Decreases Ca^{2+} release from intracellular stores. Inhibits histone deacetylase (HDAC). Induces apoptosis in several cell lines.
MG132	Biomol (PI-102)	20-50uM	Potent membrane-permeable proteasome inhibitor. Blocks cleavage of poly (ADP-ribose) polymerase and induce apoptosis.

Table 2.7 Drugs. Some drugs listed in this table were used during this study, but the data were not shown in the thesis. Abbreviations: FCCP, Carbonyl cyanide 4-(trifluoromethoxy) phenylhydrazone; MG132, carbobenzoxy-Leu-Leu-leucinal**.**

2.2.11 Cytotoxicity determination assay

The cytotoxicity determination (LDH) assay (Roche 11644793001) was performed followed the manufacture's protocol. The CHO cells were seeded at 5000 per well in the 96-well dish. Cells were treated with drugs in 100ul DMEM medium with one background control (no LDH), one low control (spontaneous LDH) and one high control (maximum LDH) for 3 hrs. The assay medium was removed, transferred to another microplate, and then incubated with 100ul reaction mixtures up to 30min at 20ºC in the dark. The absorbance of the samples was measured by the plate-reader at 490-492nm. All tests were performed in triplicate.

2.2.12 Quantification in cell biology

Transfected or induced cells were analyzed using a Nikon Eclipse 80i fluorescence light microscope under the 40X objective, and quantified in 4 randomly chosen fields comprising at least 100 cells.

*Transfection efficiency = (Transfected cells / DAPI-positive cells) * 100%.*

In this study, compared to diffuse SOD1 staining, SOD1 inclusions were defined as intense sometimes saturated accumulations of partially or fully peri-nuclear staining. The inclusion incidence was calculated as follows:

*Inclusion incidence = (Cells with inclusions / Total transfected cells) * 100%.*

2.2.13 Confocal microscopy

Images were recorded by a Zesis LSM700 confocal microscope with excitation/emission wavelengths showed in the Table 2.1.

2.2.14 Image processing

Images were exported from LSM browser and processed in Adobe Photo CS6 and Adobe Illstrator CS6 for cropping, annotation and adjustment.

2.2.15 Statistical analysis

The statistical analysis was performed in Microsoft Excel to calculate the mean and standard error, using an unpaired two-sample t-test. ANOVA is performed using SPSS with post-hoc analysis. The type of post-hoc test is dependent on whether the variances are homogeneous (Tukey HSD) or heterogeneous (Dunnett T3). Previous experience in Cheetham lab has shown a minimum of 400 subjects would be sufficient to detect a difference between two populations at 0.005 significances in the cell model.

Band intensity and area on Western blot or Coomassie brilliant blue staining gel was calculated using ImageJ, and repeated 3 times each measurement.

Chapter 3

SOD1 aggregation and seeding potential *in vitro*

3.1 Introduction

Since the first mutation of Cu/Zn superoxide dismutase was reported to cause fALS in 1993 (Rosen et al. 1993), more than 170 SOD1 mutations have been described to date. Significant research carried out afterwards has aimed to characterize the effects of mutant SOD1 on folding, stability and activity *in vitro*. In this chapter, I describe my investigations of recombinant SOD1 expressed and purified from *E. coli.*

Recombinant holo-SOD1^{WT} (Figure 1.2) is very stable. It has been suggested to be functionally active even in 10M urea, 6M GdmCl, 4% SDS (Forman & Fridovich 1973) or at 80°C (Roe et al. 1988). Compared to SOD1^{WT}, mutations in SOD1 resulted in reduced structural stability and alterations in net repulsive charge (Sandelin et al. 2007; Shi et al. 2014), enzymatic activity (Yiwari et al. 2009) and thermodynamic stability (Tiwari & Hayward 2006). Furthermore, loss of post-translational modifications, including ① charges of metal ion, ② disulphide bond, and ③ dimerization, also destabilized SOD1, regardless of wild type or mutant status. During protein synthesis polypeptides fold from unedited nascent chains into functional active conformations. But in the presence of mutations or upon stress, native proteins could lose post-translational modifications, unfold into destabilized structures. In term of SOD1, fully metallated (holo) SOD1 dimer (D) may lose metal ions (apo) or form metallated SOD1 monomers (M). Both holo-monomer and apo-dimer under fluctuation or stress would further fold into metal-free monomer. The equilibrium below demonstrates the dynamic shifts between multiple soluble SOD1 unfolding/misfolding structures. In the absence of metal ions and/or dimerization, destabilized SOD1 goes through several steps, thus forming distinct aggregates (A) (Hwang et al. 2010).

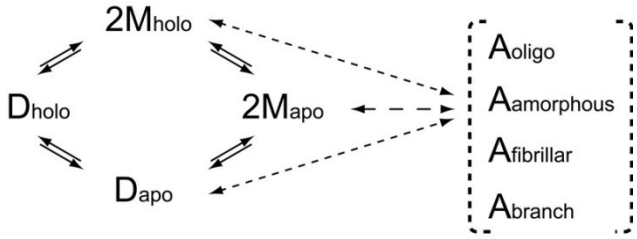

A vast amount of work using chaperones to modulate the self-assembly of aggregation prone proteins has been carried out in *cell-free* systems. Much of this has focused on model substrates, such as luciferase or citrate synthase, but there have also been detailed investigations of neurodegeneration related polypeptides. In 2006, Wilhelmus *et al* reported small Hsps such as Hsp27, Hsp22, αB-crystallin and Hsp20, not HSPB2/B3 bound to and reduced the aggregation of D-Aβ1–40 (Wilhelmus et al. 2006). Evans *et al* (2006) reported that Hsp90 with the help of Hsp70/DnaJB1 suppressed Aβ1–40 oligomers from further aggregation (Evans et al. 2006). In 2011, Bruinsma *et al* reported smHsp family members including Hsp27, Hsp22, αB-crystallin, and HspB2/B3

bound to and inhibited mature α-syn^{MT} fibril formation (Bruinsma et al. 2011). In the same year, Pemberton *et al* (2011) reported that Hsc70 sequestered soluble α-syn in a complex in the absence of ATP (Pemberton et al. 2011). Interestingly, the affinity of Hsc70-α-syn was diminished upon addition of ATP of with its co-chaperones DnaJA1 or DnaJB1. Guzhova *et al* (2011) reported Hsp70 bound to polyQ in adenosine triphosphate-dependent manner and suppressed polyQ aggregation formation in a dose-dependent manner (Guzhova et al. 2011). Labbadia *et al* (2012) reported HSJ1a not only suppressed polyQ aggregation formation, but also inhibited the ability of brain extract from R6/2 mice to seed soluble Htt (Labbadia et al. 2012), suggesting HSJ1 might be able to prevent seeding based aggregation. Yerbury *et al* (2013) reported the smHsp Hsp27 suppressed SOD1 aggregate formation growth, after the lag phase when the aggregate nuclei was formed, and αB-crystallin directly bound to SOD1 aggregates, formed high molecular weight complexes (Yerbury et al. 2013). In 2014, Månsson *et al* (2014) reported that purified DnaJB6 can suppress fibrillation of polyQ peptides far more efficiently than polyQ expanded protein fragments *in vitro* (Mansson et al. 2014). Månsson *et al* (2014) also reported than DnaJB6 retard Aβ42 fibril proliferation in a dose-dependent manner (Mansson et al. 2014). Collectively, these date suggest that chaperone manipulation is potentially promising to suppress aggregation formation *in vitro*.

Therefore, in this chapter, I explore if HSJ1 proteins could modulate SOD1 aggregation formation and seeding potential *in vitro*. An *in vitro* cell-free system was developed using purified recombinant SOD1 proteins. At first, a range of different approaches were tested for their ability to simulate SOD1 unfolding, or induce SOD1 to aggregate. Furthermore, experiments were designed to clarify whether the preformed SOD1 aggregates possess the ability to stimulate soluble SOD1 sedimentation and if HSJ1 could inhibit SOD1 spontaneous or seeded aggregation.

3.2 Results

3.2.1 Recombinant SOD1 expression and purification

To enable recombinant protein expression and purification, the SOD1 open reading frame (ORF) cDNA for WT, G93A and G85R were cloned into pET-14b (Figure 3.1A). The pET system is capable producing large quantities of recombinant proteins in prokaryotic systems. Appropriate in frame restriction sites XhoI/BamHI were introduced by PCR before cloning into pGEM-T and then pET-14b. Sequencing results confirmed that there were no PCR-driven mutations. Recombinant SOD1 expression was induced by IPTG in *E.coli.* BL21(DE3)pLysS [genotype: F^- *ompT hsdS*$_B$(rB^- mB^-) *gal dcm* (DE3) pLysS (Cam^R)], and purification protocol was developed using Ni^{2+} affinity chromatography matrix (section 2.1.5), which binds the N-terminal 6x histidine tag through the immobilized Ni^{2+} ions with high specificity and affinity.

3.2.1.1 Expression of recombinant SOD1

To verify the expression level and the molecular weight of recombinant SOD1, un-induced and induced bacterial cells were lysed, resolved by SDS-polyacrylamide gel and analysed by Coomassie brilliant blue staining and western blot (Figure 3.1B). Monomer $SOD1^{WT}$ and $SOD1^{G93A}$ migrated with the predicted mobility (SOD1 16kDa+ 6xHis tag <1kDa+ link 2kDa= 19kDa). However, a mobility shift for $SOD1^{G85R}$ was observed at faster migration than the other two.

As described in Chapter 1, G93A and G85R are single amino acid substitution mutations, suggesting the three recombinant SOD1 proteins generated in this chapter should possess very similar molecular weight. However, $SOD1^{G85R}$ and $SOD1^{D90A}$ have been reported to show a faster mobility on SDS-polyacrylamide gel compared to $SOD1^{WT}$ and other SOD1 mutants (Hayward et al. 2002). It was suggested that the conformations of $SOD1^{G85R}$ and $SOD1^{D90A}$ were more compact due to the mutation sites altering their structure, thereby resulting in the different mobility if the denaturation was not fully completed.

The $SOD1^{G85R}$ mobility shift was advantageous, as it enabled the discrimination of $SOD1^{G85R}$ from $SOD1^{WT}$ and $SOD1^{G93A}$ based on mobility when those SOD1 proteins were co-incubated.

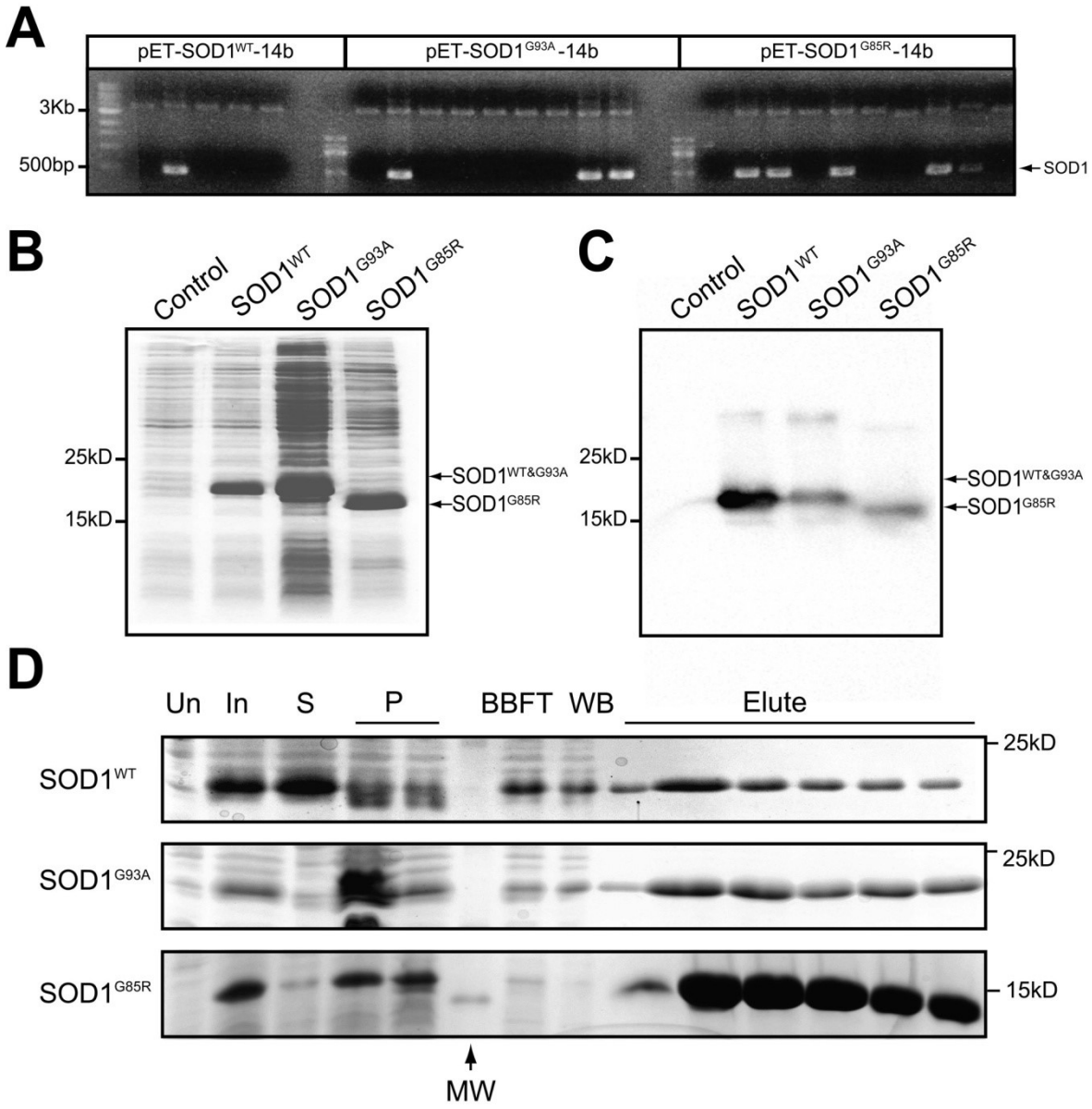

Figure 3.1 Expression and purification of recombinant SOD1. (A) PCR screen of pET-14b subcloning. Plasmid extracted from individual colonies as indicated, amplified using SOD1 primers and GoTaq enzyme. PCR products were resolved by 1% agarose gel to detect the presence of amplified SOD1 bands at 450bp. **(B)** SDS-PAGE of bacterial lysates obtained from non-induced negative control (control) or 0.5mM IPTG-induced cells expressing SOD1. SOD1 WT and mutants were resolved on 15% SDS-polyacrylamide gel, stained with Coomassie brilliant blue. **(C)** Immunoblot with rabbit anti-SOD100 polyclonal (1:3000) and goat anti-rabbit HRP (1:20000). SOD1 specific immunoreactive bands are highlighted by arrows. The positions of MW markers are indicated on the right. **(D)** Coomassie brilliant blue staining showed the purification of recombinant SOD1. Compared to uninduced (Un) sample, SOD1 was enriched upon IPTG induction (In), bacteria were lysed, centrifuged to separate soluble (S) and pellet (P) fractions before loading onto a Ni-NTA column. The columns were washed twice with washing buffer (WB) to remove the non-specific binding after binding buffer flow through (BBFT); SOD1 proteins in the eluted fractions indicated the final purity of product.

3.2.1.2 Purification of recombinant SOD1

To remove the impurities (such as bacterial chaperones or other proteins that might interacted with either SOD1 or HSJ1) and concentrate SOD1 for further detailed studies, immobilised metal ion affinity chromatography (IMAC) protein purification strategy named Ni-NTA was applied. Cell lysates are loaded onto Ni^{2+} affinity matrixes and washed thoroughly. 6x-fold His tagged SOD1 were eluted under native or denaturing conditions (Figure 3.1D). The Coomassie stained SDS-PAGE show that compared to un-induced negative control, there was robust expression of SOD1. Sedimentation (Lane S-P) showed that the $SOD1^{WT}$ protein was present mostly in the soluble fraction with a proportion insoluble, but $SOD1^{G93A}$ and $SOD1^{G85R}$ were present mainly in the insoluble fraction. This determined the purification strategies. Thus, $SOD1^{WT}$ expressing bacteria were lyzed under native non-denaturing conditions, whereas $SOD1^{G93A}$ and $SOD1^{G85R}$ expressing bacteria were lysed under denaturing conditions by the addition of 7-8M. Both native-state WT and denatured SOD1 mutants were eluted.

3.2.2 Recombinant HSJ1 expression and purification

pET-9d HSJ1 expression plasmids were described previously by Cheetham *et al* (1994). The recombinant HSJ1 also expressed in BL21(DE3)pLysS stain and purified using Ni-NTA agarose.

3.2.2.1 Expression of recombinant HSJ1

To examine the expression level and molecular weight of recombinant HSJ1, un-induced and induced cell cultures were lysed, resolved by SDS-polyacrylamide gel and analysed by Coomassie brilliant blue staining and western blot (Figure 3.2A). Based on their mobility on SDS-polyacrylamide gel, HSJ1a migrated close to 35kDa protein ladder (HSJ1a 32kDa + 6xHis <1kDa + link 2kDa =35kDa), while HSJ1b (HSJ1b 36kDa + 6xHis <1kDa + link 2kDa =39kDa) migrated at a higher position above HSJ1a, which is consistent with the results previously published by the Cheetham lab.

3.2.2.2 Purification of recombinant HSJ1

The purification strategy for HSJ1 was identical to the protocol used to purify $SOD1^{WT}$. Cell lysates are loaded onto the IMAC resin and washed. 6xHis tagged HSJ1a and HSJ1b are purified under native conditions to keep their original conformation (Figure 3.2C). Compared to the negative control (uninduced), specific bands were enriched in lane ‘In’ following IPTG induction, indicating the expression of HSJ1 proteins. Based on sedimentation (lane S-P), both HSJ1a and HSJ1b were mainly present in soluble fractions. Therefore recombinant HSJ1 was purified and eluted under native state.

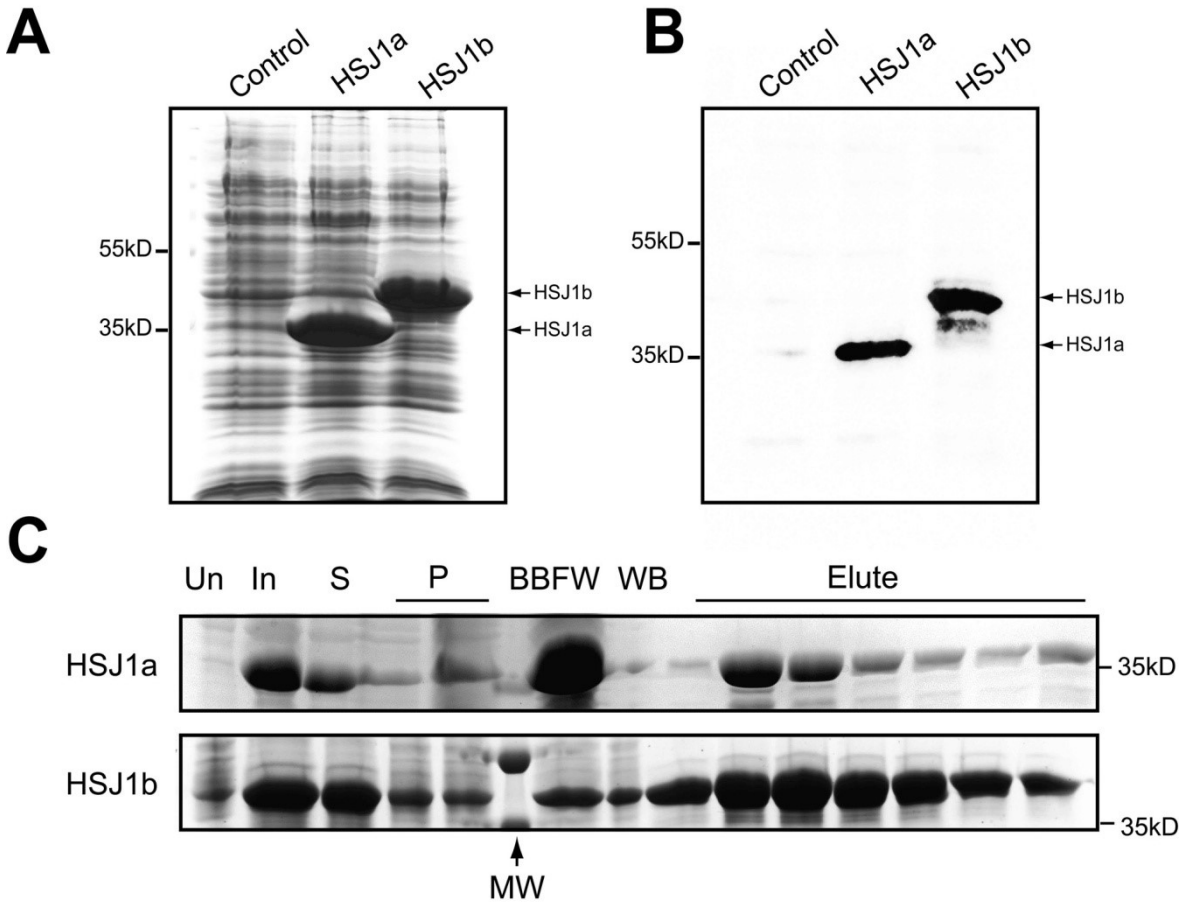

Figure 3.2 Expression and purification of recombinant HSJ1. (A) SDS-PAGE of bacterial lysates obtained from non-induced negative control or 0.5mM IPTG-induced cells expressing HSJ1. HSJ1a and HSJ1b were resolved on 12% SDS-polyacrylamide gel, stained with Coomassie brilliant blue. **(B)** Immunoblot with sheep anti-HSJ1 polyclonal (1:2000) and goat anti-sheep HRP (1:20000). HSJ1 specific immunoreactive bands were detected after 3h 0.5mM IPTG induction are highlighted by arrows. The positions of MW markers are indicated on the right. **(C)** Coomassie brilliant blue staining showed the purification of recombinant HSJ1. Compared to uninduced (Un) sample, HSJ1 was enriched upon IPTG induction (In), bacteria were lysed in binding buffer, separated into soluble (S) and pellet (P) fraction before loading onto a Ni-NTA column. The column was washed twice by washing buffer (WB) to remove the non-specific impurities after binding buffer flow through (BBFT), the HSJ1 proteins in the eluted fractions indicated the final purity of product.

3.2.3 Effect of heating on SOD1 sedimentation

The fully metallated SOD1 under physiological environment has been reported to be remarkably stable (Tm≈90°C) (Roe et al. 1988), but can show decreased activity, metal-binding loss, structural stability after a long incubation time *in vitro* (e.g., 300uM SOD1, pH=7.0, 37°C for 300hrs) (Banci et al. 2007). This aggregation exhibited an exponential increase phase, seeding, and heterogeneous nucleation.

To test the thermo-stabilities of recombinant SOD1, heating treatment was applied, as heating was considered as a potential ideal aggregation-inducing condition, as it can be applied or removed immediately. After cooling, there were no extra inducers left to affect the sample. Sedimentation was used to assess protein aggregation, the fractions were then resolved by SDS-polyacrylamide gel and analysed by Coomassie brilliant blue staining (Figure 3.3)

There was no significant increase in the insoluble fraction of $SOD1^{WT}$ after heating at 65°C for 24hrs (7%, compared to~4% of the control left at 20°C). In addition, there were also similar slight increase in the pellet fraction of $SOD1^{G93A}$ (9%, compared to~5%) and $SOD1^{G85R}$ (9%, compared to~4%). Statistical analysis showed there were no significant differences between untreated and treated SOD1. In conclusion, upon such harsh heating treatment, the majority of SOD1 wild-type and mutant proteins remained soluble (>90%).

These data suggested that $SOD1^{WT}$, $SOD1^{G93A}$ and $SOD1^{G85R}$ all possessed high stability towards heating, although in theory, mutations in SOD1 should dramatically decrease its thermostablity. $SOD1^{G93A}$ and $SOD1^{G85R}$ could have such a high resistance towards heating stress was due to the method of purification and the presence of metal ions. This will be further discussed in the section 3.3.

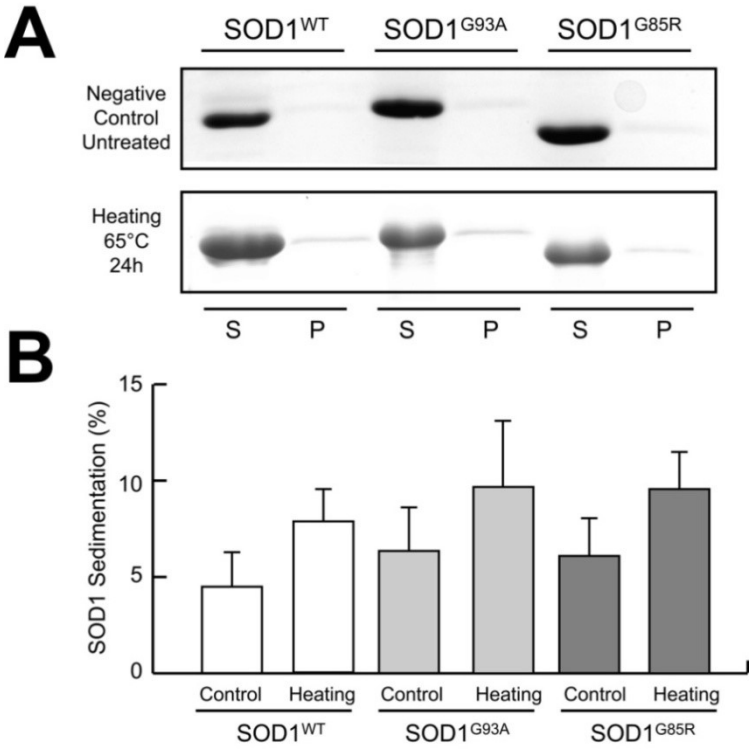

Figure 3.3 Effect of heating on SOD1 sedimentation. (A) SDS-PAGE of SOD1 soluble and insoluble fractions upon heating treatment. Coomassie Brilliant Blue stained 12 % SDS-polyacrylamide gel showed sedimentation of 10ug purified SOD1 treated at 20°C (negative control) or 65°C for 24hrs. Samples were centrifuged at 13000g for 60mins at 4°C to separate the supernatant (S) from the pellets (P), and resolved by SDS-PAGE. **(B)** Quantification of the percentages of SOD1 WT (white) and G93A (pale grey) and G85R (grey) sedimented into insoluble pellet fractions following heating treatment. Mean band intensity and statistical analysis was calculated as described in Material and Methods (Error bar=SD; n=5).

3.2.4 Effect of de-metallization & reduction of disulphide bonds on SOD1 sedimentation

As discussed in Chapter 1, SOD1 is metal ion-dependent enzyme. It is reported that loss of metal ions disrupted SOD1 tertiary structure and function. In addition, reduction of disulphide bonds also unfolded SOD1 from its native physiological structure.

To investigate the stability of recombinant SOD1 proteins, treatment with EDTA, which chelates divalent cations, or the reducing agent DTT were co-incubated with soluble SOD1 prior to sedimentation, resolution by SDS-polyacrylamide gel and analysis by Coomassie brilliant blue staining (Figure 3.4).

EDTA or DTT treatment did not enhance the sedimentation of $SOD1^{WT}$, whose baseline percentage of insoluble fraction was between 2~4%. For the $SOD1^{G93A}$, only a small percentage became insoluble after EDTA treatment, In contrast, more $SOD1^{G93A}$ sedimented into pellet fraction after DTT treatment. Furthermore, for the $SOD1^{G85R}$, EDTA treatment stimulated ~20% to form sedimentable aggregates; however, $SOD1^{G85R}$ mainly remained soluble after DTT treatment. Based on analysis of 5 replicates, these data suggest that de-metallization and reduction of disulfide bonds showed potential sedimentation effects towards $SOD1^{MT}$.

3.2.5 Effect of hydrophobicity caused by calcium on SOD1 sedimentation

Calcium was reported to increase the β-sheet content and hydrophobicity of SOD1 *in vitro* (Leal et al. 2013), and to increase SOD1 aggregation via nitric oxide in cultured motor neurons (Kim et al. 2007). The level of calcium was also reported to increase in spinal and brain stem motor neurons in ALS patients as well as ALS animal models (Redler & Dokholyan 2012; Von Lewinski & Keller 2005). Therefore, an assay was developed to test if calcium could induce SOD1 sedimentation in a cell-free system. SOD1 proteins were incubated with calcium at different concentrations, then centrifuged, sedimented, resolved by SDS-polyacrylamide gel and analysed by Commassie brilliant blue staining. (Figure 3.5 A)

Compared to the untreated SOD1 following 5mM calcium treatment, both $SOD1^{G93A}$ and $SOD1^{G85R}$ were induced to form insoluble sedimentable material (~40%, compared to 5%, ***$p<0.005$), whereas $SOD1^{WT}$ remained soluble. Nevertheless, after 10mM calcium treatment, WT, G93A and G85R were all induced to sediment into the pellet fraction. Both $SOD1^{G93A}$ and $SOD1^{G85R}$ showed a greater tendency to aggregate than $SOD1^{WT}$ following calcium incubation at 5mM. The role calcium plays in a SOD1 cell model was further investigated in Chapter 4.

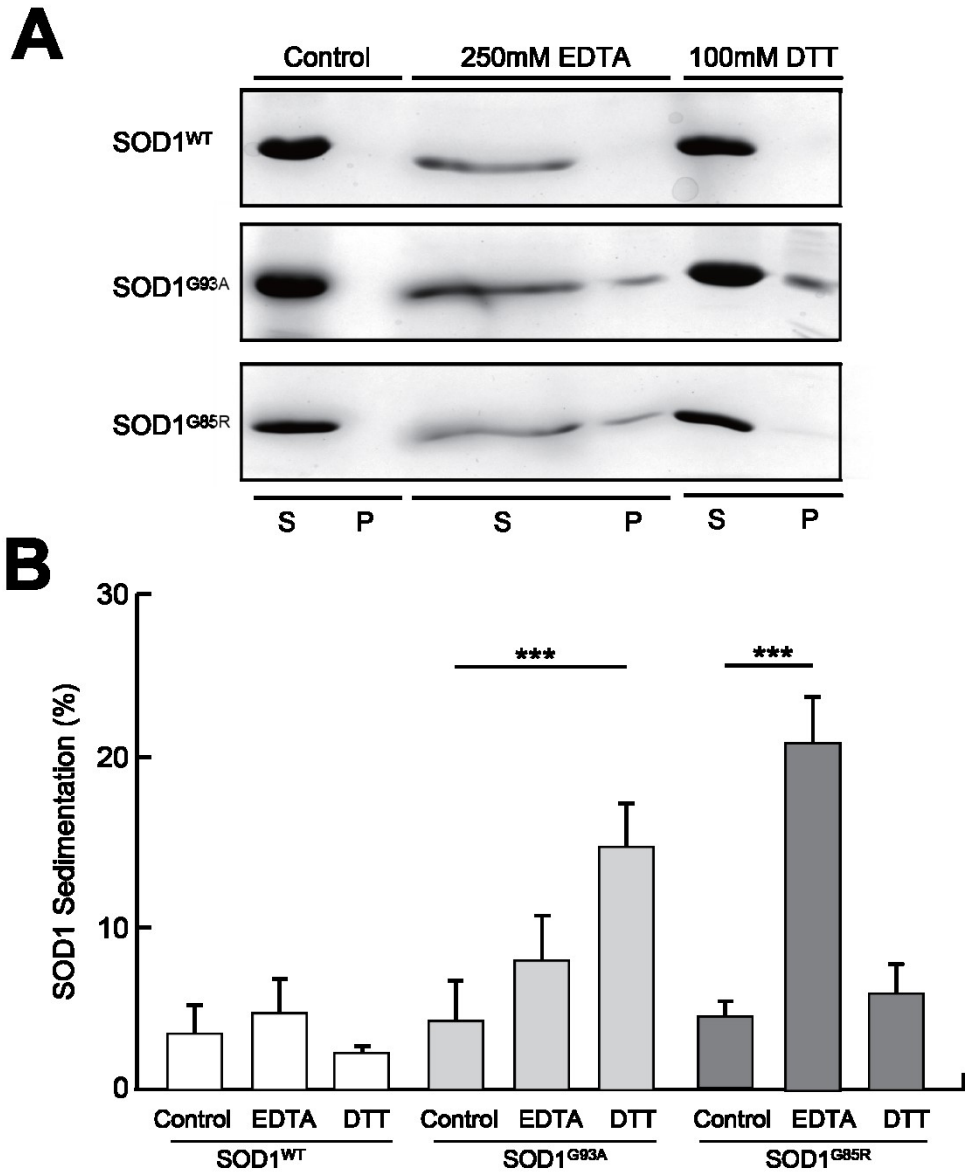

Figure 3.4 Effect of EDTA or DTT on SOD1 stability. (A) SDS-PAGE of SOD1 sedimentation upon EDTA or DTT treatment. Coomassie brilliant blue staining showed sedimentation of 10ug pre-purified SOD1 treated with control buffer (ddH_2O), 250mM EDTA or 100mM DTT respectively at 20°C for 16hrs. Samples were centrifuged at 17000g for 60mins at 4°C to separate the supernanent (S) from pellets (P), the fractions were resolved on 12% SDS polyacrylamide gel. **(B)** Quantification of the mean percentage of purified SOD1 WT (white bar) G93A (pale grey bar) and G85R (grey bar) sedimented into insoluble fractions following ddH_2O/EDTA/DTT treatment. Band intensity and statistical analysis were performed as described in Material and Methods (Error bar=SD; ***$p<0.005$; n=5).

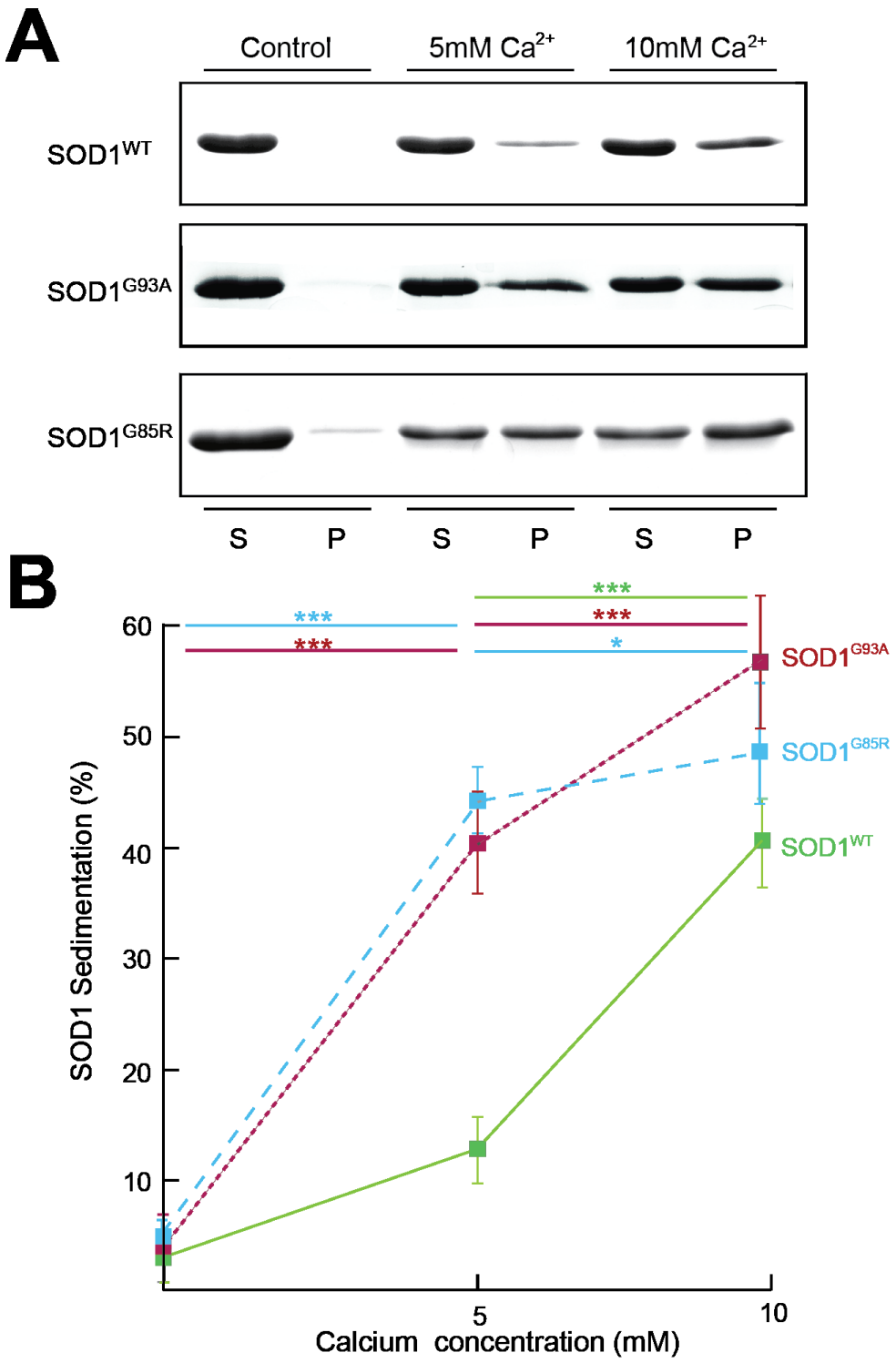

Figure 3.5 Effect of calcium on SOD1 sedimentation. (A) SDS-PAGE of SOD1 sedimentation upon calcium treatment. Coomassie brilliant blue stained 12 % SDS-polyacrylamide gel showed sedimentation of 10ug purified soluble $SOD1^{WT}$, $SOD1^{G93A}$ and $SOD1^{G85R}$ treated with control buffer (ddH_2O), 5mM $CaCl_2$ or 10mM $CaCl_2$ respectively at 22°C for 3hrs as indicated. Samples were separated at 13000g for 60mins at 4°C to separate the supernatant (S) from the pellets (P), and resolved by SDS-PAGE. **(B)** Quantification of the mean percentage of SOD1 WT (green) G93A (red) and G85R (blue) sedimented into insoluble fractions following combination treatment. Band intensity and statistical analysis were performed as described in Materials and Methods (Error bar=SD; *p<0.05, ***p<0.005; n=5).

3.2.6 Effect of combined inducers on SOD1 sedimentation

To promote the aggregation process, multiple inducers were combined to test if their effects on SOD1 aggregation induction could be enhanced. 2,2,2-trifluoroethanol (TFE) was used as positive control (Munch & Bertolotti 2010).

The combination of calcium and DTT, or combination of EDTA and DTT were tested on SOD1. Induced samples were centrifuged, resolved by SDS-polyacrylamide gel and analysed by Coomassie brilliant blue staining (Figure 3.6).

$SOD1^{WT}$ remained soluble under 10% (v/v) TFE treatment, however, both $SOD1^{G93A}$ and $SOD1^{G85R}$ predominantly sedimented into the pellet fraction. In addition, the combination of calcium and DTT treatment could rapidly trigger both $SOD1^{G93A}$ and $SOD1^{G85R}$ to form pellets (>90%), and showed little effect on WT (~7%). EDTA/DTT treatment also stimulated the sedimentation of SOD1 after at least 12h incubation at 42°C, whilst the $SOD1^{G93A}$ and $SOD1^{G85R}$ fully sedimented, approximately 20% of $SOD1^{WT}$ was sedimented under the same conditions. Compared to the positive control, calcium/DTT treatment induced similar aggregation in the SOD1 mutants, yet showed smaller effects on $SOD1^{WT}$; therefore, this combination was applied in the subsequent studies.

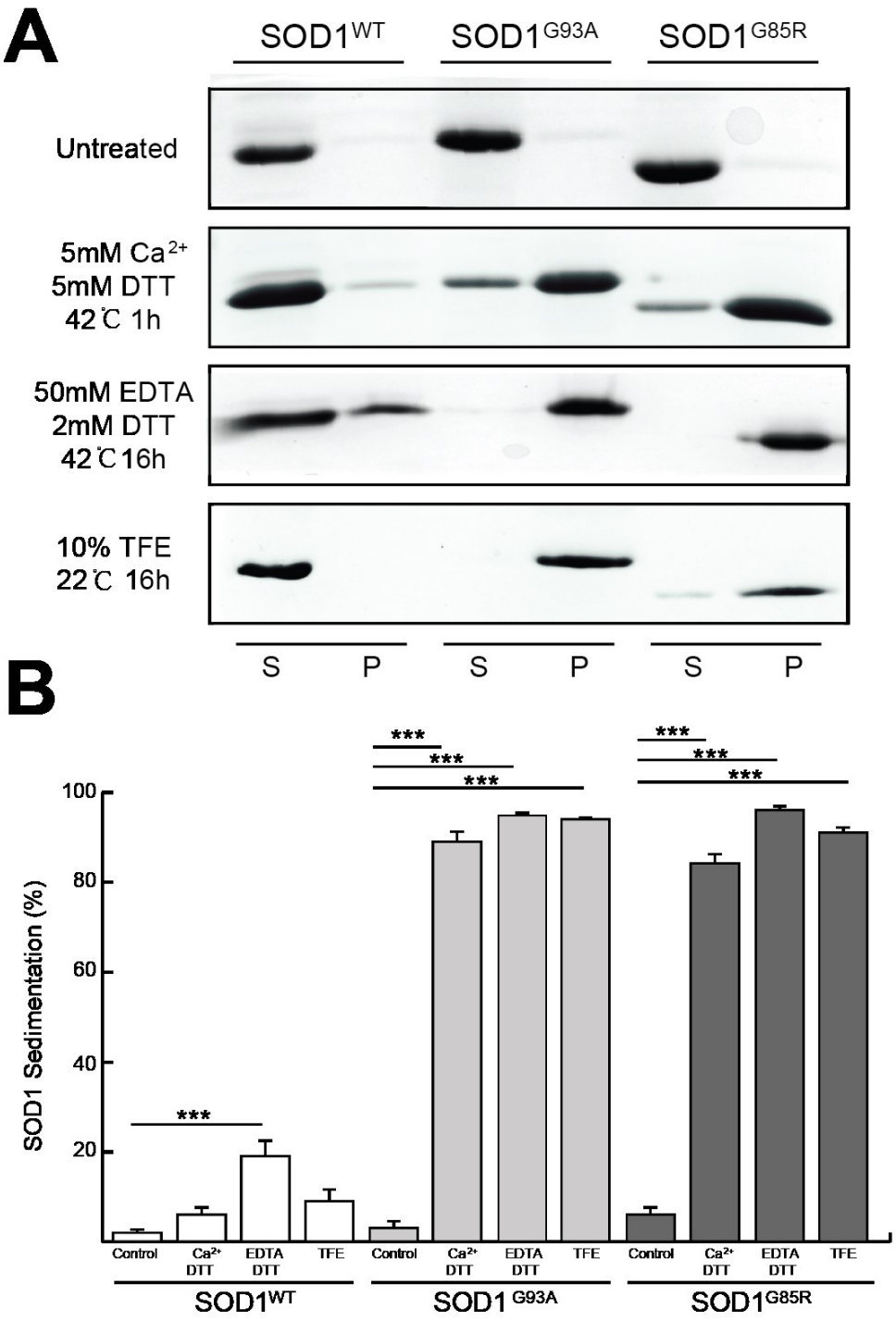

Figure 3.6 Combination of inducers to sediment SOD1. (A) SDS-PAGE of SOD1 sedimentation upon multiple inducer treatments. Coomassie brilliant blue stained 12 % SDS-polyacrylamide gel showed sedimentation of 10ug purified soluble SOD1 treated with control buffer (ddH_2O), 10% TFE, calcium/DTT, EDTA/DTT as indicated. Samples were centrifuged at 17000g for 60mins at 4°C to separate the supernatant (S) from the pellets (P), and resolved by SDS-PAGE as described in Material and Methods. **(B) Q**uantification of the mean percentage of SOD1 WT (white) G93A (pale grey) and G85R (grey) sedimented into insoluble fractions following combination treatments. Band intensity and statistical analysis were performed according to Materials and Methods. (Error bar=SD; ***p<0.005; n=5).

3.2.7 Effect of removal metal ion on soluble SOD1 structure

3.2.7.1 ANS binding affinity & stabilities of apo-SOD1

Various states of unfolded SOD1 have been classified in terms of disulphide and metallization status, including disulphide reduced, disulphide oxidized, fully metallated and metal-free states (Figure 1.4) (Ip et al. 2011). Banci *et al* (2008) reported that NMR and X-ray diffraction showed cysteine 6 and 111 in apo-SOD1 were surface exposed and interacted with other apo-SOD1 molecules to form oligomers (Banci et al. 2008), which was essential for loss of stability and further aggregation.

To generate apo-state SOD1, low concentration of EDTA at mild acid environment (pH=3.5~5.5) (Oztug Durer et al. 2009) was applied. Treated samples were co-incubated with ANS, a fluorophore that interacts with exposed hydrophobic surfaces within β-sheet structures, and the fluorescence spectra measured on an SAFIRE fluorescence plate reader (Figure 3.7A). In addition, the samples were centrifuged, separated, resolved by SDS-polyacrylamide gel and analysed by Coomassie brilliant blue staining (Figure 3.7.B).

When free in the neutral solution, ANS alone was excited with an emission peak at 520nm. The emission spectrum for holo-SOD1^{WT} was indistinguishable from that of the no protein control, indicating the hydrophobic surfaces of holo-SOD1^{WT} were still buried within SOD1 and showed no increased ANS binding. However, a slight blue shift to a peak at 490-500nm as well increased intensity of fluorescence emission was observed with purified untreated SOD1^{G93A} and SOD1^{G85R}. In addition, the fluorescence intensity of SOD1 increased after incubation in the apo-generation buffer. Compared to holo-SOD1^{WT}, treated SOD1^{WT} showed a higher ANS fluorescence signal (300a.u., compared to 250a.u.). Similarly, compared to untreated SOD1 mutant proteins, both apo-SOD1^{G93A} and apo-SOD1^{G85R} showed much stronger increase of intensity of fluorescence emission (450 a.u., compared to 350a.u.), suggesting treatment with EDTA in the mild acid environment altered the structure of SOD1 and exposed hydrophobic regions, so that they were available for ANS binding. Under the same treatment, apo-SOD1^{MT} showed stronger fluorescence intensity compared to apo-SOD1^{WT} (450a.u., compared to 250a.u.). In addition, both of untreated SOD1^{MT} proteins exhibited higher intensity of fluorescence emission than that of apo-SOD1^{WT}, indicating the SOD1^{MT} protein generated from denaturing conditions had more exposed hydrophobic residues than EDTA-treated SOD1^{WT}. There were no significant differences in the sedimentation between holo-SOD1 and low pH-EDTA generated apo-SOD1. In this mild acid environment, SOD1^{WT} was soluble under 5mM EDTA treatment. Nevertheless, a small amount of SOD1^{G93A} and SOD1^{G85R} became insoluble.

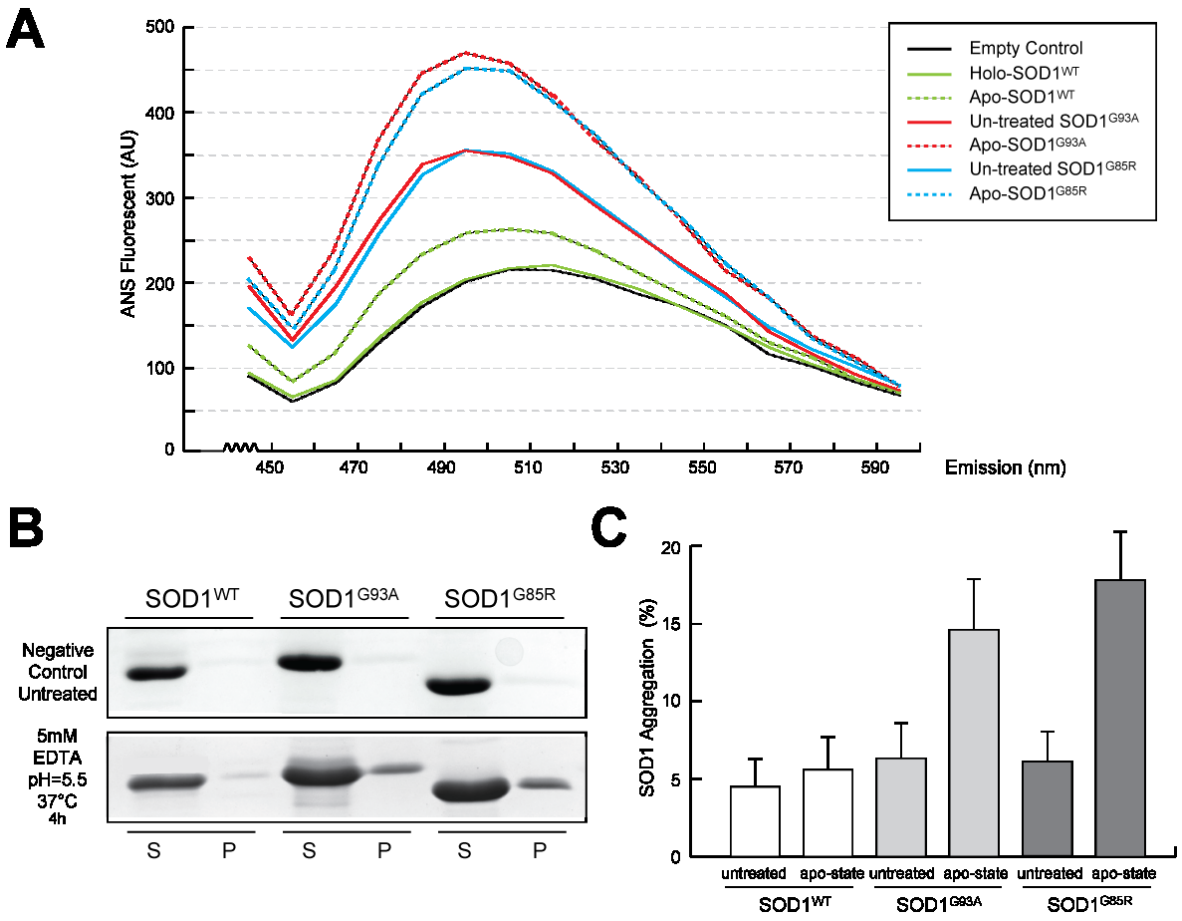

Figure 3.7 Effect of apo-state generation on SOD1 unfolding and stability. (A) ANS fluorescence emission spectra of untreated or apo-SOD1. The emission spectra from 410nm to 600nm of 5ug untreated SOD1 WT (green), G93A (red) and G85R (blue) in ddH_2O with the excitation wavelength at 390nm, or upon incubation with apo-generation buffer at 37°C for 4hrs were measured, overlaid with the emission spectrum of unbound ANS in no protein control (black) (n=3). **(B)** SDS-PAGE of apo-SOD1 sedimentation. Coomassie brilliant blue stained 12 % SDS-polyacrylamide gel showed sedimentation of 10ug purified soluble SOD1 WT, G93A and G85R treated with 5mM EDTA (final pH=5.5) at 37°C for 4hrs as indicated. Samples were centrifuged to separate the supernatant (S) from the pellets (P), and resolved by SDS-PAGE. **(C)** Quantification of the mean percentage of SOD1 WT (white bar) G93A (pale grey bar) and G85R (grey bar) sedimented into insoluble pellet fractions following apo-SOD1 generation procedure. Band intensity and statistical analysis were as described in Material and Methods (Error bar: SD; n=3).

3.2.7.2 ANS binding assay of mixture of $SOD1^{WT}$& $SOD1^{MT}$

As discussed in Chapter 1, the majority of mutations causing fALS are inherited in an autosomal dominant manner. This means that within patients' cells, $SOD1^{WT}$ is likely co-translated with SOD1 mutant and they could potentially interact. Therefore, it is important to investigate the effects of $SOD1^{MT}$ on $SOD1^{WT}$ on unfolding and/or misfolding before aggregation is triggered. To explore whether $SOD1^{MT}$ promoted conformational changes of $SOD1^{WT}$ during the metal-free state generation, an ANS binding assay was carried out. The same amount of purified $SOD1^{WT}$ and $SOD1^{MT}$ were co-incubated in the apo-generation buffer, or separately incubated and mixed immediately before measurement. Samples were incubated in the ANS working buffer, and the fluorescence intensity was measured (Figure 3.8).

The ANS fluorescence emission spectra showed there was an increase in fluorescence intensity of co-incubated $SOD1^{G93A}$/$SOD1^{WT}$, compared to separately incubated $SOD1^{G93A}$/$SOD1^{WT}$ mixture (370a.u., compared to 351a.u.). Increased fluorescence intensity was also observed in co-incubated $SOD1^{G85R}$/$SOD1^{WT}$ (389a.u., compared to 339a.u.), indicating that in the presence of $SOD1^{MT}$, $SOD1^{WT}$ is promoted more β-sheet contents and hydrophobic areas were more exposed for ANS to bind upon treatment. In addition, holo-$SOD1^{WT}$ was also treated using the same apo-generation buffer without the soluble $SOD1^{MT}$. This showed similar results to Figure 3.7 and confirmed the conformational changes of $SOD1^{WT}$ during the apo-generation process.

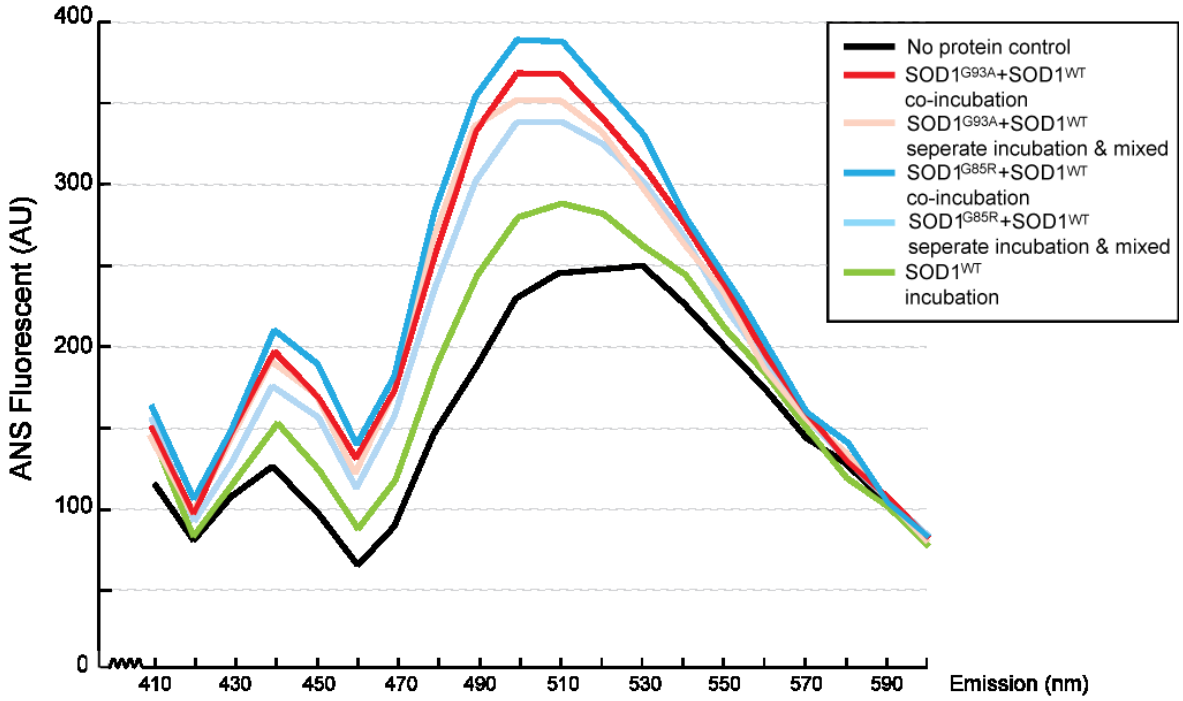

Figure 3.8 Effects of SOD1^{MT} on SOD1^{WT} unfolding during apo-state generation. ANS fluorescence emission spectra of mixture of SOD1 mutant and SOD1^{WT}. The emission spectra from 410nm to 600nm of SOD1 mixture of ① 2.5ug G93A and 2.5ug WT were co-incubated (red); ② 2.5ug G93A and 2.5ug WT were incubated in apo-generation buffer separately and mixed before measurement (pale red); ③ 2.5ug G85R and 2.5ug WT were co-incubated (blue); ④ 2.5ug G85R and 2.5ug WT were incubated in apo-generation buffer separately and mixed before measurement (pale blue); ⑤ 5ug WT (green) was incubated in apo-generation buffer with the excitation wavelength at 390nm. All the samples were treated at 37°C for 4hrs in apo-generation buffer, overlaid with the emission spectrum of unbound ANS in no protein control (black) (n=6).

3.2.8 Effect of preformed $SOD1^{MT}$ aggregation on soluble SOD1 sedimentation

3.2.8.1 Effect of preformed $SOD1^{MT}$ aggregates on soluble $SOD1^{WT}$

In section 3.2.7, experiments were designed to explore the effects of $SOD1^{MT}$ on $SOD1^{WT}$ during the de-metallation process. In this section I explored the effects of $SOD1^{MT}$ aggregation on $SOD1^{WT}$ after the soluble $SOD1^{MT}$ had aggregated into insoluble pellets, as SOD1 aggregation is one of the hallmarks of SOD1 related fALS disease.

3.2.8.1.1 Effect of $SOD1^{MT}$ aggregates on holo-$SOD1^{WT}$

To investigate the effects of preformed $SOD1^{MT}$ to seed the aggregation of $SOD1^{WT}$, small amount of $SOD1^{MT}$ aggregates were added into soluble holo-$SOD1^{WT}$ and partially or fully de-metallated $SOD1^{WT}$. Treated $SOD1^{WT}$ samples were incubated in ANS working buffer, and the fluorescence intensity was measured (Figure 3.9A), or co-incubated with preformed aggregates, separated, resolved by SDS-polyacrylamide gel and analyzed by Coomassie brilliant blue staining (Figure 3.9B). The ANS fluorescence emission spectra showed an increase of fluorescence intensity for the treated $SOD1^{WT}$ samples [358a.u. of partially demetallized (pd)-$SOD1^{WT}$, 391.a.u. of apo-$SOD1^{WT}$], compared to the untreated $SOD1^{WT}$ (256 a.u.), which indicated more hydrophobic surfaces of $SOD1^{WT}$ were exposed, and conformational changes had occurred, therefore the treated samples were destabilized from native state.

When the preformed SOD1 aggregates were mixed with holo-$SOD1^{WT}$, only a small amount of the $SOD1^{WT}$ was sedimented. In contrast, an increased sedimentation was observed in when pd-$SOD1^{WT}$ was mixed with mutant aggregates (58% for G93A seeds, and 54% for G85R seeds), compared to that of holo-$SOD1^{WT}$. When the same amount of aggregates were co-incubated with more destabilized apo-$SOD1^{WT}$, more $SOD1^{WT}$ was recruited into the insoluble pellet fractions (68% for G93A seeds, and 62% for G85R seeds), suggesting that preformed SOD1 aggregates showed little sedimentation effect towards holo-$SOD1^{WT}$, but could effectively recruit pd- and apo-$SOD1^{WT}$ (Figure 4.9B). Therefore, Cu/Zn charged SOD1 showed a strong resistance towards the ability of SOD1 aggregates to stimulate further sedimentation.

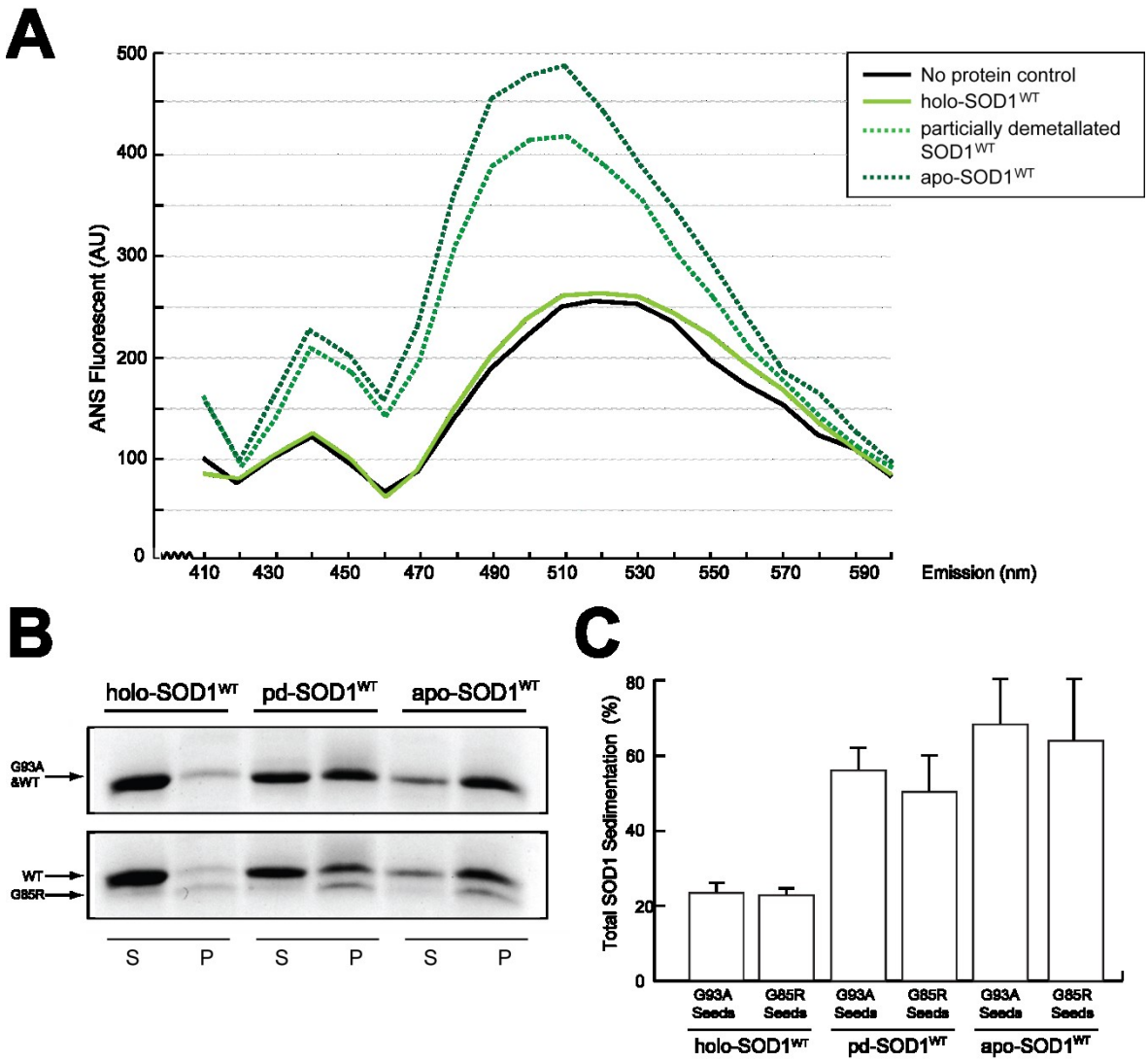

Figure 3.9 Effect of SOD1^{MT} aggregates on SOD1^{WT} at different demetallation stages. (A) ANS fluorescence emission spectra of untreated/treated WT. The emission spectra from 410nm to 600nm of 5ug WT treated with ① ddH_2O at 22°C (green); ② 5mM EDTA at 42°C for 8hrs (pH=5.5) (darker green, dash line); ③ 5mM EDTA at 42°C for 16hrs (pH=5.5) (darkest green, dash line) with the excitation wavelength at 390nm overlaid with the emission spectrum of unbound ANS in no protein control (black) (n=3). **(B)** SDS-PAGE of WT sedimentation upon the co-incubation with SOD1 aggregates. Coomassie brilliant blue stained 12 % SDS-polyacrylamide gel showed sedimentation of mixture of 9ug untreated/treated WT with 1.6ug preformed SOD1 aggregates, which were incubated at 42°C for 48hrs. Samples were centrifuged to separate the supernatant (S) from the pellets (P), and resolved by SDS-PAGE (refer to Materials and Methods). **(C)** Quantification of the percentage of mean SOD1 sedimented into insoluble pellet fraction following the incubation. Band intensity and statistical analysis was performed according to Material and Methods (Error bar: SD; n=3).

3.2.8.1.2 Effect of $SOD1^{MT}$ aggregates on apo-$SOD1^{WT}$

To further investigate the effects of preformed $SOD1^{MT}$ seeds on $SOD1^{WT}$ aggregation, 1.6ug of $SOD1^{MT}$ aggregates were added to 9ug of soluble apo-$SOD1^{WT}$, the samples were incubated for 48hrs, fractionated, resolved by SDS-polyacrylamide gel and analyzed by Coomassie brilliant blue staining (Figure 3.10.B). In this reaction, EDTA will chelate with Ca^{2+}, which removed the effects of Ca^{2+} after mixing. Furthermore, the pH was also adjusted back to 7.0 by pH=12 phosphate buffer. Therefore, the reaction environment for the seeding was adjusted such that the seeding could be triggered by the SOD1 aggregates alone, not by inducers, such as calcium or low pH during the long-time incubation.

Preformed SOD1 aggregates were co-incubated with/without the apo-$SOD1^{WT}$. $SOD1^{MT}$ were confirmed to form insoluble aggregates. On the basis of time point 0 sample (lane 5-6), apo-$SOD1^{WT}$ was mainly soluble when it was mixed with aggregates (total SOD1 sedimentation: 23% for G93A and 21% for G85R), suggesting the further sedimentation was triggered in the after incubation. In addition, when soluble $SOD1^{G93A}$ or $SOD1^{G85R}$ were mixed with apo-$SOD1^{WT}$ (lane 7-8), only a relatively small amount of $SOD1^{WT}$ was sedimented (28% for G93A and 27% for G85R), suggesting the incubation itself had little effect on the sedimentation of soluble $SOD1^{WT}$. Only in the presence of preformed SOD1 aggregates was apo-$SOD1^{WT}$ stimulated to form insoluble pellets (lane 3-4) (72% for G93A, and 68% for G85R). In conclusion, preformed SOD1 could trigger the apo-$SOD1^{WT}$ further sedimentation, thus accelerating aggregation process *in vitro*.

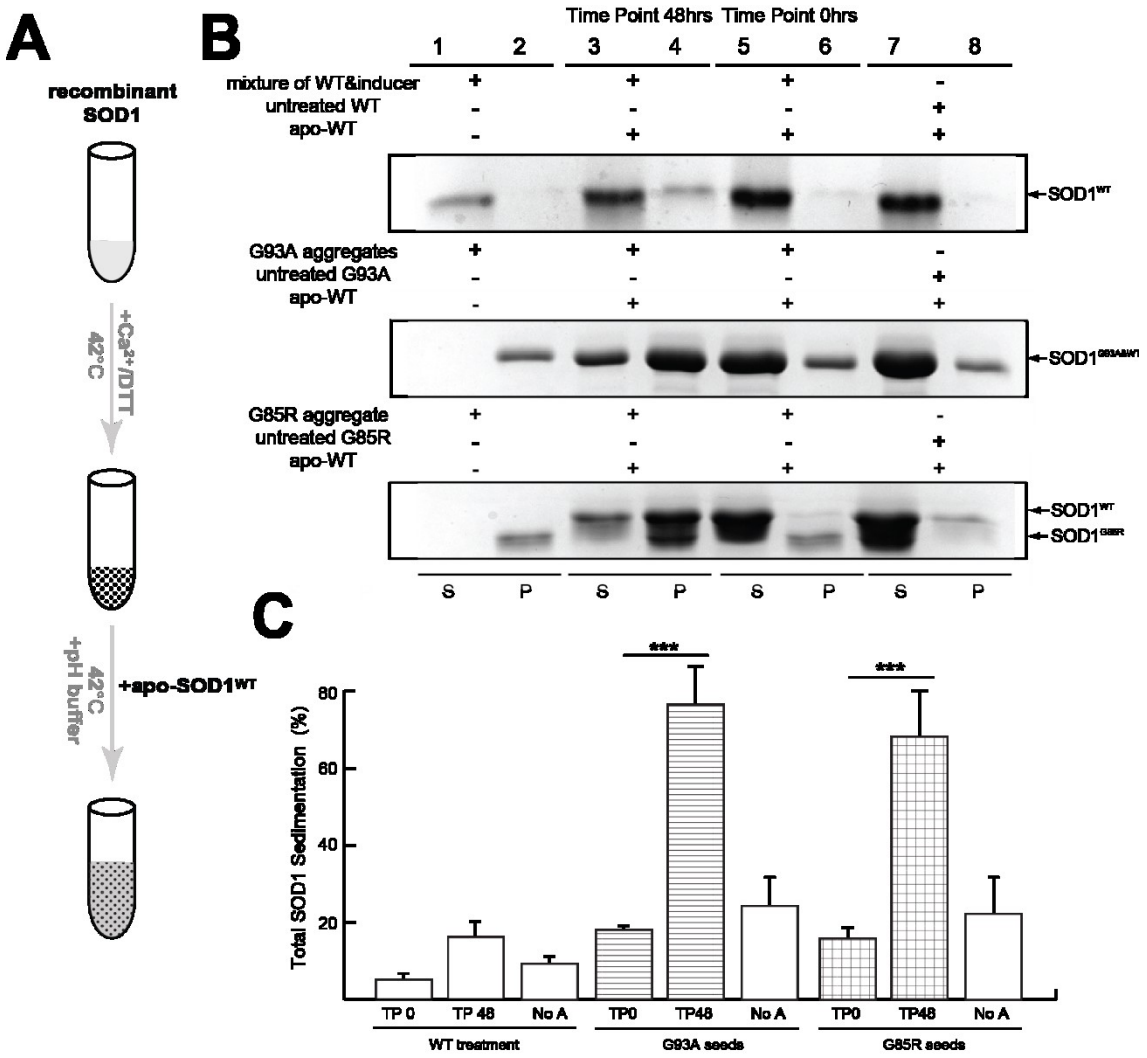

Figure 3.10 Effect of SOD1 aggregates on apo-SOD1^{WT} sedimentation. (A) Schematic illustration of *in vitro* seeding assay. **(B)** SDS-PAGE of SOD1^{WT} sedimentation upon the co-incubation with SOD1 aggregates. Coomassie brilliant blue stained 12% SDS-polyacrylamide gel showed sedimentation of 9ug apo-WT co-incubated with (top) mixture of 1.6ug WT& inducer; (middle) 1.6ug G93A aggregates; (lower) 1.6ug G85R aggregates at 42°C for 48hrs. Samples from timepoint 0hrs (TP0) and timepoint 48hrs (TP48) were centrifuged to separate the supernatant (S) from the pellets (P) with no aggregates control (No A), and resolved by SDS-PAGE, the shading represented the presence of preformed aggregates. **(C)** Quantification of the percentage of apo-WT sedimented into insoluble pellet fraction following the incubation. Band intensity and statistical analysis was performed according to Material and Methods (Error bar: SD; n=3; ***p<0.005).

3.2.8.2 Effect of preformed SOD1^{MT} aggregates on soluble SOD1^{MT}

The experiments performed in section 3.2.8.1 using SOD1 mutant aggregates to seed SOD1^{WT} aggregation provided insights into the process of aggregate formation. Although cross-seeding between different mutants is not an event observed in the neurons of ALS patients, I wanted to exploit the difference in mobility between SOD1^{G93A} and SOD1^{G85R} to further characterize the process of spontaneous or seeded SOD1 aggregation.

3.2.8.2.2 Effect of preformed SOD1^{MT} aggregates on untreated SOD1^{MT}

To investigate the effects of preformed SOD1^{MT} seeds, preformed aggregates were mixed with soluble purified yet untreated SOD1^{MT}, or apo-SOD1^{MT} exploiting the difference in mobility between SOD1^{G93A} and SOD1^{G85R}. Treated samples were co-incubated in ANS working buffer, and fluorescence spectra were measured (Figure 3.7A), or co-incubated with preformed aggregates, fractionated, resolved by SDS-polyacrylamide gel and analyzed by Coomassie brilliant blue staining (Figure 3.11).

An increased sedimentation was observed in the mixture of apo-SOD1^{MT} and mutant aggregates (92% for G93A, and 87% for G85R) compared to that of untreated control (22% for G93A and 29% for G85R), suggesting the preformed SOD1 aggregates showed stronger sedimentation effect towards apo-SOD1 mutant than the untreated SOD1 mutant protein.

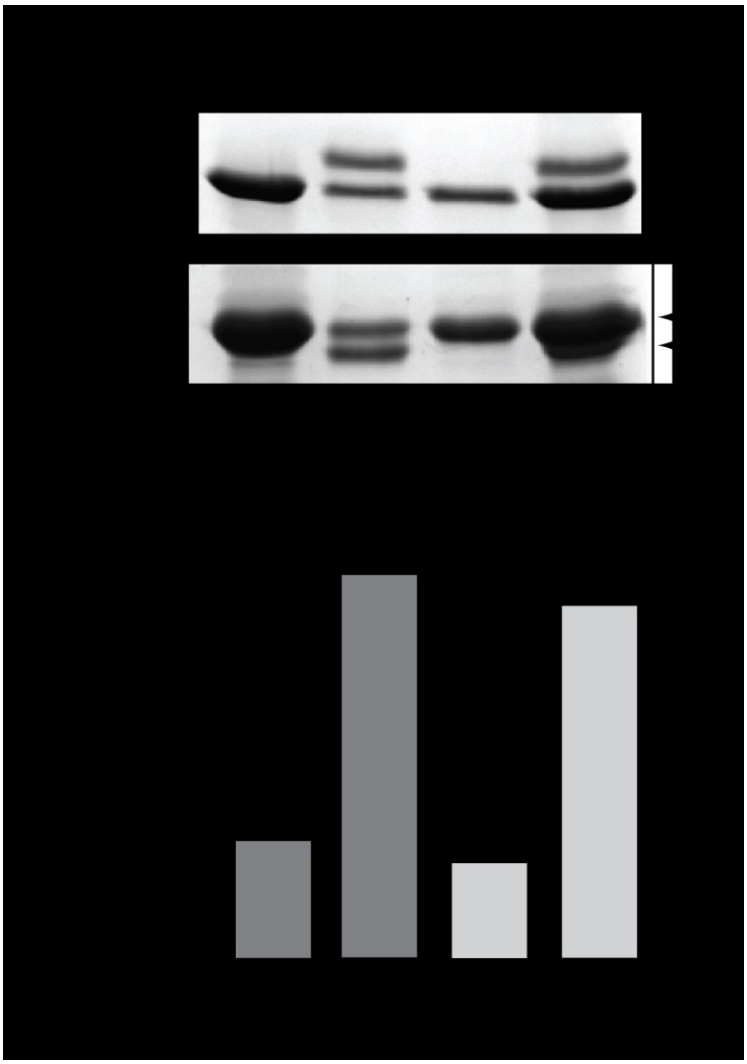

Figure 3.11 Effect of SOD1 aggregates on untreated or EDTA treated soluble SOD1$^{MT.}$ (A) SDS-PAGE of soluble MT sedimentation upon the co-incubation with SOD1 aggregates. Coomassie brilliant blue stained 12 % SDS-polyacrylamide gel showed sedimentation of mixture of 9ug untreated/treated G93A (light grey) with 1.6ug preformed G85R aggregates, or 9ug untreated/treated G85R (dark grey) with 1.6ug preformed G93A aggregates which were incubated at 42°C for 48hrs. Samples were centrifuged to separate the supernatant (S) from the pellets (P), and resolved by SDS-PAGE (refer to Material and Methods). **(B)** Quantification of the percentage of total SOD1 sedimented into insoluble pellet fraction following the incubation. Band intensity and statistical analysis was performed according to Material and Methods (Error bar: SD; ***p<0.005; n=3).

3.2.8.2.2 Effect of preformed $SOD1^{MT}$ aggregates on apo-$SOD1^{MT}$

To further investigate the effects of $SOD1^{MT}$ aggregates on apo-$SOD1^{MT}$ sedimentation, preformed $SOD1^{G93A}$ aggregates were mixed with soluble apo-$SOD1^{G85R}$. In addition, the preformed $SOD1^{G85R}$ were added into soluble apo-$SOD1^{G93A}$. All samples were incubated, separated, resolved by SDS-polyacrylamide gel and analysed by Coomassie brilliant blue staining (Figure 3.12)

In the cross-seeding assay, preformed G93A aggregates were co-incubated with apo-$SOD1^{G85R}$, and G85R aggregates were co-incubate with apo-$SOD1^{G93A}$. Aggregates formation was confirmed by lane 1-2. Based on time point 0 (lane 3-4), apo-$SOD1^{G93A}$ and apo-$SOD1^{G85R}$ were mainly soluble, indicating the further aggregation happened afterwards. In the presence of preformed aggregates, apo-$SOD1^{G93A}$ and apo-$SOD1^{G85R}$ were recruited to the insoluble fractions (~82% for G93A, and ~79% for G85R), which is similar to apo-$SOD1^{WT}$. On the basis of no aggregates control (lane 7-8), both apo-$SOD1^{G93A}$ and apo-$SOD1^{G85R}$ stayed soluble, indicating the spontaneous sedimentation rate is lower than mixture of aggregates and apo-$SOD1^{MT}$ (~42% for G93A and ~37% for G85R). Therefore, this cross-seeding assay suggested aggregates in this system stimulated further sedimentation of soluble apo-SOD1.

In addition, compared to seeding assay of $SOD1^{WT}$, the cross-seeding assay revealed that preformed SOD1 aggregates possessed higher sedimentation effects on $SOD1^{MT}$, rather than the apo- or holo-$SOD1^{WT}$, which is in agreement with the ANS data that suggested SOD1 mutants had a more open conformation.

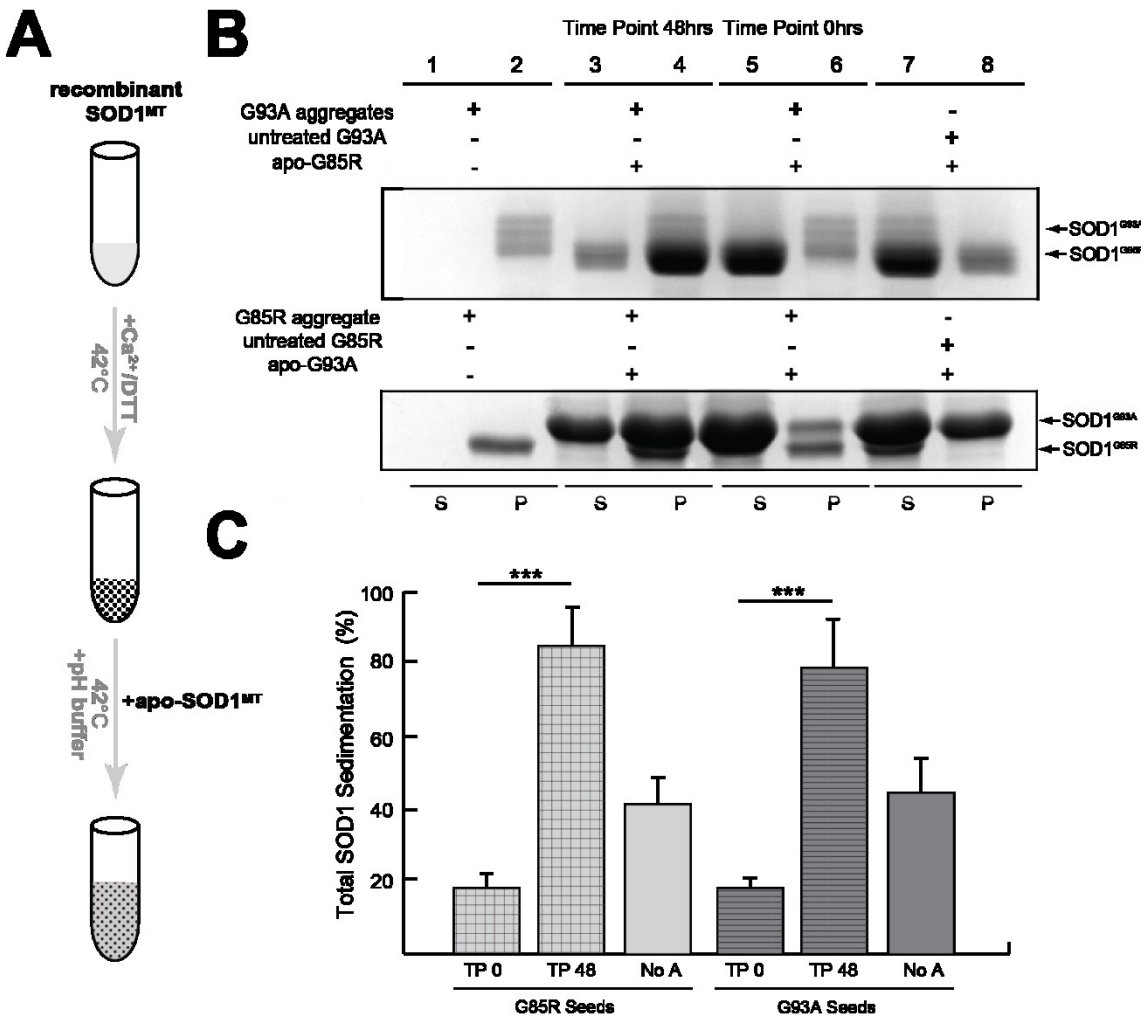

Figure 3.12 Effect of SOD1 aggregates on apo-SOD1^{MT} sedimentation. (A) Schematic illustration of *in vitro* seeding assay. **(B)** SDS-PAGE of G93A (light grey) or G85R (dark grey) sedimentation upon the co-incubation with different SOD1 aggregates. Coomassie brilliant blue stained 12 % SDS-polyacrylamide gel showed sedimentation of 9ug apo-G93A co-incubated with ① mixture of 1.6ug G85R& inducer; ② 1.6ug G85R aggregates at 42°C for 48hrs. Samples were centrifuged to separate the supernatant (S) from the pellets (P), and resolved by SDS-PAGE, the shading represented the presence of preformed aggregates. **(C)** Quantification of the mean percentage of apo-MT sedimented into insoluble pellet fraction following the incubation. Band intensity and statistical analysis was performed according to Materials and Methods (Error bar: SD; ***p<0.005; n=3).

3.2.9 Effect of HSJ1 on SOD1 aggregation formation

3.2.9.1 Effect of HSJ1 on SOD1 aggregation formation under reducing environment

To investigate effects of HSJ1 on SOD1 sedimentation, an assay was developed to test if HSJ1a or HSJ1b can affect SOD1 sedimentation. SOD1 samples were treated with inducers (calcium/DTT) in the presence or absence of HSJ1 proteins, were fractionated, resolved by SDS-polyacrylamide gel and analysed by Coomassie brilliant blue staining (Figure 3.13).

Using different combination of inducers in the reducing environment, $SOD1^{G93A}$ formed insoluble pellets (lane 1-2), while $SOD1^{WT}$ remained mainly soluble, suggesting $SOD1^{WT}$ possessed a more stable conformation to resist stress. Furthermore, in the presence of purified HSJ1, $SOD1^{G93A}$ sedimentation was significantly reduced by both HSJ1a (lane 3-4) and HSJ1b (lane 5-6), compared to the no chaperone control. However, because of the high intrabatch variation, no statistical analysis was performed for this assay.

This experiment suggested that HSJ1 might directly interact with SOD1 upon stresses, which delayed SOD1 sedimentation.

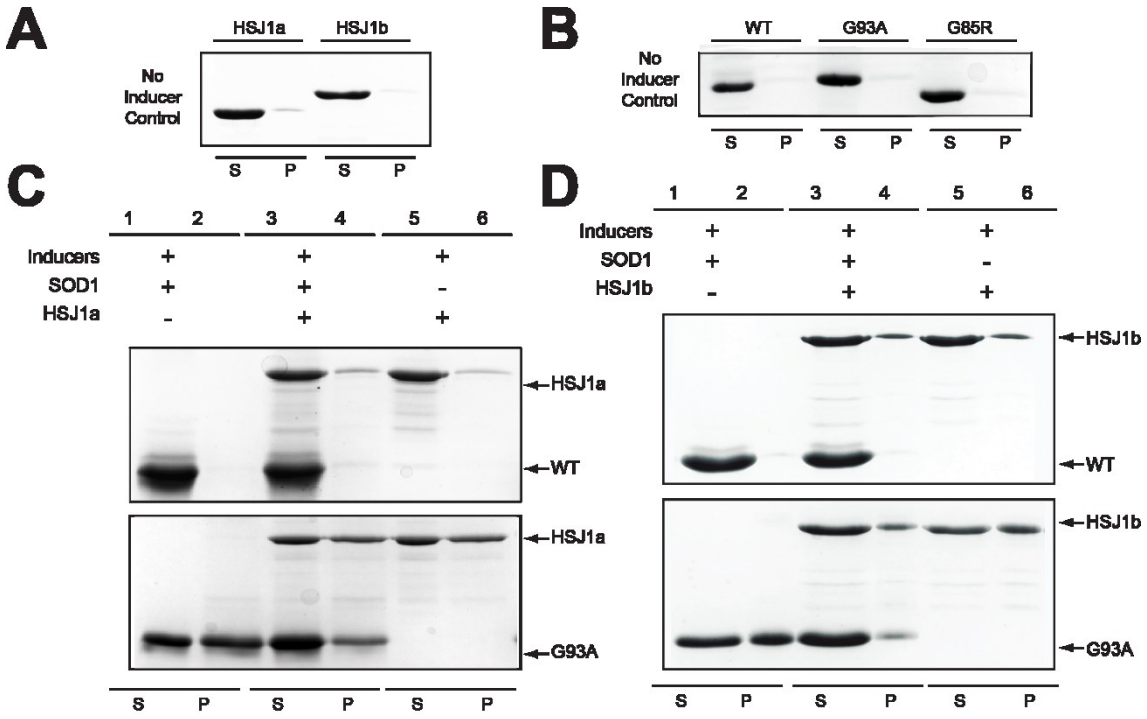

Figure 3.13 Effect of HSJ1 on SOD1 sedimentation under reducing environment. (A-B) Coomassie Brilliant Blue stained 12% SDS-polyacrylamide gel showing sedimentation of 5ug untreated HSJ1 (A) and SOD1 (B) **(C-D)** Coomassie Brilliant Blue stained 12% SDS-polyacrylamide gel showing sedimentation of 7.5ug purified SOD1 that was co-incubated with (lane 3-4) / without (lane 1-2) 7.5ug purified HSJ1a (C) or HSJ1b (D) treated with 3mM calcium/5mM DTT for 35min at 37°C. Samples were centrifuged to separate the supernatant (S) from the pellets (P), and resolved by SDS-PAGE as described in Materials and Methods (n=5).

3.2.10 Effect of HSJ1 on SOD1 aggregation seeding soluble SOD1

The experiments performed in section 3.2.8 simulated the events that could happen after $SOD1^{MT}$ aggregate formation in ALS patients. Those preformed SOD1 aggregates showed sedimentation effects towards either apo-$SOD1^{WT}$ or apo-$SOD1^{MT}$ As the seeding phenomena represented the step that SOD1 aggregates spread and expand, it is important to investigate whether HSJ1 has the ability to inhibit SOD1 aggregates from further expansion.

3.2.10.1 Effect of HSJ1 on SOD1 aggregation seeding apo-$SOD1^{WT}$

To further investigate the effects of HSJ1 on SOD1 aggregates seeding soluble $SOD1^{WT}$, preformed SOD1 aggregates were mixed with apo-$SOD1^{WT}$ in the presence or absence of HSJ1. All the samples were co-incubated, separated, resolved by SDS-polyacrylamide gel and analysed by Coomassie brilliant blue staining. $SOD1^{MT}$ aggregate formation for the seed is shown in lane 1-2. When co-incubated with apo-$SOD1^{WT}$, both $SOD1^{G85R}$ aggregates and $SOD1^{G93A}$ aggregates promoted further sedimentation of soluble apo-$SOD1^{WT}$ (lane 3-4) (69% and 72% respectively). However, in the presence of either HSJ1 isoform (lane 5-6), the percentage of insoluble WT was significantly reduced (54% for G93A seeds, and 49% for G85R seeds).

Interestingly, the preformed SOD1 aggregates recruited all of the soluble HSJ1a or HSJ1b to the sedimented pellet. A no aggregate-seed control showed there was less spontaneous sedimentation of apo-$SOD1^{WT}$, soluble $SOD1^{G93A}$ or $SOD1^{G85R}$, or HSJ1 during the incubation process.

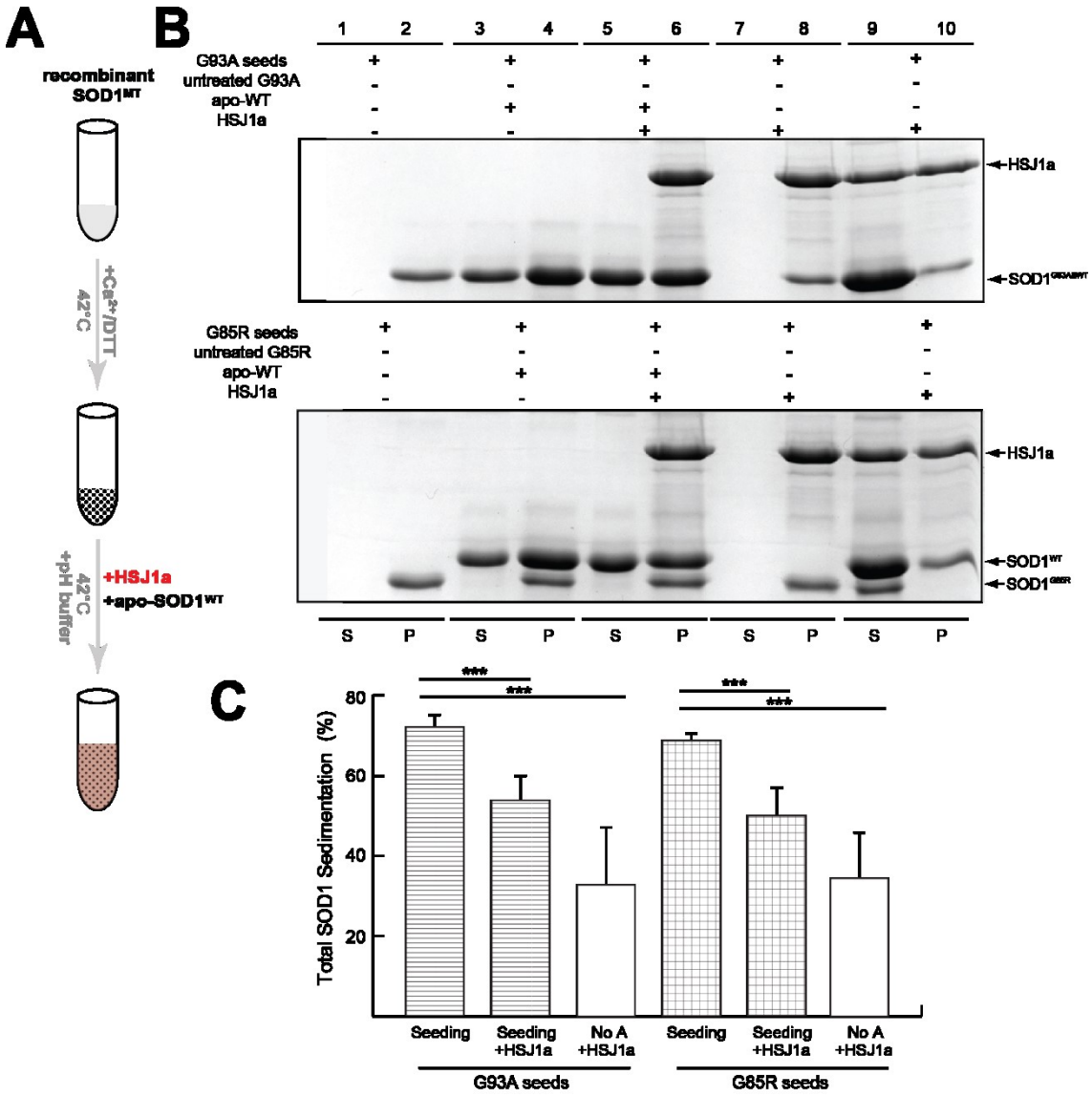

Figure 3.14 Effect of HSJ1a on preformed aggregates-induced SOD1^{WT} sedimentation. (A) Schematic illustration of HSJ1a inhibition SOD1 seeding assay. **(B)** Coomassie Brilliant Blue stained 12% SDS-polyacrylamide gel showing sedimentation of 10ug soluble SOD1^{WT} that was co-incubated with (lane 5-6) / without (lane 2-3) 8ug HSJ1a in 42°C for 48hrs. Samples were centrifuged to separate the supernatant (S) from the pellets (P), and resolved by SDS-PAGE as described in Materials and Methods, the shading represented the presence of preformed aggregates. **(C)** Quantification of the mean percentage of total SOD1 sedimented into insoluble pellet fraction with HSJ1a. Band intensity and statistical analysis was performed according to Material and Methods (Error bar: SD; n=3, ***p<0.005).

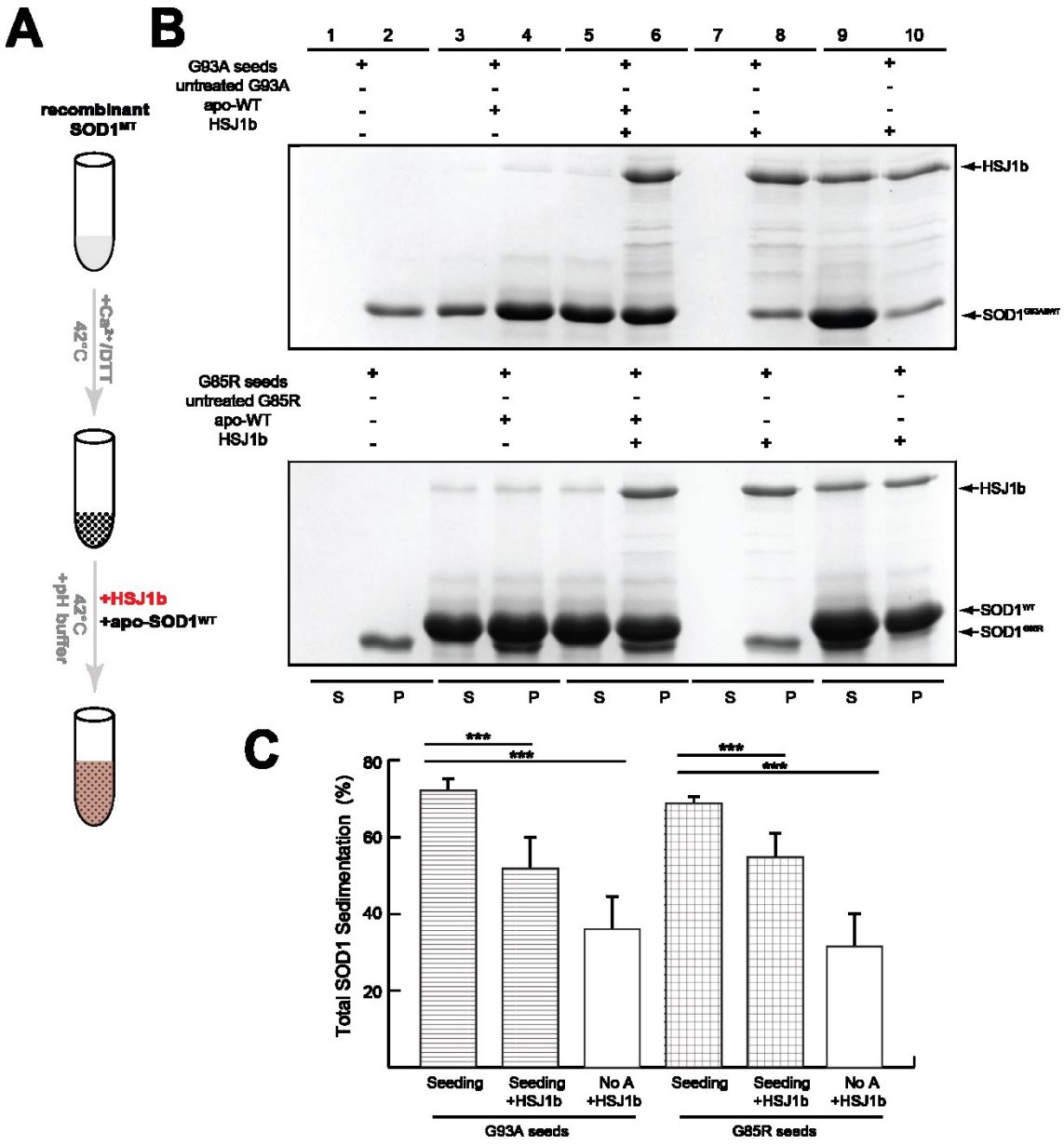

Figure 3.15 Effect of HSJ1b on preformed aggregates-induced SOD1^{WT} sedimentation. (A) Schematic illustration of HSJ1b inhibition SOD1 seeding assay. **(B)** Coomassie Brilliant Blue stained 12% SDS-polyacrylamide gel showing sedimentation of 10ug soluble SOD1^{WT} that was co-incubated with (lane 5-6) / without (lane 2-3) 8ug HSJ1b in 42°C for 48hrs. Samples were centrifuged to separate the supernatant (S) from the pellets (P), and resolved by SDS-PAGE as described in Materials and Methods, the shading represented the presence of preformed aggregates. **(C)** Quantification of the mean percentage of total SOD1 sedimented into insoluble pellet fraction with HSJ1b. Band intensity and statistical analysis was performed according to Material and Methods (Error bar: SD; n=3, ***p<0.005).

3.2.10.2 Effect of HSJ1 on SOD1 aggregate seeding apo-SOD1^{MT}

To further investigate the effect of HSJ1 on soluble SOD1^{MT} in the presence of SOD1 aggregates, preformed SOD1 aggregates mixed with/without HSJ1, and then co-incubated with apo-SOD1^{MT}. All the samples were fractionated, resolved by SDS-polyacrylamide gel and analysed by Coomassie brilliant blue staining (Figure 3.16).

SOD1^{MT} formed insoluble aggregate seeds, which were confirmed by lane 1-2. In the co-incubation reaction, preformed SOD1^{G93A} aggregates triggered the sedimentation of soluble apo-SOD1^{G85R} (lane 3-4), compared to HSJ1a (lane 5-6) or HSJ1b (lane 7-8) treatment. Both HSJ1a and HSJ1b (63% of HSJ1a and 58% of HSJ1b, compared to 92%) significantly inhibited apo-SOD1^{G85R} from sedimentation. Similarly, SOD1^{G85R} aggregates stimulated sedimentation of apo-SOD1^{G93A} (lane 3-4). Both HSJ1 isoforms significantly reduced apo-SOD1^{G93A} sedimentation (60% of HSJ1a and 64% of HSJ1b, compared to 87%) as well as apo-SOD1^{G85R} sedimentation.

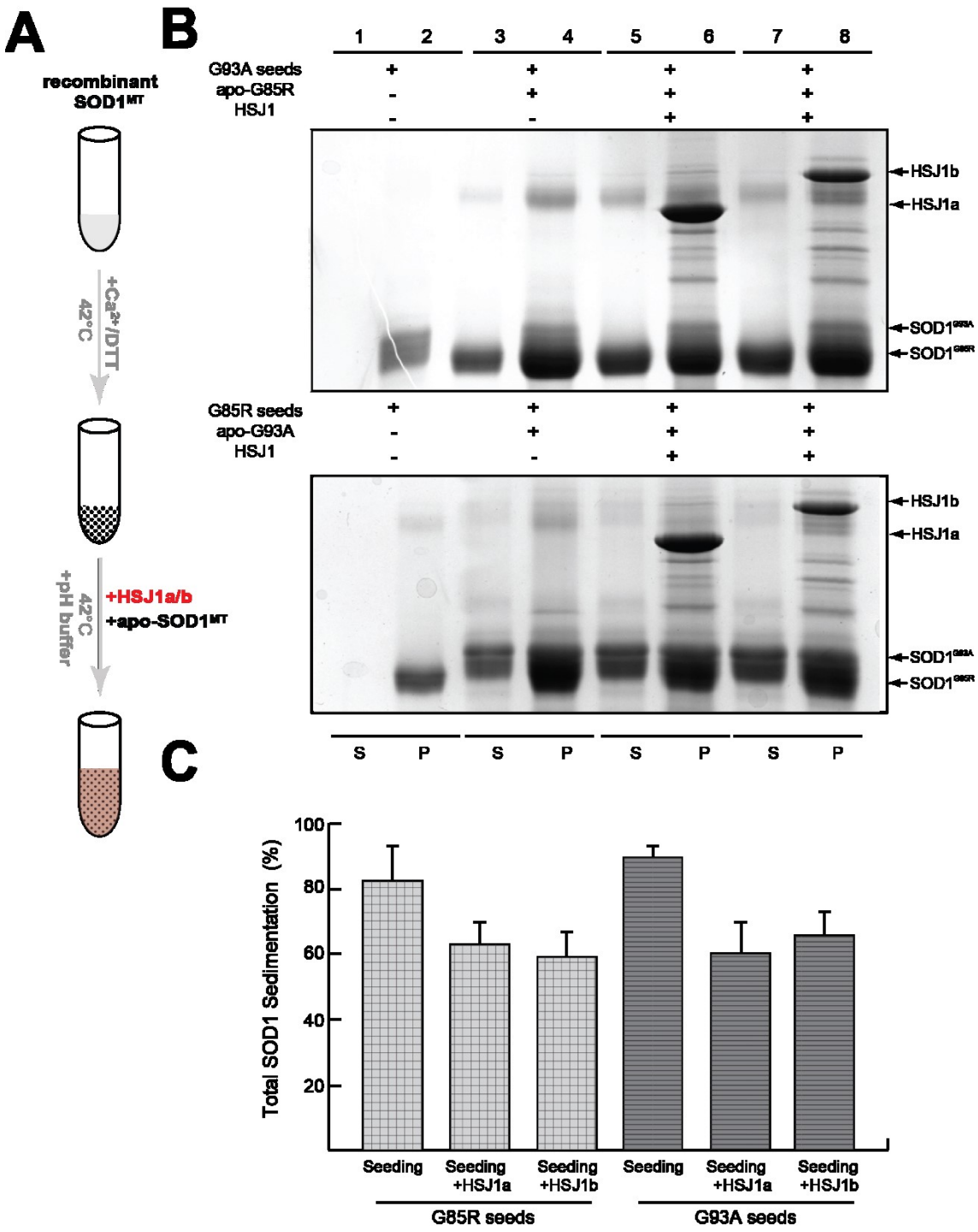

Figure 3.16 Effect of HSJ1 on preformed aggregates-induced SOD1^{MT} sedimentation. (A) Schematic illustration of HSJ1 inhibition SOD1 seeding assay. **(B)** Coomassie Brilliant Blue stained 12% SDS-polyacrylamide gel showing sedimentation of 9ug soluble SOD1 G93A (light grey) or G85R (dark grey) that was co-incubated with (lane 5-6) / without (lane 2-3) 8ug HSJ1a or HSJ1b in 42°C for 48hrs. Samples were centrifuged to separate the supernatant (S) from the pellets (P), and resolved by SDS-PAGE (refer to Materials and Methods), the shading represented the presence of preformed aggregates. **(C)** Quantification of the mean percentage of total SOD1 sedimented into insoluble pellet fraction with HSJ1. Band intensity and statistical analysis was performed according to Materials and Methods (Error bar: SD; n=3).

3.3 Discussion

SOD1-associated ALS is a neurodegenerative disorder with diverse symptoms and durations, which is largely affected by symptoms spread along the neuraxis until the motor neurons involved in respiration degenerated leading to breathing problems (Hardiman et al. 2011; Wood-Allum & Shaw 2010). The mechanism of how the disease spreads is one of the major unsolved questions for ALS research. Numerous studies have been performed to investigate the diverse consequences brought by SOD1 mutations biophysically and/or biochemically, using SOD1 proteins expressed in bacteria, yeast or insect. In this chapter, with the aim to explore the seeding potential of SOD1 aggregates generated *in vitro*, and to verify if HSJ1 could modulate this aggregation or seeding potential, recombinant SOD1 proteins were generated using pET-expression system and relevant *E.coli* stain.

Not every protein is suitable for prokaryotic expression. Luckily, there are only two post-translational modifications of SOD1 specific to eukaryotes: ① cleavage of the N-terminal methionine and ② acetylation of the adjacent alanine, suggesting SOD1 expressed in the *E. co.li* BL21 (DE3) pLysS strain is similar to SOD1 produced in mammalian cells, theoretically. The difference between wild-type and mutant SOD1 has already shown at this step: under the same induction conditions, $SOD1^{WT}$ stayed in the soluble fraction, yet $SOD1^{MT}$ formed inclusions. Therefore, $SOD1^{WT}$ was purified under native state to keep its native conformation, while $SOD1^{MT}$ was purified with denaturing conditions, and refolded later in a native buffer (1XPBS) with 5% glycerol as physical chaperone. A certain concentration of Cu^{2+} and Zn^{2+} were added into the dialysis buffer, aiming to load metal ions onto SOD1 protein. Similarly, recombinant HSJ1 was purified using *E.coli* and IMAC as well.

Several attempts were carried out to improve the solubility of $SOD1^{MT}$ in the bacterial expression system, including lower culture temperature, longer induction time, different culture medium (such as M9 medium) and adding 5% of ethanol into the culture medium. These attempts did not optimise the solubility. However, a few more could be done in the future: ① co-expression with CCS (~30kDa) or PDI (~ 57kDa); ② adding low concentration of Cu^{2+} and Zn^{2+} into the culturing medium; ③ use SHuffle or PURExpress strain; or ④ further codon modifications to avoid fast translation.

SOD1 sedimentation can be induced by demetallation, reduction of disulfide bonds and increased hydrophobicity.

Previous work has suggested recombinant SOD1 could be thermally labile; in particular an unpublished thesis (Noah, Worchester Polyechnic Institute, 2010) used heating between 50°C-60°C to induce SOD1 sedimentation, which was monitored by the

turbidity using 90° light scattering at 450nm. In Cohen's study, recombinant SOD1 samples (~pH 7.0) heated for 16 hours was enough to promote a high percentage of SOD1 to form insoluble pellets. The exponential growth phase of aggregate formation was observed after 6h treatment. In addition, Munch et al (2010) reported that heating of various SOD1 mutants (A4V, H46R, G93A, E100G, S134N, L144F) under native conditions in the presence of Sypro Orange resulted in significant increase in the fluorescence between 55-85°C (Munch & Bertolotti 2010). Interestingly, the recombinant SOD1 proteins generated in this study proved to be extremely stable. As shown in Figure 4.3, SOD1 proteins remained soluble after heating at 65°C for 24h. Therefore, attempts using heating as the inducing environment failed. Early attempts were made to purify recombinant $SOD1^{G93A}$ under native conditions, but the purities and yields were not satisfactory. Similarly, recombinant $SOD1^{G85R}$ blocked the Ni-NTA column during native purification process. However, those poorly native purified $SOD1^{G93A}$ could be triggered to form insoluble pellets by heating at 42°C for 30min (data not shown). Comparison between $SOD1^{MT}$ purified using denaturing conditions with subsequent refolding in the presence of metal ions suggested that high thermostablity shown in this chapter is probably due to them refolding back to a low free energy state. In addition, Cu^{2+} and Zn^{2+} ions may stabilize the tertiary structure. This was confirmed by the ANS binding assay.

Other than heating, chelating reagents aimed at removal of the Cu^2 /Zn^{2+} ions, such as EDTA, or reducing reagents aimed at breaking disulfide bonds, such as DTT were also applied to test the stability of SOD1. $SOD1^{WT}$ showed high solubility following EDTA or DTT treatment. In contrast, $SOD1^{G93A}$ exhibited higher sensitivity towards DTT, instead of EDTA, whereas $SOD1^{G85R}$ showed higher sedimentation percentage following EDTA treatment, rather than DTT. The different sedimentation effects of EDTA and DTT on SOD1 mutants are possibly due to different metal binding and β-barrel contents.

Leal *et al* (2013) reported that calcium increased recombinant SOD1 β-sheet contents and hydrophobicity (Leal et al. 2013), promoted oligomerization and conformational heterogeneity, thus enhancing SOD1 aggregation, which was confirmed by ANS spectroscopy. The results described in this chapter agree with Leal *et al*. Calcium showed a higher sedimentation inducing ability on $SOD1^{G93A}$ and $SOD1^{G85R}$, rather than $SOD1^{WT}$ (Figure 3.5B). The presence of calcium was shown to promote SOD1 sedimentation independent of oxidizing or reducing conditions. The effects of calcium on SOD1 sedimentation *in vitro* are physiologically relevant to ALS pathology, as calcium was reported to be overloaded within specific neurons of ALS patients (Leal & Gomes 2015), and SOD1 inclusions were also observed in those tissues. In addition to SOD1, calcium was shown to induce α-synuclein aggregation in cell culture and *in vitro*

(Follett et al. 2013). Calcium selectively affected dopaminergic neurons that were particularly vulnerable to alterations in homeostasis, correlating calcium overload with the onset of the neurodegenerative diseases (Surmeier et al. 2011; Mosharov et al. 2009).

Compared to all the inducers discussed above, 20% TFE was commonly applied as SOD1 sedimentation inducer in cell-free system. Munch *et al* (2010) used it to expose the hydrophobic surface of SOD1 mutants, thus inducing aggregation, which was shown by dot blot (Munch & Bertolotti 2010). For several reasons, 20% TFE was not used extensively in this thesis: ① 20% TFE had a strong aggregation inducing ability, which sedimented $SOD1^{WT}$ and $SOD1^{MT}$ indistinguishably (data not shown). ② TFE functions as a strong acid that affect the tertiary structures, often used as protein denaturant, therefore can be considered as non-physiological.

In addition, sonication, low pH, agitation and shaking have been reported to simulate SOD1 to form amyloid-like aggregates. However, cell culture-based experiments have shown that inclusions formed by SOD1 are distinct from those formed by pathogenic proteins associated with classical amyloid diseases (Hwang et al. 2010). Therefore, considering ALS is not classified as an amyloid diseases, those conditions above should be avoided in cell-free system in principle.

However, even when high concentrations of EDTA, DTT or calcium were applied to SOD1 proteins, the sedimentable pellet fractions still did not reach ~100%. Therefore, different inducers were combined to promote the aggregation process. It is worth noting that chelating agents such as EDTA cannot be applied with divalent metal ions, and oxidizing reagents such as H_2O_2 cannot mixed with reducing reagents either. Considering SOD1 inclusions generally form in cytoplasm of damaged motor neurons, the environment of which is reducing, the combination of calcium and DTT was chosen as the inducers for further experiments.

Apo-state is essential for soluble SOD1 to be seeded by aggregates

Before apo-SOD1 generation, different conditions were tested to optimize the best conditions for preformed aggregates to seed further aggregation. However, none of those showed a significant difference between time point 0 and long-time incubation samples (data not shown). Therefore, I destabilized the $SOD1^{WT}$ prior to seeding.

NMR studies have shown that the apo-state of SOD1 is different from holo-state in solution, even though they appear identical in the crystal state (Banci et al. 2009). The apo-SOD1 is disordered and destabilized. It showed flexible loop structures that connected SOD1 β-strands, resulting in a variety of unstable conformations. There are 2 major methods to generate the apo-state of SOD1, ① using hydrophobic resin or ②

using chelating reagents under a mild acid environment (pH= 3.5-5.5) (Oztug Durer et al. 2009) to remove the charged metal ions. To be consistent with earlier experiments, the second method was chosen in this study. 5-20mM EDTA has been used to fully turn holo-SOD1 into apo-SOD1 in several published studies. Munch *et al* (2010) reported that EDTA induced apo-state SOD1 was still soluble, yet it began to unfold, change confirmation, which could be detected by conformation sensitive dye Sypro Orange, and could be easily triggered to aggregate.

In my study, preformed SOD1 aggregates stimulated soluble apo-$SOD1^{WT}$ sedimentation, whereas holo-$SOD1^{WT}$ was unaffected. Some of my earlier experiments suggested that the holo-$SOD1^{WT}$ stayed soluble even if it began to degrade. Before using EDTA, different strategies were applied, including urea (3.5-4M), long time incubation (up to 168h) or increasing the seeds/soluble $SOD1^{WT}$ ratio (1:1). None of those modifications show any effect on stimulating $SOD1^{WT}$ sedimentation. Under the same incubation environment/time, the more demetallated $SOD1^{WT}$ was the more protein aggregated into insoluble fractions, suggesting that seeding could only be initiated after holo-$SOD1^{WT}$ lost metal ions and changed its conformation. Not all SOD1 mutants required the apo-state to form aggregates, Rodriguez *et al* (2002) reported several SOD1 mutants, such as S134N and D101N, directly aggregated from native state following heating treatment under native condition (Rodriguez et al. 2005).

Preformed SOD1 aggregates stimulated soluble SOD1 sedimentation

After the experiment using same amount of seeds to sediment de-metallated $SOD1^{WT}$, another assay was carried out. Comparing the sedimentation at time point 0 samples (initiation point) to the no aggregate seed control (spontaneous self-aggregation), only in the presence of pre-induced aggregates could a significant amount of apo- $SOD1^{WT}$ to be rapidly triggered to sediment. These assays suggested the seeding process could be accelerated after ① first aggregate formation and ② global unfolding/misfolding of soluble SOD1.

Furthermore, cross-seeding experiments were also carried out to characterize the spontaneous and seeded sedimentation of different SOD1 mutants. When the ratio between seeds and soluble $SOD1^{MT}$ was 1:1, soluble SOD1 mutants could be triggered to form insoluble pellets directly from the holo-state, revealing holo-$SOD1^{WT}$ possessed higher resistance towards aggregation seeding than untreated mutants. However, after I reduced the aggregate seed, the ratio of sedimented soluble SOD1 was also significantly reduced. The failure of seeding experiments between SOD1 aggregates and untreated SOD1 mutant indicated that apo-state is also necessary for efficient recruitment of soluble $SOD1^{MT}$ to sedimentable pellets in the presence of small amount

of seeding material. Although when the seed amount became high enough, it could trigger the $SOD1^{MT}$ to form insoluble fractions from native state.

To date, there have been several studies performed in cell-free systems to investigate the seeding potential of SOD1 aggregates. Chia *et al* (2010) reported that self-seeded fibrillization shortened the lag times compared to spontaneous sedimentation of SOD1 proteins including WT, A4V, G37R and G93A under the mild denaturing conditions (0.5M GdnHCl; pH=4.0) using ThT fluorescence assay (Chia et al. 2010). Similar results were also observed in the WT/MT cross-seeding assay. Interestingly, in Chia's study, there were no differences between spontaneous fibrillization and self-seeded fibrillization reactions of $SOD1^{G85R}$. Furthermore, Gupta *et al* (2012) reported the mean lag time of seeded aggregation was reduced with the higher dilution of Htt seeds in a HD cell-free system (Gupta et al. 2012), indicating seeding is highly dose-dependent of the seeds.

To date, studies performed in cell-free systems tend to utilize insoluble material generated from the brain or spinal cord of transgenic mice as potential seeds. For the future reference, the brain extract from $SOD1^{G93A}$ mice could be applied to simulate $SOD1^{WT}$ sedimentation.

In this chapter, I used the sedimentation to discriminate aggregates from soluble proteins. Sedimentation is regarded as a good read out of aggregation as insolubility is one of the most important features of aggregates, it is practical. But the disadvantage is sedimentation cannot easily capture small aggregates and soluble oligomers. Light scattering of the turbidity of SOD1 samples at 450nm has also been applied in other *in vitro* experiments (data now shown) (Furukawa et al. 2013a); however, the readings of turbidity were not replicable in this study. Interestingly, filter trap is generally regarded as a good strategy to analyse aggregated proteins; however, lysates from cells transiently expressing $SOD1^{MT}$ inclusions showed negative results in filter trap assay in previous attempts in the Cheetham lab, which raise the question whether filter trap is an appropriate read-out in this study, therefore, filter trap was not applied to analyse SOD1 sedimentation in this chapter. In addition, methodology such as CD and FT-IR are also helpful as these methods could detect the changes of secondary structure in a low microgram range.

HSJ1 inhibited SOD1 aggregation formation *in vitro.*

In this study, I tested if HSJ1 could inhibit soluble SOD1 aggregation *in vitro*. Under the reducing environment (calcium/DTT), $SOD1^{G93A}$ began to spontaneously sediment into the insoluble fraction in the absence of HSJ1. In the presence of HSJ1a or HSJ1b, $SOD1^{G93A}$ spontaneous sedimentation was reduced. Different concentrations of

calcium and DTT were combined to explore suitable environment to sediment $SOD1^{G85R}$, however all the trials failed as HSJ1 was more insoluble than $SOD1^{G85R}$ under these conditions (data not shown).

These experiments suggested that HSJ1 could directly inhibit SOD1 aggregation, indicating that HSJ1 could function as anti-aggregation chaperone within cells under oxidative or reducing environment potentially without other chaperones. Disappointingly, the data obtained from these experiments are highly variable.

Previously the Cheetham lab has shown that HSJ1a can reduce SOD1 aggregation in a cell model or an animal model. The ability of purified recombinant HSJ1a and HSJ1b to inhibit SOD1 aggregation formation in a cell-free system is still equally important, as it suggests that HSJ1 might directly interact with SOD1 without being the co-chaperone of Hsp70. The cell based work suggested that HSJ1 activity was higher when the chaperone could interact with Hsp70 and activity was reduced by an H31Q mutation (Novoselov et al. 2013). The specific domains required for HSJ1-SOD1 interaction in this cell-free system remain unclear; however, this could be explored with mutants of HSJ1a and b, and the effect of other purified chaperones tested in a reconstituted chaperone system. In addition, it is also worth exploring if HSJ1 is also able to inhibit SOD1 aggregation under oxidized environment (H_2O_2) in the cell-free system.

HSJ1 inhibited the SOD1 aggregates from further expansion *in vitro*

Labbadia *et al* (2012) reported HSJ1a inhibited GST tagged Htt Q51 aggregation in a cell-free reconstituted system using filter trap (Labbadia et al. 2012). Furthermore, the ability of insoluble material extracted from brains of R6/2 transgenic mice to seed further Q51 aggregation was reduced when the insoluble material was extracted from R6/2:hHSJ1a brains, suggesting that HSJ1a could inhibit the ability of aggregated Htt to promote further aggregation. Inspired by this work, I designed an assay to investigate if HSJ1a and HSJ1b could inhibit the seeding of soluble SOD1 aggregation by preformed SOD1 aggregates.

Both HSJ1a and HSJ1b were added into SOD1 seeding system at time point 0. In this assay, HSJ1, soluble apo-$SOD1^{WT}$ and/or insoluble SOD1 aggregates were mixed and co-incubated. Compared to mixture of apo-$SOD1^{WT}$ and SOD1 aggregates, in the presence of either HSJ1a or HSJ1b, less apo-$SOD1^{WT}$ was simulated to form insoluble material, suggesting HSJ1 possessed the similar activity in inhibiting SOD1 aggregate triggered apo-$SOD1^{WT}$ sedimentation. In addition, when HSJ1 was added into the $SOD1^{MT}$ cross-seeding system, less apo-$SOD1^{G93A}$ or apo-$SOD1^{G85R}$ was trigged to sediment.

It is important that HSJ1 was confirmed to possess the activity to inhibit seeding phenomena *in vitro*. It suggested that HSJ1 not only played an important role during the SOD1 aggregation, but also could affect the ALS pathogenic process when the preformed SOD1 aggregates begin to expand. Even through animal experiments already showed that HSJ1a could mediate late-stage neuroprotection in $SOD1^{G93A}$ mice (Novoselov et al. 2013), it is still important to explore at which stage HSJ1 could function and if this could be optimised. In this chapter, I confirmed that HSJ1 could inhibit SOD1 aggregates formation, as well as the aggregates seeding soluble SOD1.

Chaperone modulation of seeded aggregation in cell-free system has also been reported in Aβ and polyQ cell-free system (Mansson et al. 2014; Mansson et al. 2014). As a member of DnaJB subfamily, DnaJB6 are reported to efficiently suppressed fibrillization of polyQ peptides with Q45 in a ThT fibrillization assay in the absence of Hsp70 or ATP, and extended the lag-phase by sequestering of Aβ42 aggregates in the cell-free system. Together, these data highlighted the anti-misfolding and anti-aggregation feature of this subfamily of DnaJB proteins, indicating the role of chaperones might not be limited to degradation or assistance of folding, but can also participate in multiple stages during aggregation process.

Collectively, SOD1 aggregation could be induced due to demetallation, reduction of disulphide bonds and increased hydrophobicity. These preformed SOD1 aggregates stimulated destabilized soluble SOD1 further sedimentation in the cell-free system. In this study, HSJ1 was observed to inhibit SOD1 sedimentation as well as seeded aggregation, indicating HSJ1 is a promising candidate chaperone targeting SOD1 misfolding and aggregation. The apo-states required to enable seeding were produced *in vitro* by destabilization, but they could occur in the cellular milieu during protein biogenesis and as the protein folds from the nascent chain. Therefore, in the next chapter, I investigated the SOD1 aggregation and seeding in a cell model.

Chapter 4

Cell models of SOD1 mutant aggregation and seeding

4.1 Introduction

As discussed in Chapter 1, one of the pathogenic hallmarks of many neurodegenerative diseases is the presence of abnormal protein aggregates, indicating the dysfunction of protein quality control. Many mutant proteins identified in inherited neurodegeneration were reported to misfold and aggregate. These microscopically visible inclusions are considered to represent at a possible end point of the protein aggregation process, which usually begins with the abnormally folded monomers that formed oligomers, and then further aggregated into protofibrils, mature fibrils or disordered aggregates. Despite protein aggregation being a prominent pathogenic mechanism, many questions regarding the mechanisms of aggregation formation and their pathological effects still need to be addressed. Interestingly, provocative findings involving prion-like self-propagation and cell-to-cell transmission phenomena have been reported in many neurodegenerative disorders, including Alzheimer's disease, Parkinson's disease, Huntington's disease as well as ALS (Table 4.1).

Native Protein	Aggregate	Disease	Subcellular Localization		Seed		Transmit		
			Native	Inclusion	*In vitro*	In cell	*In vivo*	In cell	*In vivo*
APP	ß-amyloid	AD	TM	EC	+	+	+	-	+
Tau	Tau	AD;FTD	C	C	+	+	+	+	+
α-Syn	α-Syn	PD	N	C	+	+	+	+	+
Htt	PolyQ	HD	N	N	+	+	n.d.	+	n.d.
Ataxins		SCA							
SOD1	SOD1	ALS	C	C	+	+	n.d.	+	n.d.
TDP-43	TDP-43	ALS;FTD	N	C	+	+	n.d.	n.d.	n.d.
FUS	FUS	ALS;FTD	N	C	+	n.d.	n.d.	n.d.	n.d.

Table 4.1 Prion-like phenomena in neurodegenerative disorders. Aberrations: AD, Alzheimer's disease; ALS, amyotrophic lateral sclerosis; APP, amyloid precursor protein; C, cytoplasmic; EC, extracellular; FTD, frontotemporal dementia; HD, Huntington's disease. N, nuclear; n.d., not done; PD, Parkinson's disease; PolyQ, polyglutamine; SCA, spinocerebellar ataxia; TM, transmembrane; *Table 4.1 is adapted from Polymenidou et al (2011).*

The self-propagated aggregation was initially reported in Prion diseases, such as Creutzfeldt Jakob disease (CJD), Gerstmann-Straussler-Scheinker Syndrome and fatal familial insomnia. Even through the term 'prion' refers to infectious cerebral proteopathy, emerging evidence suggests that the prion-like mechanisms are implicated in a variety of neurological and systemic diseases. Early in the 1980s (Brown et al. 1982; Gajdusek 1994), it had been speculated the amyloids were transmitted in a prion-like manner. Injection of Aß-rich brain extracts have been reported to trigger the deposition of ß-amyloid formation in the brain of APP transgenic mice (Kane et al. 2000; Meyer-Luehmann et al. 2006; Eisele et al. 2009). The Aß plaques were firstly observed in the neocortex, followed by allocortex and finally

subcortical regions (Thal et al. 2002). Similar to Aß-seeding, Tau neurofibrillary tangles can also be induced by injection of brain extract containing abnormal Tau aggregates in the $hTau^{WT}$ mice (Clavaguera et al. 2009; Iba et al. 2013; Peeraer et al. 2015), which normally does not develop AD phenotype. *In vivo*, the neurofibrillary tangles were firstly detected in the coeruleus and trans-entorhinal regions, then spread to the amygdala and interconnected neocortical areas (Braak & Del Tredici 2011). In addition, foetal dopamineric neurons expressing human α-synuclein were grafted into transgenic rodent models, which developed synuclein-positive aggregates later (Angot et al. 2012; Kordower et al. 2011; Hansen et al. 2011; Desplats et al. 2009; Freundt et al. 2012). However, all the *in vivo* approaches tested in α-synuclein seeding experiments failed to demonstrate the aggregates detected in the rodent models are the results of seeding but not translocation from the grafted neurons.

In cell models, the prion-like propagation of aggregates has been widely reported. Synthetic PolyQ formed filamentous inclusions *in vitro*, which could be internalized by cultured cells, thus mediating propagation of homotypic aggregation (Ren et al. 2009; Derkatch et al. 2004). Similarly, $SOD1^{H46R}$ (Münch et al. 2011) and $SOD1^{I149T}$ (Furukawa et al. 2013a) were observed to be internalized, and then seeded $SOD1^{MT}$ or $SOD1^{WT}$ aggregation in cultured neurons. Soon after the discovery of SOD1-seeding phenomena, fibrillar TDP-43 was reported to mediate seeded aggregation formation in cell-free systems as well as in a cell model (Furukawa et al. 2011). Interestingly, no published studies have tested that if self-propagation and transmission could be reduced or inhibited in cell model or in animal models. The aim of this study was to develop cellular models of SOD1 aggregation to later explore the potential role of HSJ1 might play in SOD1 propagation processes. Therefore I characterized $SOD1^{MT}$ aggregation and seeding. Initially, constructs expressing SOD1 with different tags were generated, with the aim of distinguishing wild-type from mutants when they were co-expressed. Then different cell lines were developed and utilized to investigate the effects of soluble $SOD1^{MT}$ or SOD1 inclusions on $SOD1^{WT}$.

4.2 Results

4.2.1 Subcellular Localization and Expression of SOD1

4.2.1.1 Non-inducible GFP-, mCherry-SOD1 constructs

Constructs of pTRE-2hyg containing the SOD1 ORF cDNA were received as gifts from Prof RI. Morimoto (Table 2.1) (Gidalevitz et al. 2009). Using the pTRE-SOD1 derived ORFs as a template, SOD1 wild-type and two mutants (G93A and G85R) were previously cloned in frame into the pEGFP-C1 plasmid (Novoselov et al. 2013). Sequencing results confirmed that there were no PCR-driven mutations. In order to co-express different types of SOD1, SOD1 inserts were released from pEGFP-C1 and re-ligated to pmCherry-C1 in frame, thus generating N-terminal mCherry-tagged SOD1 for this study (Appendix 4.1).

Pathogenic SOD1 mutations in ALS form intracellular protein inclusions (Table 1.1). Therefore, the subcellular localization and inclusion formation were compared between wild-type and mutant human SOD1 fused to a GFP-tag or a mCherry-tag at N-terminus following transient transfection of CHO cells (Figure 4.1A). Both the GFP and mCherry tagged $SOD1^{WT}$ were evenly distributed throughout cytoplasm and nucleus, only a minority (2-3%) of cells expressing wild-type were observed to form cytoplasmic inclusions. In contrast, the GFP and mCherry tagged $SOD1^{G93A}$ and $SOD1^{G85R}$ were mainly localized in the cytoplasm, forming circular peri-nuclear inclusions. The inclusion incidence was increased significantly in cells expressing G93A or G85R, compared to cells expressing $SOD1^{WT}$ (~25% compared to ~2%, ***$p<0.005$, Figure 4.1B).

To verify the expression levels and molecular weights of recombinant SOD1, untransfected and transfected cells were lysed, resolved by SDS-polyacrylamide gel and analysed by western blot (Figure 4.1C). The GFP-SOD1 was detected at mobility corresponding to approximately 45kDa, consistent with the predicted molecular weight (GFP 27kDa + SOD1 16kDa=43kDa), whereas mCherry-SOD1 migrated lower than 55kDa ladder (mCherry 27kDa + SOD1 16kDa=43kDa).

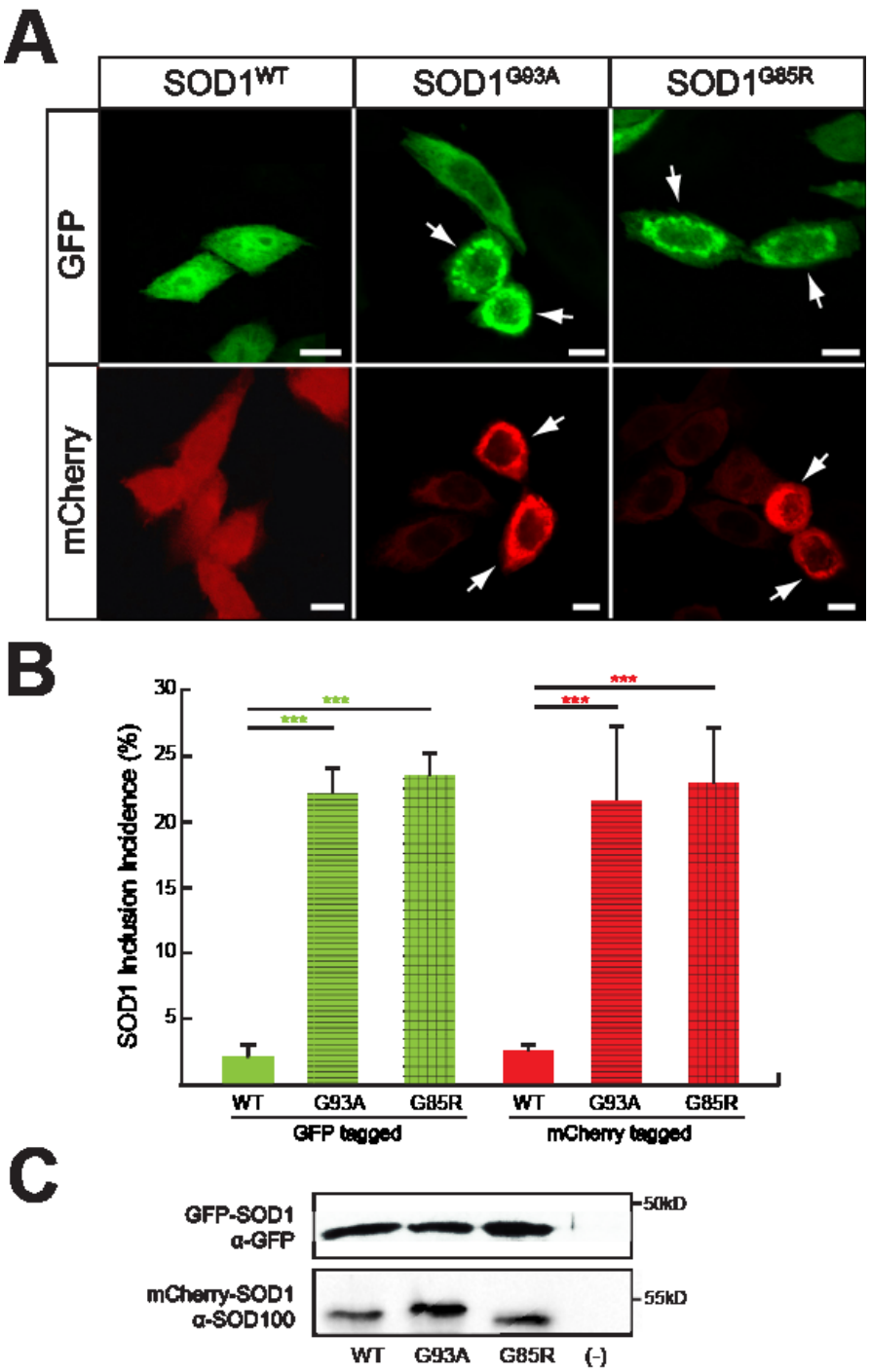

Figure 4.1 GFP-SOD1 and mCherry-SOD1 subcellular localization and immunoblot analysis. (A) Subcellular localization of SOD1. 100ng GFP-SOD1 or mCherry-SOD1 were transiently transfected into CHO cells as indicated. Cells were fixed and visualized referred to Material and Methods. Arrows highlight the presence of inclusions. Scale bar 10µm. **(B)** Quantification of mean SOD1 inclusion incidence. To assess the inclusion incidence of GFP-SOD1 (green) and mCherry-SOD1 (red), approximately 4 groups of over 100 transfected cells were scored. Student t-test. (Error bar: ±SD, ***p<0.005, n=4). **(C)** Immunoblot of cells overexpressing SOD1. Cells overexpressing GFP-SOD1 or mCherry-SOD1 were lysed 24h post-transfection, cell lysates were resolved by SDS-PAGE. GFP-SOD1 was probed with mouse anti-GFP (1:2000) monoclonal and goat anti-mouse HRP (1:20000); mCherry-SOD1 was probed with rabbit anti-SOD100 polyclonal (1:1000) and goat anti-rabbit HRP (1:20000), SOD1 specific immunoreactive bands were developed with ECL, the position of MW markers are indicated on the right.

4.2.1.2 Inducible V5-, eGFP-, mCherry-SOD1 constructs

To generate cell lines with inducible SOD1 expression, constructs of pcDNA5/FRT/TO containing SOD1 inserts were produced (Appendix 4.2-3). V5 (<2kD) and eGFP (27kD) were chosen as small tag and bigger tag respectively. Later, a mCherry fusion was required and produced by ligating the mCherry ORF in frame to pre-cut pcDNA5/FRT/TO-SOD1^{WT} construct to generate construct expressing mCherry-SOD1^{WT}.

To investigate if the inducible SOD1 vectors were consistent with the non-inducible SOD1 plasmids, hSOD1 fused to N-terminal V5-tag or eGFP-tag was transiently overexpressed in CHO cells. The subcellular localization of SOD1^{WT}, SOD1^{G93A} and SOD1^{G85R} with these tags were similar to the previous results (Figure 4.2A). SOD1^{WT} was ubiquitously expressed in the cells, whereas SOD1^{G93A} and SOD1^{G85R} were excluded from nucleus, forming peri-nuclear inclusions. The inclusion incidence of SOD1 with different tags was also similar to the data obtained in section 4.2.1.1. The basal inclusion incidence of SOD1^{WT} remained ~2%, while that of SOD1^{G93A} and SOD1^{G85R} significantly increased to ~25% (***$p<0.005$).

To confirm the expression and molecular weight of recombinant SOD1, untransfected and transfect cells were lysed, resolved by SDS-polyacrylamide gel and analysed by western blotting (Figure 4.2C). A mobility of V5-SOD1 was detected slightly lower than 25kDa, which migrated to a position higher than the predicted size (V5 <2kDa + SOD1 16kDa=18kDa). The eGFP-SOD1 was detected close to 43kDa. Interestingly, mCherry-SOD1^{WT} expressed by inducible construct appeared at the same size with eGFP-SOD1, which migrated faster than the mCherry-SOD1 expressed by uninducible constructs, yet consistent with the prediction (mCherry 27kDa + SOD1 16kDa=43kDa).

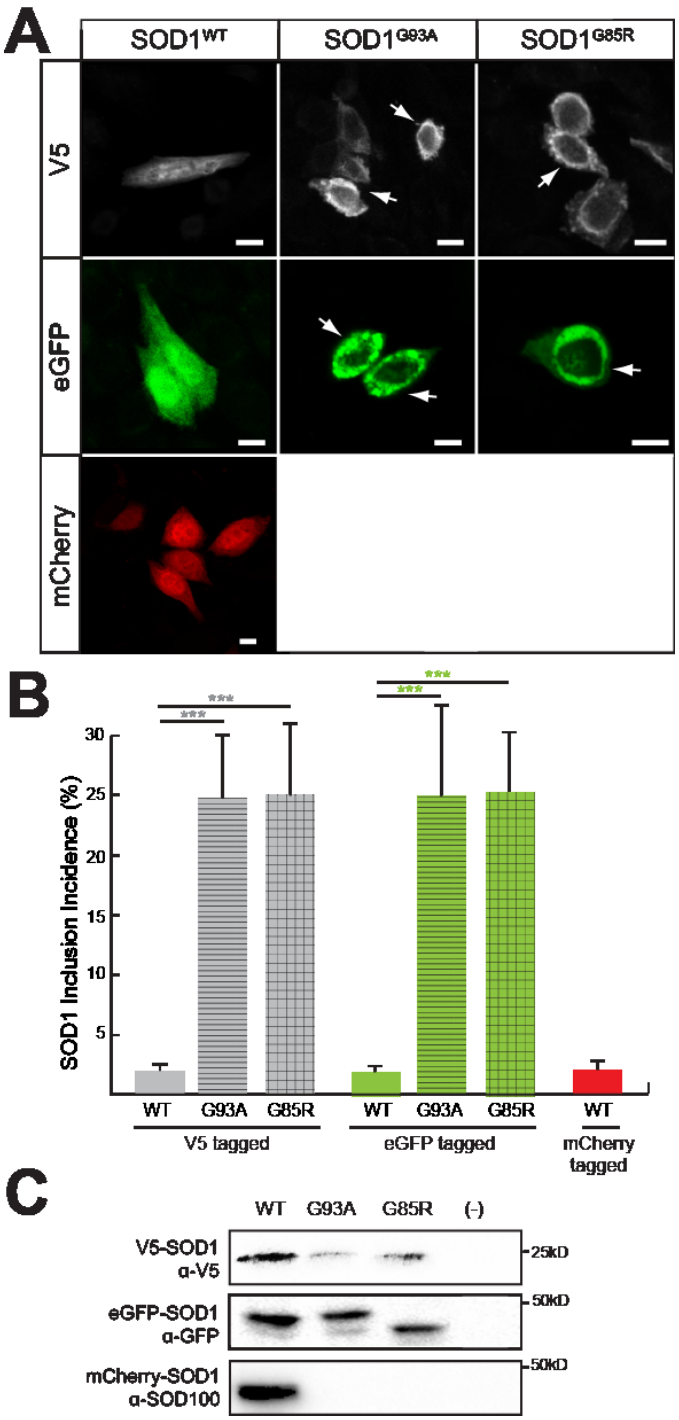

Figure 4.2 Inducible V5-SOD1 and eGFP-SOD1 subcellular localization and immunoblot analysis. (A) Subcellular localization of SOD1. 100ng V5-SOD1 or eGFP-SOD1 was transfected into CHO cells as indicated. Cells were fixed, permeablised and immunostained with mouse anti-V5 (1:200) and mouse Cy2 (1:100). Arrows highlight the presence of inclusions. Scale bar 10µm. **(B)** Quantification of mean SOD1 inclusion incidence. To assess the inclusion incidence of V5-SOD1 (grey) , eGFP-SOD1 (green) and mCherry-SOD1 (red), approximately 4 groups of over 100 transfected cells were scored. Students t-test (Error bar: ±SD; ***p<0.005; n=4). **(C)** Immunoblot of cells overexpressing SOD1. Cells overexpressing GFP-SOD1 or mCherry-SOD1 were lysed 24h post transfection, cell lysate were resolved by SDS-PAGE. V5-SOD1 was probed with mouse anti-V5 (1:1000) monoclonal and eGFP-SOD1 was probed with mouse anti-GFP (1:1000) monoclonal and goat anti-mouse HRP (1:20000), SOD1 specific immunoreactive bands were developed with ECL, the positions of MW markers are indicated on the right.

4.2.2 SOD1^{WT} is recruited by SOD1^{MT} inclusions within cells

As discussed in Chapter 1 and Chapter 3, SOD1-associated fALS is an autosomal-dominant disorder, suggesting SOD1^{MT} is co-expressed with SOD1^{WT} within patient tissue; therefore, I designed experiments to investigate the effects of SOD1 mutant proteins on SOD1^{WT} in cells.

4.2.2.1 Effects of SOD1^{MT} on soluble SOD1^{WT} in transient transfection

To investigate the effects of SOD1^{MT} expression on SOD1^{WT}, eGFP-SOD1 (WT, G93A and G85R) and mCherry-SOD1^{WT} were transiently co-overexpressed in the cell model (Figure 4.3A).

In the co-expression of eGFP-SOD1^{WT} and mCherry-SOD1^{WT}, both types of SOD1^{WT} were evenly distributed in the nucleus and cytoplasm. The inclusion incidence of SOD1^{WT} remained unchanged (2-3%). In contrast, when the SOD1^{WT} and SOD1^{MT} were co-expressed, mCherry-SOD1^{WT} was observed to be excluded from nuclei, and re-localized with SOD1^{MT}, thus exhibiting a cytoplasmic staining. In the presence of eGFP-SOD1^{MT} inclusions, SOD1^{WT} was induced to form inclusions, the inclusion incidence of which was significantly increased from basal level (2~3%) to ~10% (***$p<0.005$). However, the inclusion incidence of eGFP-SOD1^{MT} was only slightly increased when they were co-expressed with mCherry-SOD1^{WT}. These data suggested that SOD1^{MT} aggregation and inclusion formation were able to recruit soluble SOD1^{WT} when co-expressed, thus promoting the aggregation and inclusion formation of SOD1^{WT}.

4.2.2.2 Effects of SOD1^{MT} on soluble SOD1^{WT} in fused cells

The earlier data suggested that SOD1^{MT} can affect SOD1^{WT} when they are expressed at the same time. To investigate the effect of preformed SOD1^{MT} inclusions on SOD1^{WT}, a parallel experiment was carried out using PEG-mediated fusion. PEG can decentralize and restructure the cellular membrane, providing a chance to merge two connecting cells into one. Cells transiently over-expressing mCherry-SOD1 (WT, G93A and G85R) were co-incubated with cells overexpressing GFP-SOD1^{WT}, then PEG was applied to generate heterotypic cells expressing both mCherry and GFP tagged SOD1 and analysed 24hrs post fusion (Figure 4.4).

Cells expressing SOD1^{WT} exhibited similar subcellular localization compared to the results shown in section 4.2.1, which was uniformly distributed throughout the cell. However, in the cells expressing mCherry-SOD1^{MT} and GFP-SOD1^{WT}, SOD1 inclusions positive for both mCherry and GFP were observed, suggesting preformed SOD1^{MT} inclusions possessed the ability to recruit soluble, fully functional SOD1^{WT}.

Unfortunately, although this experiment was repeated several times using different conditions, homotypic fusion (i.e. GFP with GFP) predominated and because of low heterotypic fusion efficiency, there were not enough cells for statistical analysis.

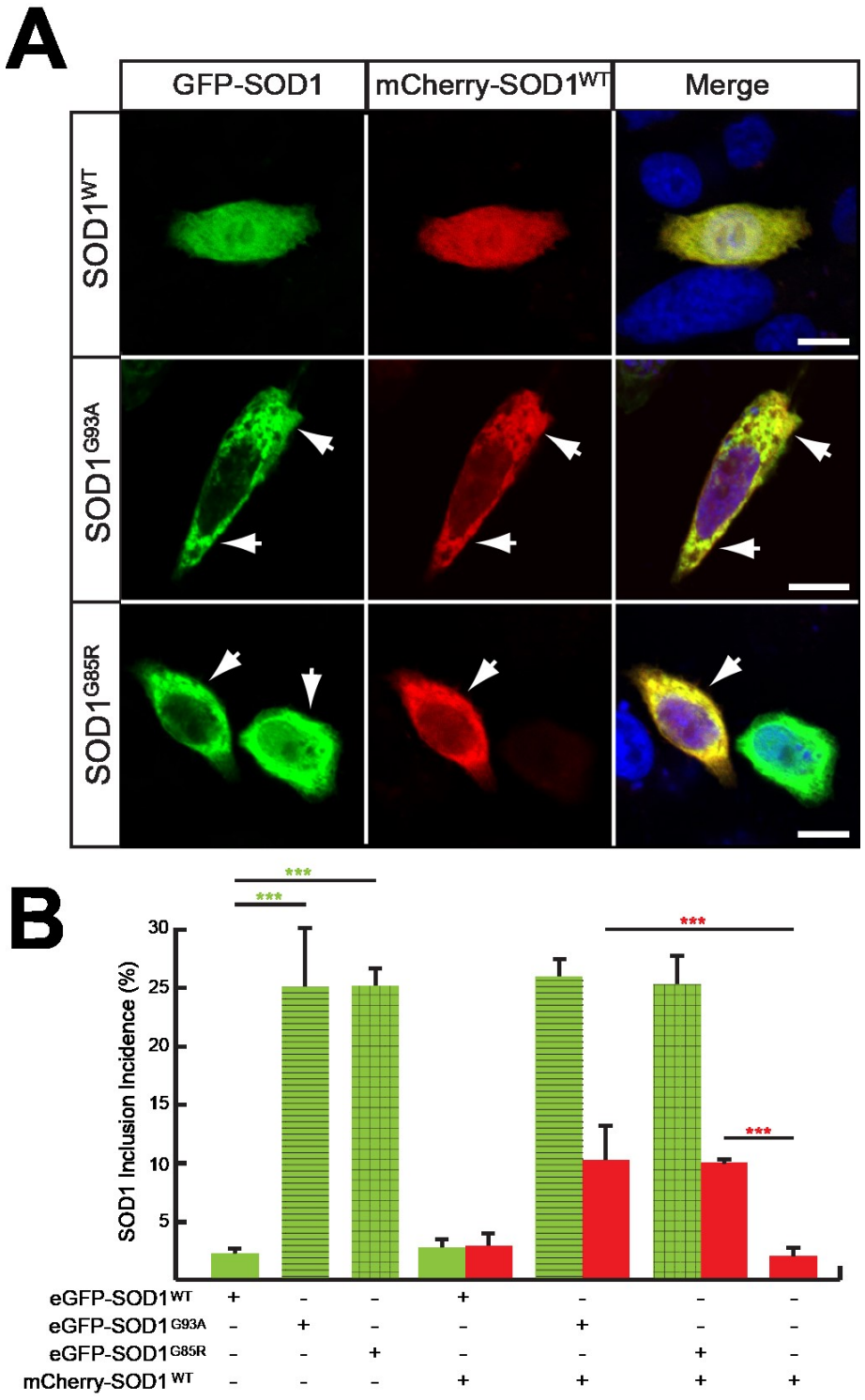

Figure 4.3 SOD1^{WT} is recruited by SOD1^{MT} in transient-transfection. (A) Co-expression of mCherry-SOD1 and GFP-SOD1. 100ng pcDNA5/FRT/TO-eGFP-SOD1 (WT, G93A and G85R) were transiently overexpressed with 25ng pcDNA5/FRT/TO-mCherry-SOD1^{WT} in CHO cells. Cells were fixed and visualized as described in the Material and Methods. Arrows highlight the presence of inclusions. Scale bar 10µm. **(B)** Quantification of mean SOD1 inclusion incidence. To assess the inclusion incidence of eGFP-SOD1 (green) and mCherry-SOD1 (red), approximately 4 groups of over 100 transfected cells were scored. Student t-test. (Error bar: ±SD; ***p<0.005; n=4).

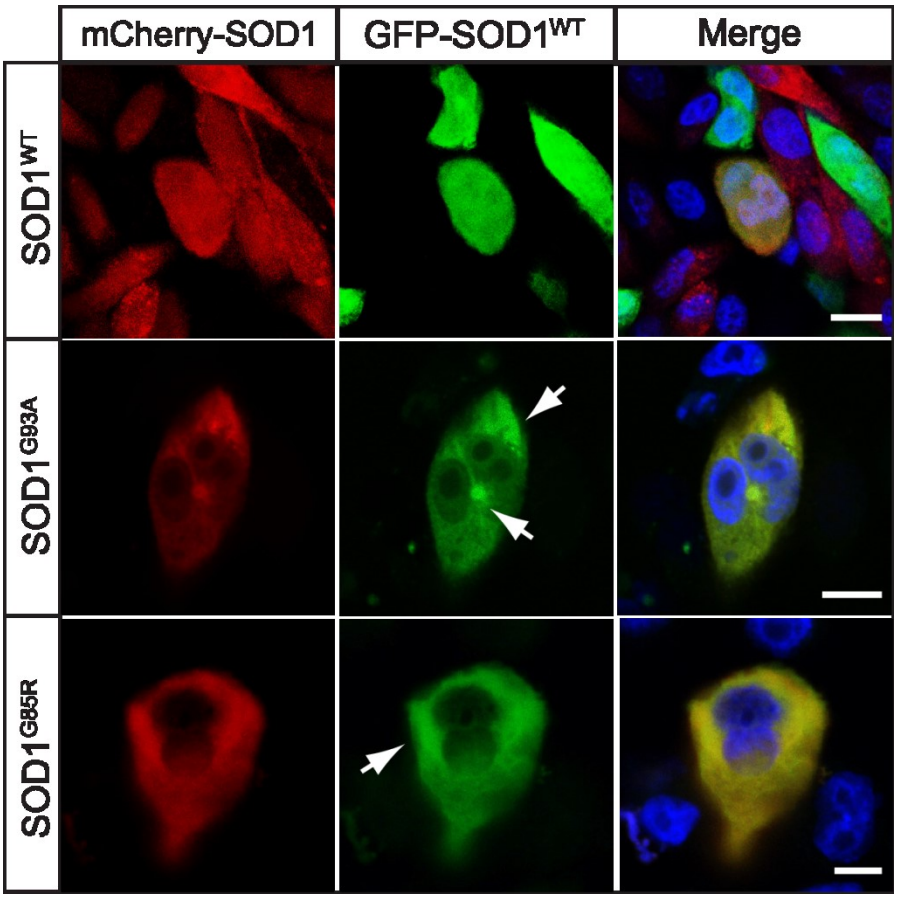

Figure 4.4 SOD1^{WT} is recruited to SOD1^{MT} inclusions in fused cells. Cells transiently overexpressed mCherry-SOD1 (WT, G93A and G85R) were co-incubated with cells overexpressed GFP-SOD1^{WT} respectively. Then cells were fused, fixed and visualized referred to Materials and Methods. Scale bar 10 μm.

4.2.3 Characterization of SOD1 stable cell lines

The above experiments highlighted that transient transfection had limitations for investigating aspects of SOD1 seeding and aggregation in cells. Some of these could be possibly be circumvented by making stable cell lines. Therefore, stable cell lines expression $SOD1^{WT}$ and $SOD1^{MT}$ were established.

4.2.3.1 Constitutive SOD1 cell lines

4.2.3.1.1 Generation of G418 selected cell lines

The general strategy and the mechanism for establishment of G418 selected cell lines is shown in Figure 2.1.

4.2.3.1.1.1 Establishment of killing curve

A standard killing curve suggested 1.5mg/ml G418 was the lowest killing concentration for CHO cells used in this study.

4.2.3.1.1.2 Cell colony selection and expansion

During the G418 selection, cells that exhibited high expression level of Neo^R survived, and untransfected cells or cells expressing low level of Neo^R were selected out, as Neo^R inactivated G418 by covalent amino or hydroxyl modification to inhibit the antibiotic-ribosome interaction. Cell colonies expressing high level of GFP-SOD1 or mCherry-SOD1, and exhibiting healthy and normal morphology were picked and then expanded.

4.2.3.1.2 Characterization of G418 selected constitutive SOD1 cell lines

In this study, 6 constitutive cell lines expressing SOD1 were generated, including GFP-$SOD1^{WT}$, GFP-$SOD1^{G93A}$, GFP-$SOD1^{G85R}$, mCherry-$SOD1^{WT}$, mCherry-$SOD1^{G93A}$, and mCherry-$SOD1^{G85R}$.

4.2.3.1.2.1 Subcellular localization of SOD1 in constitutive expression system

To compare with cells transiently overexpressing SOD1, constitutive SOD1 cell lines were analysed and quantified (Figure 4.5A) GFP-$SOD1^{WT}$ was localized in nucleus and cytoplasm indistinctively, but cells expressing mCherry-$SOD1^{WT}$ exhibited a slight higher cytoplasmic fluorescence pattern. Furthermore, $SOD1^{MT}$ was distributed mainly in the cytoplasm, which is similar to our previous observation with transient transfection (referred to section 4.2.1). Between 70-100% of the SOD1 clonal cell lines were fluorescent-positive after G418 selection compared to approximately 30% of the cells following transient transfection. The fluorescence levels of SOD1 in the transiently transfected cells were also usually higher than that of stable cell lines.

4.2.3.1.2.2 Cells with circular peri-nuclear SOD1 inclusions were mostly selected out

During the G418 selection process, I noticed that the colonies survived from antibiotic selection lacked the typical peri-nuclear inclusions observed in transient transfection (Figure 4.5A). The inclusions observed in cell lines constitutively expressing SOD1 were mostly fragmented and dot-like. Therefore, I suspected that the selection process was selecting cells with less aggregation. In addition, circular SOD1 inclusions were observed to block cell division, result in multiple nuclei thus ultimately giving rise to cell death, which partially supported this theory and explained why cells with typical peri-nuclear inclusions disappeared after G418 selection.

In addition to the lack of obvious inclusions, several other disadvantages were also noticed: ① the integration sites of GOI, the copy number and the expression level are random, which made cell lines expressing the same GOI generated from different colonies hard to compare; ② CHO cells exhibited high resistance towards G418 (the lowest killing concentration was over 1mg/ml in this study), resulting in colonies that mixed with untransfected cells. Once the G418 was removed after selection, the expression of SOD1 would be gradually reduced, even diminished, indicating the selected cell lines were not ‘stable’; ③ G418 selected cell lines failed to respond to several stress-inducing reagents in the subsequent experiments (such as MG132) as those cells already exhibit high endogenous stress signals even without the inducers. Given the disadvantages stated above, plus the desire to manipulate the expression of SOD1 at different time points, the G418 selected cell lines were discarded, and inducible cell lines were generated.

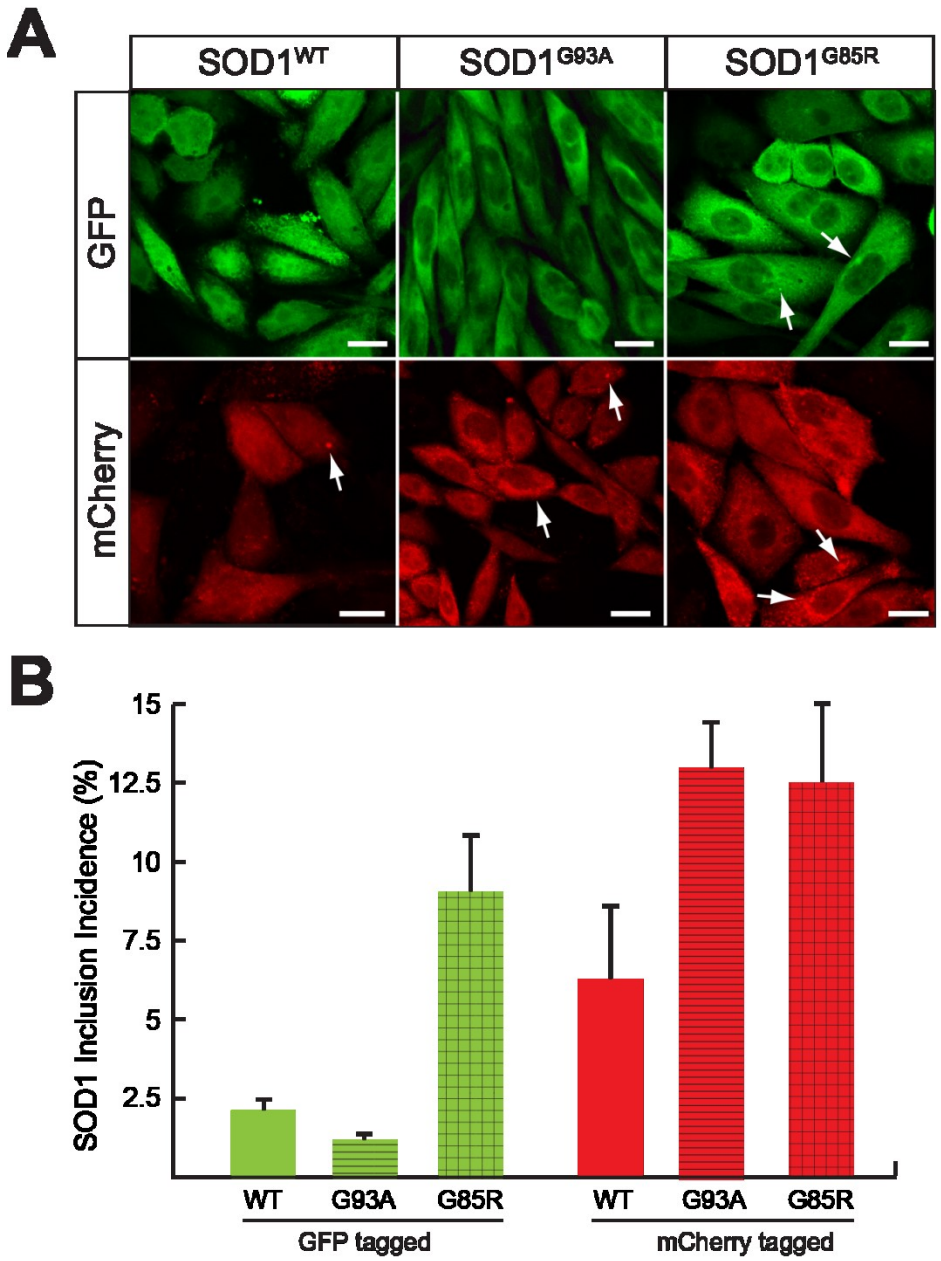

Figure 4.5 Analysis of cell lines stably expressing SOD1. (A) Subcellular localization of SOD1 in constitutive expressing cell lines. CHO cells stably expressing GFP-SOD1 or mCherry-SOD1 were indicated. Cells were fixed and virtualized as described in the Material and Methods. Scale bar: 10 μm. **(B)** Quantification of mean SOD1 inclusion incidence in constitutive cell lines. To assess the inclusion incidences of GFP-SOD1 (green) and mCherry-SOD1 (red), approximately 4 groups of over 100 cells were scored (Error bar: ±SD; n=4).

4.2.3.2 Inducible SOD1 cell lines

4.2.3.2.1 Generation of Flp-in T-Rex cell lines

4.2.3.2.1.1 Establishment of killing curves

200ug/ml zeocin, 40ug/ml blasticidin and 500ug/ml hygromycin were identified as the lowest killing concentration for CHO cells in the gradient tests.

4.2.3.2.1.2 Expression level of β-galactosidase indicated activities level of FRT site

To generate the Flp-in host cell line, CHO cells were transfected with pFRT/lacZeo plasmid containing a FRT site and then selected by zeocin. The FRT site serves as the binding and cleavage site for Flp recombinase downstream of ATG codon and β-galactosidase (β-gal)-zeocin^R (encoded by Sh ble gene) fused protein. Therefore, the activity of FRT site potentially indicated the future expression levels of GOI. The morphological changes of CHO cells under zeocin treatment were presented in Appendix 4.4.

12 colonies from zeocin selection were picked, expanded and lysed. The β-gal activity was analysed using a spectrometer (Table 4.2). According to the absorbance at 420nm, the 13th clone showed the highest emzymatic activity, the 9th and the 16th clones also possessed relatively high β-gal activity; those three colonies were expanded for further experiments, 13th clone was utilized as the host cell line for the Flp-in T-Rex system generation.

(+)	(-)	(-)	(-)
0.0210	0.0187	0.0169	0.0189
Colony 1	Colony 2	Colony 3	Colony 4
0.7739	0.7909	0.4535	0.5945
Colony 5	Colony 6	Colony 7	Colony 8
0.6885	0.5744	0.8536	0.5549
Colony 9	Colony 10	Colony 11	Colony 12
0.9385	0.8361	0.6982	0.5724
Colony 13	Colony 14	Colony 15	Colony 16
1.0703	0.7339	0.7021	0.9793

Table 4.2 Analysis of cell colonies expressing β-gal-Zeo^R. Colonies generated from zeocin selection were lysed, co-incubated with ONPG at 37 ˚C for 1h and then absorbance of products was measured at 420nm. Positive control (+): cells transiently over-expressing β-gal-ZeoR. Negative control (-): untransfected cells.

4.2.3.2.1.3 Expression level of TetR to test the control ability in the absence of Tet

The Flp-in T-Rex expression system is based on repression/ de-repression mechanism, the expression level of TetR determines the transcriptional regulation ability of 2-fold Tet operators ($TetO_2$). The regulation ability is important as high expression level of TetR is demanded to avoid leakness of the GOI. Clonal line 13 generated from zeocin selection was transfected with pcDNA6/TR_IRES_Bsd^R that contains the TetR gene. To characterize the expression levels of TetR, 8 colonies generated from Zeo/Bsd selection were lysed and the cell lysates were resolved by SDS-polyacrylamide gel, and analysed by western blotting (Figure 4.6). The expression level of TetR was quantified and compared to an internal reference protein GAPDH. According to Figure 4.6B, the 4^{th} clone and the 7^{th} clone showed relatively high expression levels of TetR, and the 6^{th} showed lowest TetR expression. Thus, the 4^{th} and 7^{th} clones were expanded and stored for further experiments.

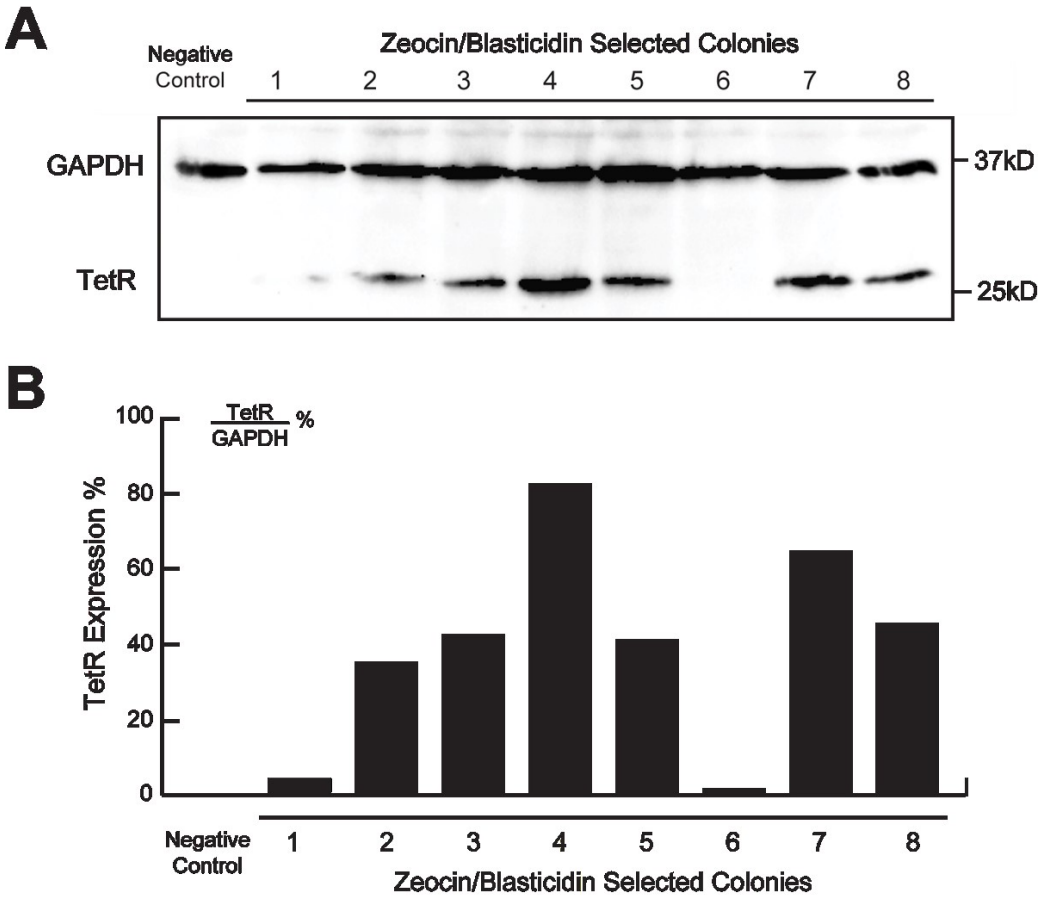

Figure 4.6 Analysis of cell colonies stably expressing TetR. (A) Immunoblot with TetR02 antibody. Colonies generated from zeocin/blasticidin selection were lysed in RIPA buffer with 3% PIC. Cell lysates were resolved by 12% SDS-polyacrylamide gel, immuno-blotted with mouse monoclonal anti-TetR02 (1:2000) or mouse monoclonal anti-GAPDH (1:20000) and goat anti-mouse HRP (1:20000), and developed with ECL, the position of MW markers are indicated on the right. **(B)** Quantification of expression level of TetR. Intensity of band generated from western blot was quantified by Image Lab (refer to Materials and Methods), and calculated as 'Tet expression % = Intensity (TetR)/ Intensity (GAPDH)'.

4.2.3.2.2 Characterization of Flp-in T-Rex SOD1 cell lines

4.2.3.2.2.1 Inducibility of Flp-in T-Rex system

Plasmid pcDNA5/FRT/TO/SOD1 and pOG44 were co-transfected into Flp-in host cells. Colonies survived from hygromycin/blasticidin selection were examined to test if the SOD1 expression could be initiated in the presence of Tet, and the transcription of SOD1 could be stopped in the absence of Tet. To examine if Flp-in T-Rex SOD1 cell lines could be turned on, cells were induced by Tet at different concentrations compared to an un-induced negative control. The cell lysates were resolved by SDS-polyacrylamide gel, and analysed by western blotting (Figure 4.7A). Taking GAPDH as an internal reference control, the expression levels of SOD1 (WT, G93A and G85R) were quantified under different concentrations of Tet. Based on immunoblotting results, the expression level of SOD1 was Tet concentration-dependent, and reached saturation at 2ug/ml. In addition, I observed that $SOD1^{WT}$ showed a relatively higher expression level than that of $SOD1^{MT}$ under same concentration of Tet treatments (134% for WT, compared to 70% for G93A and 66.9% for G85R at 3ug/ml Tet induction, normalized to GAPDH expression).

To examine if the Flp-in T-Rex system could be turned off, cells were induced by Tet, then Tet was removed from culture medium. RNA was extracted from both controls and samples (Figure 4.7B). Human SOD1 was amplified using specific primers (Appendix 4.5). Positive control showed a strong band at the expected size of 250bp, no other bands were detected. The un-induced negative control also showed a faint band at the same size, which might be endogenous SOD1 or leakiness. Replicate cells were re-cultured in the Tet-free completed medium for 24h (p24), there was a faint band presented in the PCR product at the size of 250bp as well. Collectively, these data suggest that in the SOD1 Flp-in T-Rex expressing cells could be turned on by Tet, and the translation of SOD1 could be mostly turned off in 24h after removal of Tet.

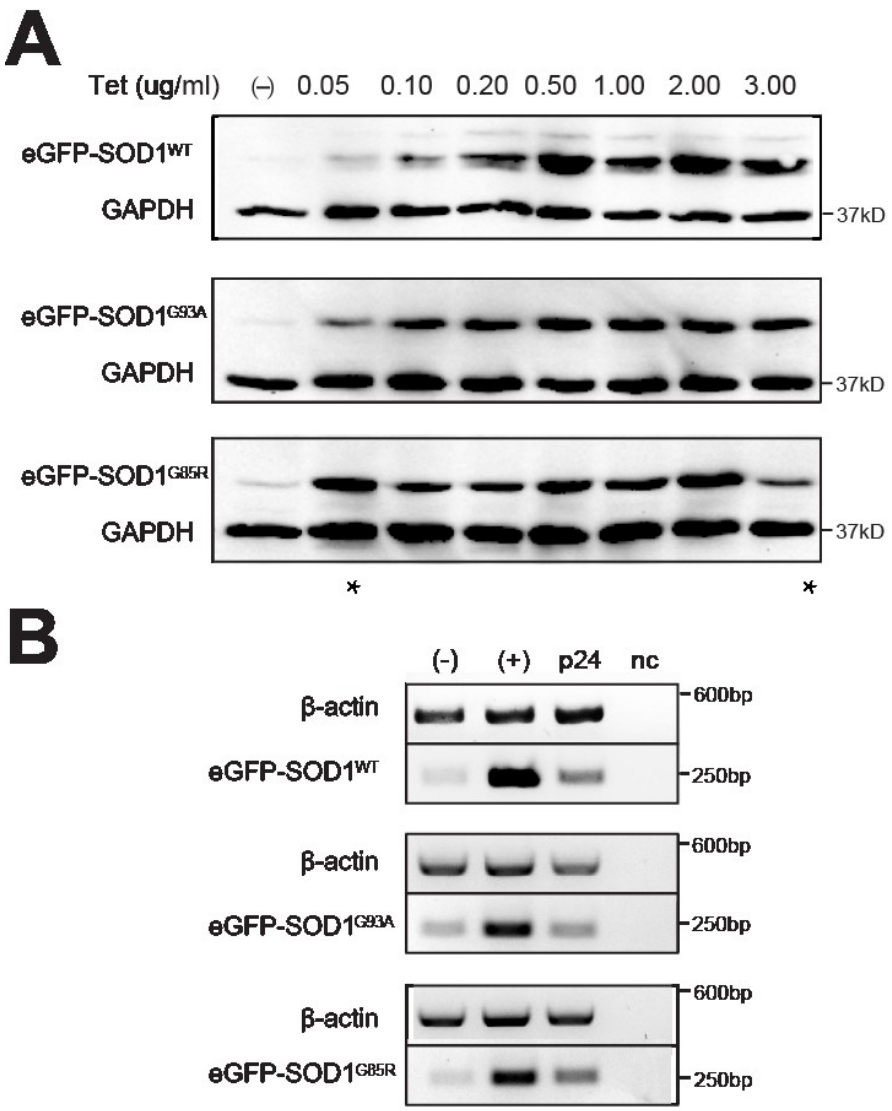

Figure 4.7 Inducible Flp-in T-Rex SOD1 cell lines. (A) Immunoblot of SOD1 cell lines that were induced by Tet at different concentrations. Cells were induced by Tet at 0.05, 0.1, 0.2, 0.5,1,2 or 3 ug/ml respectively for 48h. Cell lysate were resolved by SDS-PAGE. eGFP-SOD1 and GAPDH were probed with mouse anti-GFP (1:1000) monoclonal, anti-GAPDH (1:20000) and goat anti-mouse HRP (1:20000). eGFP or GAPDH specific immunoreactive bands was developed with ECL, the position of MW markers are indicated on the right. The star represents two lanes need to be swapped because of misloading. **(B)** RT-PCR of SOD1 cell lines that were removed from Tet. Cells were cultured at Tet-free completed medium for 24hrs post Tet induction (p24). Total RNA of samples, uninduced (-) and induced (+) was extracted and converted into cDNA as described in the Materials and Methods. RT-PCR was performed using SOD1 specific primers. Housekeeping gene β-actin was used as an internal reference. PCR products were resolved by 2% agarose gel to detect the presence of SOD1 bands at 250bp, and the presence of β-actin at 560bp.

4.2.3.2.2.2 Subcellular localization of SOD1 in inducible expression system

To compare with the cells transiently overexpressing SOD1, Flp-in T-Rex SOD1 cell lines were induced by Tet for 48h, analysed and quantified (Figure 4.8). Similar to results obtained from transient transfection, eGFP-SOD1^{WT} was indistinctively expressed throughout the cell; eGFP-SOD1^{G85R} was excluded from the nuclei, mainly distributed in the cytoplasm. Interestingly, eGFP-SOD1^{G93A} expressed by Flp-in T-Rex system exhibited a different subcellular localization: SOD1^{G93A} was evenly expressed in nuclei and cytoplasm, similar to SOD1^{WT}, instead of SOD1^{G85R}.

In the transient transfection, the transfection efficiency is 30% maximally. After 48hrs Tet induction, 100% of the cells were fluorescence positive. Compared to G418 selected cells, expression level of Flp-in T-Rex system was consistent even if the cell lines were generated from different batches or different colonies, as long as they were selected from the same host cell line. Collectively, Flp-in T-Rex system is considered as a better choice in this study for further studies because ① in theory the integration site for different GOIs are the same and ② the expression level of the same GOI is consistent, which made it comparable between WT and point mutations.

4.2.3.2.2.3 Peri-nuclear SOD1 inclusions were not observed under Tet induction

To investigate the tendency of SOD1^{MT} to form inclusions, Flp-in T-Rex eGFP-SOD1 cell lines were induced by Tet for 48hrs to reach saturation expression, analysed and quantified. As shown in Figure 4.8, cells expressing eGFP-SOD1 (WT, G93A and G85R) all showed no inclusions. In contrast to G418 selection, colonies from inducible cell lines did not express GOIs during the selection process, which suggested the selection procedure had no effects on the behaviour of GOI. According to Figure 4.7, the expression level of SOD1^{WT} is higher than that of SOD1^{MT}. I hypothesized that the reason why eGFP-SOD1 Flp-in T-Rex system failed to form inclusions, and why SOD1^{G93A} behaved more like wild type might because the expression level was too low to trigger either local fluctuation or global unfolding/misfolding.

4.2.3.2.2.4 Effects of expression levels on SOD1 inclusion formation

To investigate the effects of SOD1 expression level on inclusion formation, cells transiently transfected with eGFP-SOD1, Flp-in T-Rex eGFP-SOD1 cell line induced by Tet alone, or Flp-in T-Rex eGFP-SOD1 cell line induced by Tet and boosted by sodium butyrate were lysed, resolved by SDS-polyacrylamide gel and analysed by immuno blotting. The transfection efficiency of eGFP-SOD1 was scored before lysis of transfected cells.

As shown in Figure 4.9, eGFP-SOD1^{WT} and eGFP-SOD1^{G93A} migrated close to 45kDa, and eGFP-SOD1^{G85R} showed a slightly faster mobility. Then the expression level of eGFP-SOD1 was quantified and correlated based on an internal reference GAPDH. In this assay, I set the expression level of Tet-induced SOD1 as the standard. Under Tet/SB treatment, the expression of eGFP-SOD1 was significantly boosted compared to that of eGFP-SOD1 inducible cell lines under Tet treatment alone (156%, for WT, 142% for G93A, 138% for G85R). However, in the case of transient transfection, the expression level of SOD1 per cell was far stronger than that of Tet-induced Flp-in T-Rex system, especially when the number of transfected cells was taken into account compared to 100% of the Flp-in cells (50.8 times for WT, 35.29 times for G93A and 34.11 times for G85R), suggesting that the failure of Flp-in T-Rex system to form SOD1 inclusions might be a result of low expression levels.

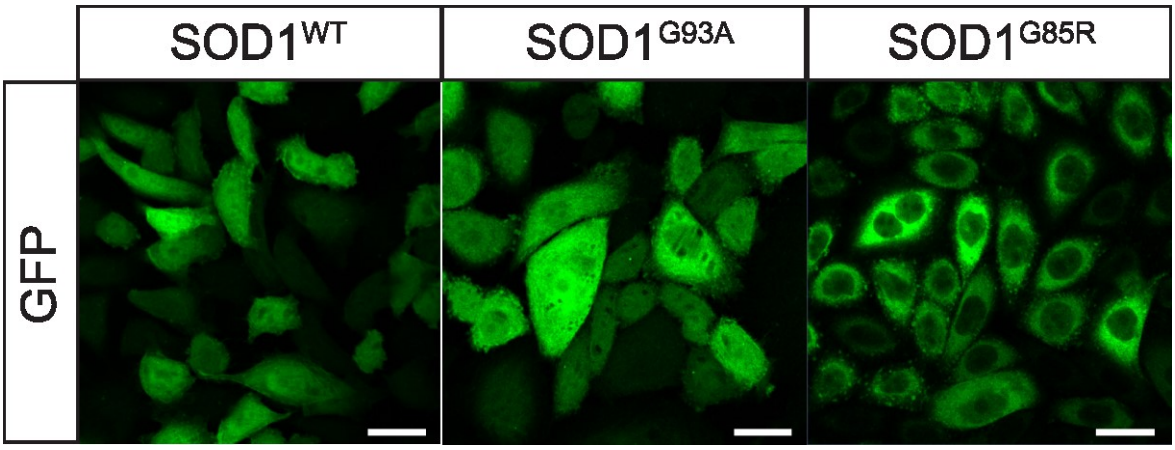

Figure 4.8 Analysis of Flp-in T-Rex system expressing SOD1. Subcellular localization of eGFP-SOD1 expressed by Flp-in T-Rex system. Cell lines expressing eGFP-SOD1 (WT, G93A and G85R) as indicated. Cells were induced by Tet (3ug/ml) alone for 48hrs, then fixed and virtualized as described in Material and Methods. Scale bar 10 μm.

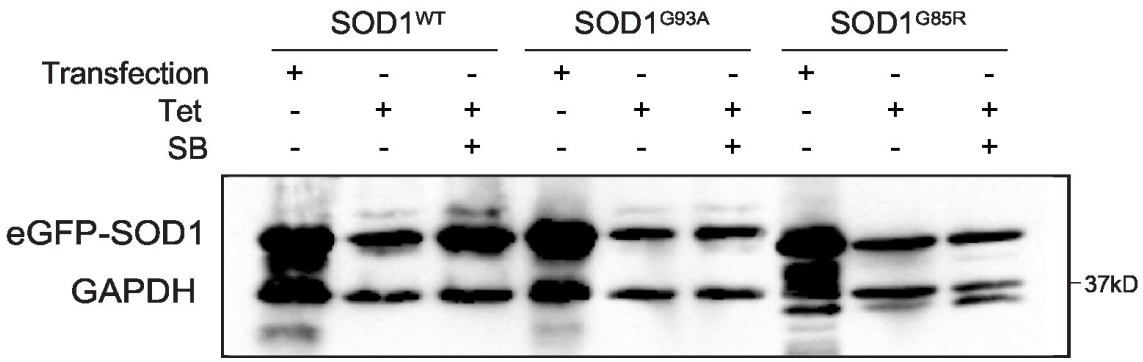

Figure 4.9 Analysis of expression levels of eGFP-SOD1 in transient transfection and Flp-in T-Rex system. Cells transiently overexpressed eGFP-SOD1 (Transfection), Flp-in T-Rex eGFP SOD1 cell lines induced by Tet (3ug/ml) alone (Tet), and Flp-in T-Rex eGFP SOD1 cell lines induced by Tet (3ug/ml) and SB (2mM) for 48hrs were resolved on SDS-PAGE. The eGFP-SOD1 and GAPDH were probed with mouse anti-GFP (1:1000) monoclonal, anti-GAPDH (1:20000) and goat anti-mouse HRP (1:20000). eGFP or GAPDH specific immunoreactive bands was developed with ECL, the position of MW markers are indicated on the right.

4.2.4 Effects of stress inducers on SOD1

As the Flp-in T-Rex system failed to form SOD1 inclusions, in this section, I explored if the stress inducers could promote aggregate formation. Inspired by my *in vitro* work described in Chapter 3, where calcium promoted $SOD1^{G93A}$ and $SOD1^{G85R}$ sedimentation, as well as the *in vivo* work described by Novoselov *et al* (2013), I focused on three representative reagents, thapsigargin (ER calcium releaser), ionomycin (trans-membrane calcium carrier) and MG132 (UPS inhibitor) to test their effects on SOD1 inclusion formation in transiently transfected cells as well as in the Flp-in T-Rex systems.

4.2.4.1 Effects of thapsigargin on SOD1 in transient transfection

Thapsigargin blocks calcium ion sequestration in the inositol trisphophate-sensitive store in the ER (Lytton et al. 1991). In this study, thapsigargin was utilized as an ER stress inducer as well as a calcium releaser to investigate if internal calcium promoted SOD1 inclusion formation. Untreated cells transiently expressing GFP-SOD1 (Figure 4.10) were compared with cells transiently overexpressing GFP-SOD1 were treated with thapsigargin (Figure 4.11). To inhibit mitochondrial calcium uptake, a low concentration of FCCP was also utilized (Friel & Tsien 1994; Babcock et al. 1997; David & Barrett 2000; Werth & Thayer 1994).

As presented in Figure 4.10, the subcellular localization of GFP-SOD1 was similar to previous observations (section 4.2.1). The inclusion incidence of $SOD1^{MT}$ was slightly reduced under FCCP treatment. FCCP can depolarize mitochondria, potentially reducing the $SOD1^{MT}$-mediated toxic abnormal reactions via mitochondria, and mitochondrial localisation was assessed with mitotracker. In the presence of inclusions, polarized mitochondria in the untreated cells were mainly distributed in the area where inclusions were localized, but showed no overlap with SOD1 inclusions. Following thapsigargin treatment, $SOD1^{WT}$ showed a significant increase of inclusion incidence (from 2.35% to 9.29%, ***$p<0.005$). However, the inclusion incidence of $SOD1^{MT}$ remained unchanged. The mitochondria under the thapsigargin treatment exhibited similar localization pattern in the presence of inclusions, but showed overlap with inclusions. Interestingly, combining thapsigargin with FCCP treatment significantly increased the inclusion incidence of $SOD1^{MT}$ (from 24.6% to 31.6% for G93A, ***$p<0.005$; 26.7% to 31.8% for G85R, **$p<0.01$). Interestingly, there was a reduction of inclusion incidence of $SOD1^{WT}$ was observed under thapsigargin/FCCP treatment (from 9.29% to 5.31%) compared to thapsigargin treatment alone. It is possible that FCCP inhibited mitochondrial calcium uptake, therefore the calcium released by

thapsigargin increased the calcium concentration in the cytoplasm, thus further promoting the SOD1 aggregation process.

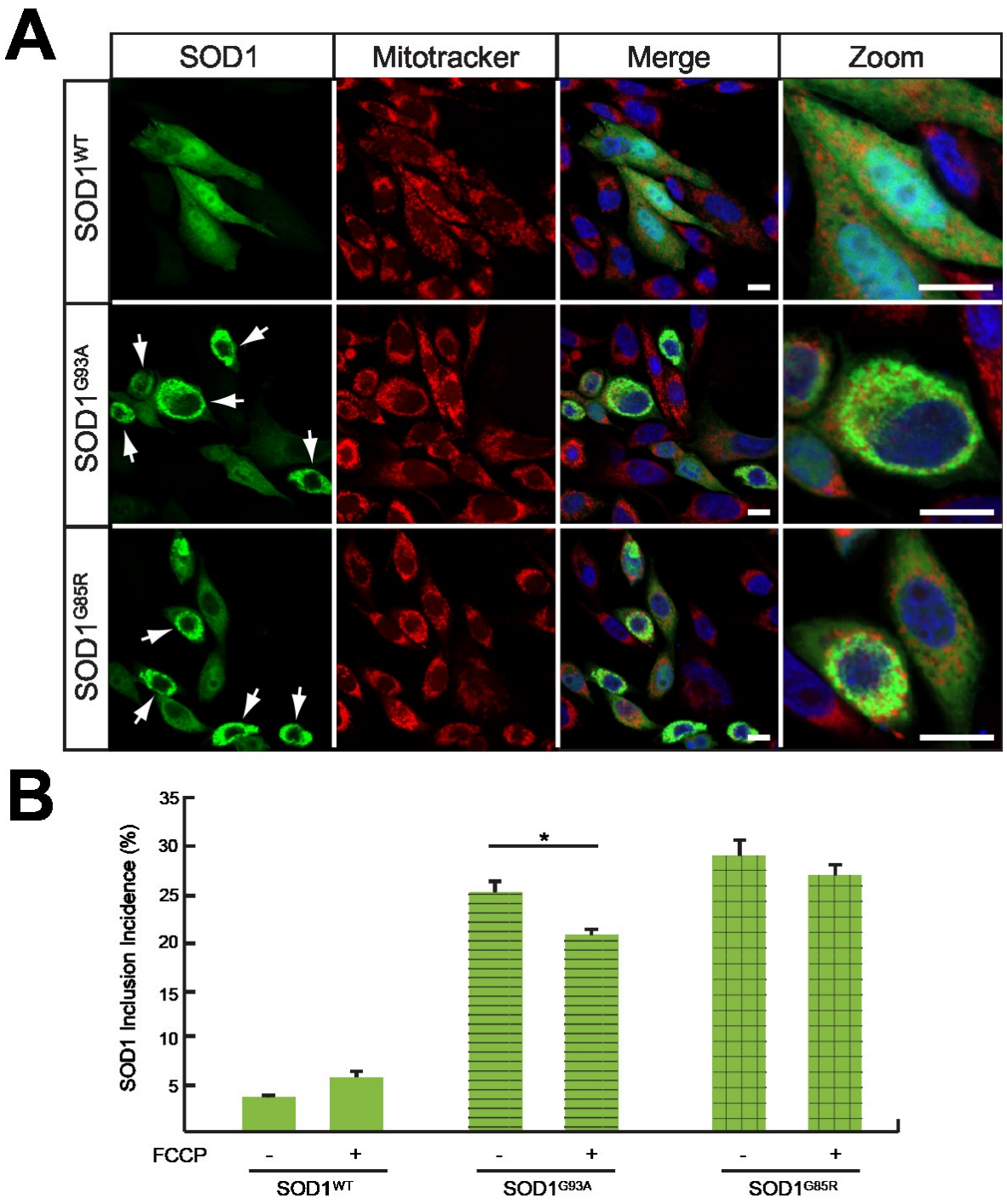

Figure 4.10 Cells transiently expressing SOD1 with Mitotracker staining. **(A)** Cells transiently expressing GFP-SOD1. 100ng pEGFP-SOD1 (WT, G93A, G85R) were transfected into cells as indicated or treated with 1uM FCCP (not shown) 24h post transfection for 3h. Mitochondria were stained with Mitotracker orange for 5min in 1xPBS before fixation. Cells then were fixed and visualized as described in Material and Methods. Arrows highlight the presences of inclusions. Scale bar: 10μm. **(B)** Quantification of mean SOD1 inclusion incidence. To assess the inclusion incidence of GFP-SOD1 (green), approximately 4 groups of over 100 transfected cells were scored. Student t-test (Error bar: ±SD; *p<0.05; n=4).

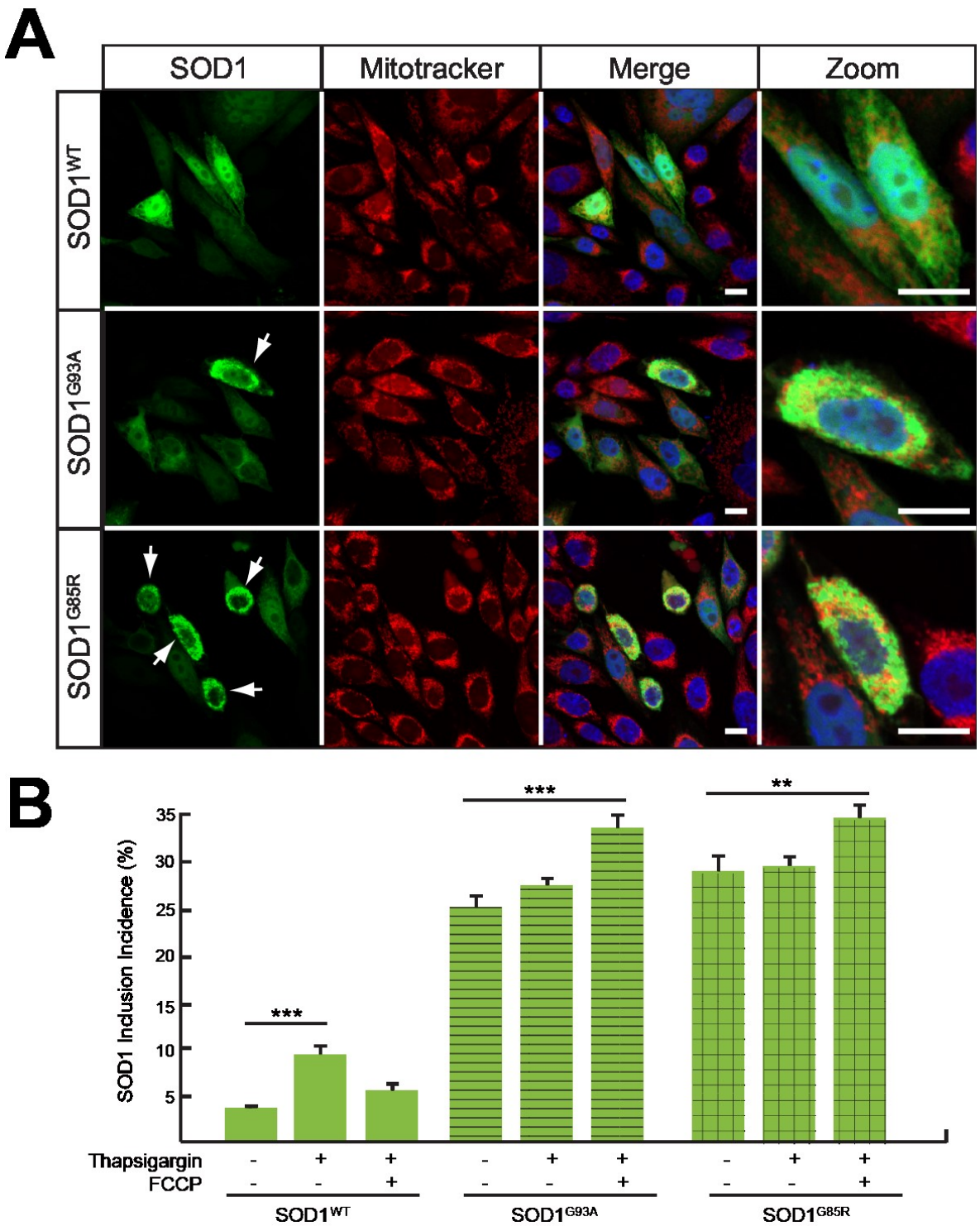

Figure 4.11 Thapsigargin treatment of cells transiently expressing SOD1. (A) Thapsigargin treatment on cell transiently expressing GFP-SOD1. 100ng pEGFP-SOD1 (WT, G93A, G85R) were transfected into CHO cells as indicated. Cells were treated with 2uM thapsigargin with (not shown) /without 1uM FCCP 24h post transfection for 3h at 37℃ in complete DMEM medium. Mitochondria were stained with Mitotracker orange for 5min in 1xPBS before fixation. Cells were fixed and visualized as described in Materials and Methods. Arrows highlight the presences of inclusions. Scale bar 10 μm. **(B)** Quantification of mean SOD1 inclusion incidence. To assess the inclusion incidence of GFP-SOD1 (green), approximately 4 groups of over 100 transfected cells were scored. Student t-test (Error bar: ±SD; **p<0.01, ***p<0.005; n=4).

4.2.4.2 Effects of thapsigargin on SOD1 in Flp-in T-Rex system

To investigate if thapsigargin promoted the SOD1 aggregation formation, the Flp-in T-Rex system expressing eGFP-SOD1 was induced by Tet and boosted by sodium butyrate, followed by the treatment with thapsigargin. Compared to untreated control cells, thapsigargin treated cells exhibited morphological changes associated with cell death, including blebbing and cell shrinkage. Interestingly, $SOD1^{G93A}$ exhibit a higher nuclear staining. Disappointingly, no SOD1 inclusion formation was observed in either $SOD1^{WT}$ or $SOD1^{MT}$ cell lines.

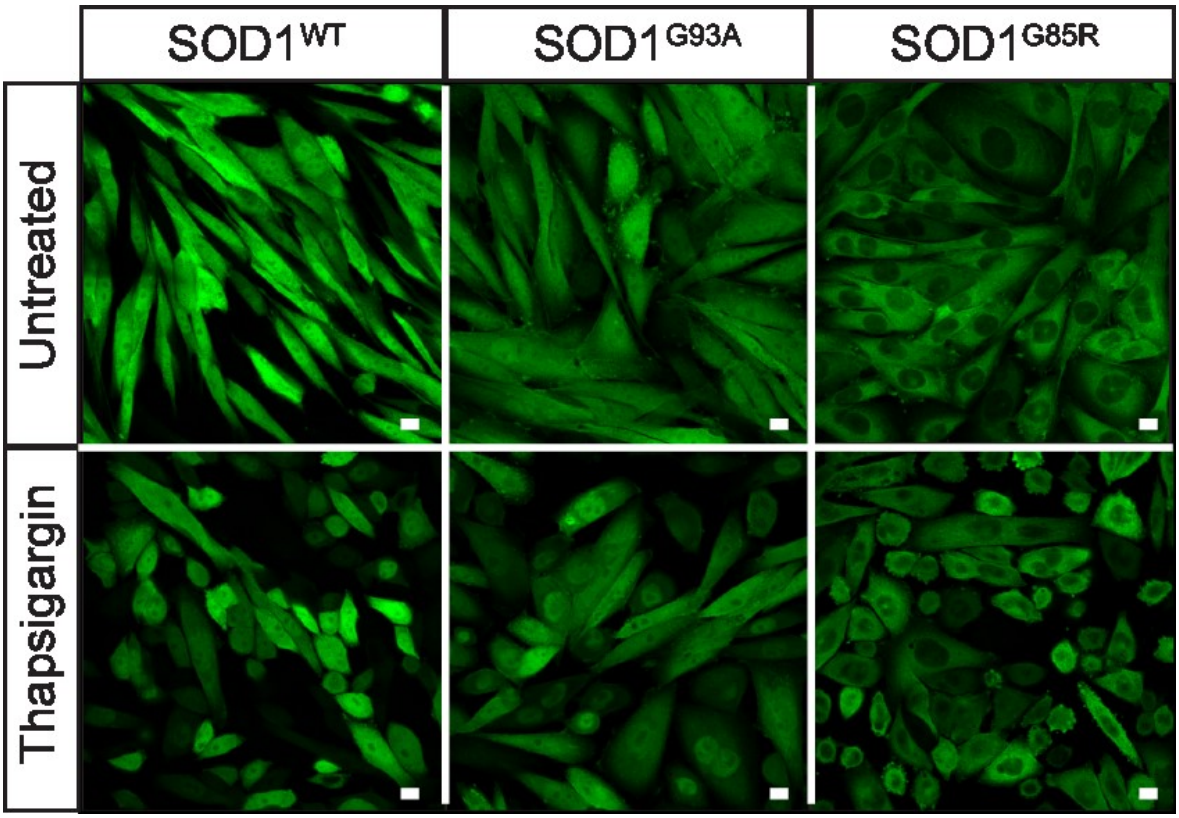

Figure 4.12 Treatment using thapsigargin on Flp-in T-Rex system expressing SOD1. Flp-in T-Rex cell lines expressing eGFP-SOD1 (WT, G93A and G85R) were turned on by Tet (3ug/ml) and boosted by sodium butyrate (2mM) for 48hrs, then treated with 100nM thapsigargin for 24hrs at 37℃ in complete DMEM medium. Cells were fixed and visualized as described in Material and Methods. Scale bar 10μm.

4.2.4.3 Effects of ionomycin on SOD1 in transient transfection

Ionomycin functions as non-selective calcium ionphore, potentiates responses to NMDA, and stimulates nitric oxide production by calmodulin-dependent constitutive NO synthase (Liu & Hermann 1978). In this study, ionomycin was applied as a transmembrane calcium uniporter to investigate if the increased calcium concentration from extracellular environment (i.e. complete DMEM medium) promoted SOD1 inclusion formation. Therefore, cells transiently expressing GFP-SOD1 were treated with/without ionomycin, then analysed and quantified.

Following the treatment with ionomycin, the inclusion incidence of both $SOD1^{WT}$ and $SOD1^{MT}$ were significantly increased (from 2.35% to 10.81% for WT, from 24.6% to 32.4% for G93A, ***$p<0.005$; from 26.7% to 32.6% for G85R, **$p<0.01$). The mitochondria in the ionomycin treated cells showed no major change in their localization pattern in the presence of inclusions, but were frequently interspersed amongst the inclusions.

The inclusion incidence of $SOD1^{WT}$ and $SOD1^{G93A}$ was increased further under ionomycin/FCCP treatment. Interestingly, massive cell death was noticed in the $SOD1^{G85R}$ under ionomycin/FCCP combined treatment. Ionomycin could be inducing mitochondrial stress as well as intrinsic apoptosis and FCCP depolarized the mitochondria, therefore ionomycin and FCCP had synergistic effects on promoting aggregation formation as well as inducing cell death.

4.2.4.4 Effects of ionomycin on SOD1 in Flp-in T-Rex system

To investigate if ionomycin promoted the SOD1 aggregation formation, the Flp-in T-Rex system expressing eGFP-SOD1 was induced by Tet and boosted by sodium butyrate, followed by the treatment with ionomycin,.

Similar to the results obtained in section 4.2.4.2, cells treated with ionomycin showed abnormal morphology, including cell shrinkage and rounded shape. $SOD1^{G93A}$ showed a higher nuclear expression compared to the untreated cells as well. However, no SOD1 inclusion formation was observed in either $SOD1^{WT}$ or $SOD1^{MT}$ cell lines.

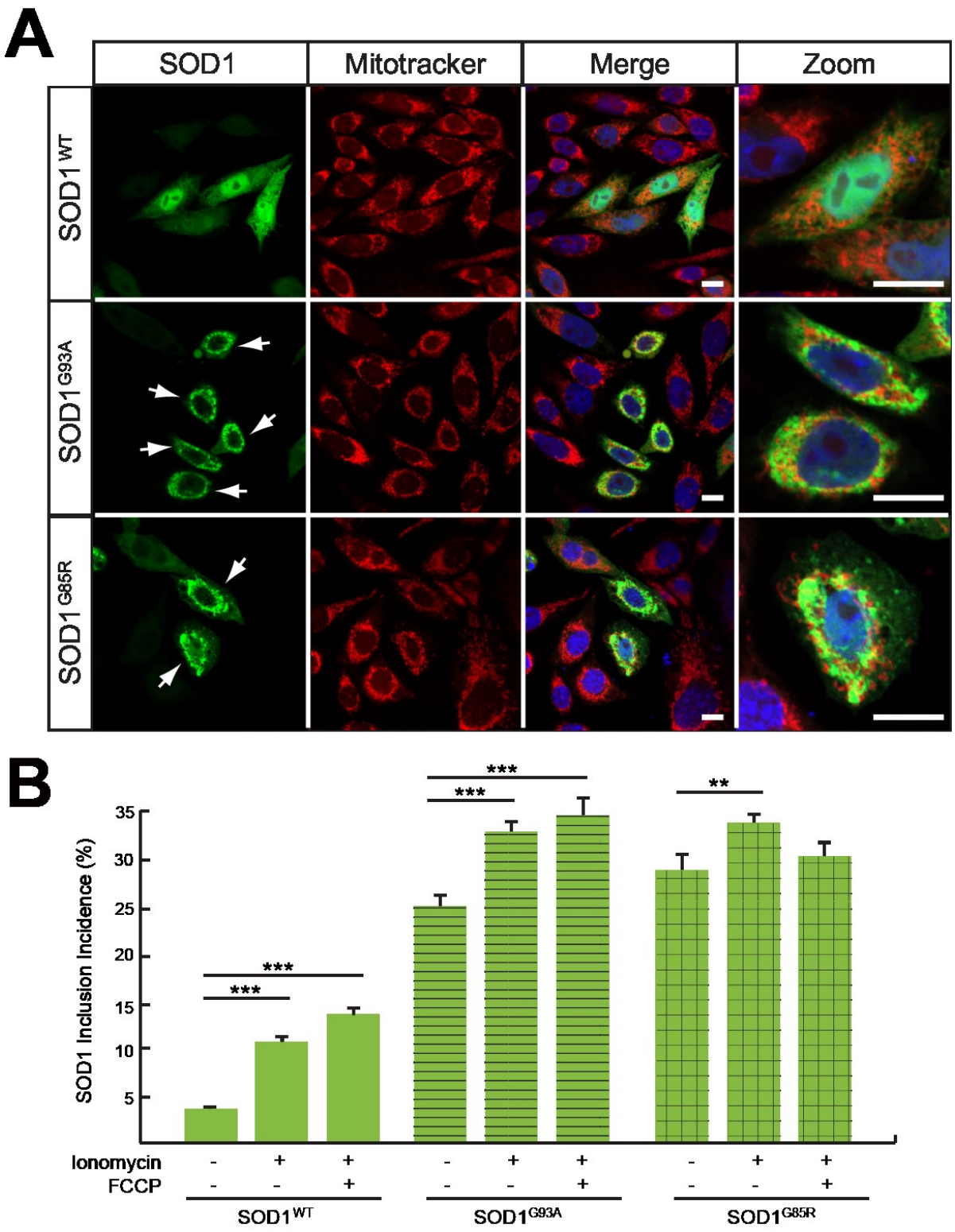

Figure 4.13 Treatment using ionomycin on cells transiently expressing SOD1. (A) Ionomycin treatment on cell transiently expressing GFP-SOD1. 100ng pEGFP-SOD1 (WT, G93A, G85R) were transfected into CHO cells as indicated. Cells were treated with 1uM ionomycin with (not shown) /without 1uM FCCP 24hrs post transfection for 3hrs at 37℃ in complete DMEM medium. Mitochondria were stained with Mitotracker orange for 5min in 1xPBS before fixation. Cells were fixed and visualized as described in Material and Methods. Arrows highlight the presence of inclusions. Scale bar 10 μm. **(B)** Quantification of SOD1 inclusion incidence. To assess the inclusion incidence of GFP-SOD1 (green), approximately 4 groups of over 100 transfected cells were scored for the t-test (Error bar: SD; **p<0.01, ***p<0.005; n=4).

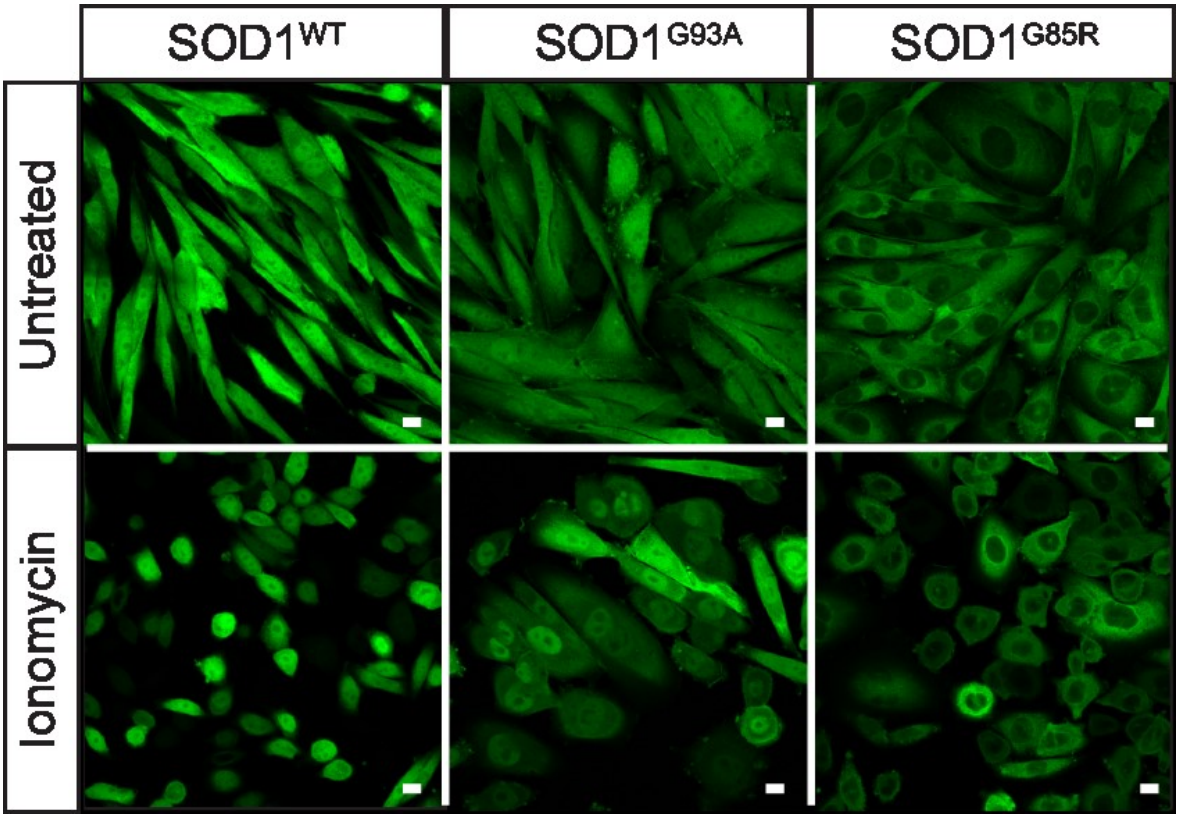

Figure 4.14 Treatment using ionomycin on Flp-in T-Rex system expressing SOD1. Flp-in T-Rex cell lines expressing eGFP-SOD1 (WT, G93A and G85R) were turned on by Tet (3ug/ml) and boosted by sodium butyrate (2mM) for 48hrs, then treated with 150nM ionomycin for 24hrs at 37℃ in complete DMEM medium. Cells were fixed and visualized as described in Material and Methods. Scale bar 10μm.

4.2.4.5 Effects of MG132 on SOD1 in transient transfection

MG132 is a potent membrane-permeable proteasome inhibitor of 26S (Sheng et al. 2006). In this study, MG132 was utilized as UPS inhibitor to investigate if the blockage of degradation mechanism contributed to SOD1 aggregation. Cells transiently expressing GFP-SOD1 were treated with/without MG132, then analysed and quantified. As shown in Figure 4.15, the inclusion incidence of GFP-SOD1^{MT} was significantly increased from ~25% to ~50% (***p<0.005). The mitochondria in the MG132 treated cells showed dot-like staining and mainly localized in the area where the SOD1 inclusions were concentrated, which showed sight overlap with the inclusions. In conclusion, SOD1 aggregation was significantly promoted when the proteasomal degradation pathway was blocked.

4.2.4.6 Effects of MG132 on SOD1 in Flp-in T-Rex system

To investigate if MG132 promoted the SOD1 aggregation formation, Flp-in T-Rex cells expressing eGFP-SOD1 were induced by Tet and boosted by sodium butyrate, followed by the treatment of MG132 (Figure 4.16-18).

Cells treated with MG132 exhibited abnormal morphology associated with cell death, including blebbing, cell shrinkage and vacuolation. SOD1^{MT} formed typical peri-nuclear inclusions under MG132 treatment but these were more prevalent. The inclusion incidence of SOD1^{G93A} significantly increased to 41.8% (***p<0.005), and that of SOD1^{G85R} increased to 90.8% (***p<0.005). Interestingly, MG132 showed little effect on cells expressing SOD1^{WT}. To explore if MG132 induced aggregation formation by increasing the expression level of SOD1 within the Flp-in T-Rex system, untreated or treated cells were lysed, resolved by SDS-polyacrylamide gel and analysed by western blot (Figure 4.17). The GAPDH was applied as an internal reference. No significant changes of expression level were detected in this assay.

As the cells expressing eGFP-SOD1 usually died 48hrs post MG132 treatment, a long-term Tet treatment was carried out, aiming to induce SOD1 inclusion formation while maintain the viability of the host cell lines. Tet/sodium butyrate induced cells were treated with high level of MG132 for short period and then cultured in medium containing Tet alone. As shown in Figure 4.18, typical peri-nuclear inclusions formed in cell lines expressing SOD1^{G93A} and SOD1^{G85R}, whereas SOD1^{WT} was still uniformly distributed in the cells, without forming any inclusions. Collectively, these data suggest inhibition of the UPS promoted the aggregation formation in the SOD1^{MT}-expressing cell lines, implying the disturbance of protein quality control, such as impaired proteasome, is important for misfolded protein to further aggregate in the SOD1-associated ALS disease model.

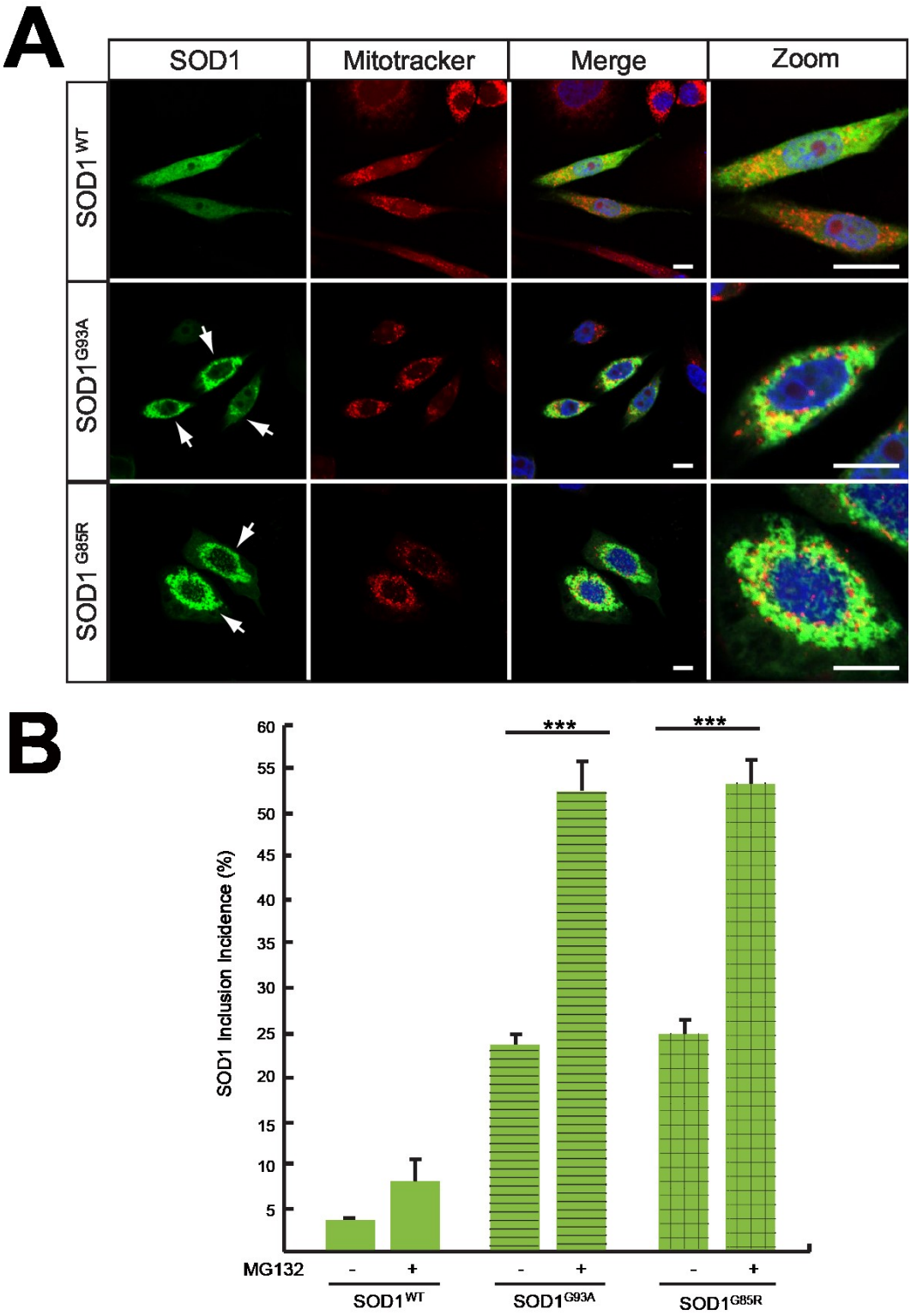

Figure 4.15 MG132 treatment of cells transiently expressing SOD1. (A) MG132 treatment on cells transiently expressing GFP-SOD1. 100ng pEGFP-SOD1 (WT, G93A, G85R) were transfected into CHO cells as indicated. Cells were treated with 20uM MG132 24hrs post transfection for 3hrs at 37℃ in complete DMEM medium. Mitochondria were stained with Mitotracker orange for 5min in 1xPBS before fixation. Cells were fixed and visualized as described in Material and Methods. Arrows highlight the presence of inclusions. Scale bar 10 μm. **(B)** Quantification of mean SOD1 inclusion incidence. To assess the inclusion incidence of GFP-SOD1 (green), approximately 4 groups of over 100 transfected cells were scored. Student t-test (Error bar: ±SD; ***p<0.005; n=4).

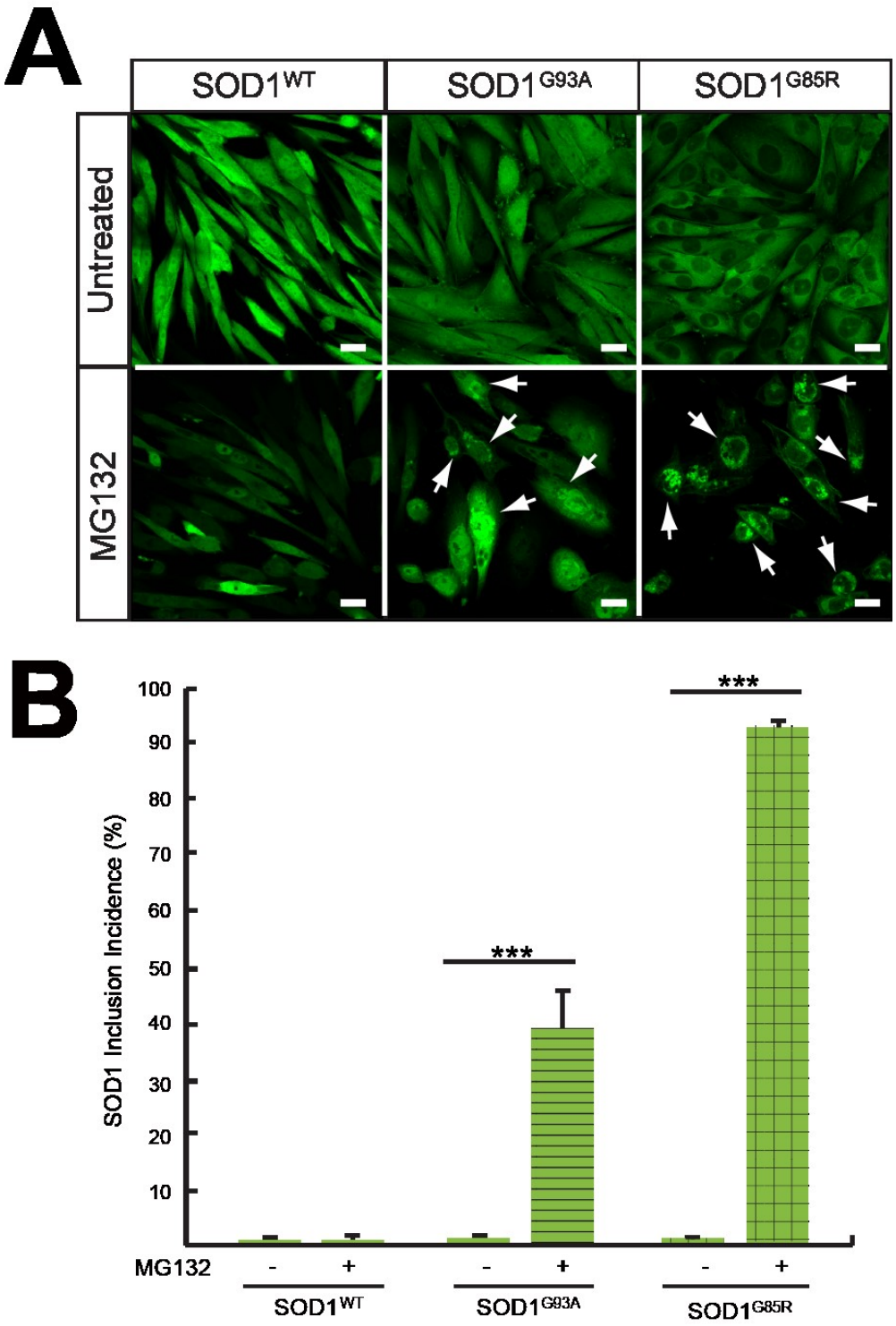

Figure 4.16 Treatment using MG132 on Flp-in T-Rex system expressing SOD1. Flp-in T-Rex cell lines expressing eGFP-SOD1 (WT, G93A and G85R) were turned on by Tet (3ug/ml) and boosted by sodium butyrate (2mM) for 48h, then treated with 400nM MG132 for 24hrs at 37℃ in completed DMEM medium. Cells were fixed and visualized as described in Materials and Methods. Scale bar 10μm. **(B)** Quantification of mean SOD1 inclusion incidence. To assess the inclusion incidence of GFP-SOD1 (green), approximately 4 groups of over 100 cells were scored. Student t-test (Error bar: ±SD; ***p<0.005; n=4).

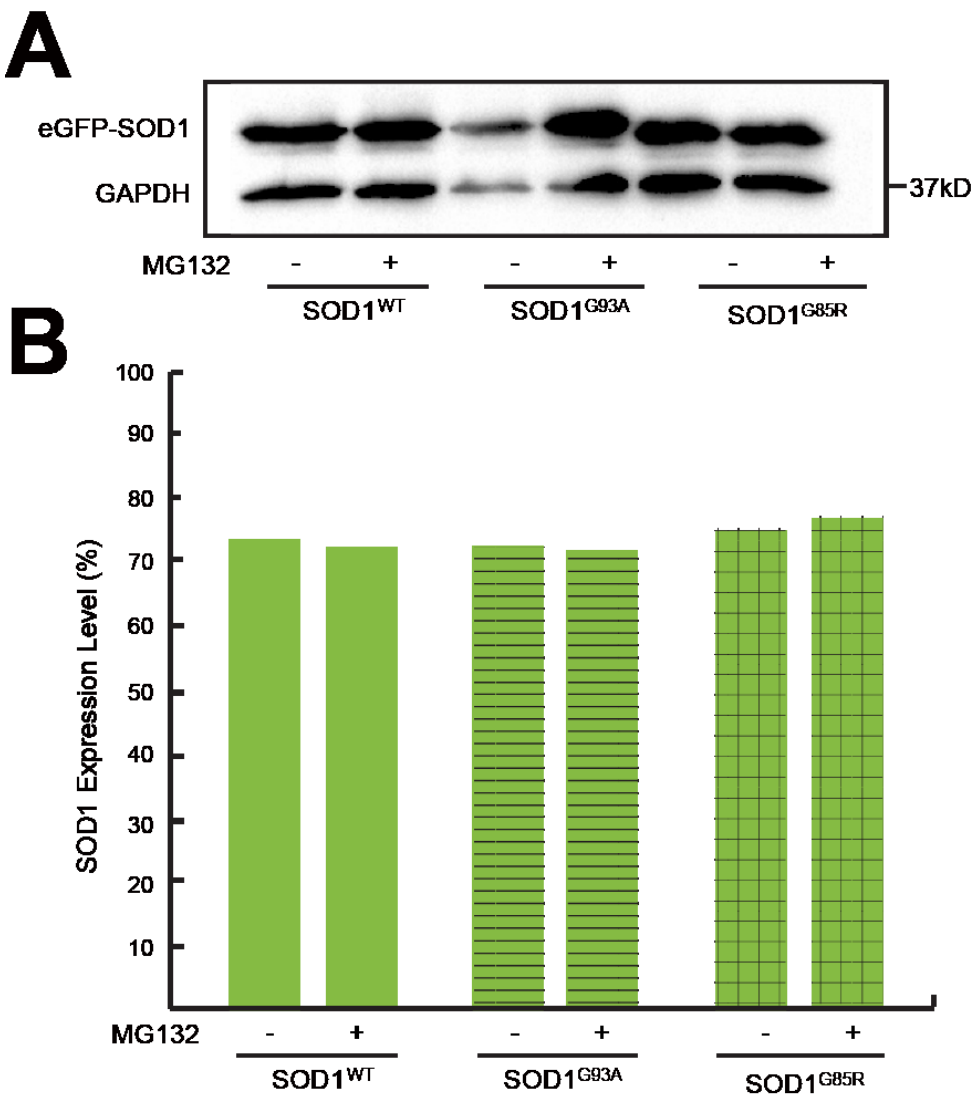

Figure 4.17 Analysis of effects of MG132 on expression levels of eGFP-SOD1 Flp-in T-Rex system. (A) MG132 treatment on eGFP-SOD1 expressed by Flp-in T-Rex system. Flp-in T-Rex eGFP-SOD1 cell lines were turned on by Tet (3ug/ml) and boosted by sodium butyrate (2mM) for 48h, then treated with 400nM MG132 for 24hrs at 37℃ in completed DMEM medium. Cell lysates were resolved by SDS-PAGE prior to transfer to nitrocellulose. SOD1 and GAPDH were probed with mouse anti-GFP (1:1000) monoclonal, anti-GAPDH (1:20000) and goat anti-mouse HRP (1:20000). eGFP or GAPDH specific immunoreactive bands were developed with ECL, MW markers are labelled on the right of panels. **(B)** Quantification of expression levels of eGFP-SOD1. Intensity of bands generated from immune-blot was quantified by ImageJ (refer to Materials and Methods), and calculated as 'SOD1 expression % = Intensity (eGFP)/ Intensity (GAPDH)' (n=1).

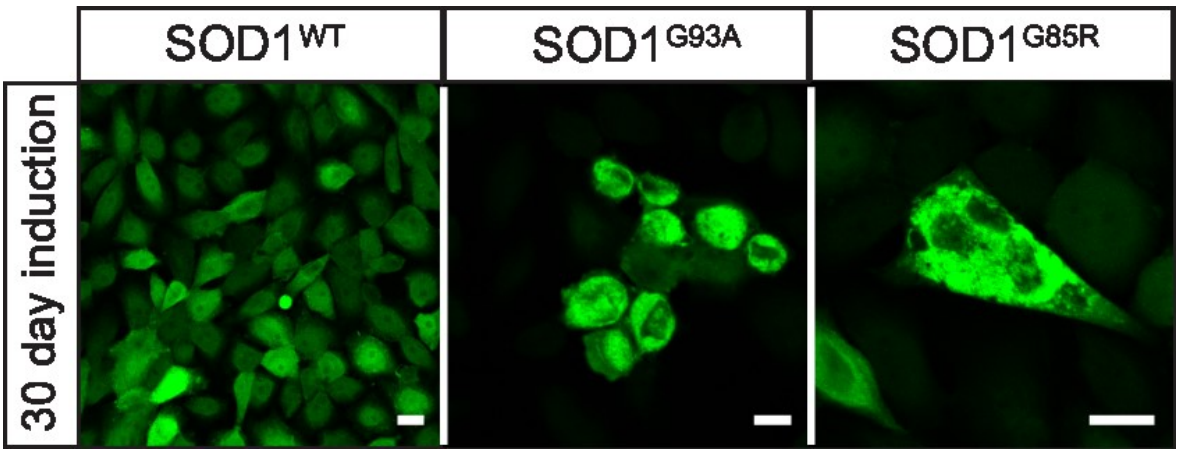

Figure 4.18 Long-term MG132 treatment of eGFP-SOD1 Flp-in T-Rex system. Flp-in T-Rex cell lines expressing eGFP-SOD1 (WT, G93A and G85R) were turned on by Tet (3ug/ml) and boosted by sodium butyrate (2mM) for 48hrs, treated with 20uM MG132 for 3hrs at 37℃ in completed DMEM medium, then re-cultured in DMEM medium containing Tet for another 72hrs. Such treatment was repeated 6 times in total. Then cells were fixed and visualized as described in Materials and Methods. Scale bar 10μm.

4.2.5 Effects of SOD1 inclusions on SOD1 inducible cell lines

Since the inducible Flp-in T-Rex system had been generated, I was able to manipulate the expression of $SOD1^{WT}$ before or after the presence of SOD1 inclusions, providing insights into the potential mechanism of seeding phenomena. Therefore, in this and the next section, non-inducible transiently transfected GFP-SOD1 was utilized with the aim of producing SOD1 inclusions under different parameters using TetR-regulated cells.

4.2.5.1 Effects of SOD1 inclusions on pre-induced $SOD1^{WT}$

To examine if SOD1 inclusions were able to seed pre-existing soluble $SOD1^{WT}$ in the Flp-in T-Rex system, non-inducible GFP-SOD1 was transfected into pre-induced mCherry-$SOD1^{WT}$ cell lines. Flp-in T-Rex system was turned on for 48hrs, and then turned off 24hrs before transfection. I performed a 7-day long seeding assay, and reactions for different time points were stopped and then analysed right after fixation. The inclusion incidence of non-inducible GFP-SOD1 was analysed 24hrs post transfection (Figure 4.19A). The day transfection performed was marked as day 0, therefore GFP-SOD1 was detectable from day 1.

As shown in Figure 4.19B-E, no mCherry tagged SOD1 inclusions were observed up to day 7, which is consistent with my earlier experiments performed in G418 selected SOD1 cell lines. The GFP-$SOD1^{G93A}$ and GFP-$SOD1^{G85R}$ failed to alter the subcellular localization of mCherry-$SOD1^{WT}$ expressed by Flp-in T-Rex system, a phenomenon frequently observed in previous preliminary tests in this study. Additionally, there was no significant increase of GFP-SOD1 inclusion incidence when $SOD1^{MT}$ was transiently overexpressed in the pre-induced mCherry-$SOD1^{WT}$ Flp-in T-REx system, suggesting inclusions generated from transient transfection were not ideal seeds for the pre-induced $SOD1^{WT}$.

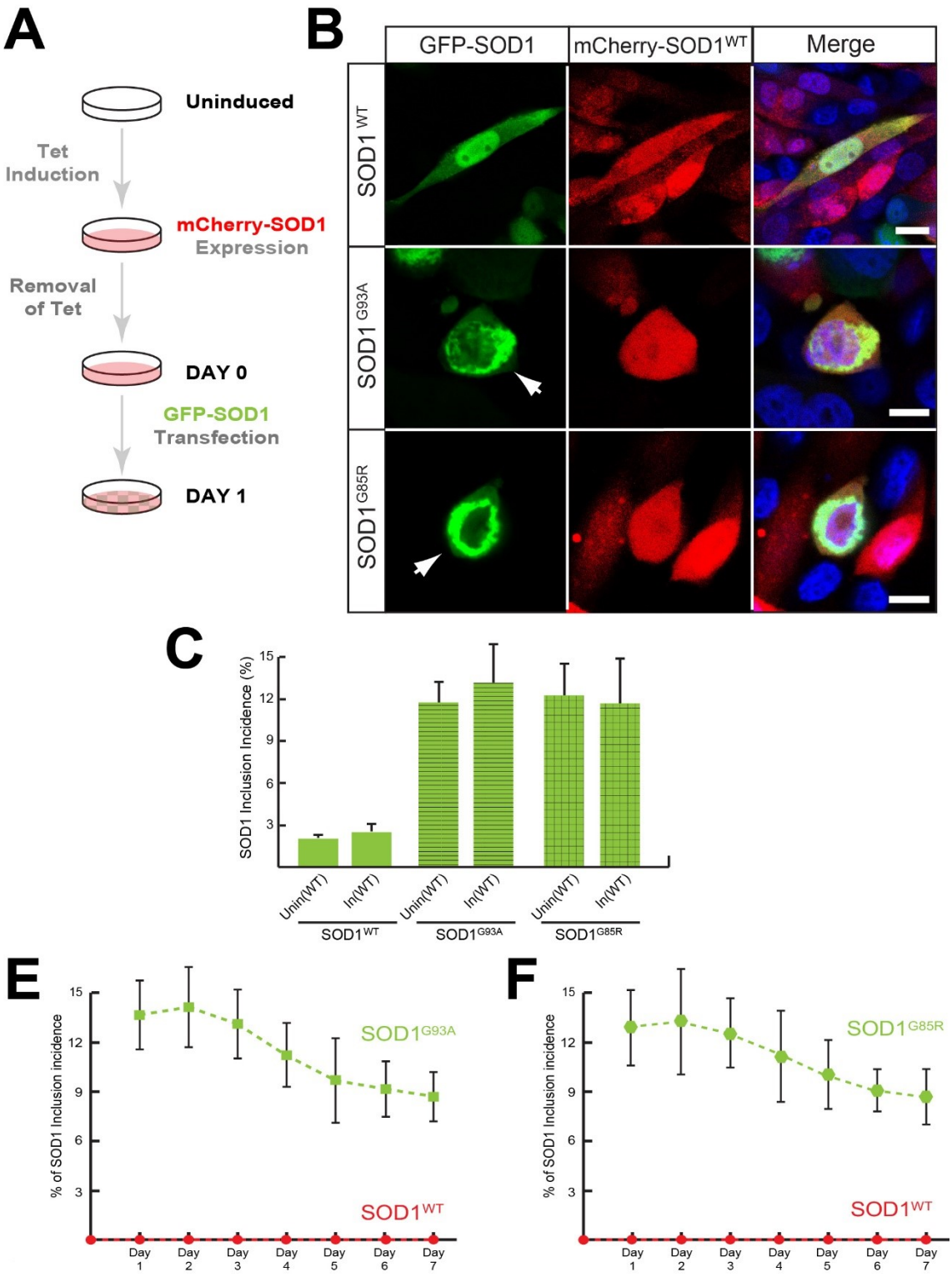

Figure 4.19 SOD1 inclusions showed little seeding effects on pre-induced SOD1^{WT}. (A) Schematic illustration of the seeding assay. **(B)** 200ng plasmids expressing GFP-SOD1 were transfected into cells. Flp-in T-Rex system expressing mCherry-SOD1^{WT} was turned on by 3ug/ml Tet and turned off 24hrs before transfection. Cells were fixed from day 1 to day 7 post-induction respectively as described in Material and Methods. Arrows highlight the presence of inclusions. Scale bar 10 μm. **(C-E)** Quantification of mean SOD1 inclusion incidence. To assess the percentage of GFP-SOD1 inclusions (green), mCherry-SOD1 inclusions (red), approximately 4 groups of over 100 fluorescently positive cells were scored. Student t-test (Error bar: ±SD; n=4).

4.2.5.2 Effects of preformed SOD1 inclusions on SOD1^{WT}

To examine whether the preformed SOD1 inclusions were able to seed newly expressed SOD1^{WT} in the Flp-in T-Rex system, GFP-SOD1 was transfected into uninduced mCherry-SOD1^{WT} cell lines. 24h post transfection, Flp-in T-Rex system was turned on by Tet and boosted by sodium butyrate (Figure 4.20A). Reactions were stopped at different time points and then analysed right after fixation. Therefore, the day Flp-in system turned on was marked as day 0.

As presented in Figure 4.20B, mCherry tagged SOD1^{WT} were excluded from the area where GFP-SOD1^{MT} localized in inclusions at in day 7. No co-localization was observed between GFP-SOD1^{MT} inclusions and mCherry-SOD1^{WT}. The dot-like aggregates of mCherry tagged inclusions that emerged by day 4 did not co-localize with or be recruited to the pre-formed inclusions in this seeding assay. It is possible that the reason why SOD1^{WT} was excluded was because the structure of inclusions formed within cells was too compact for SOD1^{WT} to co-localize. Collectively, SOD1 seeding phenomena did not occur in the stable cell line generated in this study.

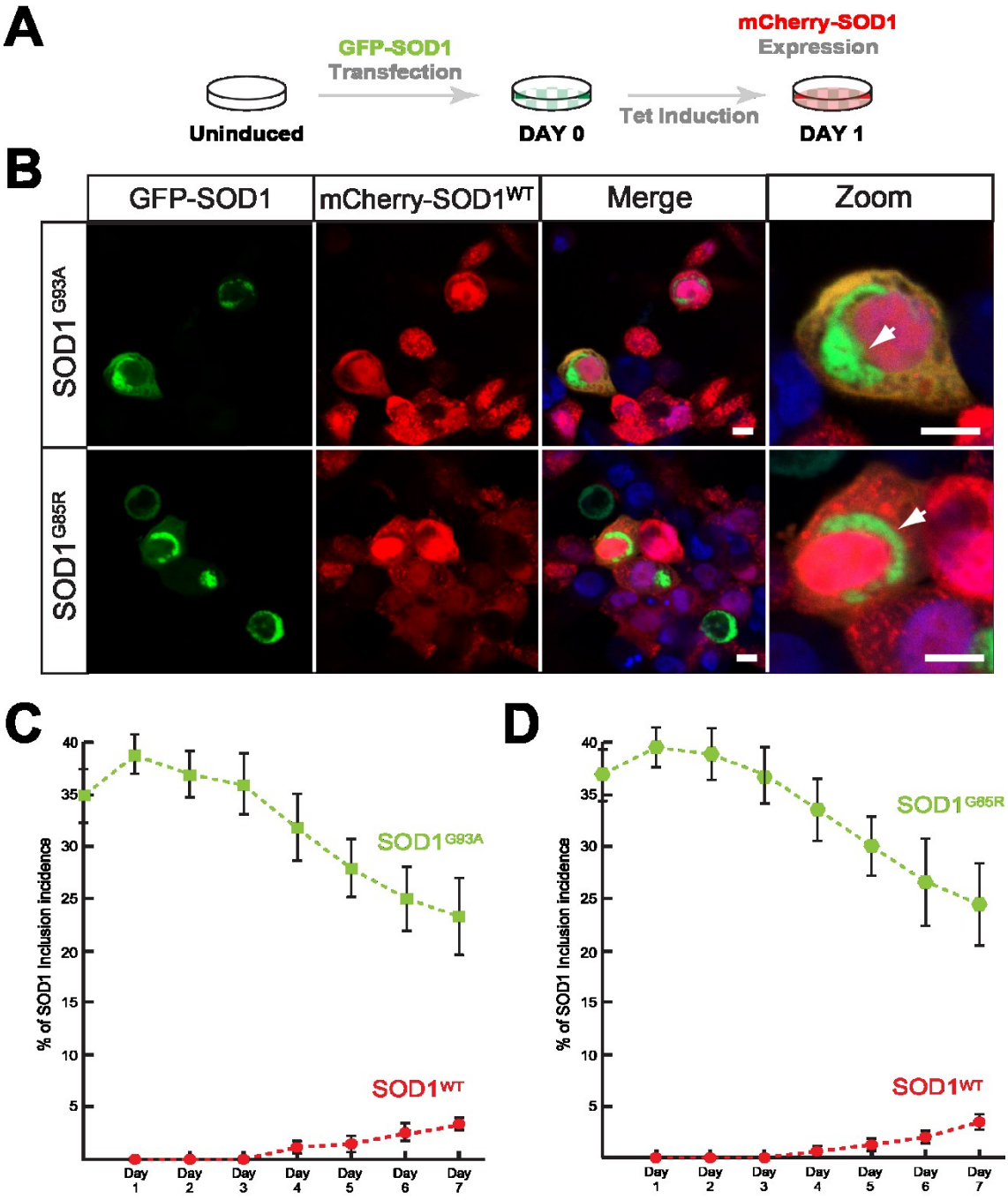

Figure 4.20 SOD1^{WT} is excluded from pre-formed SOD1 inclusions in the seeding assay. (A) Schematic illustration of the seeding assay. **(B)** 200ng plasmids expressing GFP-SOD1 were transfected into cells. Flp-in T-Rex system expressing mCherry-SOD1^{WT} was turned on by 3ug/ml Tet and boosted by sodium butyrate (2mM) 24hrs post transfection. Cells were fixed from day 1 to day 7 post-induction respectively according to the Materials and Methods. Arrows highlight the inclusions. Scale bar 10 μm. **(C-D)** Quantification of mean SOD1 inclusion incidence. To assess the percentage of GFP-SOD1 inclusions (green), mCherry-SOD1 inclusions (red), approximately 4 groups of over 100 fluorescently positive cells were scored. Student t-test (Error bar: ±SD; n=4).

4.3 Discussion

SOD1^{G93A} and SOD1^{G85R} formed peri-nuclear inclusions in the cell model

In this chapter, I investigated the effects of SOD1 mutant proteins in a cell model, therefore several constructs and cell lines were generated for this purpose. Plasmids expressing SOD1^{WT} or SOD1^{MT} were pre-tested in transient transfection to characterize the subcellular localization, inclusion incidence as well as apparent molecular weight. In contrast to SOD1^{WT}, both SOD1^{G93A} and SOD1^{G85R} were excluded from nuclei in the transient transfection, and formed peri-nuclear inclusions (Figure 4.1-4.2). The inclusions formed in the cytoplasm showed typical circular peri-nuclear localization, which is consistent with previous published results of GFP-SOD1^{G93A} (Novoselov et al. 2013). The potential effects of SOD1 aggregates have been fully discussed in section 1.3.5, in this chapter, I will focus on their potential recruitment effects and seeding ability.

Accumulation of misfolded and aggregated is a prominent pathological features common to many neurodegenerative diseases, including ALS. When the capacity of UPS and/or chaperone refolding system are overwhelmed, ubiquitylated, aggregated proteins can be actively transported to a structure named aggresome. Aggresome formation is recognized as a cellular response, which is accompanied by redistribution of the intermediate filament protein vimentin to form a cage surrounding the aggregated substrates at the microtubule-organizing centre (Olzmann et al. 2008). The microscopically visible inclusions observed in this study within cells transiently overexpressing SOD1^{MT} occasionally resembled aggresomes, as bright juxtanuclear structures. Recent finding suggest that aggresome formation is mediated by microtubule-based transport of the aggregated substrates to the centrosome, a process regulated by several proteins, including histone deacetylase 6, E3 ubiquitin-protein ligase parkin, deubiquitinating enzyme ataxin-3, and ubiquilin-1 (Zaarur et al. 2008; Chin et al. 2010; Viswanathan et al. 2011; Ouyang et al. 2012; Zhou et al. 2014). To further investigate whether SOD1 inclusions observed in this study have the features of an aggresome, several microtubule inhibitors (such as paclitaxel, vincristine sulfate or docetaxel) and/or vimentin antibodies could be applied.

Generation of constitutive cell lines

Two different types of cell lines were generated in this study, i.e., constitutive expressing cell line and inducible cell line. Initially, fluorescently tagged constitutive SOD1 expressing cell lines were established, including GFP-SOD1 and mCherry-SOD1. The stable cell lines exhibited similar subcellular localization of SOD1 compared to SOD1 expressed transient transfection. However, the typical peri-nuclear SOD1

aggregates were rarely observed in the G418 selected cells (Figure 4.5), as the cells expressing large inclusions gradually died in the selection. It is likely that there was selection against cells expressing aggregated pathogenic proteins, and only cells with less intrinsic stress to form selectable clones. It is worth mentioning that dot-like aggregates were mainly observed in unhealthy or dying cells during the G418 selection, which might indicate the local unfolding or misfolding of SOD1, however, these dot aggregates did not form peri-nuclear inclusions after long-term culture. The lack of inclusions and obvious morphologically detectable protein aggregation in the G418 selected stable cell lines was considered as a problem to study for seeding and transmission assay. Experiments using immunoblot and RT-PCR also suggested the presence of stress response signals even in the $SOD1^{WT}$ cell lines (data not shown). When considered in combination with the disadvantages highlighted in section 4.2.3.1, the constitutive SOD1 expressing cell lines were discarded, and the inducible cell lines, which would not be subject to pathogenic protein related selection were generated.

Generation of inducible cell lines

The Flp-in T-Rex system was utilized to generate inducible cell lines (Figure 2.2.B). Flp-in host cell line contains a FRT site that was integrated into a certain site in the genome, and the TetR that controls the transcription of GOI. Using this host cell line provided a number of advantages: ① the FRT site enables the same insertion position into the genome for different GOIs. ② GOI would not express during the selection process, reducing the uncertainties and side effects caused by expression of GOI. ③ Expression of GOI could be induced by Tet at any time.

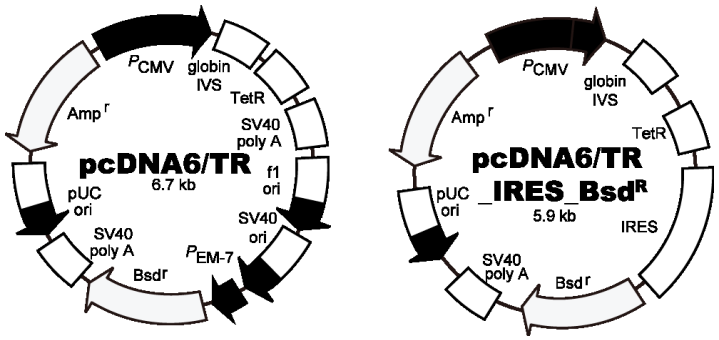

Figure 4.21 Structural comparison between pcDNA6/TR and modified pcDNA6/TR_IRES_Bsd^R.

My first attempt to produce host cell line failed. Host cells lost inducibility and GOI began to express during Hgy selection. I thought that the reason that the former Flp-in host cell line unsuccessful was because cells transfected with pcDNA6/TR plasmid lost the TetR gene expression, while the Bsd^R gene kept expressing. A modified TetR expressing plasmid (Figure 4.22) used for Gateway T-Rex cell line generation combated this problem (Gomez-Martinez et al. 2013). Prof Hergovich group (UCL)

ligated the TetR fragment with the Bsd^R gene under the control of an internal ribosome entry site (IRES), thus enabling TetR and Bsd^R to be driven by the same promoter and then co-translated on the same mRNA. Using pcDNA6/TR_IRES_Bsd^R, the Flp-in host cell line was successfully generated.

pT-Rex DEST30-eGFP'-SOD1 plasmids were also generated. The selection procedure and mechanisms of gateway T-Rex cell line are shown in Figure 2.3. Compared to Flp-in T-Rex system, Gateway T-Rex possesses certain advantages: ① it is easier to generate, as it only required two steps of selections, i.e., G418 and Bsd; ② easier to subclone. However, the Flp-in T-Rex system has unparalleled advantages: ① the expression levels of same GOI from different colonies or from different batches are consistent; ② the integration sites for different GOIs were the same in theory. Therefore, I chose to use Flp-in T-Rex system in this study for further investigations. With the help of inducible cell lines, I was able to manipulate the SOD1 to expression at different time points. Yet, one disadvantage of T-Rex system was noticed in this study and by another student at the institute (Rosalina Guarascio's work on Tau): it was difficult to transfect pre-induced cell lines (the transfection efficiency was ~5%). The transfection efficiency slightly increases if the T-Rex system were turned off before transfection. The reasons for this are unclear.

SOD1 expressed by Flp-in T-Rex system failed to form inclusions

By using Flp-in T-Rex system, I ruled out the possibility that selection process affected SOD1 inclusion formation. Surprisingly, $SOD1^{G93A}$ and $SOD1^{G85R}$ cell lines not only showed lower expression level compared to $SOD1^{WT}$ under the same Tet concentration, but also failed to form inclusions after long-time (up to 2 months) of continuous Tet induction. The phenomenon that $SOD1^{WT}$ showed higher expression level than $SOD1^{MT}$ partially confirmed the hypothesis that $SOD1^{WT}$ mRNA formed ribonucleic complex, thus increasing protein half-life, while $SOD1^{MT}$ mRNA disrupted this process (Ge et al. 2006). It is also possible that the misfolded SOD1 proteins have been successfully degraded by cellular quality control therefore showing no accumulated aggregates in the Flp-in T-Rex system.

When the expression levels of SOD1 expressed by transient transfection and SOD1 induced by Tet in Flp-in T-Rex system with/without the boost of sodium butyrate were compared, the level of SOD1 proteins expressed by transient transfection were 30-50 times higher in each cell than SOD1 expressed by Flp-in T-Rex cells for 48h without the SB boost, and 15-25 times higher than cells with the SB boost. It is possible that SOD1 mutant expressed by Flp-in T-Rex system failed to form inclusions was due to insufficient expression level, which might not be able to trigger aggregation. Therefore,

I attempted to promote inclusion formation in the Flp-in T-Rex system using drug treatments.

Jaarsma *et al* (2000) observed a series of neurodegenerative changes in transgenic mice expressing high level of $SOD1^{WT}$, including mitochondrial vacuolization in the spinal cord and the brain stem, axonal abnormities and loss of motor neurons with a mild ALS phenotype (Jaarsma et al. 2000). Early in 1999, Beaulieua *et al* reported a late onset motor neuron death in transgenic mice overexpressing $peripherin^{WT}$ (Beaulieu et al. 1999). Recently, Mitchell *et al* (2013) reported that overexpression of FUS^{WT} also caused motor neuron degeneration in an age-and dose-dependent manner (Mitchell et al. 2013). These data suggested that high expression level of wild-type protein can also be delirious to cells.

In this chapter, I used the inclusion incidence as a method to assess SOD1 aggregation. In addition to morphological changes, other biophysical/biochemical methods had been tested in the Cheetham lab previously. Dr. Sergey Novselov and Dr. Heather Smith confirmed that $SOD1^{MT}$ aggregates appeared to be negative on filter traps (data not shown) yet polyQ was shown to be positive, which bring us the question of different structure of aggregates. Matsumoto et al (2006) interpreted that SOD1 aggregation is porous, and nascent proteins were diffuse among the SOD1 aggregates (Matsumoto et al. 2006). In contrast, Htt Q103 aggregates are 'hard and compacted', containing a single exterior surface surrounding the core to which soluble Htt or other proteins could interact. In addition, Wendy Mustill's PhD thesis showed sedimentation to separate the soluble or insoluble fraction of SOD1 proteins expressed in the cell model could be applied to assess aggregation, which could be used for future SOD1-related work.

Increased calcium and blockade of UPS promote SOD1 aggregation formation

Initially inspired by my *in vitro* work that combination of calcium and DTT promoted the sedimentation of recombinant $SOD1^{G93A}$ and $SOD1^{G85R}$ (Chapter 3), several calcium manipulators were chose to promote SOD1 aggregation formation. In this study, thapsgargin and ionomycin increased the SOD1 inclusion incidence in transient transfection, yet showed little effect on inclusion formation in the Flp-in T-Rex system. Interestingly, with the help of small amount of FCCP, the inclusion incidence of $SOD1^{MT}$ was increased yet that of $SOD1^{WT}$ was reduced, which might partially confirm that increased calcium concentration in the cell model contribute to SOD1 aggregation.

Increased calcium has been observed in the spinal cord of ALS animal models as well as ALS patients, suggesting it is a common event (Palecek et al. 1999; Vanselow & Keller 2000; Tateno et al. 2004). However, the calcium manipulators tested in my cell

model seemed to show a modest effect. In fALS, mutant proteins such as VAPB (De vos et al. 2012; Mórotz et al. 2012), ALS2 (Lai et al. 2006), Ataxin-2 (J. Liu et al. 2009) or Matrin 3 (Alexander Valencia et al. 2007) have been reported to either potentiate calcium deregulation or result in an increased vulnerability to the effects of upregulated calcium. Emerging findings suggest calcium influx could directly contribute to SOD1 misfolding and aggregation as an environmental factor. However, the indirect effects of calcium are more significant and more correlated to SOD1-mediated cell death, including promoting the SOD1-BCl-2 interaction (Pasinelli et al. 2004; Pedrini et al. 2010), mitochondrial dysfunction, ER stress, excytotoxicity and ultimately apoptosis (Appel et al. 2001; Kawamata & Manfredi 2010; Leal & Gomes 2015; Kaus & Sareen 2015).

Compared to calcium manipulators, MG132 exhibited a far more significant effect on promoting SOD1 aggregation formation, indicating that proteasome inhibition exhibited a direct influence on SOD1-associated aggregation. Under MG132 treatment, ~40% of $SOD1^{G93A}$ and ~90% of $SOD1^{G85R}$ cells from Flp-in T-Rex formed peri-nuclear inclusions. Given the misfolded SOD1 is mainly degraded via UPS (Novoselov et al. 2013), UPS inhibition potentially resulted in accumulation of large scale of misfolded proteins, thus leading to the global aggregation formation even in the low expression level of $SOD1^{MT}$. However, no increase in SOD1 expression levels was detected following MG132 treatment, which would suggest that there was not a major increase in misfolded proteins because of failed degradation. Although it is possible that an increase in misfolded SOD1 was not detected because the protein was either insoluble and did not enter the gel or the antigen was not accessible to the antibody, because of misfolding and/or aggregation.

$SOD1^{WT}$ is recruited to SOD1 inclusions

As a preliminary test for the SOD1 aggregate seeding assay, $SOD1^{MT}$ were co-expressed with $SOD1^{WT,}$ to explore if SOD1 mutant aggregates possessed the ability to further propagate and recruit $SOD1^{WT}$. $SOD1^{WT}$ was observed to co-localize with $SOD1^{MT}$, excluded from nucleus, forming inclusions. Tsang *et al* (2011) reported the nuclear SOD1 expression is essential for homeostasis, as SOD1 functions as a nuclear transcription factor to combat oxidative stress, thus maintaining genomic stability (Tsang et al. 2014). Therefore, change of subcellular localization of $SOD1^{WT}$ might potentially be relevant to dominant disease situation. Different fluorescent tags provide the opportunity to distinguish wild-type from mutants without any concerns of epitope availability. The inclusion incidence of $SOD1^{WT}$ was significantly increased from the basal level to ~10%, indicating when co-expressed with $SOD1^{MT}$, fully functional

$SOD1^{WT}$ is recruited to form inclusions containing both wild-type and mutant proteins, thus enhancing the aggregation process.

Then another experiment using fused cells was also carried out with the aim to explore the effects of preformed SOD1 inclusions on $SOD1^{WT}$. Cells expressing mCherry-SOD1 (WT, G93A and G85R) were fused with cells expressing GFP-$SOD1^{WT}$ respectively. In the heterotypic PEG-mediated fusion, $SOD1^{WT}$ was observed to co-localize with preformed SOD1 inclusions, which is consistent with the MT/WT recruitment assay. It is worth noting that the heterotypic fusion efficiency too low for quantification. Several methods were applied to optimize, including increase the cell density in the PEG fusion system, using stable cell lines instead of transiently-transfected cells, co-incubation of the two cell lines before fusion, and extending the time of PEG treatment were applied. None of these methods significantly increased the efficiency of heterotypic fusion. Although these preliminary experiments suggested $SOD1^{WT}$ could co-localize with and further recruited by mutant inclusions the data are not possible to extend.

Overexpression of $SOD1^{MT}$ showed little effects on pre-induced $SOD1^{WT}$

SOD1 aggregates released by one cell have been reported to be taken up by the neighbouring cells (Münch et al. 2011). To simulate this scenario, pre-produced mCherry-$SOD1^{WT}$ cell lines were transfected with GFP-SOD1. As opposed to initial expectations, there was little or no effect on inclusion incidence of either GFP-SOD1 or mCherry-$SOD1^{WT}$. Additionally, in the presence of inclusions, the alteration of subcellular localization of mCherry-$SOD1^{WT}$ was not observed.

Similar results were also observed in G418 selected constitutive mCherry-SOD1 cell lines (data not shown). I considered the reason that GFP-SOD1 inclusions failed to seed soluble mCherry-SOD1 (WT, G93A and G85R) was due to the constitutive cell line generation procedure, as the G418 selection could have selected cells that had enhanced anti-aggregation processes. However, the assays performed in T-Rex system and G418 selected cells confirmed transfection of aggregation probe SOD1 into the presence of already folded $SOD1^{WT}$ will not lead to recruitment.

The reasons for this are not clear but could be related to the behaviour described in Chapter 3 where folded $SOD1^{WT}$ was resistant to the effects of $SOD1^{MT}$ until the protein was destabilised. This suggests that the intrinsic stability of folded SOD1 in cells renders it highly resistant to the seeding potential of $SOD1^{MT}$. In contrast, when $SOD1^{WT}$ and $SOD1^{MT}$ are co-expressed and synthesized at the same time then the potential to form mixed heterodimers exists and this is likely to destabilise $SOD1^{WT}$ and enhance the seeding potential of $SOD1^{MT}$. It might be informative in future to use cell

treatments that could destabilise folded SOD1^{WT} and test if this improves the ability of SOD1^{MT} to recruit SOD1^{WT} to aggregates.

Newly synthesized SOD1^{WT} is excluded from pre-existing SOD1 inclusions

Next, I tried to simulate SOD1 seeding phenomenon by introducing GFP-SOD1 inclusions into the uninduced mCherry-SOD1^{WT} cell lines first, then inducing synthesis of SOD1^{WT}. According to Munch *et al* (2011) (Münch et al. 2011), pre-labelled SOD1^{H46R} inclusions were able to seed GFP-SOD1^{H46R} stably expressed by Neuro-2a cells, forming enlarged green inclusions after 1 month incubation, and the internalized seeds could only be observed before 7 or 8 days post-treatments.

Interestingly, the opposite phenomena were observed in this study. In the presence of inclusions, mCherry-SOD1^{WT} was excluded from the area containing SOD1 inclusions. It is possible that the inclusions generated from transient transfection were too compact for soluble SOD1^{WT} to get access. Interestingly, dot-like mCherry-SOD1^{WT} inclusions began to form in the cells from day 4 onwards, but these were not positive for GFP. These mCherry-SOD1^{WT} puncta could be related to disturbances in the cellular proteostasis machinery related to the expression of GFP-SOD1^{MT} and the formation of inclusions. Indeed if the SOD1^{MT} aggregation has inhibited the proteasome this itself might stimulate further aggregation, although this was not observed in the GFP-SOD1^{WT} cell line and could be a feature of mCherry tagged SOD1. This phenomenon could be explored in more detail later, but it appears to be indirect as there was no recruitment of evidence of a direct interaction between the different SOD1 tagged proteins.

Several studies have used recombinant SOD1^{MT} to generate insoluble materials in cell-free system, then added these sedimented ‘aggregates’ into cell culture medium for seeding assay (Münch & Bertolotti 2011; Furukawa et al. 2013b). I attempted to use 6xHis-SOD1 aggregates produced in the cell-free system as seeds added into medium for incubation with SOD1 expressing cells (Appendix 4.6). However, the aggregates generated *in vitro* only attached to the outer membrane of the cells, and did not enter the intracellular compartments. After months of failed trials, I chose to introduce seeding by transfection instead.

Recently, Pokrishevsky *et al* (2016) reported that TDP-43 or FUS could induce hSOD1^{WT} misfolding propagated from cell-to-cell via conditioned media, and seeded endogenous hSOD1^{WT} aggregation in the recipient cells in a prion-like manner (Pokrishevsky et al. 2016). However, Kabashi *et al* (2011) reported the opposite results that TDP43 and FUS acted in a pathogenic pathway that was independent of SOD1. In transgenic zebrafish, SOD1^{WT} failed to rescue the phenotype observed upon

overexpression of $TDP43^{MT}$ or FUS^{R521H} or upon knockdown of Tardbp or Fus; similarly, $TDP43^{WT}$ or FUS^{WT} also failed to rescue the phenotype induced by $SOD1^{G93A}$ (Kabashi et al. 2011). In this study, I also tried to use TDP43 or FUS mutants to induce $SOD1^{WT}$ aggregation by transient overexpressed in CHO cells (data not shown), but no increase in inclusions of SOD1 was observed.

My *in vitro* experiments suggested that the seeded aggregation could only be triggered after the $SOD1^{WT}$ was destabilized. In the future, experiments could be performed to explore if GFP-SOD1 inclusions were able to seed the calcium manipulator-treated or metal ion chelating agent-treated cells expressing mCherry-$SOD1^{WT}$. However, due to the limitation of time, this issue could be further investigated in the future studies.

In conclusion, the seeding of SOD1 aggregation *in vitro* appears to be extremely difficult and is likely to require the target protein to be still folding from a nascent chain or the destabilization of folded and intact homodimers.

Chapter 5

Chaperone manipulation of SOD1 using cell models

5.1 Introduction

In SOD1-associated ALS, SOD1 mutant proteins have been reported to mediate harmful reactions due to gain of function, resulting in disrupted homeostasis in motor neurons (Chapter 1). Misfolded or aggregated $SOD1^{MT}$ has been reported to abnormally interact with several proteins that do not interact with $SOD1^{WT}$, suggesting a potential gain of function. These proteins include chaperone machinery members, DnaJB1(Takeuchi, Kobayashi, Yoshihara, et al. 2002) and HSPA4 (Urushitani et al. 2004); ER stress markers, PDI (Chen et al. 2012) and Derlin-1 (Homma et al. 2013; Nishitoh et al. 2008); UPS components, RNF19A (Niwa et al. 2007), polyubiquitin-C (Basso et al. 2006) and ubiquitin-protein ligase (Miyazaki et al. 2004); mitochondrial proteins, VDAC1 (Keinan et al. 2013; Israelson et al. 2010; Tan et al. 2013) and Tomm40 (Nishitoh et al. 2008); cellular environment maintainer Rac1/Nox2 complex (Kanekura et al. 2005; Li et al. 2011); axonal transportation units kinesin/dynactin complex (Teuling et al. 2008); apoptotic proteins Bcl-2 (Pedrini et al. 2010; Pasinelli et al. 2004; Tan et al. 2013; Cova et al. 2006); autophagy related proteins, LAMP2 (Osellame & Duchen 2013) and p62 (Gal et al. 2007; Gal et al. 2009). A series of consequences could result from these $SOD1^{MT}$-mediated toxic interactions, including oxidative stress, protein aggregation, mitochondrial dysfunction, ER stress, excitotoxicity, neuroinflammation, and impaired axonal transport (Figure 1.1).

To date, several chaperones have been reported to reduce SOD1 mutant aggregation and/or increase viability in cell models. Urushitani *et al* (2004) reported that Hsc70 reduced $SOD1^{G93A}$ aggregation, and CHIP further promoted the proteasomal degradation of SOD1 by ubiquitinating Hsc70 (Urushitani et al. 2004). In 2006, Koyama *et al* reported that overexpression of Hsp70 reduced accumulation of insoluble $SOD1^{H46R}$ via UPS a cell model (Koyama et al. 2006). Yamashita (2007) discovered that expression of Hsp105 suppressed $SOD1^{G93A}$ inclusion formation in cultured cells (Yamashita et al. 2007). Crippa *et al* (2010) reported Hsp22 (HSPB8) promoted the autophagic removal of $SOD1^{G93A}$ by forming HspB8/Bag3/Hsc70/CHIP multimeric complex (Crippa et al. 2010). However, overexpression of Hsp70, Hsp27 and αB-crystallin in SOD1 transgenic mice showed little neuro-protective effects (Liu et al. 2005; Krishnan et al. 2008; Karch & Borchelt 2010). In 2013, Novoselov *et al* reported that HSJ1a (DNAJB2a) not only inhibited $SOD1^{G93A}$ inclusion formation in a cell model, but also mediated late-stage neuron-protection in $SOD1^{G93A}$ mice (Novoselov et al. 2013). Given that HSJ1 functions as a potential suppressor of misfolded or aggregated proteins and was effective at reducing the aggregation of recombinant $SOD1^{MT}$ (Chapter 3), I hypothesized that both of HSJ1 isoforms could affect SOD1 misfolding,

isoforms reduce SOD1 aggregation formation and potentially inhibited SOD1 inclusion-mediated seeding.

Therefore, in this chapter, experiments were designed to explore the potential role that HSJ1 might play in SOD1 aggregation and propagation process. Constructs expressing HSJ1 were tested first followed by the generation of cell lines with the inducible Flp-in T-Rex system, which was then combined with the SOD1 reagents described in Chapter 4 in to investigate the effects of HSJ1 expression on $SOD1^{MT}$ cells.

5.2 Results

5.2.1 Subcellular Localization and Expression of HSJ1

5.2.1.1 Non-inducible myc-HSJ1

Constructs of pCMV-tag3a containing the HSJ1 ORF cDNAs were cloned previously in the Cheetham lab (Chapple & Cheetham 2003; Westhoff et al. 2005). To examine the subcellular localization of two isoforms of HSJ1, N-terminal myc-tagged HSJ1a or HSJ1b was transiently transfected into CHO cells (Figure 5.1A). HSJ1a was expressed uniformly in the cytoplasm and nucleus; In contrast, HSJ1b appeared to decorate the ER due to prenylation at its C-terminal CAAX box as previously described (Chapple & Cheetham 2003). To verify the expression and molecular weights of recombinant HSJ1, untransfected and transfected cells were lysed, resolved by SDS-polyacrylamide gel and analysed by immuno-blotting (Figure 5.1B). The myc-HSJ1a migrated with a mobility corresponding to approximately 35kDa (myc 1.5kDa + HSJ1a 32kDa + link 1kDa = 34.5kDa), and myc-HSJ1b (myc 1.5kDa + HSJ1b 36kDa + link 1kDa = 38.5kDa) was detected between 35kDa to 55kDa, which were consistent with published results.

5.2.1.2 Inducible V5-, and eGFP-HSJ1

An HSP plasmid library on pcDNA5/FRT/TO backbone cloned by Hageman *et al* (Hageman et al. 2007), was received as a gift from Prof. HH Kampinga (Groningen). To verify the subcellular localization, N-terminal V5-tagged or eGFP-tagged HSJ1 was transiently overexpressed in CHO cells (Figure 5.2A). The subcellular localizations were consistent with the results obtained in previous section.

To examine the expression level and molecular weights of recombinant HSJ1, untransfected and transfected cells lysed, resolved by SDS-polyacrylamide gel and analysed by western blotting (Figure 5.4.B). V5-HSJ1a was detected close to 35kDa, consistent with the predicted molecular weight (V5 1.5kDa + HSJ1a 32kDa = 33.5kDa), and V5-HSJ1b migrated to a position between 35kDa and 55kDa (V5 1.5kDa + HSJ1b 36kDa = 37.5kDa). In addition, the eGFP-HSJ1a appeared at a position slightly above 55kD ladder (eGFP 27kDa + HSJ1a 32kDa = 59kDa). The mobility of eGFP-HSJ1b was detected lower than 70kDa ladder, which is consistent with our prediction (eGFP 27kDa + HSJ1b 36kDa = 63kDa).

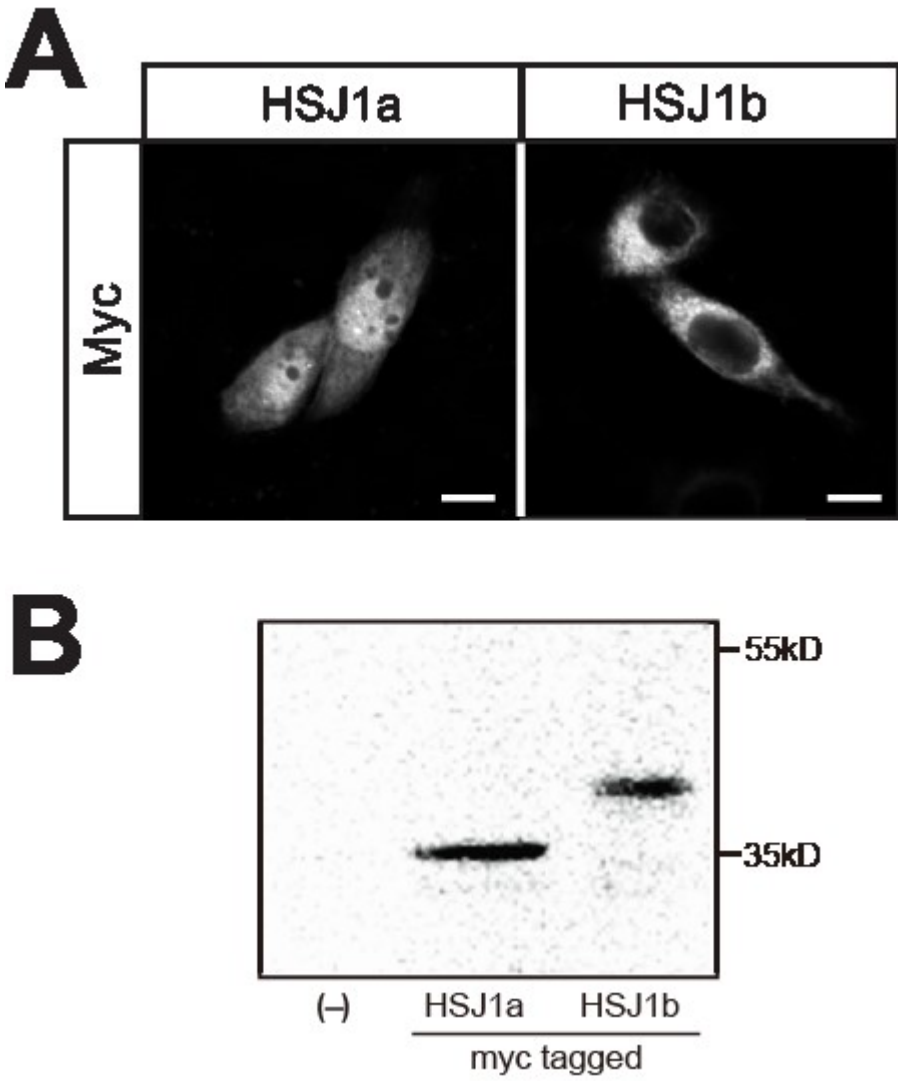

Figure 5.1 myc-HSJ1 subcellular localization and immunoblot analysis. (A) Subcellular localization of overexpressed HSJ1. 100ng myc-HSJ1 was transiently overexpressed in CHO cells as indicated. Cells were fixed, permeablised and immunostained with mouse anti-myc (1:1000) and mouse Cy3 (1:100) as described in Materials and Methods. Scale bar 10 µm. **(B)** Immunoblot of cells overexpressing HSJ1. CHO cells overexpressing myc-HSJ1 were lysed 24hrs post transfection, cell lysates were resolved by SDS-PAGE. The myc-HSJ1 was probed with mouse anti-myc (1:1000) monoclonal and goat anti-mouse HRP (1:30000), HSJ1 specific immunoreactive bands were developed with ECL, the position of MW markers are indicated on the right.

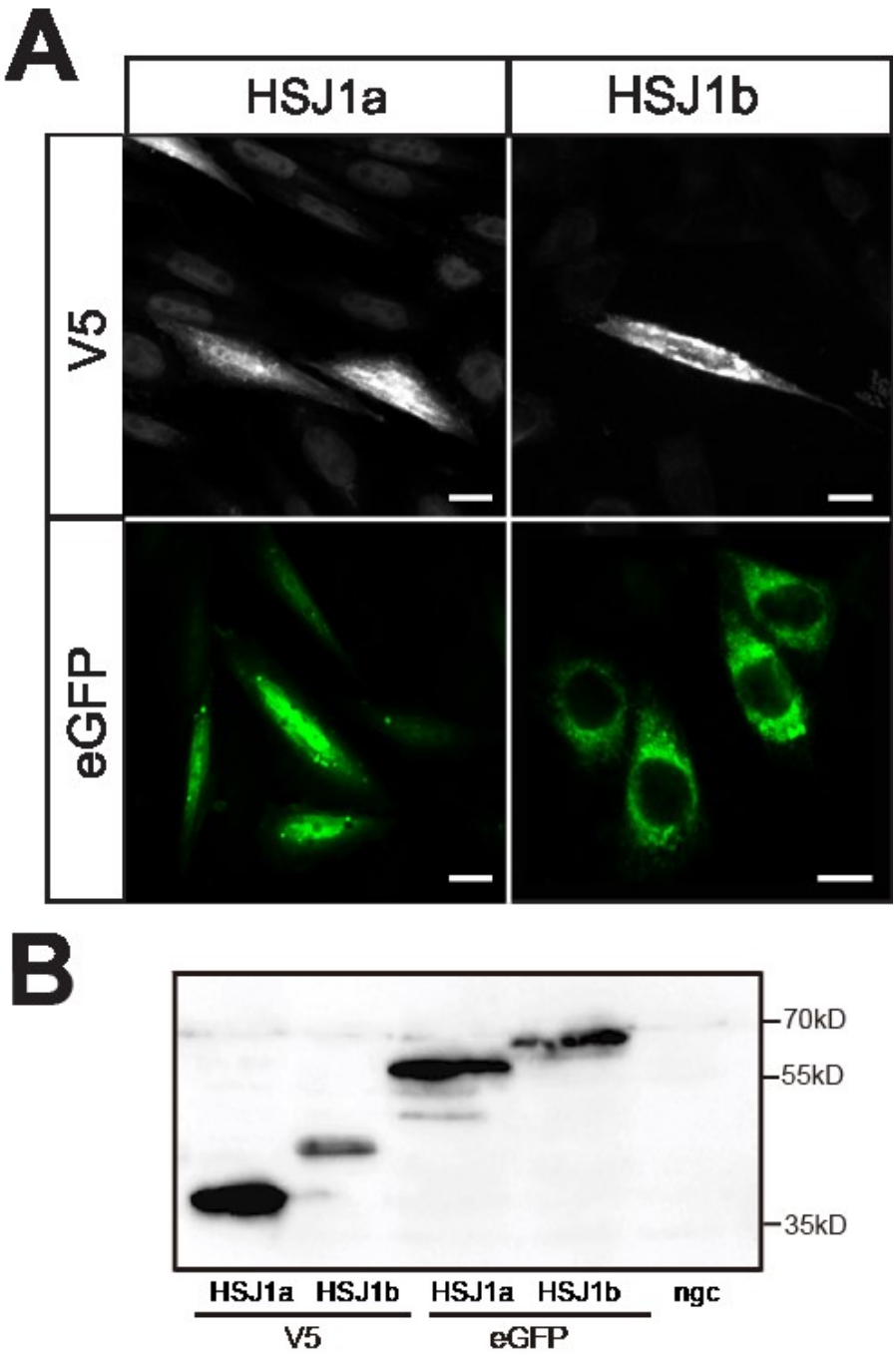

Figure 5.2 Inducible HSJ1 subcellular localization and immunoblot analysis. (A) Subcellular localization of overexpressed SOD1. 100ng V5 or eGFP-HSJ1 was transiently overexpressed in CHO cells respectively as indicated. Cells were fixed, permeablised and immunostained with mouse anti-V5 (1:100) and mouse Cy3 (1:100) as described in Material and Methods. Scale bar 10 μm. **(B)** Immunoblot of cells overexpressing HSJ1. CHO cells overexpressing inducible HSJ1 were lysed 24hrs post transfection, cell lysate were resolved by SDS-PAGE. HSJ1 was probed with sheep anti-HSJ1 (1:1000) polyclonal and goat anti-sheep HRP (1:20000), HSJ1 specific immunoreactive bands were developed with ECL, the position of MW markers are indicated on the right.

.

5.2.2 Effect of HSJ1 on SOD1 inclusion formation in transient-transfection

Novoselov *et al* (2013) reported that that HSJ1a reduced $SOD1^{G93A}$ aggregation by enhancing the ubiquitylation of SOD1, thus promoting degradation via UPS in a cell model. To examine if HSJ1a and HSJ1b both inhibit SOD1 inclusion formation, and/or co-localized with inclusions, eGFP-SOD1 was transiently overexpressed with V5-tagged HSJ1a (Figure 5.3) or HSJ1b in CHO cells (Figure 5.4). HSJ1a was expressed evenly in the cytoplasm and nucleus when co-expressed with $SOD1^{WT}$. In contrast, HSJ1a was excluded from nuclei, and co-localized with $SOD1^{MT}$ inclusions when co-expressed with either $SOD1^{G93A}$ or $SOD1^{G85R}$. HSJ1b was different to HSJ1a, and had a mainly ER localization in the co-expression with non-aggregated $SOD1^{G93A}$ and $SOD1^{G85R}$. However, HSJ1b exhibited a partial overlapping staining pattern with inclusions in the presence of aggregated $SOD1^{MT}$.

No significant reduction of $SOD1^{WT}$ inclusion incidence was observed following HSJ1 expression. Whereas, inclusion incidence of $SOD1^{G93A}$ was significantly reduced with HSJ1a (11.47%, compared to 25.00%, ***$p<0.005$) or HSJ1b (10.85%, compared to 25.00%, ***$p<0.005$) expression. Similarly, $SOD1^{G85R}$ was shown to form fewer inclusions in the co-expression with either HSJ1a (10.85% compared to 25.17%, ***$p<0.005$) or HSJ1b (10.31% compared to 25.17%, ***$p<0.005$), suggesting both HSJ1 isoforms possess the ability to prevent misfolded SOD1 from aggregation.

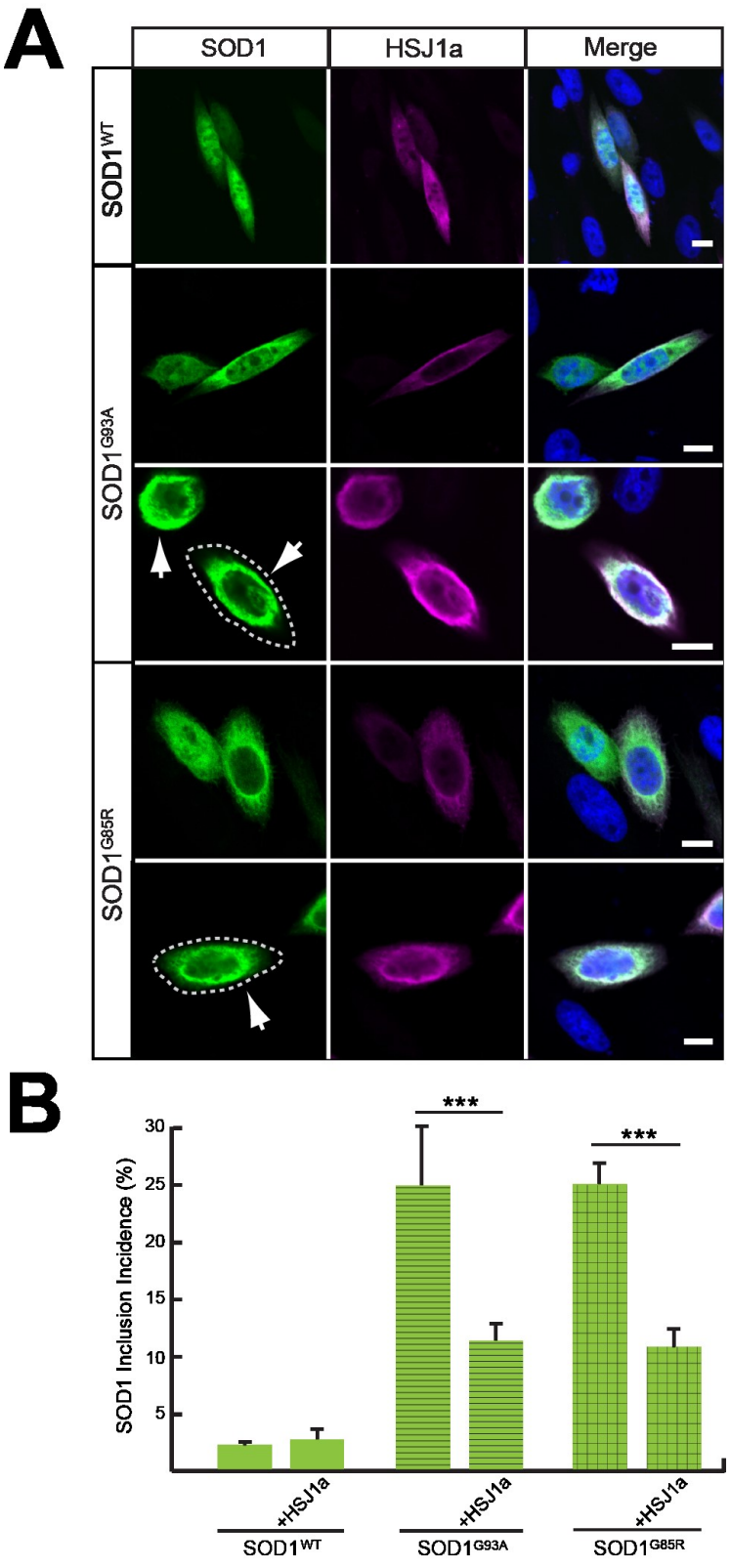

Figure 5.3 HSJ1a reduces SOD1 inclusion incidence in transient transfection. (A) Co-expression of SOD1 and HSJ1a. 100ng pcDNA5/FRT/TO-V5-HSJ1a and 100ng pcDNA5/FRT/TO-eGFP-SOD1 were transiently overexpressed in CHO cells as indicated. Cells were fixed, permeablised and immunostained with mouse anti-V5 (1:1000) and mouse Cy3 (1:100) as described in Materials and Methods. Scale bar 10 µm. **(B)** Quantification of mean SOD1 inclusion incidence. To assess the inclusion incidence of eGFP-SOD1 (green), approximately 4 groups of over 100 transfected cells were scored. Student t-test (Error bar: ±SD; ***p<0.005; n=4).

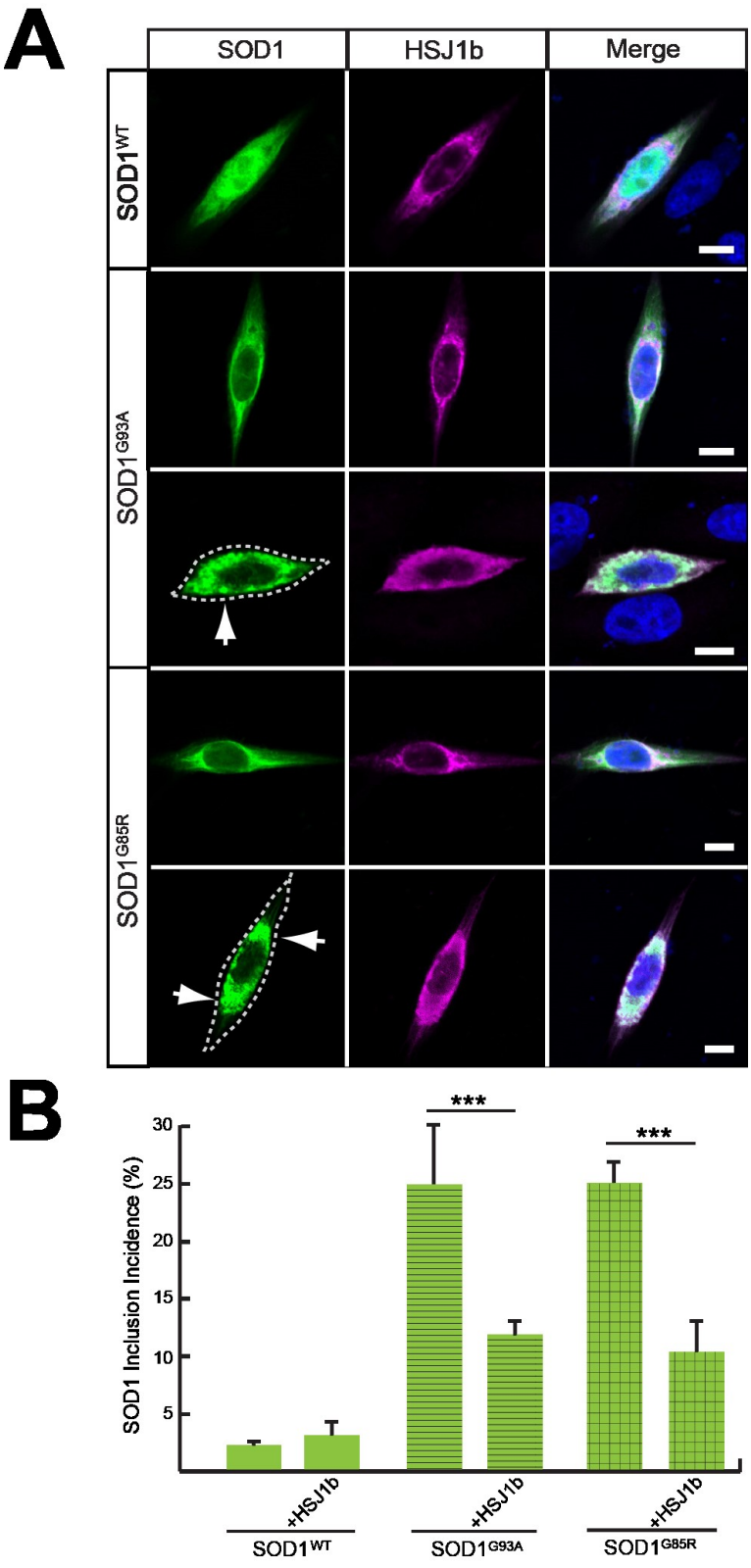

Figure 5.4 HSJ1b reduces SOD1 inclusion incidence in transient transfection. (A) Co-expression of SOD1 and HSJ1b. 100ng pcDNA5/FRT/TO-V5-HSJ1b and 100ng pcDNA5/FRT/TO-eGFP-SOD1 were transiently overexpressed in CHO cells as indicated. Cells were fixed, permeablised and immunostained with mouse anti-V5 (1:1000) and mouse Cy3 (1:100) as described in Materials and Methods. Scale bar 10 µm. **(B)** Quantification of mean SOD1 inclusion incidence. To assess the inclusion incidence of eGFP-SOD1 (green), approximately 4 groups of over 100 transfected cells were scored. Student t-test (Error bar: ±SD; ***p<0.005; n=4).

5.2.3 Co-immunoprecipitation of HSJ1 and SOD1

Novoselov *et al* (2013) showed that HSJ1a could interact with SOD1 (WT and G93A) using immunoprecipitation. HSJ1a^{WT} preferentially bound to SOD1^{G93A} rather than SOD1^{WT}. Additionally, HSJ1a^{H31Q} and HSJ1a$^{\Delta UIM}$ retained the ability to bind SOD1^{G93A}. Given the neuro-protective nature of HSJ1, it was important to test if both HSJ1a^{WT} and HSJ1b^{WT} interact with SOD1^{WT}, SOD1^{G93A} and SOD1^{G85R}. Therefore, eGFP-HSJ1 and V5-SOD1 were co-transfected into cells, and then the cell lysates were immunopufiried with a V5, eGFP or IgG control antibody. As shown in Figure 5.5, a small portion of eGFP-HSJ1a and eGFP-HSJ1b were detected in the SOD100 purifications, and V5-SOD1^{WT}, SOD1^{G93A} and SOD1^{G85R} were also detected in the reciprocal eGFP purifications, suggesting both isoforms of HSJ1 can form a complex with SOD1. In addition, eGFP-HSJ1 or V5-SOD1 was not enriched with a control IgG, which confirmed the specificity of HSJ1-SOD1 interaction. It is worth noting that compared to SOD1^{WT}, both HSJ1a and HSJ1b were enriched for the SOD1 mutants in SOD100 purifications, indicating HSJ1 binds preferentially to the misfolded SOD1.

5.2.4 Effects of HSJ1 on the conformation of SOD1^{MT}

Given that HSJ1 appears to interact with SOD1 and HSJ1 possesses the ability to reduce SOD1 aggregation, I hypothesized HSJ1 would be able to assist folding of SOD1 mutants and help to correct the conformation of misfolded SOD1, thus inhibiting the inclusion formation. To examine this hypothesis, a specific SOD1 exposed dimer interface (SEDI) antibody was used (epitope shown in Figure 1.3), which selectively recognizes monomer-misfolded SOD1, as the dimer interface containing SEDI epitope is abnormally exposed in the presence of mutations (Liu et al. 2012). Therefore, eGFP-SOD1^{MT} was co-transfected into cells with eGFP, eGFP-HSJ1a or eGFP-HSJ1b. Cell lysates were subsequently immunoprecipitated with SEDI antibody.

As shown in Figure 5.6, SEDI recognized SOD1 with/without HSJ1 co-expression indiscriminately when used for immunoblotting in the input as proteins were denatured in SDS-PAGE. In contrast, SOD1^{G93A} and SOD1^{G85R} were specially enriched in SEDI purifications. Interestingly, SEDI antibody failed to recognize SOD1 mutants when they were co-expressed with either HSJ1a or HSJ1b. In this case, there were two possibilities: a) HSJ1a and HSJ1b promoted the conformational changes of SOD1^{MT}, assist folding of nascent SOD1^{MT}, thus making them more wild-type like. Or b) with co-expression of HSJ1a or HSJ1b, the SEDI epitope was buried inside the protein or by a protein complex, which made it unrecognizable for SEDI antibody in the immunoprecipitation. So far, HSJ1 is a promising candidate to inhibit aggregation formation in the SOD1 cell model.

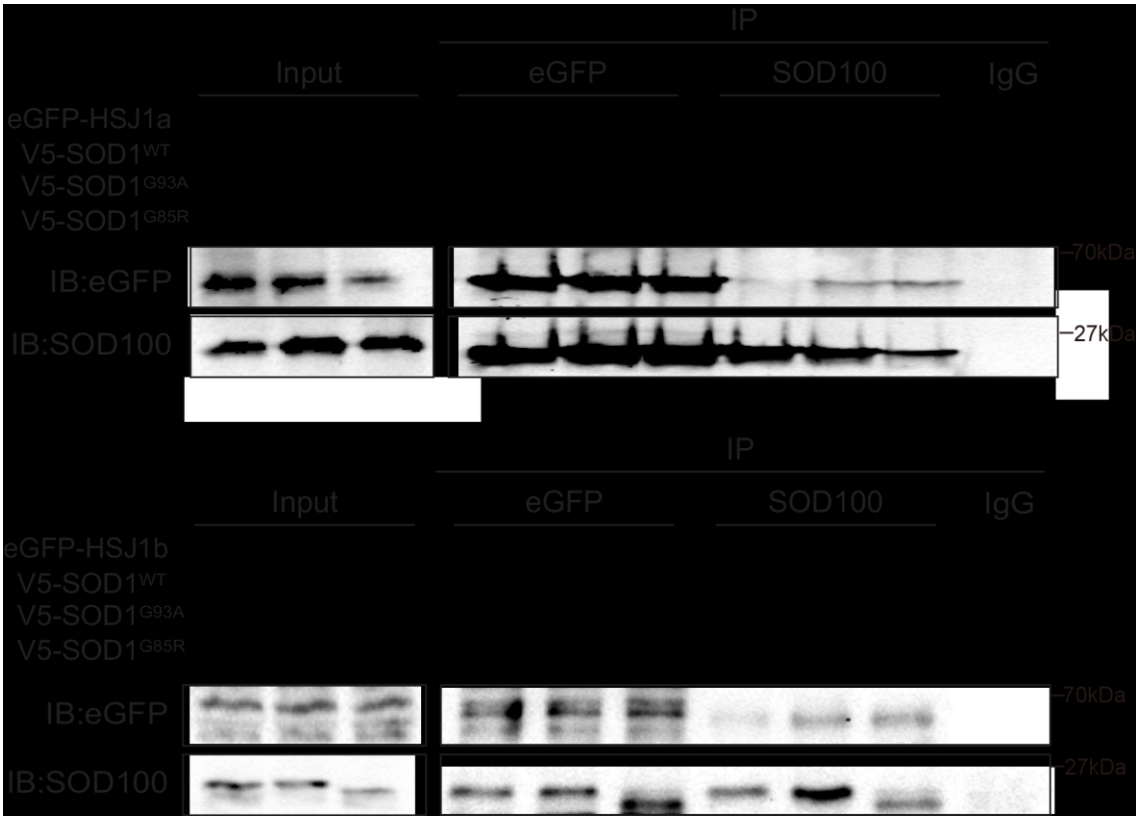

Figure 5.5 HSJ1 co-immunoprecipitates with SOD1. HEK293 cells were transfected with 1ug of pcDNA5/FRT/TO/V5-SOD1 and 1ug of pcDNA5/FRT/TO-eGFP-HSJ1. 24 hours post transfection, cell lysates were incubated with rabbit anti-SOD100 (1:100) as or rabbit anti-GFP (1:50) at 4℃ overnight, then co-incubated with protein G dynabeads for 3hrs at 4℃. Then purified immuno-complexes were resolved by SDS-PAGE and probed with mouse monoclonal anti-GFP (1:1000), mouse monoclonal anti-V5 (1:1000) and goat anti-mouse HRP (1:20000), HSJ1 or SOD1 specific immunoreactive bands were developed with ECL, the position of MW markers are indicated on the right (n=5).

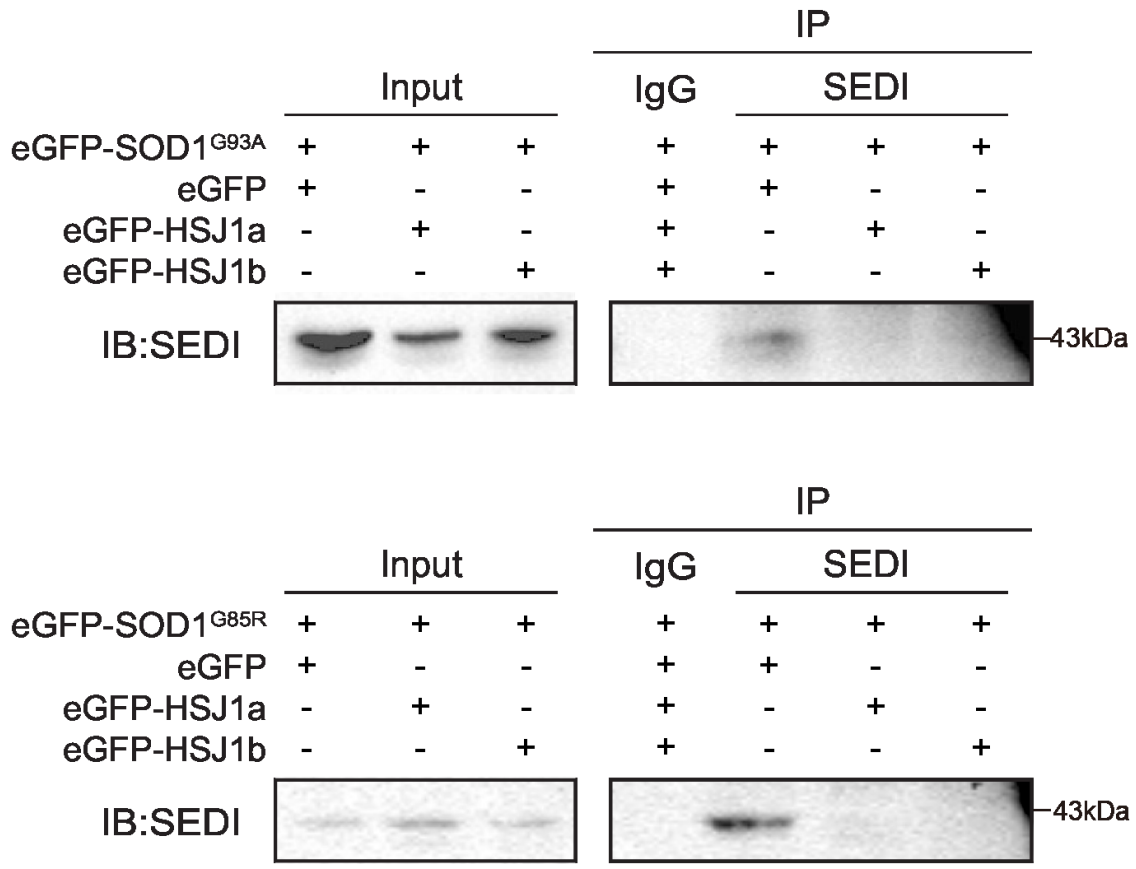

Figure 5.6 HSJ1 promotes the conformational change of SOD1^{MT}. HEK293 cells were transfected with 1ug pcDNA5/FRT/TO-eGFP-SOD1 mutant (G93A or G85R) and 1ug pcDNA5/FRT/TO-eGFP, pcDNA5/FRT/TO-eGFP-HSJ1a or pcDNA5/FRT/TO-eGFP-HSJ1b. 24 hours post transfection, cell lysates were incubated with affinity purified rabbit anti-SEDI (1:200) at 4℃ overnight, then co-incubated with protein G Dynabeads for 3hrs at 4℃. The purified immuno-complexes were resolved by SDS-PAGE and probed with rabbit anti-SEDI (1:500) and goat anti-rabbit HRP (1:20000), SOD1 specific immunoreactive bands were developed with ECL, the position of MW markers are indicated on the right (n=5).

5.2.5 Effects of HSJ1 on recruitment effects of SOD1 inclusions

As shown in section 4.2.2, co-expression of $SOD1^{MT}$ and $SOD1^{WT}$ in cells induced $SOD1^{WT}$ to re-localize and form inclusions containing both WT and MT. To test if HSJ1 could inhibit the recruitment effects of $SOD1^{MT}$ inclusions, V5-HSJ1a or V5 HSJ1b was transiently overexpressed with eGFP-SOD1 (WT, G93A and G85R) and mCherry-$SOD1^{WT}$. Co-expression of V5-HSJ1, eGFP-$SOD1^{WT}$ and mCherry-$SOD1^{WT}$ was used as negative control in this assay. Compared to Figure 5.4, subcellular localization of either HSJ1a (Figure 5.6) or HSJ1b (Figure 5.7) remained the same. HSJ1a was evenly distributed within the cells, and HSJ1b exhibited an ER-staining pattern. In addition, HSJ1 showed no influence on inclusion incidence of either eGFP-$SOD1^{WT}$ or mCherry-$SOD1^{WT}$.

In contrast, in the presence of eGFP-$SOD1^{MT}$ inclusions, the subcellular localization of either V5-HSJ1 or mCherry-$SOD1^{WT}$ was altered. The mCherry-$SOD1^{WT}$ was excluded from nuclei, exhibited a cytoplasmic expression and partially co-localized with the inclusions. Similarly, V5-HSJ1 was shown to co-localize with the inclusions as well. The inclusion incidence of either eGFP-$SOD1^{MT}$ or mCherry-$SOD1^{WT}$ was reduced with HSJ1a co-expression (11.94% compared to 25.84% for eGFP-$SOD1^{G93A}$ ***$p<0.005$, 6.98% compared to 10.22% for mCherry-$SOD1^{WT}$; 10.92% compared to 25.84% for eGFP-$SOD1^{G85R}$ ***$p<0.005$, 7.36% compared to 10.04% for mCherry-$SOD1^{WT}$). Similar reductions in inclusion incidence for eGFP-$SOD1^{MT}$/mCherry-$SOD1^{WT}$ was also observed for the co-expression with HSJ1b (11.73% compared to 25.84% for eGFP-$SOD1^{G93A}$ ***$p<0.005$, 7.36% compared to 10.22% for mCherry-$SOD1^{WT}$; 10.97% compared to 25.84% for eGFP-$SOD1^{G85R}$ ***$p<0.005$, 8.02% compared to 10.04% for mCherry-$SOD1^{WT}$). Interestingly, in this triple-expression assay, HSJ1 seems to more effectively reduce SOD1 inclusion formation. The reduction of inclusion incidence observed in the mCherry-$SOD1^{WT}$ was not significant, however, this might be because the overall level of inclusion incidence was low and the difference is too small for the variability of the assay.

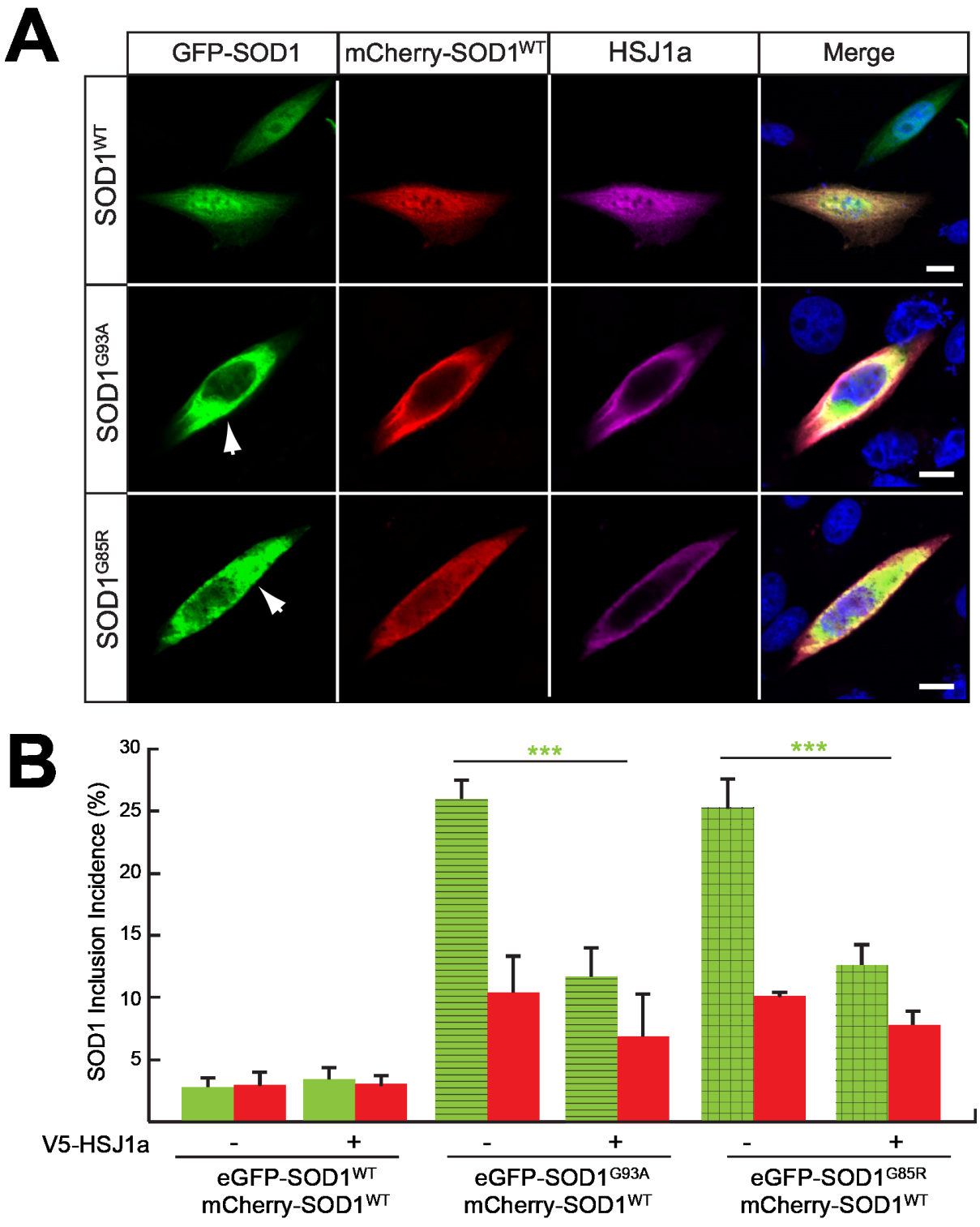

Figure 5.7 HSJ1a reduces the recruitment effects of SOD1^{MT} inclusions in transiently-transfection. (A) Cells transiently overexpressed 100ng pcDNA5eGFP-SOD1 (WT, G93A and G85R), 25ng pcDNA5/FRT/TO-mCherry-SOD1^{WT} and 100ng pcDNA5/FRT/TO-V5 HSJ1a, pcDNA5/FRT/TO was applied as stuffer plasmid. Cells were fixed, permeablised and immunostained with mouse anti-V5 (1:100) and mouse Cy5 (1:100) as described in Material and Methods. Arrows highlight the presence of inclusions. Scale bar 10 µm. **(B)** Quantification of mean SOD1 inclusion incidence. To assess the inclusion incidence of eGFP-SOD1 (green) and mCherry-SOD1 (red), approximately 4 groups of over 100 transfected cells were scored. Statistical analysis were performed referred to Material and Methods (Error bar: ±SD; ***p<0.005; n=4)

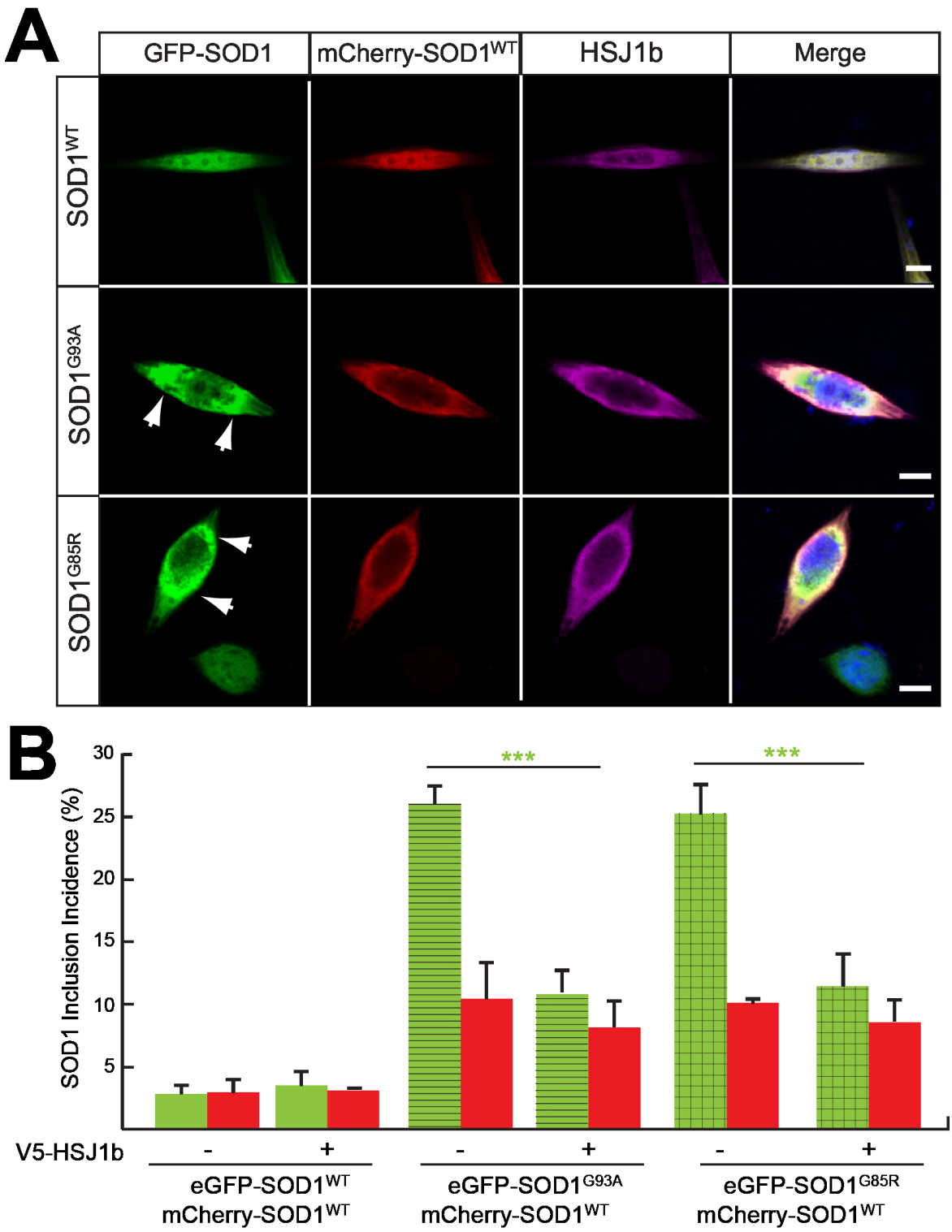

Figure 5.8 HSJ1b reduces the recruitment effects of SOD1^{MT} inclusions in transiently-transfection. (A) Cells transiently overexpressed 100ng pcDNA5eGFP-SOD1 (WT, G93A and G85R), 25ng pcDNA5/FRT/TO-mCherry-SOD1^{WT} and 100ng pcDNA5/FRT/TO-V5 HSJ1b, pcDNA5/FRT/TO was applied as stuffer plasmid. Cells were fixed permeablised and immunostained with mouse anti-V5 (1:100) and mouse Cy5 (1:100) as described in Material and Methods. Arrows highlight the presence of inclusions. Scale bar 10 µm. **(B)** Quantification of mean SOD1 inclusion incidence. To assess the inclusion incidence of eGFP-SOD1 (green) and mCherry-SOD1 (red), approximately 4 groups of over 100 transfected cells were scored. Statistical analysis were performed referred to Material and Methods (Error bar: ±SD; ***p<0.005; n=4).

5.2.6 Characterization of HSJ1 stable cell lines

5.2.6.1 Inducible HSJ1 cell lines

5.2.6.1.1 Generation of Flp-in T-Rex cell lines

The generation strategy for the Flp-in host cell line was identical with the protocol described in section 4.2.4.2.2.

5.2.6.1.2 Characterization of Flp-in T-Rex HSJ1 cell lines

5.2.6.1.2.1 Regulation of Flp-in T-Rex HSJ1 cell lines

Plasmid pcDNA5/FRT/TO/HSJ1 and pOG44 were co-transfected into Flp-in host cells to generate inducible V5 or eGFP-HSJ1 cell lines. Colonies generated from Hyg/Bsd selection were examined to explore if the expression of HSJ1 could be induced by Tet, and if the transcription of HSJ1 could be stopped once the Tet is removed from culture system. To examine if Flp-in T-Rex HSJ1 cell lines could be turned on, cells were induced by Tet at different concentration compared to an un-induced negative control, then cell lysates were resolved by SDS-polyacrylamide gel, and analysed by immunoblotting (Figure 5.9A). Taking GAPDH as an internal control, the expression levels of HSJ1a and HSJ1b were quantified under different concentrations of Tet. Based on immunoblot results, the expression level of HSJ1 was Tet concentration-dependent as well, and reached saturation at 2ug/ml. To examine if the Flp-in T-Rex HSJ1 cell lines could be turned off, cells were induced by Tet and compared to an un-induced negative control, then inducers were removed from the culture medium and then RNA was extracted (Figure 5.9B). Human HSJ1 was amplified using specific primers (Appendix 5.1). The positive induced sample showed a strong band at the expected size of 140bp for HSJ1a and at the size of 280bp for HSJ1b, no other bands were detected. The un-induced negative control also showed a faint band, suggesting some leaky expression. After cells were re-cultured in no-inducer medium 24-post Tet induction (p24), there was also a faint band presented in the PCR product at the expected size of 140bp for HSJ1a, and 280bp for HSJ1b. In conclusion, these data suggest HSJ1 expression could be turned on by Tet, and the transcription of HSJ1 could be mostly turned off 24h after removal of Tet.

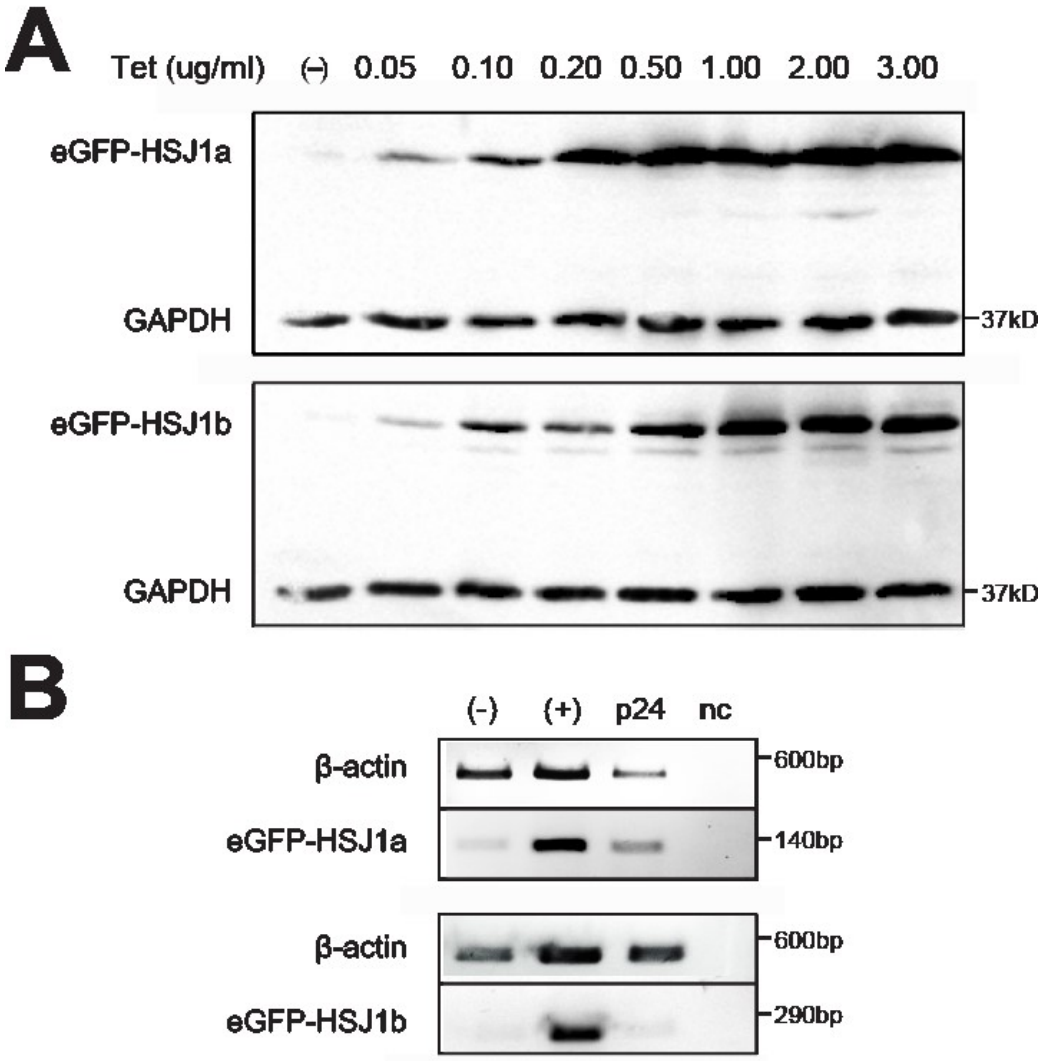

Figure 5.9 Inducible Flp-in T-Rex HSJ1 cell lines. (A) Immunoblot of HSJ1 that was induced by Tet at different concentrations. Cells were induced by Tet at 0.05, 0.1, 0.2, 0.5,1,2 or 3 ug/ml respectively for 48hrs. Cell lysate were resolved on SDS-PAGE. The eGFP-HSJ1 and GAPDH were probed with mouse anti-GFP (1:2000) monoclonal, anti-GAPDH (1:10000) and goat anti-mouse HRP (1:20000). eGFP or GAPDH specific immunoreactive bands was developed with ECL, MW markers are labelled on the right of panels. **(B)** Expression of HSJ1 was turned off by removal of Tet. Cells were cultured in Tet-free completed medium for 24hrs post Tet induction (p24). Total RNA of samples, uninduced (-) and induced (+) was extracted and converted into cDNA as described in Material and Methods. RT-PCR was performed using HSJ1 specific primers. Housekeeping gene β-actin was used as an internal reference. PCR products were resolved by 2.5% agarose gel to detect the presence of HSJ1a bands at 140bp or HSJ1b bands at 280bp, and the presence of β-actin at 560bp.

5.2.6.1.2.2 Subcellular localization of HSJ1 in inducible mammalian expression system

To compare with the cells transiently overexpressed HSJ1, Flp-in T-Rex eGFP-HSJ1 cell lines were induced by Tet for 24hrs, analysed and quantified (Figure 5.10A, upper panel). Similar to the transient transfection, eGFP-HSJ1a was evenly localised throughout the cell, and eGFP-HSJ1b showed classic ER staining.

5.2.6.1.2.3 HSJ1 inclusions form after long time induction or with sodium butyrate treatment

As discussed above, expression level of GOI in Flp-in T-Rex system took 48h to reach saturated expression under Tet induction, which can be boosted by sodium butyrate. Interestingly, dot-inclusions were observed 48hrs post Tet induction or 24hrs post Tet/sodium butyrate treatment. To explore the potential inclusion incidence, Flp-in T-Rex eGFP-HSJ1 cell lines were induced by Tet for 24hrs with or without sodium butyrate treatment, then analyzed and quantified (Figure 5.10B). In contrast to eGFP-SOD1 expressed by Flp-in T-Rex system, eGFP-HSJ1 cell lines showed a basal inclusion incidence at 10% 24hrs post Tet induction. Once boosted with SB, the expression level as well as the inclusion incidence were significantly increased (9.6% compared to 41.9% for HSJ1a, and 10.3% compared to 41.4% for HSJ1b). It is likely that HSJ1 formed inclusions in the Flp-in T-Rex system due to high expression level.

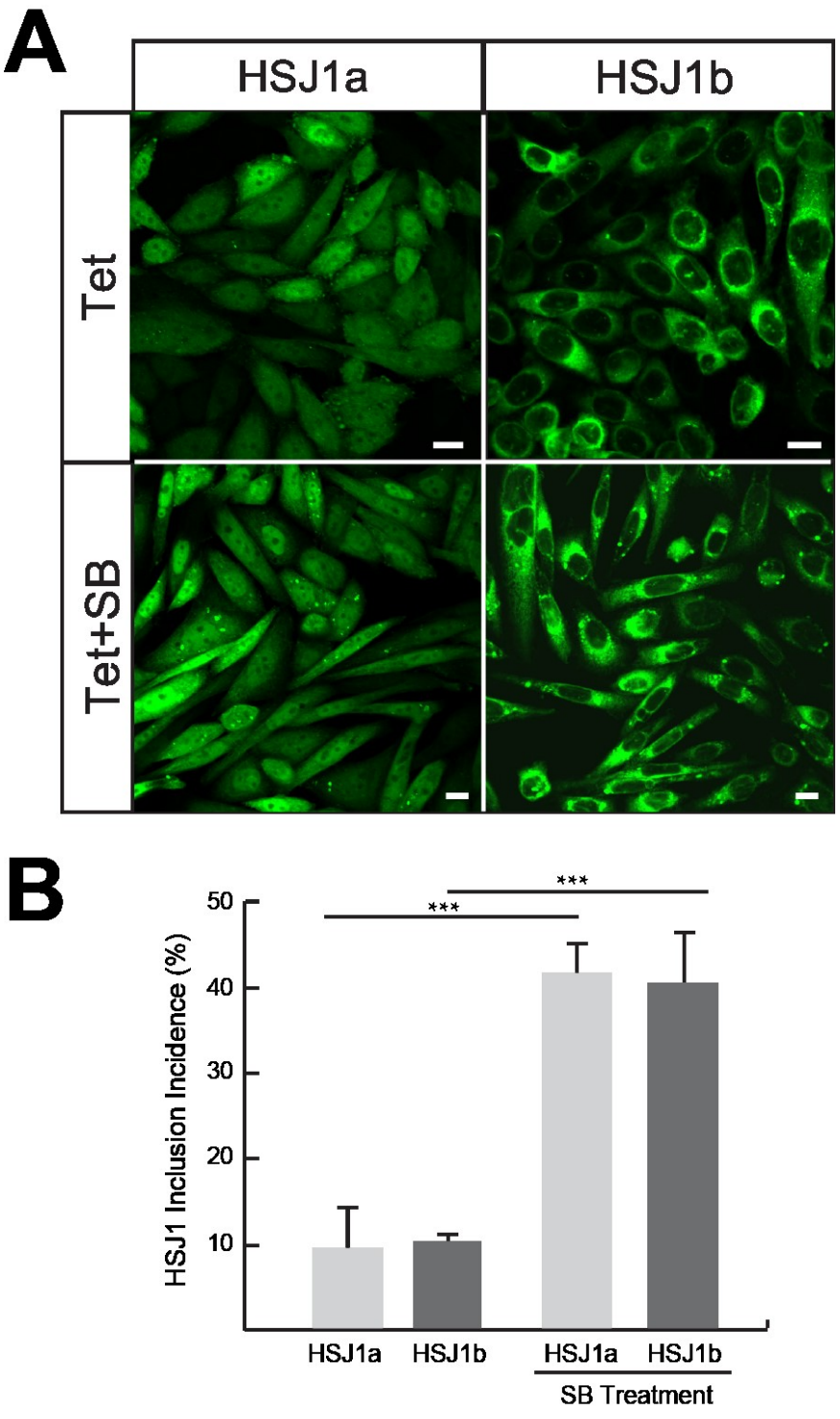

Figure 5.10 Analysis of inducible cell lines that expressing SOD1. (A) Subcellular localization of eGFP-HSJ1 in Flp-in T-Rex system. Cell line expressing eGFP-HSJ1a or HSJ1b as indicated. Cells were induced by Tet (3ug/ml) with/without sodium butyrate (2mM) for 24hrs, then fixed and visualised as described in Material and Methods. Scale bar 10 μm. **(B)** Quantification of mean HSJ1 inclusion incidence in Flp-in T-Rex system. To assess the inclusion incidence of GFP-HSJ1, approximately 4 groups of over 100 cells were scored. Student t-test (Error bar: ±SD; ***p<0.005; n=4).

5.2.7 Effect of inducible HSJ1 expression on SOD1 inclusion formation

Since the inducible Flp-in T-Rex system had been generated, I was able to manipulate the expression of HSJ1 before or after the presence of SOD1 inclusions, providing the opportunity to explore the role of HSJ1 in SOD1-mediated ALS aggregation progression. Therefore, in this and the next section, non-inducible GFP-SOD1 was used to produce ectopic SOD1 outside the control of TetR.

5.2.7.1 Effect of pre-induced HSJ1 on SOD1 inclusion formation

To explore the effect of pre-existing HSJ1 on SOD1 inclusion formation, non-inducible GFP-SOD1 was transiently over-expressed in the pre-induced V5-HSJ1 cell lines, the expression of HSJ1 was turned off 24h before the SOD1 transfection was performed (Figure 5.11A). The inclusion incidence of $SOD1^{WT}$ remained the same compared to section 4.2.1. In contrast I observed that in the cells pre-expressing HSJ1a or HSJ1b, fewer SOD1 inclusions formed compared to the uninduced HSJ1 cell lines. $SOD1^{G93A}$ inclusion incidence was 10.37% in the uninduced cells and 6.68% in the cells expressing HSJ1a (*$p<0.05$). Similar results were also observed in the HSJ1b-expressing cell lines (6.83% in induced cells, compared to 10.19% in the uninduced cell lines, *$p<0.05$). Additionally, $SOD1^{G85R}$ also formed fewer inclusions in the presence of either HSJ1a (6.63% in induced cells, compared to 10.14% in the uninduced cell lines) or HSJ1b (6.98% in induced cells, compared to 10.09% in the uninduced cell lines. These data suggested that pre-induced HSJ1 showed modest inhibition effects on SOD1 inclusion formation.

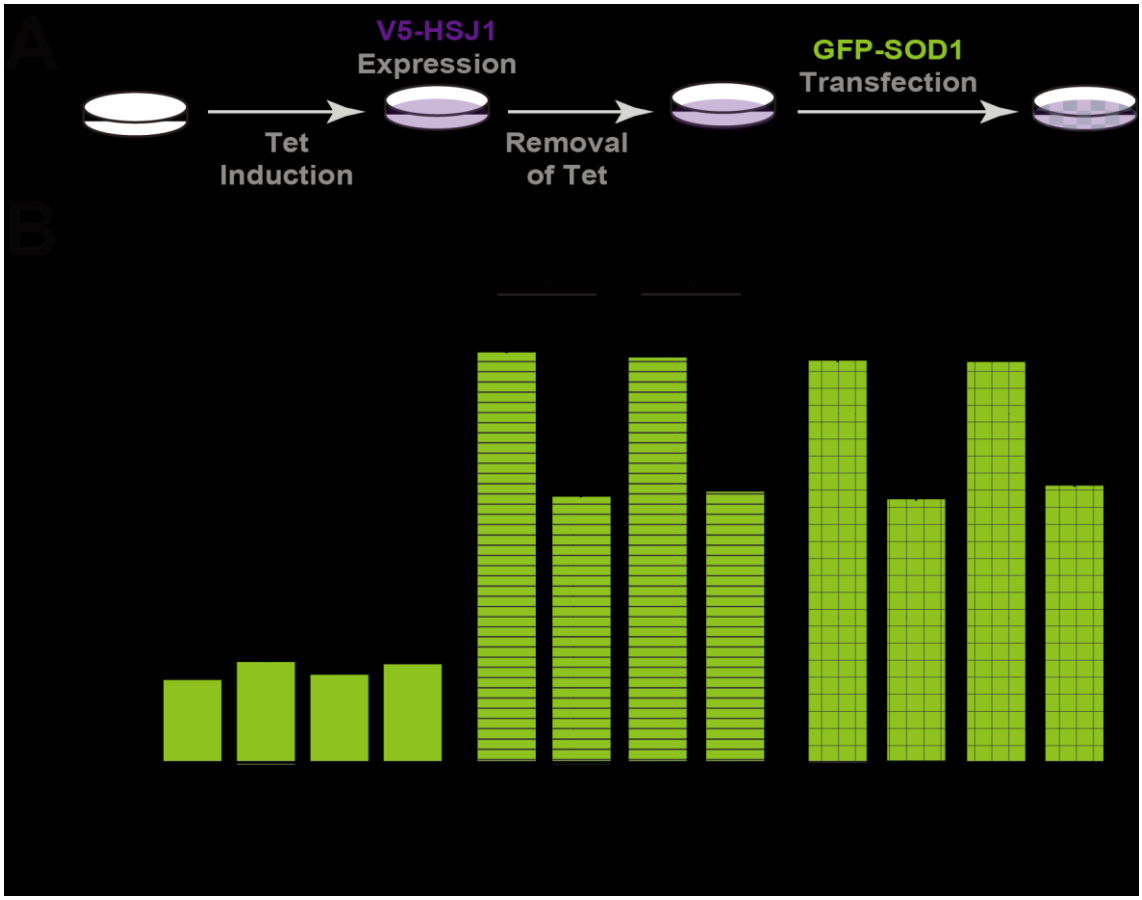

Figure 5.11 Effect of pre-induced HSJ1 on SOD1 inclusion formation. (A) Schematic illustration of SOD1 expression in pre-induced HSJ1 cell lines. **(B)** Quantification of mean SOD1 inclusion incidence. 200ng of pEGFP-SOD1 (WT, G93A and G85R) plasmids were transfected into uninduced V5-HSJ1a [unIn(A)], induced V5-HSJ1a [In(A)], uninduced V5-HSJ1b [unIn(B)] and induced V5-HSJ1b [In(B)] Flp-in T-Rex system. Cells were fixed 24hrs post transfection as described in Material and Methods. To assess the inclusion incidence of GFP-SOD1, approximately 4 groups of over 100 transfected cells were scored. Student t-test (Error bar: ±SD; *p<0.05; n=4).

5.2.7.2 Effect of HSJ1 on preformed SOD1 inclusions

To investigate if HSJ1 possess the activity to disassemble preformed SOD1 inclusions, non-inducible GFP-SOD1^{MT} was transiently overexpressed in the uninduced V5-HSJ1 cell lines. 24hrs post transfection, HSJ1 expression was induced by Tet and boosted by sodium butyrate (Figure 5.12-14).

One-way analysis of variance (ANOVA) was performed between two groups of uninduced cells and cells expressing HSJ1. The cells were transfected, treated with SB to induce HSJ1, or untreated, and fixed at the same time. The *F* value and the p value (Appendix 5.2) of ANOVA test regarding inclusion incidence SOD1 confirmed there was significant difference between uninduced and induced cells (*p<0.05). Post-hoc tests were used for multi-group comparison as indicated in Appendix 5.4 after verification of homogeneity of variance (Appendix 5.3).

In this comparison, SOD1^{WT} was taken as a negative control. As shown in Figure 5.12, inclusion incidence of SOD1^{WT} remained between 1-2% while the transfection efficiency decreased during the Tet induction, and no significant difference of SOD1 inclusion incidence was detected between uninduced and induced cells at the same time-point. Surprisingly, SOD1 inclusion incidence was significantly reduced after induction of HSJ1 expression 24hrs and 48hrs post induction. In cells transiently expressing SOD1^{G93A}, inclusion incidence of time point 0 was 30.80%. 24hrs post induction of HSJ1a, inclusion incidence of SOD1 was reduced to 15.07% compared to cells without expression of HSJ1a (34.23%, ***p<0.005). At time point 48hrs, HSJ1a further reduced the SOD1 inclusion incidence to 6.27%, showing a reducing inclusion incidence compared to that of cells transiently expressed SOD1^{G93A} (16.58%, ***p<0.005). Similar results were also observed in cells expressing HSJ1b. SOD1^{G93A} inclusion incidence was significantly reduced at 24hrs (19.57% compared to 35.09%, ***p<0.005) and 48hrs (7.28% compared to 13.19%, ***p<0.005) in comparison with control cells.

To ensure that these reductions were not due to cell death, the percentage of living cells expressing GFP-SOD1 was calculated. Compared to uninduced cells at 24hrs and 48hrs post-induction, there was a non-significant increase in transfected cells when HSJ1 was expressed. Therefore, the reduction of inclusion incidence is a result of expression of HSJ1, instead of cell death. In addition, expression of HSJ1 might increase the viability of cells expressing SOD1^{MT}, which will need further experiments to verify.

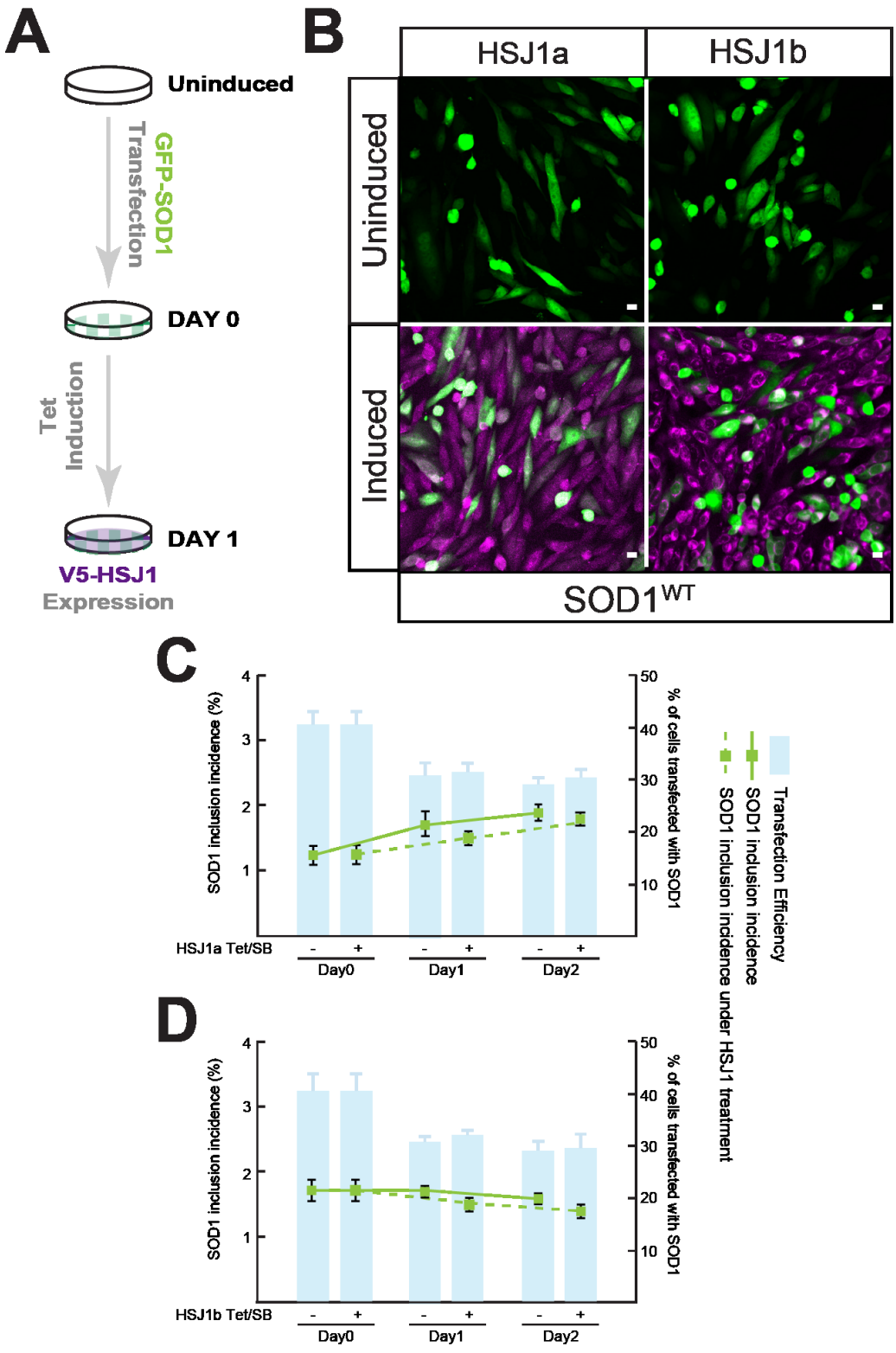

Figure 5.12 HSJ1 showed little effects on preformed SOD1^{WT} inclusion. (A) Schematic illustration of inclusion disassembly assay. **(B)** SOD1 expression in inducible V5-HSJ1 cell lines. 200ng plasmids expressing uninducible GFP-SOD1^{WT} were transfected into uninduced cell lines. Flp-in T-Rex system expressing V5-HSJ1 was turned on by 3ug/ml Tet and boosted by 2mM sodium butyrate 24hrs post-transfection. Cells were fixed, permeablised and immunostained with rabbit anti-V5 (1:1000) and rabbit Cy5 (1:1000) at 0hrs, 24hrs and 48hrs post-induction respectively as described in Material and Methods. Scale bar 10 µm. **(C)** Quantification of mean SOD1 inclusion incidence. To assess the inclusion incidence of GFP-SOD1 (green) as well as the percent of transfected cells (blue) at day 0, day 1 and day2, approximately 4 groups of over 100 transfected cells were scored. Multi-group comparisons of the means were carried out by one-way ANOVA with post-hoc contrasts by Dunett T3. Statistical significance was set at $p<0.05$. (Error bar: ±SD; n=4).

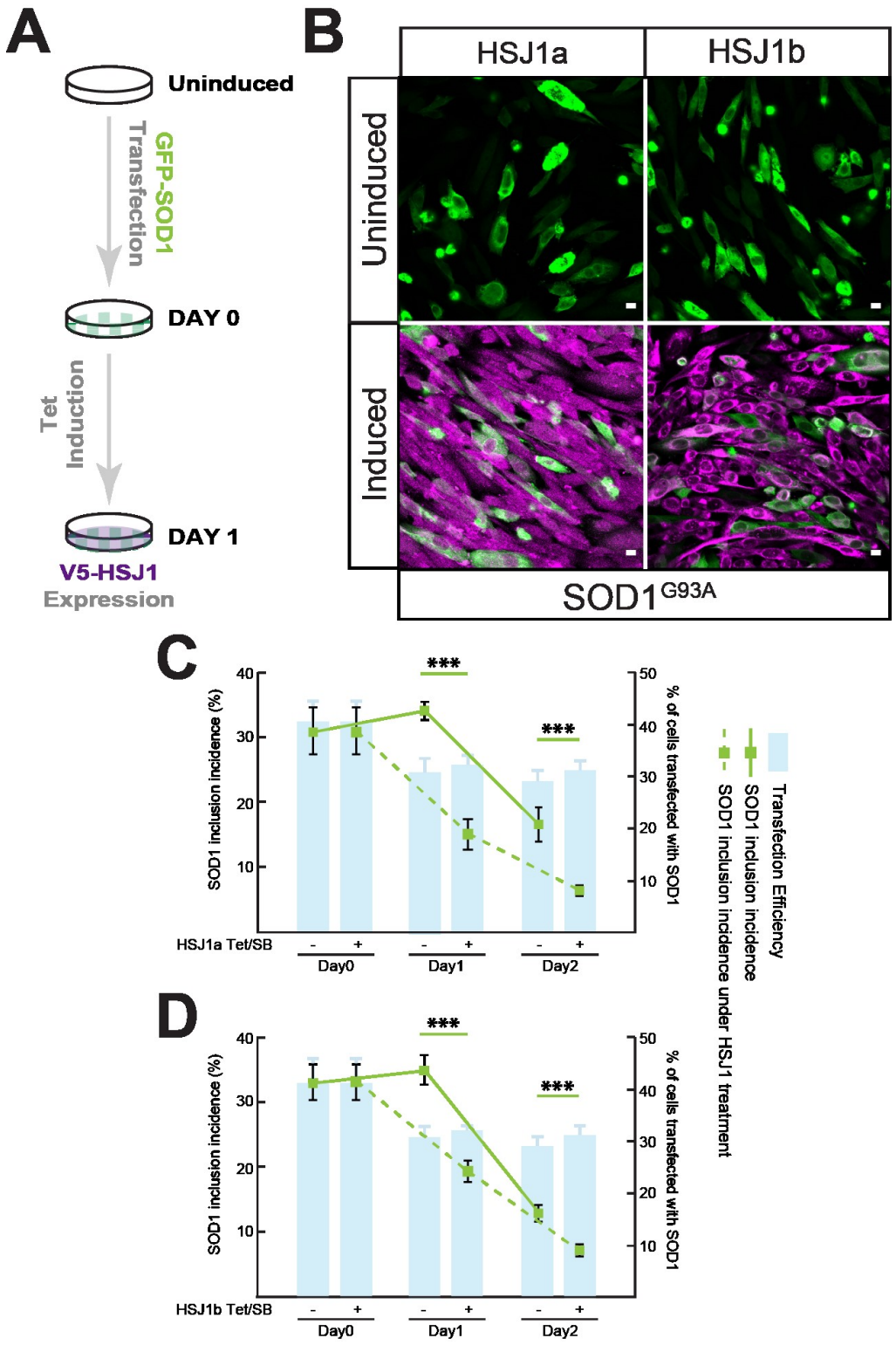

Figure 5.13 HSJ1 reduced preformed SOD1^{G93A} inclusions. (A) Schematic illustration of inclusion disassembly assay. **(B)** SOD1 expression in inducible V5-HSJ1 cell lines. 200ng plasmids expressing uninducible GFP-SOD1^{G93A} were transfected into uninduced cell lines. Flp-in T-Rex system expressing V5-HSJ1 was turned on by 3ug/ml Tet and boosted by 2mM sodium butyrate 24hrs post-transfection. Cells were fixed, permeablised and immunostained with rabbit anti-V5 (1:1000) and rabbit Cy5 (1:1000) at 0hrs, 24hrs and 48hrs post-induction respectively as described in Material and Methods. Scale bar 10 μm. **(C)** Quantification of mean SOD1 inclusion incidence. To assess the inclusion incidence of GFP-SOD1 (green) as well as the percent of transfected cells (blue) at day 0, day 1 and day2, approximately 4 groups of over 100 transfected cells were scored. Multi-group comparisons of the means were carried out by one-way ANOVA with post-hoc contrasts by Tukey HSD. Statistical significance was set at $p<0.05$. (Error bar: ±SD; ***$p<0.005$; n=4).

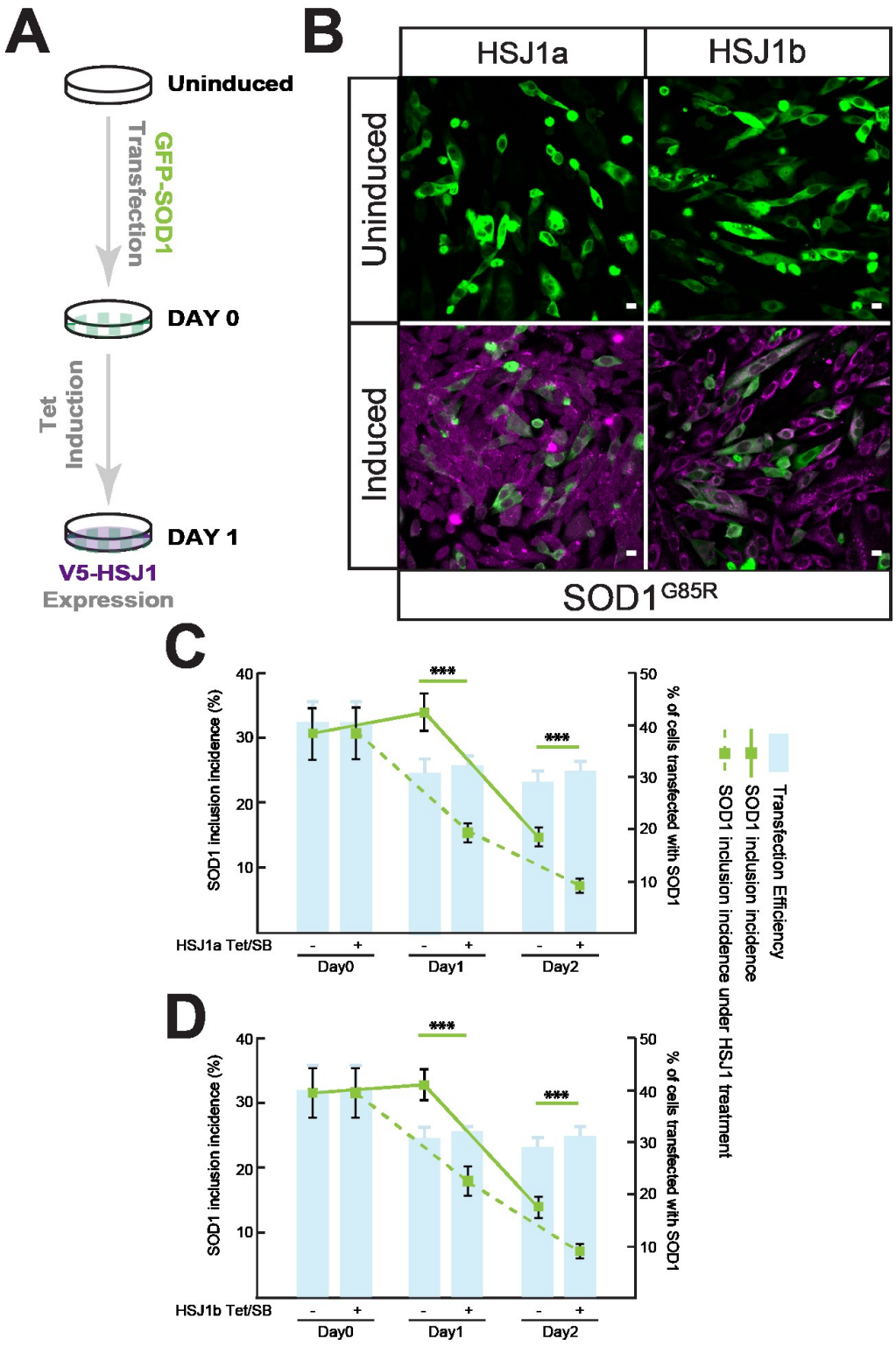

Figure 5.14 HSJ1 reduced preformed SOD1^{G85R} inclusions. (A) Schematic illustration of inclusion disassembly assay. **(B)** SOD1 expression in inducible V5-HSJ1 cell lines. 200ng plasmids expressing uninducible GFP-SOD1^{G85R} were transfected into uninduced cell lines. Flp-in T-Rex system expressing V5-HSJ1 was turned on by 3ug/ml Tet and boosted by 2mM sodium butyrate 24hrs post-transfection. Cells were fixed, permeablised and immunostained with rabbit anti-V5 (1:1000) and rabbit Cy5 (1:1000) at 0hrs, 24hrs and 48hrs post-induction respectively as described in Material and Methods. Scale bar 10 μm. **(C)** Quantification of mean SOD1 inclusion incidence. To assess the inclusion incidence of GFP-SOD1 (green) as well as the percent of transfected cells (blue) at day 0, day 1 and day2, approximately 4 groups of over 100 transfected cells were scored. Multi-group comparisons of the means were carried out by one-way ANOVA with post-hoc contrasts by Tukey HSD. Statistical significance was set at $p<0.05$. (Error bar: ±SD; ***$p<0.005$; n=4).

5.2.8 Effects of SOD1 expression on cell-stress responses

As discussed in Chapter 1 as well as brief introduction of this chapter, SOD1 mutant protein expression can lead to a variety of cellular consequences that can lead to toxic gain of function. As mutant SOD1 failed to form inclusions in the Flp-in T-Rex system, I further investigated if proteins involved in ALS-related stress pathways as well as the potential candidate proteins that $SOD1^{MT}$ can aberrantly interact with were affected by overexpression of $SOD1^{MT}$. I focused on ER stress, as well as Bcl-2 and Derlin-1 that $SOD1^{MT}$ was reported to co-aggregate with *in vivo*.

5.2.8.1 Effects of SOD1 overexpression on ER stress signal pathways

5.2.8.1.2 UPR markers were not upregulated in the presence of overexpressed SOD1

To investigate if overexpression of SOD1 induced ER stress and/or triggered the UPR, the Flp-in T-Rex system was induced by Tet to express eGFP-SOD1 in the absence of selection antibiotic, RNA was extracted from uninduced controls and induced samples. Specific primers were designed to amplify the endogenous UPR markers by RT-PCR. As shown in Figure 5.15, several UPR markers including tXBP-1, BiP, Chop, PDI, eIF2a and ATF4 were amplified and analyzed. Based on 3 replicates, I failed to detect any differences in the RNA level of these markers in the cells expressing eGFP-SOD1. Therefore, it is likely that the expression level of eGFP-$SOD1^{MT}$ was too low to trigger ER stress and UPR, or up-regulate ER chaperone expression.

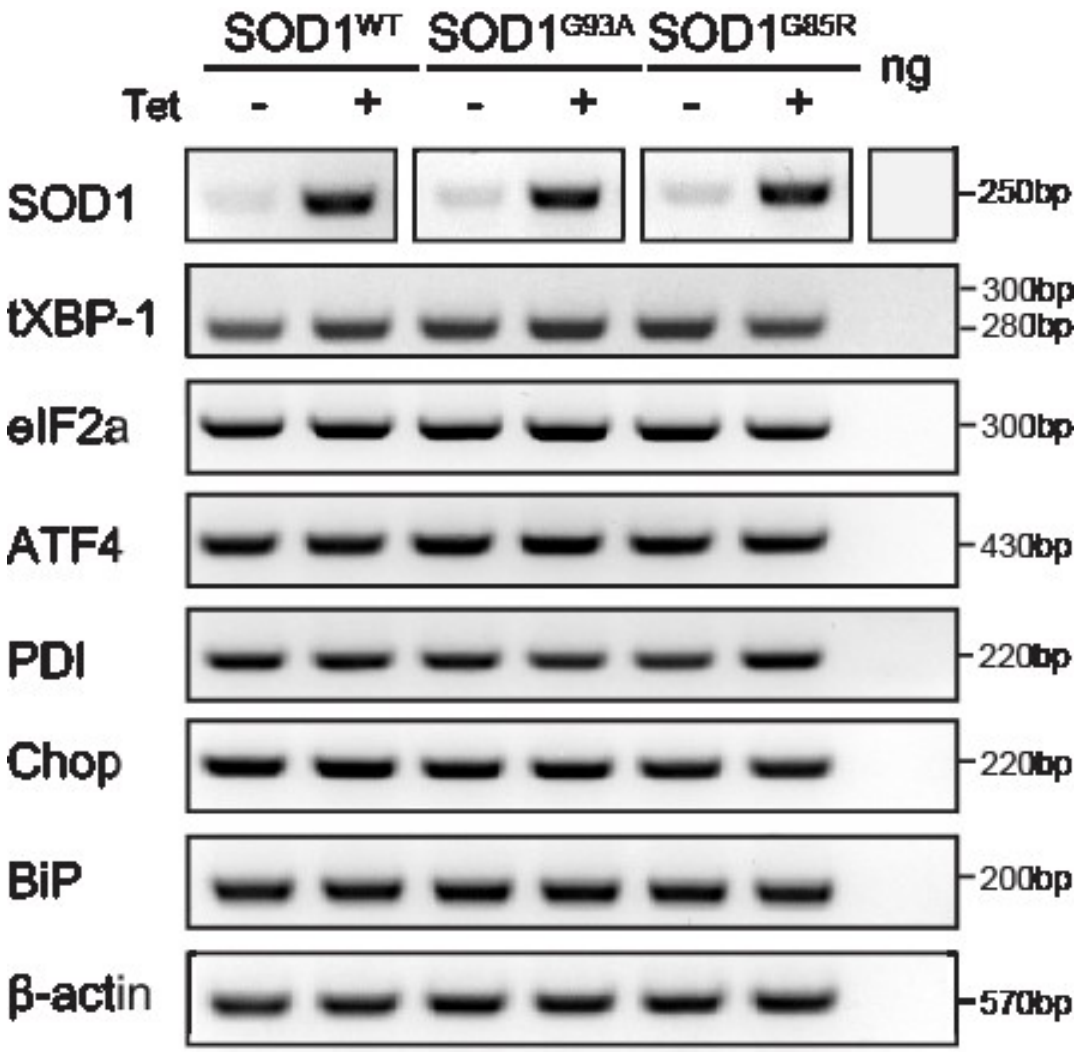

Figure 5.15 RT-PCR of UPR signalling pathways in cells overexpressing SOD1. Flp-in T-Rex system expressing SOD1 (WT, G93A, G85R) were induced by Tet in the absence of selection antibiotic for 48hrs. Total RNA of samples were extracted and converted into cDNA as described in Material and Methods. RT-PCR was performed using specific primers, which were presented in detail in the appendix. No transcriptase was used as negative control (ng), and housekeeping gene β-actin was used as an internal reference. RT-PCR products were resolved by 2.5% agarose gel to detect the presence of XBP-1(spliced at 279bp, unspliced at 305bp), BiP (206bp), Chop (222bp), ATF4 (434bp), eIF2a (297bp), SOD1 (250bp) and β-actin (570bp) (n=3).

5.2.8.1.3 Effects of SOD1 overexpression on BCL-2 and Derlin-1

In addition, to investigate if overexpression of $SOD1^{MT}$ affected the expression of potential interacting protein candidates, Flp-in T-Rex system expressing eGFP-SOD1 was induced in the absence of selection antibiotic, RNA was extracted from uninduced controls and samples. Specific primers were designed to amplify the endogenous BCL-2 and Derlin-1. As shown in Figure 5.16A, overexpression of $SOD1^{WT}$ slightly upregulated BCL-2. In contrast, the expression of BCL-2 RNA (isoform 1) was down-regulated in the presence of $SOD1^{MT}$, indicating the expression level of BCL-2 was affected when $SOD1^{MT}$ was expressed. Interestingly, overexpression of all three SOD1 proteins (WT, G93A and G85R) stimulated an upregulation of Derlin-1 at the mRNA level, although the mutants appeared to have a stronger effect. Together, these data suggested that overexpression of SOD1 altered the expression level of potential interacting protein candidates.

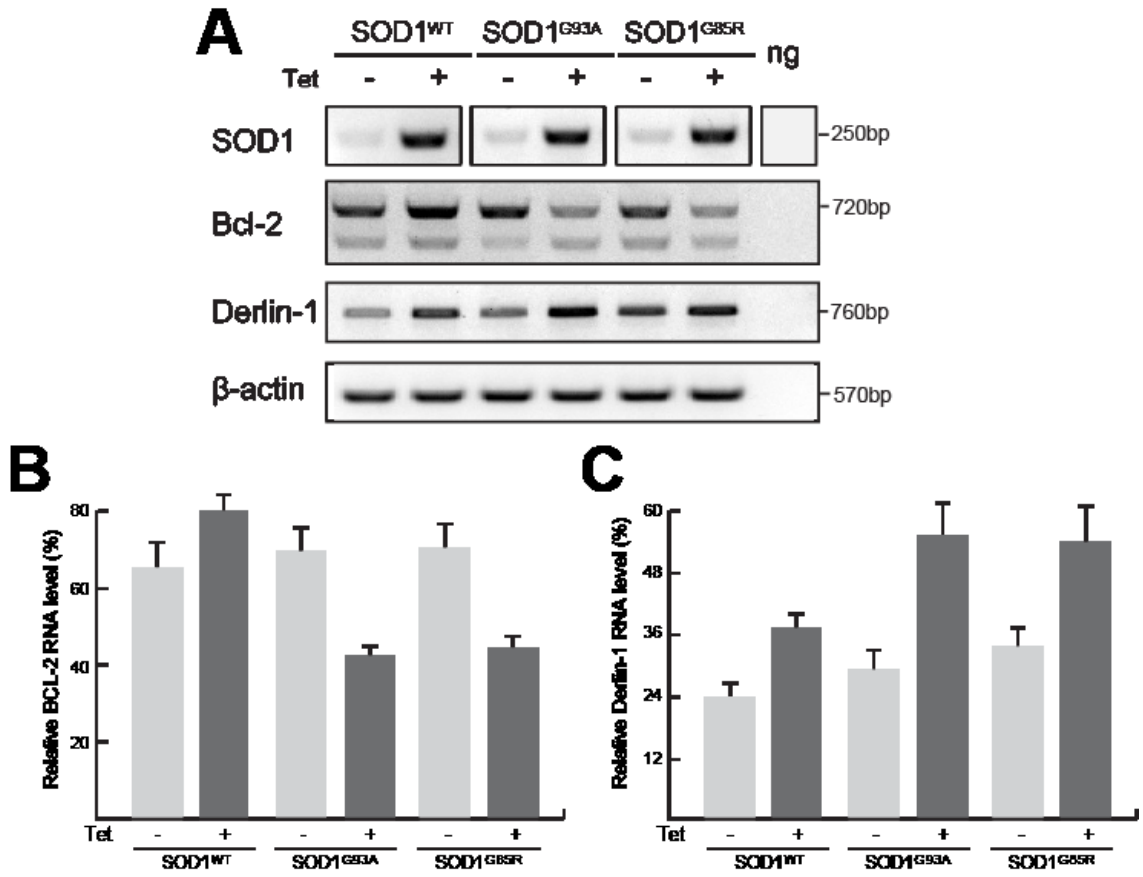

Figure 5.16 RT-PCR of BCL-2 and Derlin-1 in cells overexpressing SOD1. (A) Flp-in T-Rex system expressing SOD1 (WT, G93A, G85R) were induced by Tet in the absence of selection antibiotic for 48h. Total RNA of samples were extracted and converted into cDNA as described in Material and Methods. RT-PCR was performed using specific primers, which were presented in detail in the appendix. No transcriptase was used as negative control (ng), and housekeeping gene β-actin was used as an internal reference. RT-PCR products were resolved by 2.5% agarose gel to detect the presence of BCL-2 (720bp), Derlin-1 (760bp), SOD1 (250bp) and β-actin (570bp). **(B)** Quantifications of relative amount of RNA. The relative RNA level of BCL-2 or Derlin-1 was normalized to β-actin with the mean ± SD plotted (n=3).

5.2.8.2 Effects of HSJ1 overexpression on ER stress signal pathways

5.2.8.2.1 Effects of HSJ1a on UPR sensor proteins under ER stress

Unpublished data from the Cheetham lab (Heather Smith PhD Thesis) suggests that UPR markers were activated in the spinal cord of $Hsj1^{-/-}$ mice compared to that of $Hsj1^{+/+}$ mice at P10, suggesting that HSJ1 might play a protective role against ER stress. To further confirm this hypothesis, I induced ER stress using thapsigargin or DTT in the Flp-in T-Rex system expressing HSJ1. Cells were lysed, resolved by SDS-polyacrylamide gel and analysed by immuno-blotting (Figure 5.17). Interestingly, cell death was observed in the cells expressing HSJ1b upon drug treatments, suggesting that the expression of HSJ1b could sensitise cells to ER stress. Therefore, I could only explore the potential role of HSJ1a on ER stress in this section.

As shown in Figure 5.17A, overexpression of HSJ1a alone showed no major effects on activating the UPR sensor proteins. Moreover, the cleaved ATF6 showed a reduction when HSJ1a is expressed. Treatment with thapsigargin led to an increase in IRE1 and eIF2α phosphorylation in either uninduced or induced Flp-in T-Rex HSJ1a cells. However, upon DTT treatment, cells expressing HSJ1a exhibited a reduced level of p-eIF2α as well as cleaved ATF6, and an increased level of uncleaved ATF6, yet showed no obvious changes in the p-IRE1a, suggesting expression of HSJ1a could potentially modulate ER stress via the PERK and ATF6 pathways.

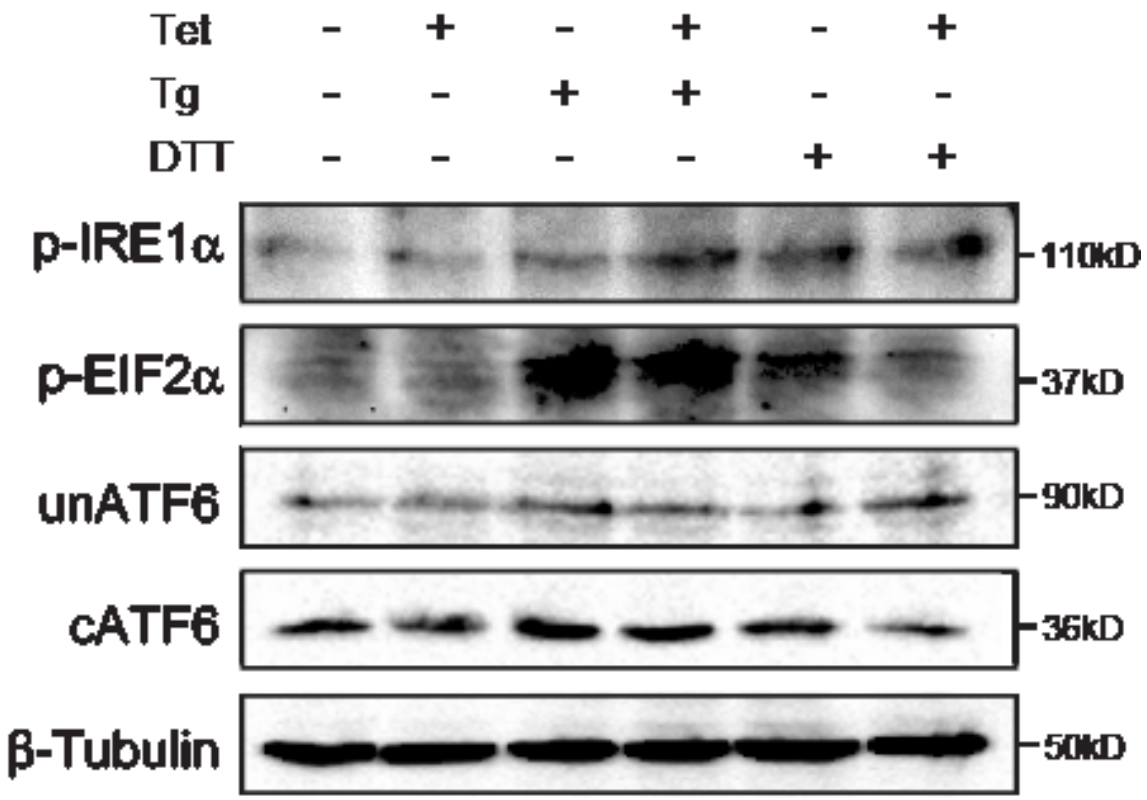

Figure 5.17 Immunoblot analysis of UPR sensors in cells expressing HSJ1a. Immunoblot of cells overexpressing HSJ1 upon drug treatment. Flp-in T-Rex system was turned on by Tet for 24h without the selection antibiotics, treated with thapsigargin (800nM) or DTT (2mM) for 1h. Cell lysates were resolved by SDS-PAGE and probed with rabbit polyclonal p-IRE1a (1:3000), rabbit polyclonal p-eIF2α (1:3000), mouse monoclonal ATF6 (1:2000), mouse monoclonal beta-tubulin (1:5000) with either goat anti-rabbit HRP (1:30000) or goat anti-mouse HRP (1:30000). UPR specific immunoreactive bands were developed with ECL, the position of MW markers are indicated on the right.

5.2.8.2.2 Effect of HSJ1a on UPR signalling pathways under ER stress

In addition to immunoblot analysis of UPR sensors, total RNA was also extracted from uninduced control and cells expressing HSJ1a with/without thapsigargin or DTT treatment. As shown in Figure 5.18, several UPR markers were amplified and analyzed. The total XBP-1 was fully spliced under thapsigargin and DTT treatment, suggesting the IRE1α pathway was activated as expected. A significant increase in the RNA level was observed for Chop, suggesting PERK UPR branch was also activated. However, in contrast to the phosphorylation data in Figure 5.17, I did not detect any difference between cells expressing HSJ1a and uninduced cells upon thapsigargin treatment, or DTT treatment. I think this could be because of the treatment time (1 hour) was too short for the UPR signalling to pass through the entire network, only the immediate upstream responses were activated. Therefore, in the future a detailed time course of the effect of HSJ1a on the UPR activation process should be considered.

Furthermore, I investigated if HSJ1a expression would affect the expression of either BCL-2 or Derlin-1 under stress. Therefore, I amplified endogenous BCL-2 and Derlin-1 from RNA samples extracted from the Flp-in T-Rex system expressing HSJ1a upon thapsigargin or DTT treatment. As shown in Figure 5.19, the RNA level of either BCL-2 was mildly reduced upon drug treatment. Interestingly, in the presence of HSJ1a, the RNA levels of BCL-2 and were partially restored and that of Derlin-1 was upregulated; suggesting HSJ1a might play a pro-survival role under stress.

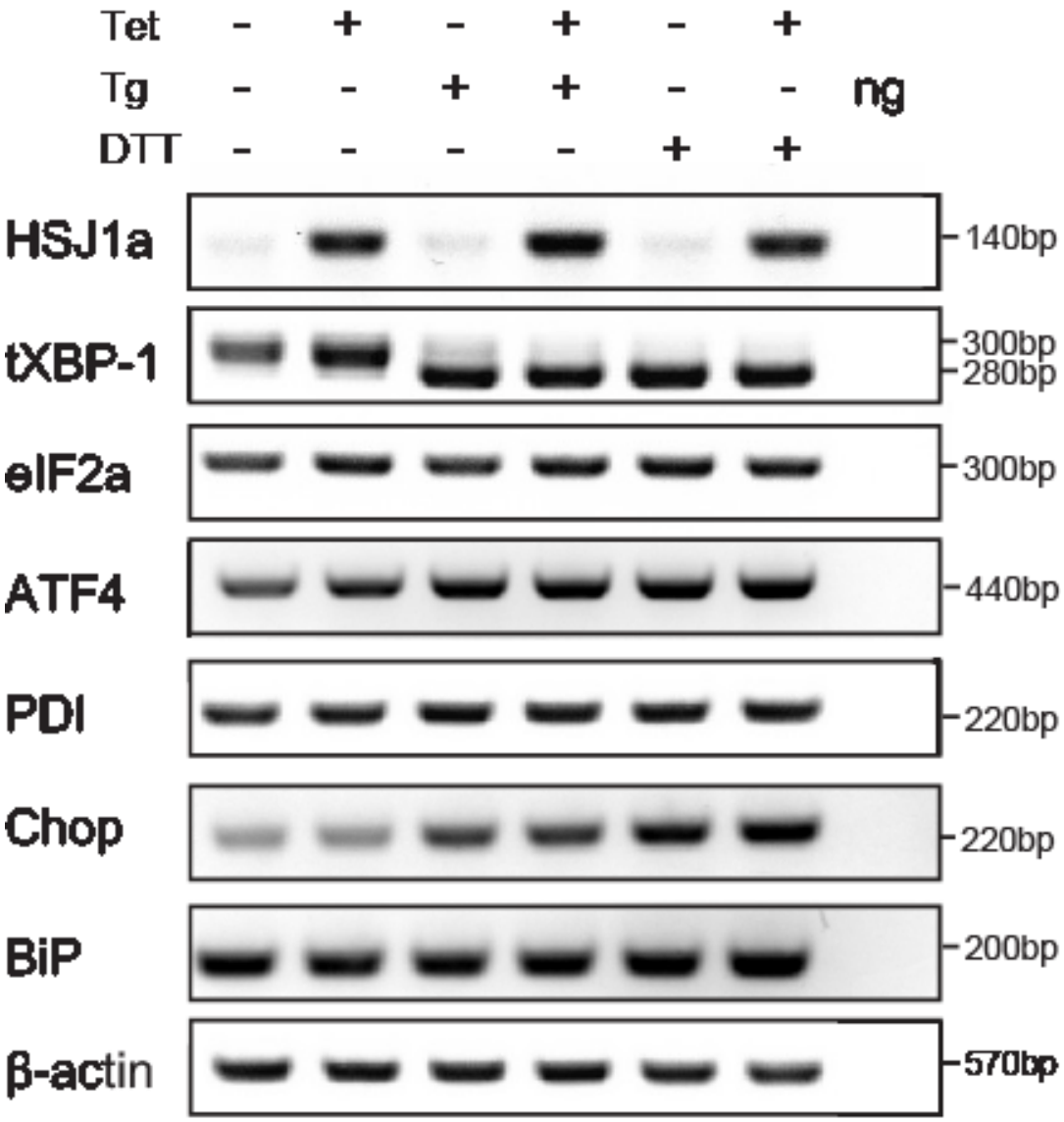

Figure 5.18 RT-PCR of UPR signalling pathways in cells overexpressing HSJ1a. Flp-in T-Rex system expressing eGFP-HSJ1a induced by Tet in the absence of selection antibiotic for 48h. Cells were treated with thapsigargin (800nM) or DTT (2mM) for 1hr. Total RNA of samples were extracted and converted into cDNA as described in Material and Methods. RT-PCR was performed using specific primers, which were presented in detail in the appendix. Housekeeping gene β-actin was used as an internal reference. RT-PCR products were resolved by 2.5% agarose gel to detect the presence of XBP-1(spliced at 279bp, unspliced at 305bp), BiP (206bp), Chop (222bp), ATF4 (434bp), eIF2a (297bp), HSJ1a (140bp) and β-actin (570bp) (n=3).

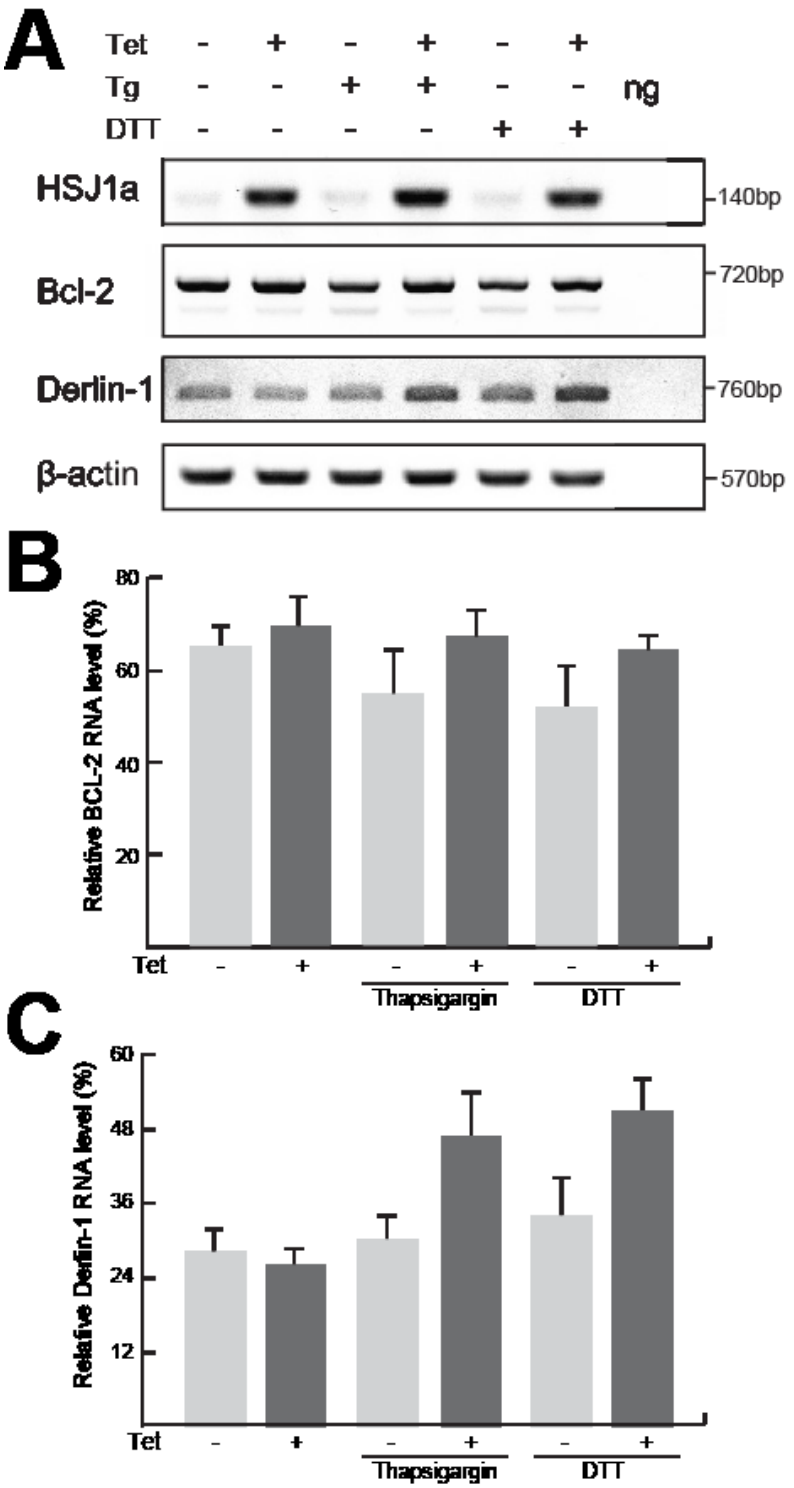

Figure 5.19 RT-PCR of BCL-2 and Derlin-1 in cells overexpressing HSJ1a. (A) Flp-in T-Rex system expressing eGFP-HSJ1a induced by Tet in the absence of selection antibiotic for 48h. Total RNA of samples were extracted and converted into cDNA as described in Material and Methods. RT-PCR was performed using specific primers, which were presented in detail in the appendix. Housekeeping gene β-actin was used as an internal reference. RT-PCR products were resolved by 2.5% agarose gel to detect the presence of BCL-2, Derlin-1, HSJ1a (140bp) and β-actin (560bp). **(B)** Quantifications of relative amount of RNA. The relative RNA level of BCL-2 or Derlin-1 is normalized to β-actin with mean ±SD (n=3).

5.3 Discussion

The two isoforms of HSJ1 both inhibited SOD1 inclusion formation

Novoselov *et al* (2013) reported that compared to GFP-SOD1^{WT}, GFP-SOD1^{G93A} was excluded from nuclei and formed peri-nuclear inclusions in the cytoplasm. The molecular chaperone HSJ1a co-localized, interacted with SOD1^{G93A} and promoted unbiquitylation of SOD1 inclusions, hence reducing SOD1 aggregation in a J-domain and UIM-dependent manner. HSJ1a not only plays a protective role in the cell model, but also ameliorated the disease progression and improved motor neuron survival of SOD1^{G93A} mice (Novoselov et al. 2013). In this study, I investigated the potential stages at which HSJ1 could reduce SOD1^{MT} aggregation. Several constructs and cell lines were generated for this purpose.

Similar to HSJ1a, HSJ1b was also confirmed to significantly reduced SOD1^{MT} inclusion incidence in the co-transfection (Figure 5.4) Previous work in the Cheetham lab (Wendy Mustill PhD thesis) demonstrated the incidence of insoluble SOD1^{G93A} aggregates were decreased in the presence of either HSJ1a and HSJ1b, and the soluble SOD1 protein was presented in the soluble fraction, indicating both HSJ1 isoforms inhibited insoluble SOD1 aggregation formation in cell models. Furthermore, Blumen et al (2012) showed that both HSJ1a and HSJ1b could reduce inclusion formation by SOD1^{A4V}. I used immunoprecipitation, to show that both HSJ1a and HSJ1b were able to form a complex with SOD1^{WT}, SOD1^{G93A} and SOD1^{G85R}. Interestingly, HSJ1 is enriched in SOD1 mutant immunopurification, suggesting HSJ1 preferentially recognized and bound to misfolded client protein.

In addition, I used a conformational antibody SEDI that was designed to specifically recognized misfolded SOD1 by immunoprecipitation (Liu et al. 2012). I observed that the SEDI antibody was able to recognize SOD1^{G93A} and SOD1^{G85R} in the control, yet failed to immunopurify the two SOD1 mutants in the co-expression with either eGFP-HSJ1a or eGFP-HSJ1b, indicating HSJ1 might assist the folding of SOD1 mutants, thus making the conformation of SOD1 mutant unrecognisable for SEDI. It is also possible that the HSJ1 proteins could be masking the SEDI epitope by binding that site. Novoselov *et al* (2013) performed similar immunopurification assays *in vivo* using the C4F6 antibody, yet observed no reduction of SOD1^{G93A} with HSJ1a overexpression. This could be because the epitope of C4F6 might be on the surface of SOD1^{G93A} protein therefore C4F6 could recognize SOD1^{G93A} in spite of conformational changes or dimerization. There are now several conformational specific antibodies (epitopes shown in Figure 1.4) targeting SOD1 that can be used to study the conformation of SOD1 (Ayers et al. 2014; Liu et al. 2012; Rakhit et al. 2007) and these could be used in

the future to further distinguish folded $SOD1^{MT}$ from misfolded $SOD1^{MT}$ and test the effect of HSJ1 proteins.

Data collected in this section raise an interesting question: what are the roles of the subdomains of HSJ1 play in anti-SOD1 aggregation function? To further investigate this question, Novoselov *et al* (2012) generated a substitution mutation in the J-domain (H31Q) which disrupted the interaction with Hsp70, and a 4 point mutation (S219A/E222A/S262A/E265A) which disrupted the ubiquitination function of UIM domains (Figure 1.7). Compared to $HSJ1a^{WT}$, the J domain mutation $HSJ1a^{H31Q}$ lost the ability to supress $SOD1^{G93A}$ inclusion formation, whereas the UIM mutation could partially reduce $SOD1^{G93A}$ inclusion incidence. In addition, Novoselov *et al* (2012) observed increased co-immunoprecipitation binding between $SOD1^{G93A}$ and $HSJ1a^{H31Q}$, suggesting HSJ1 mutants bind the misfolded client protein non-productively. The J-domain plays a critical role in simulating substrates loading onto Hsp70. Therefore, loss of J-domain activity would potentially disturb the interaction between HSJ1 and Hsp70, thus preventing the Hsp70-substrates binding. Furthermore, Ottaviani *et al* (2016) reported that phosphorylation within second UIM domain was accompanied by a reduced activity of HSJ1 to bind ubiquitylated clients, and to exert its chaperone activity. Therefore, inactivation of UIM domain would presumably fail to recognize ubiquitylated substrates, resulting in decreased Ub-client binding as well as ubiquitinchain hydrolysis of the substrates.

HSJ1 inhibited the recruitment effect of SOD1 inclusions

Subsequently, I investigated if HSJ1 could inhibit the recruitment effect of $SOD1^{MT}$ to $SOD1^{WT}$. HSJ1 was co-expressed with $SOD1^{MT}$ as well as $SOD1^{WT}$. The inclusion incidence of $SOD1^{G93A}$ or $SOD1^{G85R}$ was significantly reduced when co-expressed with HSJ1a or HSJ1b at 1:1 ratio. In this recruitment assay, the inclusion incidence of eGFP-$SOD1^{MT}$ was also significantly reduced with HSJ1 co-expression, as the mCherry-$SOD1^{WT}$ was shown to form fewer inclusions in the presence of eGFP-$SOD1^{MT}$ inclusions. This triple co-expression expression confirmed that HSJ1 inhibited SOD1 inclusion formation in the presence of $SOD1^{WT}$, as well as altered the recruitment effects of SOD1 inclusions. So far, several independent groups reported that $SOD1^{MT}$ induced the conformation changes of $SOD1^{WT}$ and co-aggregated (Prudencio et al. 2010; Qualls et al. 2013; Witan et al. 2009; Prudencio et al. 2009; Audet et al. 2010), yet no published work has demonstrated if these specific changes could be inhibited or delayed. Therefore, it is interesting that HSJ1 could prevent $SOD1^{MT}$ from recruiting soluble $SOD1^{WT}$ in a cell model. In these preliminary tests with transient transfection, there was a promising effect of HSJ1 for inhibiting aggregation formation and propagation. Therefore, I further explored if HSJ1 could modulate the

SOD1-associated ALS disease progression by manipulating the inducible Flp-in T-Rex system.

Pre-induced HSJ1 showed subtle inhibition effects on SOD1 inclusion formation

Next, I investigated if pre-synthesised HSJ1 would inhibit SOD1 inclusion formation (section 5.2.7.1). Non-inducible GFP-SOD1 was transiently overexpressed in pre-induced HSJ1 cell lines. I observed a subtle reduction in SOD1 inclusion incidence in the presence of pre-produced HSJ1 expression. The inclusion incidence of $SOD1^{G93A}$ and $SOD1^{G85R}$ was reduced from ~10% to ~7% 24h post transfection (*$p<0.05$ for G93A). This is a smaller effect than the effect observed when the proteins were transfected or expressed together. It is possible that the expression level of transiently transfected SOD1 was much higher than pre-induced HSJ1; therefore, there was not sufficient HSJ1 to interact with the mutant SOD1. Previous studies of HSJ1a and mutant Htt have suggested HSJ1a is still effective at a 10 fold molar excess of Htt (Labbadia et al 2012). My earlier comparisons of transient transfection and the inducible SOD1 cell lines suggested the difference could be 30-50 fold (section 4.2.3.2.2.4), so it might be that the levels of HSJ1 were too low for full effect. In addition, the pre-synthesised HSJ1 might be reduced during the experiment, even though the half life appeared quite long, as the GFP signal was still detectable one month after turning off the Flp-in T-Rex HSJ1 expression system (data not shown).

HSJ1 disassembled pre-existed SOD1 inclusions

Furthermore, I investigate if HSJ1 proteins could disassemble pre-existing SOD1 inclusions. The non-inducible GFP-SOD1 was transiently overexpressed in the uninduced HSJ1 cell lines, which were turned on 24hrs post transfection. Surprisingly, the inclusion incidence of SOD1 was significantly reduced at time point 24hrs as well as 48 hrs post Tet/sodium butyrate induction. The transfection efficiency was calculated as a reference to confirm that the reason of reduction of SOD1 aggregation was not due to inclusion-mediated cell death. So far, no published work has reported that overexpression of chaperones could disassemble pre-exited pathogenic inclusions in cell models of neurodegenerative diseases. However, Ortega et al (2010) reported similar results using an inducible HD mouse model. The N-mutHtt trigged UPS impairment in the adult neurons but this was only transient while IBs were readily detectable (Ortega et al. 2010).

The data presented in Chapter 3 showed that HSJ1a and HSJ1b could co-sediment with mutant SOD1 aggregates suggesting that the interaction is direct, and the recombinant proteins could be used to test this interaction outside of the cellular context where other chaperones are present. Interestingly, in an ATP regeneration

system, purified HSJ1 failed to disassemble the preformed SOD1 aggregates (data not shown). It is an interesting question why HSJ1 is able to disassemble preformed aggregates in the cellular environment but not in the cell-free system. What are the potential factors that co-facilitate this process? Can the combination of HSJ1 and its co-factor disassemble the preformed SOD1 aggregates *in vivo*? All these questions need to be further verified in the future studies. A dual inducible cell line or an inducible animal model could be generated for this purpose.

Furthermore, parallel experiments using the inducible HSJ1 cells to investigate if HSJ1 is able to disassemble other preformed pathogenic aggregates such as polyQ, Tau, parkin, C9orf72, TDP-43 and Fus, should also be performed, which can help us to further confirmed the anti-aggregation property of HSJ1.

In addition to inhibiting SOD1 aggregate seeding potential, HSJ1 was also tested if it could disassemble preformed SOD1 aggregates with/without the help of co-chaperones in ATP-regeneration system (data not shown). Cells transiently expressed Hsp110, Hsp105, Hsp70, and Hsc70 were lysed respectively and then the cell lysates were added into ATP-regeneration system containing preformed SOD1 aggregates and soluble HSJ1. Disappointingly, no soluble fraction of SOD1 was observed following HSJ1 treatment in the reconstituted system, even when different combinations of cell lysates containing Hsps were tested. In contrast to our results, Gao et al (2015) reported that a specific human Hsp70 chaperone system (Hsc70/DnaJB1/Apg20) efficiently disassembles preformed α-syn fibrils into non-toxic monomers in an ATP-reconstituted system (Gao et al. 2015). These multiple recombinant chaperone system containing HSJ1 could be utilized in the future work to test if it is able to disassemble pre-induced SOD1 aggregates in this study.

HSJ1a showed modest inhibition effects in ER stress

As SOD1 failed to aggregate in the Flp-in T-Rex system, it was not possible to use this system to test the effects of seeding and transmission. Therefore, I explored other potential deleterious effects of SOD1 overexpression. Preliminary experiments that investigated UPR induction in the Cheetham lab, revealed the elevated levels of p-IRE1a, p-eIF2a and cleaved ATF6 when $SOD1^{G93A}$ was transiently overexpressed in a cell model. Similar to what has been shown in transgenic mice (discussed in Chapter 1). In addition, HSJ1 knock-out mice show ER stress (Heather Smith PhD thesis). Therefore, I investigated if SOD1 induced ER stress in Flp-in T-Rex system and if HSJ1 expression rescued cells from ER stress. Interestingly, the inducible SOD1 stable cell lines showed no elevated RNA levels of UPR markers. This is most likely due to the low expression level of $SOD1^{MT}$. Preliminary experiments on SOD1 stable cell lines

suggested that the ER stress signals could be enhanced with thapsigargin treatment and this could be followed up in more detail.

Interestingly, HSJ1a showed a modest inhibition of UPR induction via the PERK and ATF6 branches after DTT treatment, but exhibited no differences in expression levels of any UPR sensors under thapsigargin treatment. To date, only a few chaperones have been reported to modulate ER stress. BiP is known to regulate UPR activation and overexpression of BiP reduced CHOP induction associated with ER stress and attenuates apoptosis (Wang et al. 1996; Gu et al. 2010; Morris et al. 1997). In 2003, $P58^{IPK}$, a DNAJ family member was reported to inhibit ER stress by inhibiting p-eIF2a signaling in human retinal capillary endothelial cells (Van Huizen et al. 2003). Bruchmann et al (2013) reported that overexpression of Bag5 in malignant prostate tissue inhibited ER-stress induced apoptosis by suppressing PERK-eIF2-ATF4 activity while enhancing the IRE1-Xbp1 axis of this pathway (Bruchmann et al. 2013; Yang et al. 2007). It is worth noting that Flp-in T-Rex expressing HSJ1b underwent cell death following drug treatment, this suggests that overexpression of HSJ1b already affected ER stress and the ER stress response; the pro-death signalling pathway was triggered upon drug treatments. These data might suggest that HSJ1a is potentially a better candidate protein for future therapeutic development, compared to HSJ1b, as HSJ1b mainly localized on the ER surface. However, the potential effects of HSJ1b on ER stress still need to be further addressed given the role HSJ1b played in ERAD (Meimaridou et al. 2011) as well as its anti-aggregation activity. Further experiments are required to explore if HSJ1b expression alone could cause ER stress, or to investigate the consequences of drug treatment on HSJ1b Flp-in T-Rex system with low expression level.

As no induction of ER stress markers was detected in Flp-in T-Rex system expressing SOD1, I focused on the proteins that $SOD1^{MT}$ has been shown to interacted with, such as BCL-2 and Derlin-1. When $SOD1^{MT}$ was induced in the system, the mRNA level of BCL-2 was significantly reduced. Pasinelli et al (2004) reported that $SOD1^{G93A}$ bound to and co-aggregated with BCL-2 in spinal cord mitochondria *in vivo* (Pasinelli et al. 2004). It was suggested that $SOD1^{G93A}$ causes mitochondrial dysfunction by promoting conformational changes of BCL-2 (Pasinelli et al. 2004). In addition, there was an increase level of Derlin-1 mRNA detected when SOD1 was expressed. Nishitoh et al (2008) reported $SOD1^{MT}$ interacted as well as co-aggregated with Derlin-1, thus triggering the ER stress (Nishitoh et al. 2008). However, how SOD1 changes the transcriptional level of BCL-2 or Derlin-1 still remains to be resolved. It is possible that HSJ1 could be implicated in SOD1-mediated ALS pathology in a novel way that that has not been investigated before. Preliminary experiment (data not shown) in this study

suggested both HSJ1a and HSJ1b could reduce the $SOD1^{G85R}$-BCL-2 interaction in an SOD100 immunoprecipitation assay. It is possible that in addition to reducing or disassambling SOD1 aggregation, HSJ1 could promote motor neuron survival by inhibiting the aberrant interactions such as SOD1-BCL-2 and restoring BCL-2 expression, thereby rescuing neurons from stress-induced apoptosis. So far, no published work has reported if chaperones could prolong neuron survival by inhibiting $SOD1^{MT}$-mediated interactions, these questions need to be further explored.

Chapter 6

Conclusions and Perspective

The folding of a polypeptide into a functionally active structure depends on the intrinsic properties of the protein sequence as well as the protein folding machinery. Protein folding process is highly co-operative and complicated, making the characterization and recognition of conformational transitions and equilibrium intermediates difficult. In 1980s, an energy landscape theory published by Joseph Bryngelson and Peter Wolynes introduced 'the principle of minimal frustration' (Bryngelson & Wolynes 1987). This theory suggested the funnelled energy landscapes allow the protein to fold to native state via various pathways and intermediates. This description is consistent with the classical thermodynamic and kinetic principles of protein folding (Figure 6.1), and supported by computational simulations as well as experiments.

However, every polypeptide has a finite tendency to misfold. Mutational or environmental changes can destabilize and increase the free energy of the native fold relative to that of the fully unfolded state or partially folded state before the major free energy barrier, resulting a higher population of non-native state protein accumulations. As in those two states, hydrophobic and backbone moieties are solvent exposed, which are accessible for intermolecular interactions, and thus greatly enhancing the propensity of aggregation.

Jahn & Radford (2005) proposed a combined energy landscape for protein folding and aggregation starting from unfolded ensemble (Figure 6.2) (Jahn & Radford 2005). This theory suggested that aggregated proteins exhibited higher stability and lower energy content compared to native state protein, highlighting the diverse conformational states for intramolecular or intermolecular contacts. According to Jahn & Radford, a monomeric unfolded or natively folded protein must overcome energy barriers to gain access to the aggregation landscape by generating nuclei in a rate-limiting manner. The consequence of aberrant protein folding and aggregation is well recognized as a key feature of most of neurodegenerative disorders, such as Alzheimer's disease, Huntington's disease, Parkinson's disease as well as Amyotrophic lateral sclerosis. Experimental studies reported that chaperones mostly promoted the partially misfolded protein back to native state, or inhibited abnormal assembly (discussed in Chapter 1).

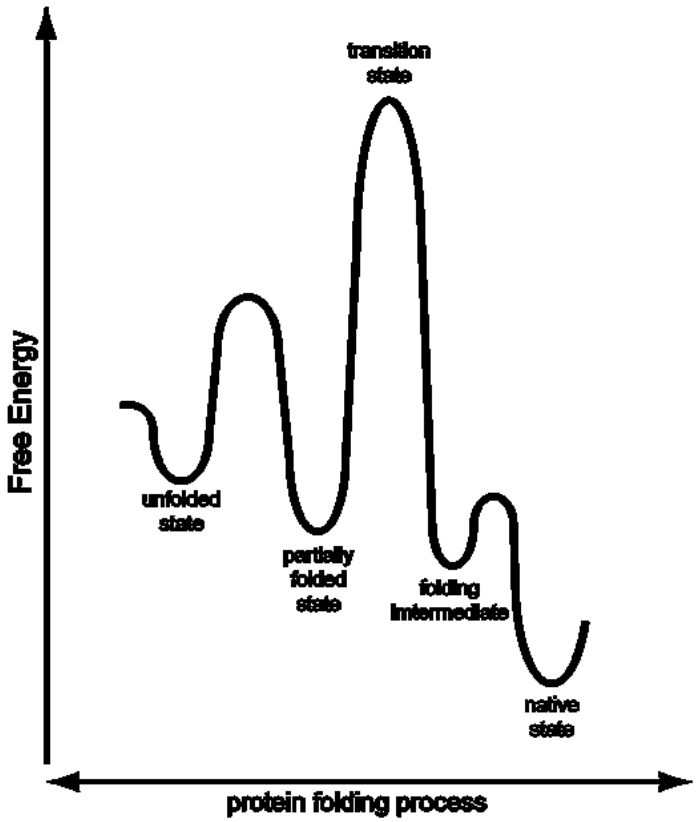

Figure 6.1 Free energy model for protein folding & unfolding. Folding was shown based on classical thermodynamic and kinetic principles. Unfolded state is composed of a large ensemble of unstructured conformations, which can partially fold, then across the free energy barrier to fold into native state. Unfolding process can be interpreted backward through the free energy barrier. Proteins adopting the unfolded, partially folded or fording intermediate could trigger the misfolding & aggregation formation.

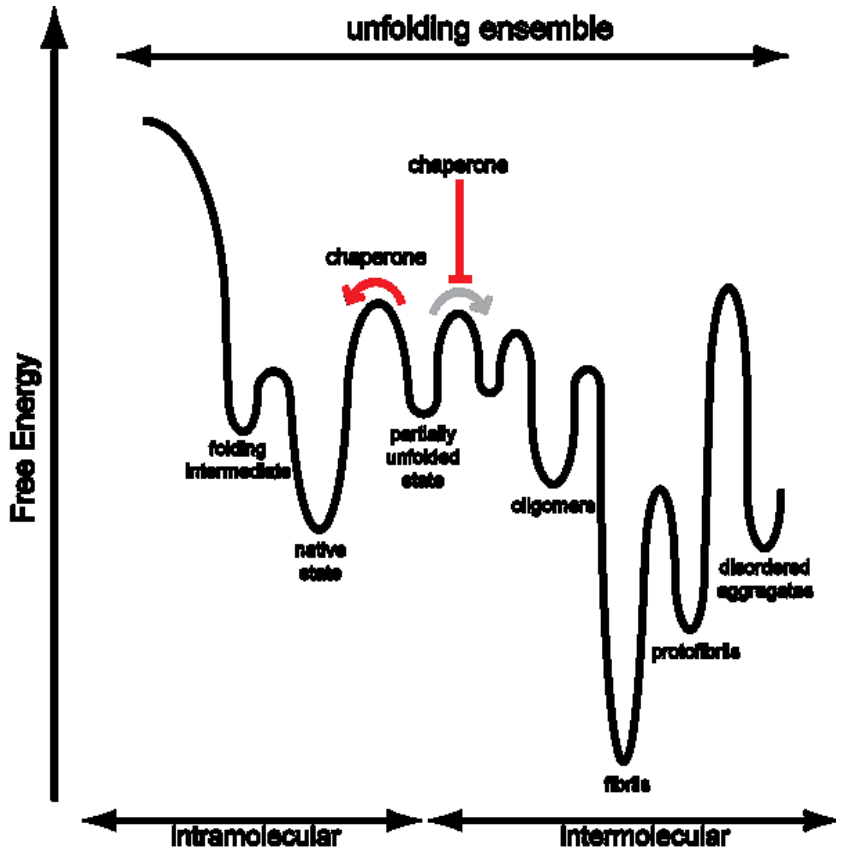

Figure 6.2 Free energy landscape of protein misfolding& aggregation. Folding into native state involves intramolecular contacts. The ruggedness of the free-energy landscape results in the accumulation of kinetically trapped conformations that need to overcame free-energy barrier. Chaperones accelerated these steps *in vivo*. When molecules fold simultaneously within the same compartment, intermolecular contacts may overlap with that of intermolecular contacts, resulting in the formations of amorphous aggregates, oligomers, fibrils and etc. Research showed molecular chaperones could promote the folding intermediate to traverse the major free-energy barrier thus folding to native state.

The work described in this thesis investigated SOD1 misfolding, aggregation and seeding potential in the context of ALS (Figure 6.3). In this study, $SOD1^{WT}$ was resistant to seeding unless the protein was destabilized and partially unfolded. Purified HSJ1 could reduce the SOD1 aggregation. In cells, HSJ1 interacted preferentially with $SOD1^{MT}$, and could reduce SOD1 inclusion formation, and disassembled pre-existing SOD1 inclusions, indicating that HSJ1 could modulate SOD1 disease-associated aggregation at different stages, shed light on HSJ1 as a potential candidate targeting misfolded and aggregated SOD1 for future investigation. This study is informative for potential therapeutic purposes. Short peptides based on the HSJ1 could be designed and synthesized after functional domains as well as co-factors implicated in disassembly of preformed aggregates have been identified, which can be utilized as anti-neurodegenerative agent for *in vivo* experiments and clinical trials.

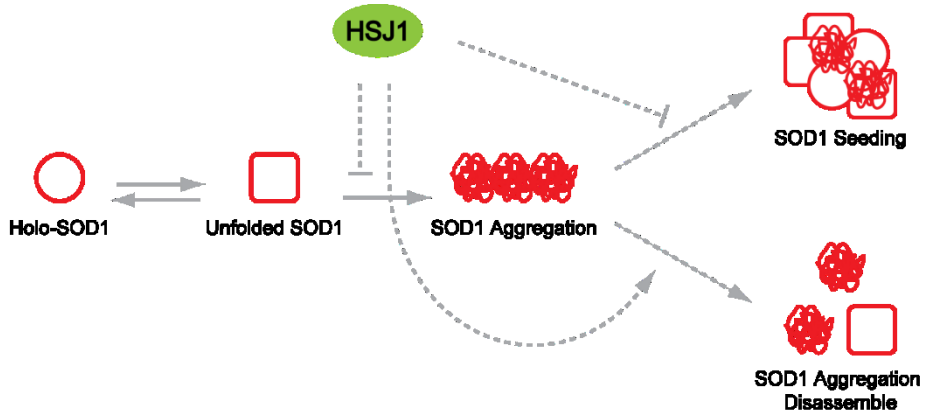

Figure 6.3 Hypothesis tested *in vitro* in this study. Processes confirmed by literatures were shown in solid line. Processes verified by experiments in this study were shown in dashed line.

The potential consequences of $SOD1^{MT}$ gain of function have been implicated in mitochondrial dysfunction, oxidative stress, ER stress, axonal transport, apoptotic cell death and autophagy (specific interacted proteins described in section 5.1). Using an inducible stable cell line expressing HSJ1a, unfolded protein response (UPR) markers were modestly reduced after ER stress inducer treatments, suggesting HSJ1a expression could potentially reduce disease-related intracellular stress. Further experiments should be carried out to investigate if HSJ1a and HSJ1b could inhibit other toxic aberrant interactions that represented the relevant pathogenic mechanisms in the cell model and *in vivo*. I also hope that the generation of iPSC-derived motor neurons could help to resolve these questions in the future.

Collectively, the data presented in this thesis builds on our understanding of the potential role HSJ1 played for SOD1-associated ALS, highlighting its neuroprotective property as well as the potential as a therapeutic target.

References

Ackerley, S. et al., 2000. Glutamate slows axonal transport of neurofilaments in transfected neurons. *Journal of Cell Biology*, 150(1), pp.165–175.

Ackerley, S. et al., 2004. P38Alpha Stress-Activated Protein Kinase Phosphorylates Neurofilaments and Is Associated With Neurofilament Pathology in Amyotrophic Lateral Sclerosis. *Molecular and cellular neurosciences*, 26(2), pp.354–64.

Aebischer, J. et al., 2011. IFNγ triggers a LIGHT-dependent selective death of motoneurons contributing to the non-cell-autonomous effects of mutant SOD1. *Cell death and differentiation*, 18(5), pp.754–68.

Ahtoniemi, T. et al., 2008. Mutant SOD1 from spinal cord of G93A rats is destabilized and binds to inner mitochondrial membrane. *Neurobiology of Disease*, 32(3), pp.479–485.

Al-Chalabi, A. et al., 1998. Recessive amyotrophic lateral sclerosis families with the D90A SOD1 mutation share a common founder: evidence for a linked protective factor. *Human molecular genetics*, 7(13), pp.2045–50.

Al-Sarraj, S. et al., 2011. p62 positive, TDP-43 negative, neuronal cytoplasmic and intranuclear inclusions in the cerebellum and hippocampus define the pathology of C9orf72-linked FTLD and MND/ALS. *Acta neuropathologica*, 122(6), pp.691–702.

Alexander Valencia, C., Ju, W. & Liu, R., 2007. Matrin 3 is a Ca2+/calmodulin-binding protein cleaved by caspases. *Biochemical and Biophysical Research Communications*, 361(2), pp.281–286.

Andersen, P.M. et al., 2003. Sixteen novel mutations in the Cu/Zn superoxide dismutase gene in amyotrophic lateral sclerosis: a decade of discoveries, defects and disputes. *Amyotrophic lateral sclerosis and other motor neuron disorders : official publication of the World Federation of Neurology, Research Group on Motor Neuron Diseases*, 4(2), pp.62–73.

Angot, E. et al., 2012. Alpha-synuclein cell-to-cell transfer and seeding in grafted dopaminergic neurons in vivo. *PLoS ONE*, 7(6).

Antonyuk, S. et al., 2005. Structural consequences of the familial amyotrophic lateral sclerosis SOD1 mutant His46Arg. *Protein science : a publication of the Protein Society*, 14(5), pp.1201–1213.

Apolloni, S. et al., 2013. The NADPH Oxidase Pathway Is Dysregulated by the P2X7 Receptor in the SOD1-G93A Microglia Model of Amyotrophic Lateral Sclerosis. *The Journal of Immunology*, 190(10), pp.5187–5195.

Appel, S.H. et al., 2001. Calcium: the Darth Vader of ALS. *Amyotrophic lateral sclerosis and other motor neuron disorders : official publication of the World Federation of Neurology, Research Group on Motor Neuron Diseases*, 2 Suppl 1(suppl 1), pp.S47–S54.

Araki, K. & Nagata, K., 2011. Protein folding and quality control in the ER. *Cold Spring Harbor Perspectives in Biology*, 3(11).

Ash, P.E.A. et al., 2013. Unconventional Translation of C9ORF72 GGGGCC Expansion Generates Insoluble Polypeptides Specific to c9FTD/ALS. *Neuron*, 77(4), pp.639–646.

Atkin, J.D. et al., 2008. Endoplasmic reticulum stress and induction of the unfolded protein response in human sporadic amyotrophic lateral sclerosis. *Neurobiology of Disease*, 30(3), pp.400–407.

Atkin, J.D. et al., 2006. Induction of the unfolded protein response in familial amyotrophic lateral sclerosis and association of protein-disulfide isomerase with superoxide dismutase 1. *The Journal of biological chemistry*, 281(40), pp.30152–65.

Audet, J.N., Gowing, G. & Julien, J.P., 2010. Wild-type human SOD1 overexpression does not accelerate motor neuron disease in mice expressing murine Sod1G86R. *Neurobiology of Disease*, 40(1), pp.245–250.

Ayers, J.I. et al., 2014. Conformational specificity of the C4F6 SOD1 antibody; low frequency of reactivity in sporadic ALS cases. *Acta neuropathologica communications*, 2(1), p.55.

Babcock, D.F. et al., 1997. Mitochondrial participation in the intracellular Ca2+ network. *Journal of Cell Biology*, 136(4), pp.833–844.

Banci, L. et al., 2007. Metal-free superoxide dismutase forms soluble oligomers under physiological conditions: a possible general mechanism for familial ALS. *Proceedings of the National Academy of Sciences of the United States of America*, 104(27), pp.11263–11267.

Banci, L. et al., 2008. SOD1 and amyotrophic lateral sclerosis: Mutations and oligomerization. *PLoS ONE*, 3(2).
Banci, L. et al., 2003. Solution structure of apo Cu,Zn superoxide dismutase: Role of metal ions in protein folding. *Biochemistry*, 42(32), pp.9543–9553.
Banci, L. et al., 2009. Structural and dynamic aspects related to oligomerization of apo SOD1 and its mutants. *Proceedings of the National Academy of Sciences of the United States of America*, 106(17), pp.6980–6985.
Banci, L. et al., 2002. Structure and dynamics of copper-free SOD: The protein before binding copper. *Protein science : a publication of the Protein Society*, 11(10), pp.2479–92..
Bannwarth, S. et al., 2014. A mitochondrial origin for frontotemporal dementia and amyotrophic lateral sclerosis through CHCHD10 involvement. *Brain*, 137(8), pp.2329–2345.
Barmada, S.J. et al., 2010. Cytoplasmic mislocalization of TDP-43 is toxic to neurons and enhanced by a mutation associated with familial amyotrophic lateral sclerosis. *The Journal of Neuroscience*, 30(2), pp.639–49.
Bartnikas, T.B. & Gitlin, J.D., 2003. Mechanisms of biosynthesis of mammalian copper/zinc superoxide dismutase. *Journal of Biological Chemistry*, 278(35), pp.33602–33608.
Basso, M. et al., 2006. Insoluble mutant SOD1 is partly oligoubiquitinated in amyotrophic lateral sclerosis mice. *Journal of Biological Chemistry*, 281(44), pp.33325–33335.
Basso, M. et al., 2013. Mutant Copper-Zinc Superoxide Dismutase (SOD1) Induces Protein Secretion Pathway Alterations and Exosome Release in Astrocytes: IMPLICATIONS FOR DISEASE SPREADING AND MOTOR NEURON PATHOLOGY IN AMYOTROPHIC LATERAL SCLEROSIS. *Journal of Biological Chemistry*, 288(22), pp.15699–15711.
Batulan, Z. et al., 2003. High threshold for induction of the stress response in motor neurons is associated with failure to activate HSF1. *The Journal of neuroscience : the official journal of the Society for Neuroscience*, 23(13), pp.5789–5798.
Beal, M.F. et al., 1997. Increased 3-nitrotyrosine in both sporadic and familial amyotrophic lateral sclerosis. *Annals of neurology*, 42, pp.644–654.
Beaulieu, J.M., Nguyen, M.D. & Julien, J.P., 1999. Late onset death of motor neurons in mice overexpressing wild-type peripherin. *Journal of Cell Biology*, 147(3), pp.531–544.
Beckman, J.S. et al., 1993. ALS, SOD and peroxynitrite. *Nature*, 364(6438), p.584.
Beers, D.R. et al., 2006. Wild-type microglia extend survival in PU.1 knockout mice with familial amyotrophic lateral sclerosis. *Proceedings of the National Academy of Sciences of the United States of America*, 103(43), pp.16021–6.
Bendotti, C. et al., 2001. Transgenic SOD1 G93A mice develop reduced GLT-1 in spinal cord without alterations in cerebrospinal fluid glutamate levels. *Journal of Neurochemistry*, 79(4), pp.737–746.
Bertolotti, A. et al., 2000. Dynamic interaction of BiP and ER stress transducers in the unfolded-protein response. *Nature cell biology*, 2(6), pp.326–332.
Blokhuis, A.M. et al., 2013. Protein aggregation in amyotrophic lateral sclerosis. *Acta Neuropathologica*, 125(6), pp.777–794.
Blumen, S.C. et al., 2012. A rare recessive distal hereditary motor neuropathy with HSJ1 chaperone mutation. *Annals of Neurology*, 71(4), pp.509–519.
Borasio, G.D. & Appel, S.H., 2003. Chapter 81 - Upper and Lower Motor Neuron Disorders. In *Neurological Disorders (Second Edition)*. pp. 1165–1176.
Borrell-Pagès, M. et al., 2006. Cystamine and cysteamine increase brain levels of BDNF in Huntington disease via HSJ1b and transglutaminase. *Journal of Clinical Investigation*, 116(5), pp.1410–1424.
Van Den Bosch, L., 2011. Genetic rodent models of amyotrophic lateral sclerosis. *Journal of biomedicine & biotechnology*, 2011, p.348765.
Bosco, D.A. et al., 2010. Mutant FUS proteins that cause amyotrophic lateral sclerosis incorporate into stress granules. *Human Molecular Genetics*, 19(21), pp.4160–4175.
Bowman, A.B. & Goldstein, L.S., 2009. Dynein and Kinesin. *Wiley Online Library*, 122(Pt 21), pp.3973–82.
Boyce, M. et al., 2005. A selective inhibitor of eIF2alpha dephosphorylation protects cells from ER stress. *Science (New York, N.Y.)*, 307(5711), pp.935–939.
Braak, H. & Del Tredici, K., 2011. The pathological process underlying Alzheimer's disease in individuals under thirty. *Acta Neuropathologica*, 121(2), pp.171–181.
Brettschneider, J. et al., 2012. Pattern of ubiquilin pathology in ALS and FTLD indicates presence of C9ORF72 hexanucleotide expansion. *Acta Neuropathologica*, 123(6), pp.825–839.

Brotherton, T.E., Li, Y. & Glass, J.D., 2013. Cellular toxicity of mutant SOD1 protein is linked to an easily soluble, non-aggregated form in vitro. *Neurobiology of Disease*, 49(1), pp.49–56.
Brown, P. et al., 1982. Alzheimer's disease and transmissible virus dementia (Creutzfeldt-Jakob disease). *Annals of the New York Academy of Sciences*, 396(1 Alzheimer's D), pp.131–43.
Bruchmann, A. et al., 2013. Bcl-2 associated athanogene 5 (Bag5) is overexpressed in prostate cancer and inhibits ER-stress induced apoptosis. *BMC cancer*, 13(1), p.96.
Bruening, W. et al., 1999. Up-regulation of protein chaperones preserves viability of cells expressing toxic Cu/Zn-superoxide dismutase mutants associated with amyotrophic lateral sclerosis. *Journal of neurochemistry*, 72(2), pp.693–9.
Bruijn, L.I. et al., 1998. Aggregation and motor neuron toxicity of an ALS-linked SOD1 mutant independent from wild-type SOD1. *Science (New York, N.Y.)*, 281(5384), pp.1851–1854.
Bruijn, L.I. et al., 1997. ALS-linked SOD1 mutant G85R mediates damage to astrocytes and promotes rapidly progressive disease with SOD1-containing inclusions. *Neuron*, 18(2), pp.327–338.
Bruijn, L.I. & Cudkowicz, M., 2006. Therapeutic targets for amyotrophic lateral sclerosis: current treatments and prospects for more effective therapies. *Expert review of neurotherapeutics*, 6(3), pp.417–28.
Bruinsma, I.B. et al., 2011. Inhibition of alpha-synuclein aggregation by small heat shock proteins. *Proteins*, 79(10), pp.2956–2967.
Bryngelson, J.D.D. & Wolynes, P.G.G., 1987. Spin glasses and the statistical mechanics of protein folding. *Proceedings of the National Academy of Sciences*, 84(November), pp.7524–7528.
Calderwood, S.K. et al., 2010. Signal Transduction Pathways Leading to Heat Shock Transcription. *Signal transduction insights*, 2, pp.13–24.
Canton, T. et al., 1998. Glutamate uptake is decreased tardively in the spinal cord of FALS mice. *Neuroreport*, 9(5), pp.775–8.
Cardoso, R.M.F. et al., 2002. Insights into Lou Gehrig's Disease from the Structure and Instability of the A4V Mutant of Human Cu,Zn Superoxide Dismutase. *Journal of Molecular Biology*, 324(2), pp.247–256.
Carriedo, S.G. et al., 2000. AMPA exposures induce mitochondrial Ca(2+) overload and ROS generation in spinal motor neurons in vitro. *The Journal of neuroscience : the official journal of the Society for Neuroscience*, 20(1), pp.240–250.
Carter, B.J. et al., 2009. Redox modifier genes and pathways in amyotrophic lateral sclerosis. *Antioxidants & redox signaling*, 11(7), pp.1569–86.
Cha, J.R.C. et al., 2014. A novel small molecule HSP90 inhibitor, NXD30001, differentially induces heat shock proteins in nervous tissue in culture and in vivo (Cell Stress and Chaperones). *Cell Stress and Chaperones*, 19(3), pp.421–435.
Chapple, J.P. et al., 1999. Assignment of the neuronal cochaperone, HSJ1, to human chromosome bands 2q32-->q34 between D2S295 and D2S339 by in situ hybridization and somatic cell and radiation hybrids. *Cytogenetics and cell genetics*, 86(1), pp.62–63.
Chapple, J.P. & Cheetham, M.E., 2003. The chaperone environment at the cytoplasmic face of the endoplasmic reticulum can modulate rhodopsin processing and inclusion formation. *Journal of Biological Chemistry*, 278(21), pp.19087–19094.
Charcot, J.-M. & Joffroy, A., 1869. Deux cas d'atrophie musculaire progressive avec lésions de la substance grise et des faiseaux antéro-latéraux de la moelle épinière. *Archives de physiologie normale et pathologique*, 2, pp.744–760.
Chaussenot, A. et al., 2014. Screening of CHCHD10 in a French cohort confirms the involvement of this gene in frontotemporal dementia with amyotrophic lateral sclerosis patients. *Neurobiology of Aging*, 35(12), p.2884.e1-2884.e4.
Cheetham, M.E., Brion, J.P. & Anderton, B.H., 1992. Human homologues of the bacterial heat-shock protein DnaJ are preferentially expressed in neurons. *The Biochemical journal*, 284 (Pt 2, pp.469–76.
Cheetham, M.E. & Caplan, A.J., 1998. Structure, function and evolution of DnaJ: conservation and adaptation of chaperone function. *Cell stress & chaperones*, 3(1), pp.28–36..
Chen, H.-J. et al., 2016. The heat shock response plays an important role in TDP-43 clearance: evidence for dysfunction in amyotrophic lateral sclerosis. *Brain : a journal of neurology*, p.aww028.
Chen, X. et al., 2012. SOD1 aggregation in astrocytes following ischemia/reperfusion injury: a role of NO-mediated S-nitrosylation of protein disulfide isomerase (PDI). *Journal of Neuroinflammation*, 9(1), p.237.

Chen, Y.-Z. et al., 2004. DNA/RNA helicase gene mutations in a form of juvenile amyotrophic lateral sclerosis (ALS4). *American journal of human genetics*, 74(6), pp.1128–35.

Cheroni, C. et al., 2005. Accumulation of human SOD1 and ubiquitinated deposits in the spinal cord of SOD1G93A mice during motor neuron disease progression correlates with a decrease of proteasome. *Neurobiology of Disease*, 18(3), pp.509–522.

Chia, R. et al., 2010. Superoxide dismutase 1 and tgSOD1 mouse spinal cord seed fibrils, suggesting a propagative cell death mechanism in amyotrophic lateral sclerosis. *PloS one*, 5(5), p.e10627.

Chin, L.-S., Olzmann, J. a & Li, L., 2010. Parkin-mediated ubiquitin signalling in aggresome formation and autophagy. *Biochemical Society transactions*, 38(Pt 1), pp.144–149.

Chiu, a Y. et al., 1995. Age-dependent penetrance of disease in a transgenic mouse model of familial amyotrophic lateral sclerosis. *Molecular and cellular neurosciences*, 6(4), pp.349–362.

Chow, C.Y. et al., 2007. Mutation of FIG4 causes neurodegeneration in the pale tremor mouse and patients with CMT4J. *Nature*, 448(7149), pp.68–72.

Cintron, N.S. & Toft, D., 2006. Defining the requirements for Hsp40 and Hsp70 in the Hsp90 chaperone pathway. *Journal of Biological Chemistry*, 281(36), pp.26235–26244.

Clavaguera, F. et al., 2009. Transmission and spreading of tauopathy in transgenic mouse brain. *Nat Cell Biol*, 11(7), pp.909–913.

Clement, a M. et al., 2003. Wild-type nonneuronal cells extend survival of SOD1 mutant motor neurons in ALS mice. *Science (New York, N.Y.)*, 302(5642), pp.113–117.

Cleveland, D.W. & Rothstein, J.D., 2001. From Charcot to Lou Gehrig: deciphering selective motor neuron death in ALS. *Nature reviews. Neuroscience*, 2(11), pp.806–819.

Couratier, P. et al., 1993. Cell culture evidence for neuronal degeneration in amyotrophic lateral sclerosis being linked to glutamate AMPA/kainate receptors. *The Lancet*, 341(8840), pp.265–268.

Cova, E. et al., 2006. Modified expression of Bcl-2 and SOD1 proteins in lymphocytes from sporadic ALS patients. *Neuroscience Letters*, 399(3), pp.186–190.

Crippa, V. et al., 2010. The small heat shock protein B8 (HspB8) promotes autophagic removal of misfolded proteins involved in amyotrophic lateral sclerosis (ALS). *Human Molecular Genetics*, 19(17), pp.3440–3456.

Crow, J.P. et al., 1997. Decreased zinc affinity of amyotrophic lateral sclerosis-associated superoxide dismutase mutants leads to enhanced catalysis of tyrosine nitration by peroxynitrite. *Journal of neurochemistry*, 69(5), pp.1936–1944.

Cuervo, A.M. & Wong, E., 2014. Chaperone-mediated autophagy: roles in disease and aging. *Cell research*, 24(1), pp.92–104.

Cuevas, J., 2015. The Peripheral Nervous System. In *Reference Module in Biomedical Sciences*.

Daigle, G.G. et al., 2013. Rna-binding ability of FUS regulates neurodegeneration, cytoplasmic mislocalization and incorporation into stress granules associated with FUS carrying ALS-linked mutations. *Human Molecular Genetics*, 22(6), pp.1193–1205.

Damiano, M. et al., 2006. Neural mitochondrial Ca2+ capacity impairment precedes the onset of motor symptoms in G93A Cu/Zn-superoxide dismutase mutant mice. *Journal of Neurochemistry*, 96(5), pp.1349–1361.

David, G. & Barrett, E.F., 2000. Stimulation-evoked increases in cytosolic [Ca(2+)] in mouse motor nerve terminals are limited by mitochondrial uptake and are temperature-dependent. *The Journal of neuroscience : the official journal of the Society for Neuroscience*, 20(19), pp.7290–6.

DeJesus-Hernandez, M. et al., 2011. Expanded GGGGCC Hexanucleotide Repeat in Noncoding Region of C9ORF72 Causes Chromosome 9p-Linked FTD and ALS. *Neuron*, 72(2), pp.245–256.

Demand, J. et al., 2001. Cooperation of a ubiquitin domain protein and an E3 ubiquitin ligase during chaperone/proteasome coupling. *Current Biology*, 11(20), pp.1569–1577.

Derkatch, I.L. et al., 2004. Effects of Q/N-rich, polyQ, and non-polyQ amyloids on the de novo formation of the [PSI+] prion in yeast and aggregation of Sup35 in vitro. *Proceedings of the National Academy of Sciences of the United States of America*, 101(35), pp.12934–9.

Desplats, P. et al., 2009. Inclusion formation and neuronal cell death through neuron-to-neuron transmission of alpha-synuclein. *Proceedings of the National Academy of Sciences of the United States of America*, 106(31), pp.13010–5.

Dewey, C.M. et al., 2011. TDP-43 is directed to stress granules by sorbitol, a novel physiological osmotic and oxidative stressor. *Molecular and Cellular Biology*, 31(5), pp.1098–108.

DiDonato, M. et al., 2003. ALS mutants of human superoxide dismutase form fibrous aggregates via framework destabilization. *Journal of Molecular Biology*, 332(3), pp.601–615.

Doucette, P.A. et al., 2004. Dissociation of Human Copper-Zinc Superoxide Dismutase Dimers Using Chaotrope and Reductant: INSIGHTS INTO THE MOLECULAR BASIS FOR DIMER STABILITY. *Journal of Biological Chemistry*, 279(52), pp.54558–54566.

Duden, R., 2003. ER-to-Golgi transport: COP I and COP II function (Review). *Molecular membrane biology*, 20(3), pp.197–207.

Dunlop, J. et al., 2003. Impaired spinal cord glutamate transport capacity and reduced sensitivity to riluzole in a transgenic superoxide dismutase mutant rat model of amyotrophic lateral sclerosis. *The Journal of neuroscience : the official journal of the Society for Neuroscience*, 23(5), pp.1688–1696.

Dupuis, L. et al., 2009. Muscle mitochondrial uncoupling dismantles neuromuscular junction and triggers distal degeneration of motor neurons. *PLoS ONE*, 4(4).

Eisele, Y.S. et al., 2009. Induction of cerebral beta-amyloidosis: intracerebral versus systemic Abeta inoculation. *Proceedings of the National Academy of Sciences of the United States of America*, 106(31), pp.12926–12931.

Elam, J.S. et al., 2003. Amyloid-like filaments and water-filled nanotubes formed by SOD1 mutant proteins linked to familial ALS. *Nature structural biology*, 10(6), pp.461–467.

Elden, A.C. et al., 2010. Ataxin-2 intermediate-length polyglutamine expansions are associated with increased risk for ALS. *Nature*, 466(7310), pp.1069–1075.

Ellis, R., 1987. Proteins as molecular chaperones. *Nature*, 328(6129), pp.378–379.

Erbse, a, Mayer, M.P. & Bukau, B., 2004. Mechanism of substrate recognition by Hsp70 chaperones. *Biochemical Society transactions*, 32(Pt 4), pp.617–621.

Esser, C., Alberti, S. & Höhfeld, J., 2004. Cooperation of molecular chaperones with the ubiquitin/proteasome system. *Biochimica et Biophysica Acta - Molecular Cell Research*, 1695(1–3), pp.171–188.

Estes, P.S. et al., 2011. Wild-type and A315T mutant TDP-43 exert differential neurotoxicity in a Drosophila model of ALS. *Human Molecular Genetics*, 20(12), pp.2308–2321.

Evans, C.G., Wisén, S. & Gestwicki, J.E., 2006. Heat shock proteins 70 and 90 inhibit early stages of amyloid β-(1-42) aggregation in vitro. *Journal of Biological Chemistry*, 281(44), pp.33182–33191.

Facchinetti, F. et al., 1999. Lack of involvement of neuronal nitric oxide synthase in the pathogenesis of a transgenic mouse model of familial amyotrophic lateral sclerosis. *Neuroscience*, 90(4), pp.1483–1492.

Feng, Y. et al., 2014. The machinery of macroautophagy. *Cell research*, 24(1), pp.24–41.

Ferguson, C.J., Lenk, G.M. & Meisler, M.H., 2009. Defective autophagy in neurons and astrocytes from mice deficient in PI(3,5)P2. *Human Molecular Genetics*, 18(24), pp.4868–4878.

Ferraiuolo, L. et al., 2011. Molecular pathways of motor neuron injury in amyotrophic lateral sclerosis. *Nature Reviews Neurology*, 7(11), pp.616–630.

Ferrante, R.J. et al., 1997. Evidence of increased oxidative damage in both sporadic and familial amyotrophic lateral sclerosis. *Journal of neurochemistry*, 69, pp.2064–2074.

Filimonenko, M. et al., 2007. Functional multivesicular bodies are required for autophagic clearance of protein aggregates associated with neurodegenerative disease. *The Journal of cell biology*, 179(3), pp.485–500.

Fischer, L.R. et al., 2004. Amyotrophic lateral sclerosis is a distal axonopathy: Evidence in mice and man. *Experimental Neurology*, 185(2), pp.232–240.

Follett, J. et al., 2013. Potassium depolarization and raised calcium induces ??-synuclein aggregates. *Neurotoxicity Research*, 23(4), pp.378–392.

Foran, E. & Trotti, D., 2009. Glutamate transporters and the excitotoxic path to motor neuron degeneration in amyotrophic lateral sclerosis. *Antioxidants & redox signaling*, 11(7), pp.1587–1602.

Forman, H.J. & Fridovich, I., 1973. On the stability of bovine superoxide dismutase. The effects of metals. *Journal of Biological Chemistry*, 248(8), pp.2645–2649.

Freundt, E.C. et al., 2012. Neuron-to-neuron transmission of α-synuclein fibrils through axonal transport. *Annals of Neurology*, 72(4), pp.517–524.

Friel, D.D. & Tsien, R.W., 1994. An FCCP-sensitive Ca2+ store in bullfrog sympathetic neurons and its participation in stimulus-evoked changes in [Ca2+]i. *Journal of Neuroscience*, 14(7), pp.4007–4024..

Furukawa, Y. et al., 2011. A seeding reaction recapitulates intracellular formation of sarkosyl-insoluble transactivation response element (TAR) DNA-binding protein-43 inclusions. *Journal of Biological Chemistry*, 286(21), pp.18664–18672.

Furukawa, Y. et al., 2013a. Intracellular seeded aggregation of mutant Cu,Zn-superoxide dismutase associated with amyotrophic lateral sclerosis. *FEBS Letters*, 587(16), pp.2500–2505.

Furukawa, Y. et al., 2013b. Intracellular seeded aggregation of mutant Cu,Zn-superoxide dismutase associated with amyotrophic lateral sclerosis. *FEBS Letters*, 587(16), pp.2500–2505.

Furukawa, Y. & O'Halloran, T. V., 2005. Amyotrophic lateral sclerosis mutations have the greatest destabilizing effect on the apo- and reduced form of SOD1, leading to unfolding and oxidative aggregation. *Journal of Biological Chemistry*, 280(17), pp.17266–17274.

Gajdusek, D.C., 1994. Spontaneous generation of infectious nucleating amyloids in the transmissible and nontransmissible cerebral amyloidoses. *Molecular Neurobiology*, 8(1), pp.1–13.

Gal, J. et al., 2007. P62 Accumulates and Enhances Aggregate Formation in Model Systems of Familial Amyotrophic Lateral Sclerosis. *The Journal of biological chemistry*, 282(15), pp.11068–77.

Gal, J. et al., 2009. Sequestosome 1/p62 links familial ALS mutant SOD1 to LC3 via an ubiquitin-independent mechanism. *Journal of Neurochemistry*, 111(4), pp.1062–1073.

Gallastegui, N. & Groll, M., 2010. The 26S proteasome: assembly and function of a destructive machine. *Trends in Biochemical Sciences*, 35(11), pp.634–642.

Ganley, I.G., 2013. Autophagosome maturation and lysosomal fusion. *Essays Biochem*, 55(1), pp.65–78.

Gao, X. et al., 2015. Human Hsp70 Disaggregase Reverses Parkinson's-Linked α-Synuclein Amyloid Fibrils. *Molecular Cell*, 59(5), pp.781–793.

Garrido, C. et al., 2012. The small heat shock proteins family: The long forgotten chaperones. *International Journal of Biochemistry and Cell Biology*, 44(10), pp.1588–1592.

Ge, W. wen et al., 2006. Neuronal tissue-specific ribonucleoprotein complex formation on SOD1 mRNA: Alterations by ALS SOD1 mutations. *Neurobiology of Disease*, 23(2), pp.342–350.

Geng, J. & Klionsky, D.J., 2008. The Atg8 and Atg12 ubiquitin-like conjugation systems in macroautophagy. "Protein modifications: beyond the usual suspects" review series. *EMBO reports*, 9(9), pp.859–64.

Genin, E.C. et al., 2015. CHCHD 10 mutations promote loss of mitochondrial cristae junctions with impaired mitochondrial genome maintenance and inhibition of apoptosis. *EMBO Molecular Medicine*, 8, pp.58–72.

Gess, B. et al., 2014. Ovid: HSJ1-related hereditary neuropathies: Novel mutations and extended clinical spectrum. *Neurology*, 83(19), pp.1726–32.

Gibson, S.B. & Bromberg, M.B., 2012. Amyotrophic lateral sclerosis: Drug therapy from the bench to the bedside. *Seminars in Neurology*, 32(3), pp.173–178.

Gidalevitz, T. et al., 2009. Destabilizing protein polymorphisms in the genetic background direct phenotypic expression of mutant SOD1 toxicity. *PLoS Genetics*, 5(3).

Di Giorgio, F.P. et al., 2007. Non-cell autonomous effect of glia on motor neurons in an embryonic stem cell-based ALS model. *Nature neuroscience*, 10(5), pp.608–14.

Gkogkas, C. et al., 2008. VAPB interacts with and modulates the activity of ATF6. *Human Molecular Genetics*, 17(11), pp.1517–1526.

Glass, C.K. et al., 2010. Mechanisms Underlying Inflammation in Neurodegeneration. *Cell*, 140(6), pp.918–934.

Glick, D., Barth, S. & Macleod, K.F., 2010. Autophagy: cellular and molecular mechanisms. *The Journal of pathology*, 221(1), pp.3–12.

Gomez-Martinez, M., Schmitz, D. & Hergovich, A., 2013. Generation of stable human cell lines with Tetracycline-inducible (Tet-on) shRNA or cDNA expression. *Journal of visualized experiments : JoVE*, (73), p.e50171.

Gordon, P.H., 2013. Amyotrophic Lateral Sclerosis: An update for 2013 Clinical Features, Pathophysiology, Management and Therapeutic Trials. *Aging and disease*, 4(5), pp.295–310.

Gordon, P.H. et al., 2007. Efficacy of minocycline in patients with amyotrophic lateral sclerosis: a phase III randomised trial. *Lancet Neurology*, 6(12), pp.1045–1053.

Gowing, G. et al., 2009. Macrophage colony stimulating factor (M-CSF) exacerbates ALS disease in a mouse model through altered responses of microglia expressing mutant superoxide dismutase. *Experimental Neurology*, 220(2), pp.267–275.

Goyal, N.A. & Mozaffar, T., 2014. Respiratory and nutritional support in amyotrophic lateral sclerosis. *Current Treatment Options in Neurology*, 16(2).

Grad, L.I. et al., 2011. Intermolecular transmission of superoxide dismutase 1 misfolding in living cells. *Proceedings of the National Academy of Sciences of the United States of America*, 108(39), pp.16398–403.

Grant, B.D. & Donaldson, J.G., 2009. Pathways and mechanisms of endocytic recycling. *Nature reviews. Molecular cell biology*, 10(9), pp.597–608.

Greene, M.K., Maskos, K. & Landry, S.J., 1998. Role of the J-domain in the cooperation of Hsp40 with Hsp70. *Proceedings of the National Academy of Sciences of the United States of America*, 95(11), pp.6108–13.

Gssler, C.S. et al., 1998. Mutations in the DnaK chaperone affecting interaction with the DnaJ cochaperone (Hsp70 heat shock proteins protein folding). *Biochemistry*, 95, pp.15229–15234.

Gu, X. et al., 2010. Bip overexpression, but not CHOP inhibition, attenuates fatty-acid-induced endoplasmic reticulum stress and apoptosis in HepG2 liver cells. *Life Sciences*, 87(23–26), pp.724–732.

Guatteo, E. et al., 2007. Altered calcium homeostasis in motor neurons following AMPA receptor but not voltage-dependent calcium channels' activation in a genetic model of amyotrophic lateral sclerosis. *Neurobiology of Disease*, 28(1), pp.90–100.

Gupta, S., Jie, S. & Colby, D.W., 2012. Protein misfolding detected early in pathogenesis of transgenic mouse model of huntington disease using amyloid seeding assay. *Journal of Biological Chemistry*, 287(13), pp.9982–9989.

Gurney, M.E. et al., 1994. Motor neuron degeneration in mice that express a human Cu,Zn superoxide dismutase mutation. *Science*, 264(18), pp.1772–1775.

Guzhova, I. V. et al., 2011. Novel mechanism of Hsp70 chaperone-mediated prevention of polyglutamine aggregates in a cellular model of huntington disease. *Human Molecular Genetics*, 20(20), pp.3953–3963.

Hadano, S. et al., 2010. Loss of ALS2/Alsin exacerbates motor dysfunction in a SOD1-expressing mouse ALS model by disturbing endolysosomal trafficking. *PloS one*, 5(3), p.e9805.

Hageman, J. et al., 2007. Comparison of intra-organellar chaperone capacity for dealing with stress-induced protein unfolding. *Journal of Biological Chemistry*, 282(47), pp.34334–34345.

Haidet-Phillips, A.M. et al., 2011. Astrocytes from familial and sporadic ALS patients are toxic to motor neurons. *Nature biotechnology*, 29(9), pp.824–828.

Hallier, M. et al., 1998. The transcription factor Spi-1/PU.1 interacts with the potential splicing factor TLS. *Journal of Biological Chemistry*, 273(9), pp.4838–4842.

Hammond, C. & Hammond, C., 2015. Chapter 1 – Neurons. In *Cellular and Molecular Neurophysiology*. pp. 3–23.

Hanada, T. et al., 2007. The Atg12-Atg5 conjugate has a novel E3-like activity for protein lipidation in autophagy. *Journal of Biological Chemistry*, 282(52), pp.37298–37302.

Hansen, C. et al., 2011. α-Synuclein propagates from mouse brain to grafted dopaminergic neurons and seeds aggregation in cultured human cells. *Journal of Clinical Investigation*, 121(2), pp.715–725.

Hardiman, O., van den Berg, L.H. & Kiernan, M.C., 2011. Clinical diagnosis and management of amyotrophic lateral sclerosis. *Nature Reviews Neurology*, 7(11), pp.639–649.

Harraz, M.M. et al., 2008. SOD1 mutations disrupt redox-sensitive Rac regulation of NADPH oxidase in a familial ALS model. *Journal of Clinical Investigation*, 118(2), pp.659–670.

Hart, P.J. et al., 1998. Subunit asymmetry in the three-dimensional structure of a human CuZnSOD mutant found in familial amyotrophic lateral sclerosis. *Protein science : a publication of the Protein Society*, 7(3), pp.545–55.

Hayward, L.J. et al., 2002. Decreased metallation and activity in subsets of mutant superoxide dismutases associated with familial amyotrophic lateral sclerosis. *Journal of Biological Chemistry*, 277(18), pp.15923–15931.

He, C. & Klionsky, D.J., 2009. Regulation mechanisms and signaling pathways of autophagy. *Annual review of genetics*, 43, pp.67–93.
Hetz, C., 2012. The unfolded protein response: controlling cell fate decisions under ER stress and beyond. *Nat Rev Mol Cell Biol*.
Hetz, C. et al., 2008. Unfolded protein response transcription factor XBP-1 does not influence prion replication or pathogenesis. *Proceedings of the National Academy of Sciences*, 105(2), pp.757–762.
Hetz, C. et al., 2009. XBP-1 deficiency in the nervous system protects against amyotrophic lateral sclerosis by increasing autophagy. *Genes and Development*, 23(19), pp.2294–2306.
Higgins, C.M.J., Jung, C. & Xu, Z., 2003. ALS-associated mutant SOD1G93A causes mitochondrial vacuolation by expansion of the intermembrane space and by involvement of SOD1 aggregation and peroxisomes. *BMC neuroscience*, 4, p.16.
Hirano, A. et al., 1984. Fine structural study of neurofibrillary changes in a family with amyotrophic lateral sclerosis. *Journal of neuropathology and experimental neurology*, 43(5), pp.471–80.
Hirokawa, N. et al., 2009. Kinesin superfamily motor proteins and intracellular transport. *Nature reviews. Molecular cell biology*, 10(10), pp.682–96.
Ho, Y.S. et al., 1998. Reduced fertility in female mice lacking copper-zinc superoxide dismutase. *The Journal of biological chemistry*, 273(13), pp.7765–7769.
Homma, K. et al., 2013. SOD1 as a molecular switch for initiating the homeostatic ER stress response under zinc deficiency. *Molecular Cell*, 52(1), pp.75–86.
Hough, M. a et al., 2004. Dimer destabilization in superoxide dismutase may result in disease-causing properties: structures of motor neuron disease mutants. *Proceedings of the National Academy of Sciences of the United States of America*, 101(16), pp.5976–5981.
Howarth, J.L., Glover, C.P.J. & Uney, J.B., 2009. HSP70 interacting protein prevents the accumulation of inclusions in polyglutamine disease. *Journal of Neurochemistry*, 108(4), pp.945–951.
Huang, C. et al., 2011. FUS transgenic rats develop the phenotypes of amyotrophic lateral sclerosis and frontotemporal lobar degeneration. *PLoS Genetics*, 7(3).
Huang, T.T. et al., 1997. Superoxide-mediated cytotoxicity in superoxide dismutase-deficient fetal fibroblasts. *Archives of biochemistry and biophysics*, 344(2), pp.424–432.
Huber, A.L. et al., 2013. P58IPK-Mediated Attenuation of the Proapoptotic PERK-CHOP Pathway Allows Malignant Progression upon Low Glucose. *Molecular Cell*, 49(6), pp.1049–1059.
Van Huizen, R. et al., 2003. P58IPK, a novel endoplasmic reticulum stress-inducible protein and potential negative regulator of eIF2?? signaling. *Journal of Biological Chemistry*, 278(18), pp.15558–15564.
Hwang, Y.M. et al., 2010. Nonamyloid aggregates arising from mature copper/zinc superoxide dismutases resemble those observed in amyotrophic lateral sclerosis. *Journal of Biological Chemistry*, 285(53), pp.41701–41711.
Iba, M. et al., 2013. Synthetic tau fibrils mediate transmission of neurofibrillary tangles in a transgenic mouse model of Alzheimer's-like tauopathy. *J Neurosci*, 33(3), pp.1024–1037..
Iko, Y. et al., 2004. Domain architectures and characterization of an RNA-binding protein, TLS. *Journal of Biological Chemistry*, 279(43), pp.44834–44840.
Imai, Y. & Kohsaka, S., 2002. Intracellular signaling in M-CSF-induced microglia activation: Role of Iba1. *GLIA*, 40(2), pp.164–174.
Ip, P., Mulligan, V.K. & Chakrabartty, A., 2011. ALS-causing SOD1 mutations promote production of copper-deficient misfolded species. *Journal of Molecular Biology*, 409(5), pp.839–852.
Ishigaki, S. et al., 2002. X-linked inhibitor of apoptosis protein is involved in mutant SOD1-mediated neuronal degeneration. *Journal of Neurochemistry*, 82(3), pp.576–584.
Israelson, A. et al., 2010. Misfolded mutant SOD1 directly inhibits VDAC1 conductance in a mouse model of inherited ALS. *Neuron*, 67(4), pp.575–587.
Ittner, L.M. et al., 2015. FTD and ALS[mdash]translating mouse studies into clinical trials. *Nat Rev Neurol*, 11(6), pp.360–366.
Jaarsma, D. et al., 2000. Human Cu/Zn superoxide dismutase (SOD1) overexpression in mice causes mitochondrial vacuolization, axonal degeneration, and premature motoneuron death and accelerates motoneuron disease in mice expressing a familial amyotrophic lateral sclerosis mutant SO. *Neurobiology of disease*, 7(6 Pt B), pp.623–643.

Jahn, T.R. & Radford, S.E., 2005. The Yin and Yang of protein folding. *FEBS Journal*, 272(23), pp.5962–5970.
Jain, M.R. et al., 2008. Amyotrophic lateral sclerosis: Protein chaperone dysfunction revealed by proteomic studies of animal models. *Proteomics - Clinical Applications*, 2(5), pp.670–684.
Jaiswal, M.K. & Keller, B.U., 2009. Cu/Zn superoxide dismutase typical for familial amyotrophic lateral sclerosis increases the vulnerability of mitochondria and perturbs Ca2+ homeostasis in SOD1G93A mice. *Molecular pharmacology*, 75(3), pp.478–489.
Johansen, T. & Lamark, T., 2011. Selective autophagy mediated by autophagic adapter proteins. *Autophagy*, 7(3), pp.279–296.
Joyce, P.I. et al., 2011. SOD1 and TDP-43 animal models of amyotrophic lateral sclerosis: Recent advances in understanding disease toward the development of clinical treatments. *Mammalian Genome*, 22(7–8), pp.420–448.
Julien, J.-P., 2007. ALS: astrocytes move in as deadly neighbors. *Nature neuroscience*, 10(5), pp.535–537.
Kabashi, E. et al., 2004. Focal dysfunction of the proteasome: A pathogenic factor in a mouse model of amyotrophic lateral sclerosis. *Journal of Neurochemistry*, 89(6), pp.1325–1335.
Kabashi, E. et al., 2011. Fus and tardbp but not sod1 interact in genetic models of amyotrophic lateral sclerosis. *PLoS Genetics*, 7(8).
Kabashi, E. & Durham, H.D., 2006. Failure of protein quality control in amyotrophic lateral sclerosis. *Biochimica et biophysica acta*, 1762(11–12), pp.1038–50.
Kalmar, B. et al., 2008. Late stage treatment with arimoclomol delays disease progression and prevents protein aggregation in the SOD1G93A mouse model of ALS. *Journal of Neurochemistry*, 107(2), pp.339–350.
Kalmar, B., Lu, C.-H. & Greensmith, L., 2014. The role of heat shock proteins in Amyotrophic Lateral Sclerosis: The therapeutic potential of Arimoclomol. *Pharmacology & therapeutics*, 141(1), pp.40–54.
Kane, M.D. et al., 2000. Evidence for seeding of beta -amyloid by intracerebral infusion of Alzheimer brain extracts in beta -amyloid precursor protein-transgenic mice. *The Journal of neuroscience : the official journal of the Society for Neuroscience*, 20(10), pp.3606–11.
Kanekura, K. et al., 2005. A Rac1/phosphatidylinositol 3-kinase/Akt3 anti-apoptotic pathway, triggered by alsinLF, the product of the ALS2 gene, antagonizes Cu/Zn-superoxide dismutase (SOD1) mutant-induced motoneuronal cell death. *Journal of Biological Chemistry*, 280(6), pp.4532–4543.
Kang, J. & Rivest, S., 2007. MyD88-deficient bone marrow cells accelerate onset and reduce survival in a mouse model of amyotrophic lateral sclerosis. *J Cell Biol*, 179(6), pp.1219–1230.
Karch, C.M. & Borchelt, D.R., 2010. An examination of αb-crystallin as a modifier of SOD1 aggregate pathology and toxicity in models of familial amyotrophic lateral sclerosis. *Journal of Neurochemistry*, 113(5), pp.1092–1100.
Kato, S. et al., 2001. Copper chaperone for superoxide dismutase co-aggregates with superoxide dismutase 1 (SOD1) in neuronal Lewy body-like hyaline inclusions: an immunohistochemical study on familial amyotrophic lateral sclerosis with SOD1 gene mutation. *Acta neuropathologica*, 102(3), pp.233–8.
Kaus, A. & Sareen, D., 2015. ALS Patient Stem Cells for Unveiling Disease Signatures of Motoneuron Susceptibility: Perspectives on the Deadly Mitochondria, ER Stress and Calcium Triad. *Frontiers in cellular neuroscience*, 9(November), p.448.
Kawahara, Y. et al., 2003. Human spinal motoneurons express low relative abundance of GluR2 mRNA: an implication for excitotoxicity in ALS. *Journal of neurochemistry*, 85(3), pp.680–689.
Kawamata, H. & Manfredi, G., 2010. Mitochondrial dysfunction and intracellular calcium dysregulation in ALS. *Mechanisms of Ageing and Development*, 131(7–8), pp.517–526.
Keinan, N. et al., 2013. The role of calcium in VDAC1 oligomerization and mitochondria-mediated apoptosis. *Biochimica et Biophysica Acta - Molecular Cell Research*, 1833(7), pp.1745–1754.
Kiaei, M. et al., 2005. Celastrol blocks neuronal cell death and extends life in transgenic mouse model of amyotrophic lateral sclerosis. *Neuro-degenerative diseases*, 2(5), pp.246–254.
Kieran, D. et al., 2004. Treatment with arimoclomol, a coinducer of heat shock proteins, delays disease progression in ALS mice. *Nature Medicine*, 10(4), pp.402–405.

Kikuchi, H. et al., 2006. Spinal cord endoplasmic reticulum stress associated with a microsomal accumulation of mutant superoxide dismutase-1 in an ALS model. *Proceedings of the National Academy of Sciences of the United States of America*, 103(15), pp.6025–30.
Kim, H.J. et al., 2007. Calcium-influx increases SOD1 aggregates via nitric oxide in cultured motor neurons. *Experimental & molecular medicine*, 39(5), pp.574–582.
Kirby, J. et al., 2005. Mutant SOD1 alters the motor neuronal transcriptome: Implications for familial ALS. *Brain*, 128(7), pp.1686–1706.
Kirkinezos, I.G. et al., 2005. Cytochrome c association with the inner mitochondrial membrane is impaired in the CNS of G93A-SOD1 mice. *The Journal of neuroscience : the official journal of the Society for Neuroscience*, 25(1), pp.164–72.
Komatsu, M. et al., 2006. Loss of autophagy in the central nervous system causes neurodegeneration in mice. *Nature*, 441(7095), pp.880–884.
Komine, O. & Yamanaka, K., 2015. Neuroinflammation in motor neuron disease. *Nagoya journal of medical science*, 77(4), pp.537–549.
Kong, Q. et al., 2012. Increased glial glutamate transporter EAAT2 expression reduces epileptogenic processes following pilocarpine-induced status epilepticus. *Neurobiology of Disease*, 47(2), pp.145–154.
Kordower, J.H. et al., 2011. Transfer of host-derived alpha synuclein to grafted dopaminergic neurons in rat. *Neurobiology of Disease*, 43(3), pp.552–557.
Korolchuk, V.I., Menzies, F.M. & Rubinsztein, D.C., 2010. Mechanisms of cross-talk between the ubiquitin-proteasome and autophagy-lysosome systems. *FEBS Letters*, 584(7), pp.1393–1398.
Kostic, V. et al., 1997. Bcl-2: prolonging life in a transgenic mouse model of familial amyotrophic lateral sclerosis. *Science*, 277(5325), pp.559–562.
Koyama, S. et al., 2006. Alteration of familial ALS-linked mutant SOD1 solubility with disease progression: Its modulation by the proteasome and Hsp70. *Biochemical and Biophysical Research Communications*, 343(3), pp.719–730.
Kraft, A.D. et al., 2007. Activation of the Nrf2-ARE pathway in muscle and spinal cord during ALS-like pathology in mice expressing mutant SOD1. *Experimental Neurology*, 207(1), pp.107–117.
Kraft, C., Peter, M. & Hofmann, K., 2010. Selective autophagy: ubiquitin-mediated recognition and beyond. *Nature cell biology*, 12(9), pp.836–841.
Kriegenburg, F., Ellgaard, L. & Hartmann-Petersen, R., 2012. Molecular chaperones in targeting misfolded proteins for ubiquitin-dependent degradation. *FEBS Journal*, 279(4), pp.532–542.
Krishnan, J. et al., 2008. Over-expression of Hsp27 does not influence disease in the mutant SOD1(G93A) mouse model of amyotrophic lateral sclerosis. *Journal of neurochemistry*, 106(5), pp.2170–83.
Kuijpers, M. et al., 2013. The ALS8 protein VAPB interacts with the ER-Golgi recycling protein YIF1A and regulates membrane delivery into dendrites. *The EMBO journal*, 32(14), pp.2056–72.
Kuo, P.H. et al., 2009. Structural insights into TDP-43 in nucleic-acid binding and domain interactions. *Nucleic Acids Research*, 37(6), pp.1799–1808.
Kwak, S. et al., 2010. AMPA receptor-mediated neuronal death in sporadic ALS. In *Neuropathology*. pp. 182–188.
Kwak, S. & Kawahara, Y., 2005. Deficient RNA editing of GluR2 and neuronal death in amyotropic lateral sclerosis. *Journal of Molecular Medicine*, 83(2), pp.110–120.
Kwiatkowski, T.J. et al., 2009. Mutations in the FUS/TLS gene on chromosome 16 cause familial amyotrophic lateral sclerosis. *Science (New York, N.Y.)*, 323(5918), pp.1205–1208.
Labbadia, J. et al., 2012. Suppression of protein aggregation by chaperone modification of high molecular weight complexes. *Brain*, 135(4), pp.1180–1186.
de Lahunta, A. et al., 2009a. Chapter 6 – Lower Motor Neuron: General Somatic Efferent, Cranial Nerve. In *Veterinary Neuroanatomy and Clinical Neurology*. pp. 134–167.
de Lahunta, A. et al., 2009b. Chapter 8 – Upper Motor Neuron. In *Veterinary Neuroanatomy and Clinical Neurology*. pp. 192–220.
Lai, C. et al., 2006. Amyotrophic lateral sclerosis 2-deficiency leads to neuronal degeneration in amyotrophic lateral sclerosis through altered AMPA receptor trafficking. *The Journal of neuroscience : the official journal of the Society for Neuroscience*, 26(45), pp.11798–806.
Van Langenhove, T. et al., 2012. Ataxin-2 polyQ expansions in FTLD-ALS spectrum disorders in Flanders-Belgian cohorts. *Neurobiology of Aging*, 33(5).

Laufen, T. et al., 1999. Mechanism of regulation of Hsp70 chaperones by DnaJ cochaperones. *Proceedings of the National Academy of Sciences of the United States of America*, 96(10), pp.5452–5457.

Lautenschlaeger, J., Prell, T. & Grosskreutz, J., 2012. Endoplasmic reticulum stress and the ER mitochondrial calcium cycle in amyotrophic lateral sclerosis. *Amyotrophic lateral sclerosis : official publication of the World Federation of Neurology Research Group on Motor Neuron Diseases*, 13(2), pp.166–77.

Leal, S.S. et al., 2013. Calcium ions promote superoxide dismutase 1 (SOD1) aggregation into non-fibrillar amyloid: A link to toxic effects of calcium overload in amyotrophic lateral sclerosis (ALS)? *Journal of Biological Chemistry*, 288(35), pp.25219–25228.

Leal, S.S. & Gomes, C.M., 2015. Calcium dysregulation links ALS defective proteins and motor neuron selective vulnerability. *Frontiers in cellular neuroscience*, 9, p.225.

Lee, G.J. et al., 1997. A small heat shock protein stably binds heat-denatured model substrates and can maintain a substrate in a folding-competent state. *EMBO Journal*, 16(3), pp.659–671.

Lee, J.A. et al., 2007. ESCRT-III Dysfunction Causes Autophagosome Accumulation and Neurodegeneration. *Current Biology*, 17(18), pp.1561–1567.

Lefebvre, S. et al., 1995. Identification and characterization of a spinal muscular atrophy-determining gene. *Cell*, 80(1), pp.155–165.

Von Lewinski, F. & Keller, B.U., 2005. Ca2+, mitochondria and selective motoneuron vulnerability: Implications for ALS. *Trends in Neurosciences*, 28(9), pp.494–500.

Li, A., Zhang, X. & Le, W., 2008. Altered macroautophagy in the spinal cord of SOD1 mutant mice. *Autophagy*, 4(3), pp.290–293.

Li, J. & Buchner, J., 2012. Structure, function and regulation of the hsp90 machinery. *Biomedical journal*, 36(3), pp.106–17.

Li, M. et al., 2000. Functional role of caspase-1 and caspase-3 in an ALS transgenic mouse model. *Science (New York, N.Y.)*, 288(5464), pp.335–339.

Li, Q. et al., 2011. Alsin and SOD1 G93A proteins regulate endosomal reactive oxygen species production by glial cells and proinflammatory pathways responsible for neurotoxicity. *Journal of Biological Chemistry*, 286(46), pp.40151–40162.

Li, W.W., Li, J. & Bao, J.K., 2012. Microautophagy: Lesser-known self-eating. *Cellular and Molecular Life Sciences*, 69(7), pp.1125–1136.

Lim, P.J. et al., 2009. Ubiquilin and p97/VCP bind erasin, forming a complex involved in ERAD. *Journal of Cell Biology*, 187(2), pp.201–217.

Lima, N.M.F.V. & Nucci, A., 2011. Clinical attention and assistance profile of patients with amyotrophic lateral sclerosis. *Arquivos de neuro-psiquiatria*, 69(August 2010), pp.170–175.

Lin, P.-Y. et al., 2013. Heat shock factor 1 over-expression protects against exposure of hydrophobic residues on mutant SOD1 and early mortality in a mouse model of amyotrophic lateral sclerosis. *Molecular neurodegeneration*, 8, p.43.

Lin, Y.L. & Lai, Z.X., 2013. Superoxide dismutase multigene family in longan somatic embryos: A comparison of CuZn-SOD, Fe-SOD, and Mn-SOD gene structure, splicing, phylogeny, and expression. *Molecular Breeding*, 32(3), pp.595–615.

Lindquist, S. & Craig, E. a., 1988. The heat-shock proteins. *Annual Review of Genetics*, 22, pp.631–677.

Liu, C.M. & Hermann, T.E., 1978. Characterization of ionomycin as a calcium ionophore. *Journal of Biological Chemistry*, 253(17), pp.5892–5894.

Liu, H.-N. et al., 2012. Targeting of Monomer/Misfolded SOD1 as a Therapeutic Strategy for Amyotrophic Lateral Sclerosis. *Journal of Neuroscience*, 32(26), pp.8791–8799.

Liu, J. et al., 2009. Deranged calcium signaling and neurodegeneration in spinocerebellar ataxia type 2. *The Journal of neuroscience : the official journal of the Society for Neuroscience*, 29(29), pp.9148–62.

Liu, J. et al., 2005. Elevation of the Hsp70 chaperone does not effect toxicity in mouse models of familial amyotrophic lateral sclerosis. *Journal of Neurochemistry*, 93(4), pp.875–882.

Liu, Y. et al., 2009. Expression of amyotrophic lateral sclerosis-linked SOD1 mutant increases the neurotoxic potential of microglia via TLR2. *Journal of Biological Chemistry*, 284(6), pp.3691–3699.

Lloyd, T.E. et al., 2012. The p150 Glued CAP-Gly Domain Regulates Initiation of Retrograde Transport at Synaptic Termini. *Neuron*, 74(2), pp.344–360.

Lu, L. et al., 2007. Mutant Cu/Zn-superoxide dismutase associated with amyotrophic lateral sclerosis destabilizes vascular endothelial growth factor mRNA and downregulates its expression. *Journal of Neuroscience*, 27(30), pp.7929–7938.

Lytton, J., Westlin, M. & Hanley, M.R., 1991. Thapsigargin inhibits the sarcoplasmic or endoplasmic reticulum Ca-ATPase family of calcium pumps. *Journal of Biological Chemistry*, 266(26), pp.17067–17071.

Mackenzie, I.R.A. et al., 2007. Pathological TDP-43 distinguishes sporadic amyotrophic lateral sclerosis from amyotrophic lateral sclerosis with SOD1 mutations. *Annals of Neurology*, 61(5), pp.427–434.

Maday, S., Wallace, K.E. & Holzbaur, E.L.F., 2012. Autophagosomes initiate distally and mature during transport toward the cell soma in primary neurons. *Journal of Cell Biology*, 196(4), pp.407–417.

Majeski, A.E. & Fred Dice, J., 2004. Mechanisms of chaperone-mediated autophagy. *International Journal of Biochemistry and Cell Biology*, 36(12), pp.2435–2444.

Månsson, C., Kakkar, V., et al., 2014. DNAJB6 is a peptide-binding chaperone which can suppress amyloid fibrillation of polyglutamine peptides at substoichiometric molar ratios. *Cell Stress and Chaperones*, 19(2), pp.227–239.

Månsson, C., Arosio, P., et al., 2014. Interaction of the molecular chaperone DNAJB6 with growing amyloid-beta 42 (A??42) aggregates leads to sub-stoichiometric inhibition of amyloid formation. *Journal of Biological Chemistry*, 289(45), pp.31066–31076.

Marden, J.J. et al., 2007. Redox modifier genes in amyotrophic lateral sclerosis in mice. *Journal of Clinical Investigation*, 117(10), pp.2913–2919.

Martyshkin, D. V. et al., 2003. Fluorescence assay for monitoring Zn-deficient superoxide dismutase in vitro. *Spectrochimica Acta - Part A: Molecular and Biomolecular Spectroscopy*, 59(13), pp.3165–3175.

Matsumoto, G. et al., 2005. Structural properties and neuronal toxicity of amyotrophic lateral sclerosis-associated Cu/Zn superoxide dismutase 1 aggregates. *Journal of Cell Biology*, 171(1), pp.75–85.

Matsumoto, G., Kim, S. & Morimoto, R.I., 2006. Huntingtin and mutant SOD1 form aggregate structures with distinct molecular properties in human cells. *Journal of Biological Chemistry*, 281(7), pp.4477–4485.

Matzuk, M.M. et al., 1998. Ovarian function in superoxide dismutase 1 and 2 knockout mice. *Endocrinology*, 139(9), pp.4008–11.

Mayer, M.P. & Bukau, B., 2005. Hsp70 chaperones: cellular functions and molecular mechanism. *Cellular and molecular life sciences : CMLS*, 62(6), pp.670–84.

McCord, J.M. & Fridovich, I., 1969. Superoxide dismutase. An enzymic function for erythrocuprein (hemocuprein). *Journal of Biological Chemistry*, 244(22), pp.6049–6055.

McGoldrick, P. et al., 2013. Rodent models of amyotrophic lateral sclerosis. *Biochimica et biophysica acta*, 1832(9), pp.1421–36.

Meimaridou, E. et al., 2011. The cytosolic chaperone hsc70 promotes traffic to the cell surface of intracellular retained melanocortin-4 receptor mutants. *Molecular endocrinology (Baltimore, Md.)*, 25(9), pp.1650–1660.

Menzies, F.M. et al., 2002. Mitochondrial dysfunction in a cell culture model of familial amyotrophic lateral sclerosis. *Brain*, 125(Pt 7), pp.1522–1533.

Meusser, B. et al., 2005. ERAD: the long road to destruction. *Nature cell biology*, 7(8), pp.766–772.

Meyer-Luehmann, M. et al., 2006. Exogenous induction of cerebral beta-amyloidogenesis is governed by agent and host. *Science (New York, N.Y.)*, 313(5794), pp.1781–4.

Mitchell, J.C. et al., 2013. Overexpression of human wild-type FUS causes progressive motor neuron degeneration in an age- and dose-dependent fashion. *Acta Neuropathologica*, 125(2), pp.273–288.

Mitsumoto, H., Brooks, B.R. & Silani, V., 2014. Clinical trials in amyotrophic lateral sclerosis: why so many negative trials and how can trials be improved? *The Lancet Neurology*, 13(11), pp.1127–1138.

Miyazaki, K. et al., 2004. NEDL1, a Novel Ubiquitin-protein Isopeptide Ligase for Dishevelled-1, Targets Mutant Superoxide Dismutase-1. *Journal of Biological Chemistry*, 279(12), pp.11327–11335.

Mogk, A. et al., 2003. Small heat shock proteins, ClpB and the DnaK system form a functional triade in reversing protein aggregation. *Molecular Microbiology*, 50(2), pp.585–595.

Mori, A. et al., 2011. Derlin-1 overexpression ameliorates mutant SOD1-induced endoplasmic reticulum stress by reducing mutant SOD1 accumulation. *Neurochemistry International*, 58(3), pp.344–353.
Morimoto, N. et al., 2007. Increased autophagy in transgenic mice with a G93A mutant SOD1 gene. *Brain Research*, 1167(1), pp.112–117.
Morohoshi, F. et al., 1998. Genomic structure of the human RBP56/hTAF(II)68 and FUS/TLS genes. *Gene*, 221(2), pp.191–198.
Mórotz, G.M. et al., 2012. Amyotrophic lateral sclerosis-associated mutant VAPBP56s perturbs calcium homeostasis to disrupt axonal transport of mitochondria. *Human Molecular Genetics*, 21(9), pp.1979–1988.
Morris, J.A. et al., 1997. Immunoglobulin binding protein (BiP) function is required to protect cells from endoplasmic reticulum stress but is not required for the secretion of selective proteins. *Journal of Biological Chemistry*, 272(7), pp.4327–4334.
Mosharov, E. V. et al., 2009. Interplay between Cytosolic Dopamine, Calcium, and α-Synuclein Causes Selective Death of Substantia Nigra Neurons. *Neuron*, 62(2), pp.218–229.
Moustaqim-barrette, A. et al., 2014. The amyotrophic lateral sclerosis 8 protein, VAP, is required for ER protein quality control. *Human Molecular Genetics*, 23(8), pp.1975–1989.
Mulligan, V.K. & Chakrabartty, A., 2013. Protein misfolding in the late-onset neurodegenerative diseases: common themes and the unique case of amyotrophic lateral sclerosis. *Proteins*, 81(8), pp.1285–303.
Münch, C. et al., 2004. Point mutations of the p150 subunit of dynactin (DCTN1) gene in ALS. *Neurology*, 63(4), pp.724–726.
Munch, C. & Bertolotti, A., 2010. Exposure of hydrophobic surfaces initiates aggregation of diverse ALS-causing superoxide dismutase-1 mutants. *Journal of Molecular Biology*, 399(3), pp.512–525.
Münch, C. & Bertolotti, A., 2011. Self-propagation and transmission of misfolded mutant SOD1: Prion or prion-like phenomenon? *Cell Cycle*, 10(11), p.1711.
Münch, C., O'Brien, J. & Bertolotti, A., 2011. Prion-like propagation of mutant superoxide dismutase-1 misfolding in neuronal cells. *Proceedings of the National Academy of Sciences of the United States of America*, 108(9), pp.3548–53.
Myung, J., Kim, K.B. & Crews, C.M., 2001. The ubiquitin-proteasome pathway and proteasome inhibitors. *Medicinal research reviews*, 21(4), pp.245–73.
Nagata, T. et al., 2007. Increased ER stress during motor neuron degeneration in a transgenic mouse model of amyotrophic lateral sclerosis. *Neurological research*, 29(8), pp.767–771.
Naidoo, N., 2009. ER and aging-Protein folding and the ER stress response. *Ageing Research Reviews*, 8(3), pp.150–159.
Nandi, D. et al., 2006. The ubiquitin-proteasome system. *J Biosci*, 31(1), pp.137–155.
Neumann, M. et al., 2006. Ubiquitinated TDP-43 in frontotemporal lobar degeneration and amyotrophic lateral sclerosis. *Science (New York, N.Y.)*, 314(5796), pp.130–3.
Nishimura, A.L. et al., 2004. A mutation in the vesicle-trafficking protein VAPB causes late-onset spinal muscular atrophy and amyotrophic lateral sclerosis. *American journal of human genetics*, 75(5), pp.822–31.
Nishitoh, H. et al., 2008. ALS-linked mutant SOD1 induces ER stress- and ASK1-dependent motor neuron death by targeting Derlin-1. *Genes and Development*, 22(11), pp.1451–1464.
Niwa, J.I. et al., 2007. Disulfide bond mediates aggregation, toxicity, and ubiquitylation of familial amyotrophic lateral sclerosis-linked mutant SOD1. *Journal of Biological Chemistry*, 282(38), pp.28087–28095.
Niwa, J.I. et al., 2002. Dorfin ubiquitylates mutant SOD1 and prevents mutant SOD1-mediated neurotoxicity. *Journal of Biological Chemistry*, 277(39), pp.36793–36798.
Novoselov, S.S. et al., 2013. Molecular Chaperone Mediated Late-Stage Neuroprotection in the SOD1G93A Mouse Model of Amyotrophic Lateral Sclerosis. *PLoS ONE*, 8(8).
Olby, N., 2004. Motor neuron disease: Inherited and acquired. *Veterinary Clinics of North America - Small Animal Practice*, 34(6 SPEC.ISS.), pp.1403–1418.
De Oliveira, G.P. et al., 2014. Early gene expression changes in skeletal muscle from SOD1G93A amyotrophic lateral sclerosis animal model. *Cellular and Molecular Neurobiology*, 34(3), pp.451–462.
de Oliveira, G.P., Alves, C.J. & Chadi, G., 2013. Early gene expression changes in spinal cord from SOD1(G93A) Amyotrophic Lateral Sclerosis animal model. *Frontiers in cellular neuroscience*, 7(November), p.216.

Olzmann, J. a, Li, L. & Chin, L.S., 2008. Aggresome formation and neurodegenerative diseases: therapeutic implications. *Current medicinal chemistry*, 15(1), pp.47–60.

van Oosten-Hawle, P. & Morimoto, R.I., 2014. Organismal proteostasis: Role of cell-nonautonomous regulation and transcellular chaperone signaling. *Genes and Development*, 28(14), pp.1533–1543.

Ortega, Z. et al., 2010. Acute polyglutamine expression in inducible mouse model unravels ubiquitin/proteasome system impairment and permanent recovery attributable to aggregate formation. *The Journal of neuroscience : the official journal of the Society for Neuroscience*, 30(10), pp.3675–3688.

Osellame, L.D. & Duchen, M.R., 2013. Defective quality control mechanisms and accumulation of damaged mitochondria link Gaucher and Parkinson diseases. *Autophagy*, 9(10), pp.1633–1635.

Otomo, A. et al., 2011. Defective relocalization of ALS2/alsin missense mutants to Rac1-induced macropinosomes accounts for loss of their cellular function and leads to disturbed amphisome formation. *FEBS Letters*, 585(5), pp.730–736.

Ou, S.H. et al., 1995. Cloning and characterization of a novel cellular protein, TDP-43, that binds to human immunodeficiency virus type 1 TAR DNA sequence motifs. *Journal of Virology*, 69(6), pp.3584–3596.

Ouyang, H. et al., 2012. Protein aggregates are recruited to aggresome by histone deacetylase 6 via unanchored ubiquitin C termini. *Journal of Biological Chemistry*, 287(4), pp.2317–2327.

Oztug Durer, Z.A. et al., 2009. Loss of metal ions, disulfide reduction and mutations related to familial ALS promote formation of amyloid-like aggregates from superoxide dismutase. *PLoS ONE*, 4(3).

Palecek, J., Lips, M.B. & Keller, B.U., 1999. Calcium dynamics and buffering in motoneurones of the mouse spinal cord. *The Journal of physiology*, 520 Pt 2, pp.485–502.

Panaretou, B. et al., 2002. Activation of the ATPase activity of Hsp90 by the stress-regulated cochaperone Aha1. *Molecular Cell*, 10(6), pp.1307–1318.

Pandey, U.B. et al., 2007. HDAC6 rescues neurodegeneration and provides an essential link between autophagy and the UPS. *Nature*, 447(7146), pp.859–863.

Pardo, C.A. et al., 1995. Superoxide-Dismutase Is an Abundant Component in Cell-Bodies, Dendrites, and Axons of Motor-Neurons and in a Subset of Other Neurons. *Proceedings of the National Academy of Sciences of the United States of America*, 92, p.954–958 ST–Superoxide–Dismutase Is an Abundant.

Parone, P.A. et al., 2013. Enhancing Mitochondrial Calcium Buffering Capacity Reduces Aggregation of Misfolded SOD1 and Motor Neuron Cell Death without Extending Survival in Mouse Models of Inherited Amyotrophic Lateral Sclerosis. *Journal of Neuroscience*, 33(11), pp.4657–4671.

Parton, R.G. & Dotti, C.G., 1993. Cell biology of neuronal endocytosis. *Journal of Neuroscience Research*, 36(1), pp.1–9.

Pasinelli, P. et al., 2004. Amyotrophic lateral sclerosis-associated SOD1 mutant proteins bind and aggregate with Bcl-2 in spinal cord mitochondria. *Neuron*, 43(1), pp.19–30.

Patel, Y.J.K. et al., 2005. Hsp27 and Hsp70 administered in combination have a potent protective effect against FALS-associated SOD1-mutant-induced cell death in mammalian neuronal cells. *Molecular Brain Research*, 134(2), pp.256–274.

Paul, P. & De Belleroche, J., 2014. The role of D-serine and glycine as co-agonists of NMDA receptors in motor neuron degeneration and amyotrophic lateral sclerosis (ALS). *Frontiers in Synaptic Neuroscience*, 6(APR).

Pearl, L.H. & Prodromou, C., 2006. Structure and mechanism of the Hsp90 molecular chaperone machinery. *Annual review of biochemistry*, 75, pp.271–294.

Pedrini, S. et al., 2010. ALS-linked mutant SOD1 damages mitochondria by promoting conformational changes in Bcl-2. *Human Molecular Genetics*, 19(15), pp.2974–2986.

Peeraer, E. et al., 2015. Intracerebral injection of preformed synthetic tau fibrils initiates widespread tauopathy and neuronal loss in the brains of tau transgenic mice. *Neurobiology of Disease*, 73, pp.83–95.

Pehar, M. et al., 2004. Astrocytic production of nerve growth factor in motor neuron apoptosis: implications for amyotrophic lateral sclerosis. *Journal of neurochemistry*, 89(2), pp.464–73.

Pemberton, S. et al., 2011. Hsc70 protein interaction with soluble and fibrillar ??-synuclein. *Journal of Biological Chemistry*, 286(40), pp.34690–34699.

Pickles, S. et al., 2013. Mitochondrial damage revealed by immunoselection for ALS-linked misfolded SOD1. *Human Molecular Genetics*, 22(19), pp.3947–3959.
Pincus, D. et al., 2010. BiP binding to the ER-stress sensor Ire1 tunes the homeostatic behavior of the unfolded protein response. *PLoS Biology*, 8(7).
Plongthongkum, N. et al., 2007. Ire1 regulated XBP1 mRNA splicing is essential for the unfolded protein response (UPR) in Drosophila melanogaster. *Biochemical and Biophysical Research Communications*, 354(3), pp.789–794.
Pokrishevsky, E., Grad, L.I. & Cashman, N.R., 2016. TDP-43 or FUS-induced misfolded human wild-type SOD1 can propagate intercellularly in a prion-like fashion. *Scientific reports*, 6, p.22155.
Polymenidou, M. & Cleveland, D.W., 2008. Motor neuron disease: The curious ways of ALS. *Nature*, 454(7202), pp.284–285.
Prause, J. et al., 2013. Altered localization, abnormal modification and loss of function of sigma receptor-1 in amyotrophic lateral sclerosis. *Human Molecular Genetics*, 22(8), pp.1581–1600.
Prudencio, M. et al., 2010. An examination of wild-type SOD1 in modulating the toxicity and aggregation of ALS-associated mutant SOD1. *Human Molecular Genetics*, 19(24), pp.4774–4789.
Prudencio, M. et al., 2009. Modulation of mutant superoxide dismutase 1 aggregation by co-expression of wild-type enzyme. *Journal of Neurochemistry*, 108(4), pp.1009–1018.
Qualls, D. a et al., 2013. Features of wild-type human SOD1 limit interactions with misfolded aggregates of mouse G86R Sod1. *Molecular neurodegeneration*, 8, p.46.
Rakhit, R. et al., 2007. An immunological epitope selective for pathological monomer-misfolded SOD1 in ALS. *Nature medicine*, 13(6), pp.754–759.
Rakhit, R. & Chakrabartty, A., 2006. Structure, folding, and misfolding of Cu,Zn superoxide dismutase in amyotrophic lateral sclerosis. *Biochimica et biophysica acta*, 1762(11–12), pp.1025–1037.
Ramahi, A.A., Katirji, B. & Devereaux, M., 2014. Lower Motor Neuron Lesions. In *Encyclopedia of the Neurological Sciences*. pp. 918–922.
Ratovitski, T. et al., 1999. Variation in the biochemical/biophysical properties of mutant superoxide dismutase 1 enzymes and the rate of disease progression in familial amyotrophic lateral sclerosis kindreds. *Human Molecular Genetics*, 8(8), pp.1451–1460.
Reaume, a G. et al., 1996. Motor neurons in Cu/Zn superoxide dismutase-deficient mice develop normally but exhibit enhanced cell death after axonal injury. *Nature genetics*, 13(1), pp.43–47.
Redler, R.L. et al., 2011. Glutathionylation at Cys-111 induces dissociation of wild type and FALS mutant SOD1 dimers. *Biochemistry*, 50(32), pp.7057–7066.
Redler, R.L. et al., 2014. Non-native soluble oligomers of Cu/Zn superoxide dismutase (SOD1) contain a conformational epitope linked to cytotoxicity in amyotrophic lateral sclerosis (ALS). *Biochemistry*, 53(14), pp.2423–2432.
Redler, R.L. & Dokholyan, N. V., 2012. The complex molecular biology of Amyotrophic Lateral Sclerosis (ALS). *Progress in Molecular Biology and Translational Science*, 107, pp.215–262.
Ren, P.-H. et al., 2009. Cytoplasmic penetration and persistent infection of mammalian cells by polyglutamine aggregates. *Nature cell biology*, 11(2), pp.219–225.
Renton, A.E. et al., 2011. A hexanucleotide repeat expansion in C9ORF72 is the cause of chromosome 9p21-linked ALS-FTD. *Neuron*, 72(2), pp.257–268.
Ritz, D. et al., 2011. Endolysosomal sorting of ubiquitylated caveolin-1 is regulated by VCP and UBXD1 and impaired by VCP disease mutations. *Nature cell biology*, 13(9), pp.1116–23.
Roberts, B.R. et al., 2007. Structural Characterization of Zinc-deficient Human Superoxide Dismutase and Implications for ALS. *Journal of Molecular Biology*, 373(4), pp.877–890.
Rodriguez, J.A. et al., 2005. Destabilization of apoprotein is insufficient to explain Cu,Zn-superoxide dismutase-linked ALS pathogenesis. *Proceedings of the National Academy of Sciences of the United States of America*, 102(30), pp.10516–21.
Roe, J.A. et al., 1988. Differential scanning calorimetry of Cu,Zn-superoxide dismutase, the apoprotein, and its zinc-substituted derivatives. *Biochemistry*, 27(3), pp.950–958.
Rose, J.M. et al., 2011. Molecular chaperone-mediated rescue of mitophagy by a Parkin RING1 domain mutant. *Human Molecular Genetics*, 20(1), pp.16–27.
Rosen, D.R. et al., 1993. Mutations in Cu/Zn superoxide dismutase gene are associated with familial amyotrophic lateral sclerosis. *Nature*, 362(6415), pp.59–62.

Rothstein, J.D. et al., 1995. Selective loss of glial glutamate transporter GLT-1 in amyotrophic lateral sclerosis. *Annals of neurology*, 38(1), pp.73–84.
Rothstein, J.D., Martin, L.J. & Kuncl, R.W., 1992. Decreased glutamate transport by the brain and spinal cord in amyotrophic lateral sclerosis. *The New England journal of medicine*, 326(22), pp.1464–1468.
Sábado, J. et al., 2014. Accumulation of misfolded SOD1 in dorsal root ganglion degenerating proprioceptive sensory neurons of transgenic mice with amyotrophic lateral sclerosis. *BioMed Research International*, 2014.
Sabatelli, M., Conte, A. & Zollino, M., 2013. Clinical and genetic heterogeneity of amyotrophic lateral sclerosis. *Clinical Genetics*, 83(5), pp.408–416.
S Boillée, V., Vande Velde, C. & Cleveland, D., 2006. ALS: A Disease of Motor Neurons and Their Nonneuronal Neighbors. *Neuron*, 52(1), pp.39–59.
Sanchez, E. et al., 2016. Identification of a Large DNAJB2 Deletion in a Family with Spinal Muscular Atrophy and Parkinsonism. *Human Mutation*.
Sandelin, E. et al., 2007. Amyotrophic lateral sclerosis-associated copper/zinc superoxide dismutase mutations preferentially reduce the repulsive charge of the proteins. *Journal of Biological Chemistry*, 282(29), pp.21230–21236.
Sano, R. & Reed, J.C., 2013. ER stress-induced cell death mechanisms. *Biochimica et Biophysica Acta - Molecular Cell Research*, 1833(12), pp.3460–3470.
Sargsyan, S.A. et al., 2009. Mutant SOD1 G93A microglia have an inflammatory phenotype and elevated production of MCP-1. *Neuroreport*, 20(16), pp.1450–5.
Sasabe, J. et al., 2012. D-Amino acid oxidase controls motoneuron degeneration through D-serine. *Proceedings of the National Academy of Sciences*, 109(2), pp.627–632.
Sasaki, S. & Iwata, M., 1999. Ultrastructural change of synapses of Betz cells in patients with amyotrophic lateral sclerosis. *Neuroscience Letters*, 268(1), pp.29–32.
Saxena, S., Cabuy, E. & Caroni, P., 2009. A role for motoneuron subtype-selective ER stress in disease manifestations of FALS mice. *Nature neuroscience*, 12(5), pp.627–36.
Saxena, S. & Caroni, P., 2011. Selective Neuronal Vulnerability in Neurodegenerative Diseases: From Stressor Thresholds to Degeneration. *Neuron*, 71(1), pp.35–48.
Sephton, C.F. et al., 2011. Identification of neuronal RNA targets of TDP-43-containing ribonucleoprotein complexes. *Journal of Biological Chemistry*, 286(2), pp.1204–1215.
Shaid, S. et al., 2012. Ubiquitination and selective autophagy. *Cell Death and Differentiation*, 20(1), pp.21–30.
Shan, X. et al., 2010. Altered distributions of Gemini of coiled bodies and mitochondria in motor neurons of TDP-43 transgenic mice. *Proceedings of the National Academy of Sciences*, 107(37), pp.16325–16330.
Sharp, P.S. et al., 2008. Protective effects of heat shock protein 27 in a model of ALS occur in the early stages of disease progression. *Neurobiology of Disease*, 30(1), pp.42–55.
Shelkovnikova, T.A. et al., 2014. Multistep process of FUS aggregation in the cell cytoplasm involves RNA-dependent and RNA-independent mechanisms. *Human molecular genetics*, 23(19), pp.5211–26.
Sheng, X. et al., 2006. Roles of the ubiquitin/proteasome pathway in pollen tube growth with emphasis on MG132-induced alterations in ultrastructure, cytoskeleton, and cell wall components. *Plant physiology*, 141(4), pp.1578–1590.
Sherman, M.Y. & Goldberg, A.L., 2001. Cellular defenses against unfolded proteins: A cell biologist thinks about neurodegenerative diseases. *Neuron*, 29(1), pp.15–32.
Shi, Y., Abdolvahabi, A. & Shaw, B.F., 2014. Protein charge ladders reveal that the net charge of ALS-linked superoxide dismutase can be different in sign and magnitude from predicted values. *Protein science : a publication of the Protein Society*, 23(10), pp.1417–33.
Shipp, E.L. et al., 2003. Dynamic properties of the G93A mutant of copper-zinc superoxide dismutase as detected by NMR spectroscopy: Implications for the pathology of familial amyotrophic lateral sclerosis. *Biochemistry*, 42(7), pp.1890–1899.
Siddique T, Figlewicz DA, Pericak-Vance MA, Haines JL, Rouleau G, Jeffers AJ, Sapp P, Hung WY, Bebout J, McKenna-Yasek D, et al., 1991. Linkage of a gene causing familial amyotrophic lateral sclerosis to chromosome 21 and evidence of genetic-locus heterogeneity. *The New England journal of medicine*, 324(4), pp.232–5.
Siklós, L. et al., 1996. Ultrastructural evidence for altered calcium in motor nerve terminals in amyotropic lateral sclerosis. *Annals of neurology*, 39, pp.203–216.
Smith, H.L., Li, W. & Cheetham, M.E., 2015. Molecular chaperones and neuronal proteostasis. *Seminars in Cell and Developmental Biology*, 40, pp.142–152.

Smith, R.G. et al., 1998. Presence of 4-hydroxynonenal in cerebrospinal fluid of patients with sporadic amyotrophic lateral sclerosis. *Annals of neurology*, 44(4), pp.696–9.

Song, Y. et al., 2013. Molecular chaperone Hsp110 rescues a vesicle transport defect produced by an ALS-associated mutant SOD1 protein in squid axoplasm. *Proceedings of the National Academy of Sciences of the United States of America*, 110(14), pp.5428–33.

Soo, K.Y. et al., 2015. Rab1-dependent ER–Golgi transport dysfunction is a common pathogenic mechanism in SOD1, TDP-43 and FUS-associated ALS. *Acta Neuropathologica*, 130(5), pp.679–697.

Sou, S.N., Ilieva, K.M. & Polizzi, K.M., 2012. Binding of human BiP to the ER stress transducers IRE1 and PERK requires ATP. *Biochemical and Biophysical Research Communications*, 420(2), pp.473–478.

Sovolyova, N. et al., 2014. Stressed to death - Mechanisms of ER stress-induced cell death. *Biological Chemistry*, 395(1), pp.1–13.

Stephens, H.E., Joyce, N.C. & Oskarsson, B., 2017. National Study of Muscle Cramps in ALS in the USA. *Amyotrophic Lateral Sclerosis and Frontotemporal Degeneration*, 18(1–2), pp.32–36.

Strange, R.W. et al., 2003. The structure of holo and metal-deficient wild-type human Cu, Zn superoxide dismutase and its relevance to familial amyotrophic lateral sclerosis. *Journal of Molecular Biology*, 328(4), pp.877–891.

Su, Z. et al., 2003. Insights into glutamate transport regulation in human astrocytes: cloning of the promoter for excitatory amino acid transporter 2 (EAAT2). *Proceedings of the National Academy of Sciences of the United States of America*, 100(4), pp.1955–1960.

Subramaniam, J.R. et al., 2002. Mutant SOD1 causes motor neuron disease independent of copper chaperone-mediated copper loading. *Nature neuroscience*, 5(4), pp.301–307.

Sun, Y. & MacRae, T.H., 2005. Small heat shock proteins: Molecular structure and chaperone function. *Cellular and Molecular Life Sciences*, 62(21), pp.2460–2476.

Surmeier, D.J. et al., 2011. The role of calcium and mitochondrial oxidant stress in the loss of substantia nigra pars compacta dopaminergic neurons in Parkinson's disease. *Neuroscience*, 198, pp.221–231.

Suzuki, H. et al., 2010. Peptide-binding sites as revealed by the crystal structures of the human Hsp40 Hdj1 C-terminal domain in complex with the octapeptide from human Hsp70. *Biochemistry*, 49(39), pp.8577–84.

Suzuki, H., Lee, K. & Matsuoka, M., 2011. TDP-43-induced death is associated with altered regulation of BIM and Bcl-xL and attenuated by caspase-mediated TDP-43 cleavage. *The Journal of biological chemistry*, 286(15), pp.13171–83.

Szabo, A. et al., 1994. The ATP hydrolysis-dependent reaction cycle of the Escherichia coli Hsp70 system DnaK, DnaJ, and GrpE. *Proceedings of the National Academy of Sciences of the United States of America*, 91(22), pp.10345–10349.

Takeuchi, H., Kobayashi, Y., Yoshihara, T., et al., 2002. Hsp70 and Hsp40 improve neurite outgrowth and suppress intracytoplasmic aggregate formation in cultured neuronal cells expressing mutant SOD1. *Brain Research*, 949(1–2), pp.11–22.

Takeuchi, H., Kobayashi, Y., Ishigaki, S., et al., 2002. Mitochondrial localization of mutant superoxide dismutase 1 triggers caspase-dependent cell death in a cellular model of familial amyotrophic lateral sclerosis. *Journal of Biological Chemistry*, 277(52), pp.50966–50972.

Takuma, H. et al., 1999. Reduction of GluR2 RNA editing, a molecular change that increases calcium influx through AMPA receptors, selective in the spinal ventral gray of patients with amyotrophic lateral sclerosis. *Annals of Neurology*, 46(6), pp.806–815.

Tan, C.F. et al., 2007. TDP-43 immunoreactivity in neuronal inclusions in familial amyotrophic lateral sclerosis with or without SOD1 gene mutation. *Acta Neuropathologica*, 113(5), pp.535–542.

Tan, W. et al., 2013. Small peptides against the mutant SOD1/Bcl-2 toxic mitochondrial complex restore mitochondrial function and cell viability in mutant SOD1-mediated ALS. *The Journal of neuroscience : the official journal of the Society for Neuroscience*, 33(28), pp.11588–98.

Tashiro, Y. et al., 2012. Motor neuron-specific disruption of proteasomes, but not autophagy, replicates amyotrophic lateral sclerosis. *Journal of Biological Chemistry*, 287(51), pp.42984–42994.

Tateno, M. et al., 2004. Calcium-permeable AMPA receptors promote misfolding of mutant SOD1 protein and development of amyotrophic lateral sclerosis in a transgenic mouse model. *Human Molecular Genetics*, 13(19), pp.2183–2196.

Teive, H. et al., 2016. Distal hereditary motor neuropathy with HSJ1 chaperone mutation, presenting with peripheral motor neuropathy, associated to parkinsonism, and cerebellar ataxia. Case report. *Parkinsonism & Related Disorders*, 22, p.e154.

Teuling, E. et al., 2008. A novel mouse model with impaired dynein/dynactin function develops amyotrophic lateral sclerosis (ALS)-like features in motor neurons and improves lifespan in SOD1-ALS mice. *Human Molecular Genetics*, 17(18), pp.2849–2862.

Teuling, E. et al., 2007. Motor neuron disease-associated mutant vesicle-associated membrane protein-associated protein (VAP) B recruits wild-type VAPs into endoplasmic reticulum-derived tubular aggregates. *The Journal of neuroscience : the official journal of the Society for Neuroscience*, 27(36), pp.9801–9815.

Thal, D.R. et al., 2002. Phases of A beta-deposition in the human brain and its relevance for the development of AD. *Neurology*, 58(12), pp.1791–800.

Tiwari, A. & Hayward, L.J., 2006. Mutant SOD1 instability: Implications for toxicity in amyotrophic lateral sclerosis. *Neurodegenerative Diseases*, 2(3–4), pp.115–126.

Tiwari, A., Xu, Z. & Hayward, L.J., 2005. Aberrantly increased hydrophobicity shared by mutants of Cu,Zn-superoxide dismutase in familial amyotrophic lateral sclerosis. *Journal of Biological Chemistry*, 280(33), pp.29771–29779.

Tokuda, E. et al., 2016. Low autophagy capacity implicated in motor system vulnerability to mutant superoxide dismutase. *Acta neuropathologica communications*, 4(1), p.6.

Tradewell, M.L. et al., 2012. Arginine methylation by prmt1 regulates nuclear-cytoplasmic localization and toxicity of FUS/TLS harbouring ALS-linked mutations. *Human Molecular Genetics*, 21(1), pp.136–149.

Trotti, D. et al., 2001. Amyotrophic lateral sclerosis-linked glutamate transporter mutant has impaired glutamate clearance capacity. *Journal of Biological Chemistry*, 276(1), pp.576–582.

Trotti, D. et al., 1999. SOD1 mutants linked to amyotrophic lateral sclerosis selectively inactivate a glial glutamate transporter. *Nature neuroscience*, 2(5), pp.427–433.

Tsang, C.K. et al., 2014. Superoxide dismutase 1 acts as a nuclear transcription factor to regulate oxidative stress resistance. *Nature communications*, 5, p.3446.

Tshala-Katumbay, D.D. & Spencer, P.S., 2007. Chapter 18 Toxic disorders of the upper motor neuron system. *Handbook of Clinical Neurology*, 82, pp.353–372.

Tuladhar, A. et al., 2015. Chapter 30 – Central Nervous System. In *Translational Regenerative Medicine*. pp. 415–435.

Tummala, H. et al., 2005. Inhibition of chaperone activity is a shared property of several Cu,Zn-superoxide dismutase mutants that cause amyotrophic lateral sclerosis. *The Journal of biological chemistry*, 280(18), pp.17725–31.

Turner, B.J. & Talbot, K., 2008. Transgenics, toxicity and therapeutics in rodent models of mutant SOD1-mediated familial ALS. *Progress in Neurobiology*, 85(1), pp.94–134.

Turner, M.R. et al., 2009. Biomarkers in amyotrophic lateral sclerosis. *Lancet neurology*, 8(1), pp.94–109.

Uhlen, M. et al., 2015. Tissue-based map of the human proteome. *Science*, 347(6220), pp.1260419–1260419.

Uranishi, H. et al., 2001. Involvement of the pro-oncoprotein TLS (translocated in liposarcoma) in nuclear factor-kappa B p65-mediated transcription as a coactivator. *The Journal of biological chemistry*, 276(16), pp.13395–401.

Urushitani, M. et al., 2004. CHIP promotes proteasomal degradation of familial ALS-linked mutant SOD1 by ubiquitinating Hsp/Hsc70. *Journal of Neurochemistry*, 90(1), pp.231–244.

Urushitani, M. et al., 2006. Chromogranin-mediated secretion of mutant superoxide dismutase proteins linked to amyotrophic lateral sclerosis. *Nature neuroscience*, 9(1), pp.108–118.

Uttenweiler, A. et al., 2007. The vacuolar transporter chaperone (VTC) complex is required for microautophagy. *Molecular biology of the cell*, 18(1), pp.166–175.

Valentine, J.S. & Hart, P.J., 2003. Misfolded Cu/Zn SOD and amyotrophic lateral sclerosis. *Proceedings of the National Academy of Sciences of the United States of America*, 100(7), pp.3617–22.

Vance, C. et al., 2009. Mutations in FUS, an RNA Processing Protein, Cause Familial Amyotrophic Lateral Sclerosis Type 6. *Science*, 323(5918), pp.1208–1211.

Vanselow, B.K. & Keller, B.U., 2000. Calcium dynamics and buffering in oculomotor neurones from mouse that are particularly resistant during amyotrophic lateral sclerosis (ALS)-related motoneurone disease. *The Journal of physiology*, 525 Pt 2, pp.433–445.

Vaughan, P.S. et al., 2002. A role for regulated binding of p150(Glued) to microtubule plus ends in organelle transport. *Journal of Cell Biology*, 158(2), pp.305–319.

le Verche, V. et al., 2011. Glutamate pathway implication in amyotrophic lateral sclerosis: What is the signal in the noise? *Journal of Receptor, Ligand and Channel Research*, 4, pp.1–22.

Verma, R. et al., 2002. Role of Rpn11 metalloprotease in deubiquitination and degradation by the 26S proteasome. *Science (New York, NY)*, 298(5593), pp.611–615.

Viswanathan, J. et al., 2011. Alzheimer's Disease-Associated Ubiquilin-1 Regulates Presenilin-1 Accumulation and Aggresome Formation. *Traffic*, 12(3), pp.330–348.

Voeltz, G.K., Rolls, M.M. & Rapoport, T.A., 2002. Structural organization of the endoplasmic reticulum. *EMBO Reports*, 3(10), pp.944–950.

De vos, K.J. et al., 2007. Familial amyotrophic lateral sclerosis-linked SOD1 mutants perturb fast axonal transport to reduce axonal mitochondria content. *Human Molecular Genetics*, 16(22), pp.2720–2728.

De vos, K.J. et al., 2012. VAPB interacts with the mitochondrial protein PTPIP51 to regulate calcium homeostasis. *Human Molecular Genetics*, 21(6), pp.1299–1311.

Vukosavic, S. et al., 1999. Bax and Bcl-2 interaction in a transgenic mouse model of familial amyotrophic lateral sclerosis. *Journal of neurochemistry*, 73(6), pp.2460–8.

Walker, A.K. et al., 2013. ALS-associated TDP-43 induces endoplasmic reticulum stress, which drives cytoplasmic TDP-43 accumulation and stress granule formation. *PLoS ONE*, 8(11).

Wang, H.-Y. et al., 2004. Structural diversity and functional implications of the eukaryotic TDP gene family. *Genomics*, 83(1), pp.130–139.

Wang, J. et al., 2007. Disease-associated Mutations at Copper Ligand Histidine Residues of Superoxide Dismutase 1 Diminish the Binding of Copper and Compromise Dimer Stability. *Journal of Biological Chemistry*, 282(1), pp.345–352.

Wang, J.W. et al., 2011. The ALS-associated proteins FUS and TDP-43 function together to affect Drosophila locomotion and life span. *Journal of Clinical Investigation*, 121(10), pp.4118–4126.

Wang, L. et al., 2008. Restricted expression of mutant SOD1 in spinal motor neurons and interneurons induces motor neuron pathology. *Neurobiology of Disease*, 29(3), pp.400–408.

Wang, W. et al., 2013. The ALS disease-associated mutant TDP-43 impairs mitochondrial dynamics and function in motor neurons. *Human Molecular Genetics*, 22(23), pp.4706–4719.

Wang, X. & Michaelis, E.K., 2010. Selective neuronal vulnerability to oxidative stress in the brain. *Frontiers in Aging Neuroscience*, 2(MAR).

Wang, X., Schwartz, J.C. & Cech, T.R., 2015. Nucleic acid-binding specificity of human FUS protein. *Nucleic Acids Research*, 43(15), pp.7535–7543.

Wang, X.Z. et al., 1996. Signals from the stressed endoplasmic reticulum induce C/EBP-homologous protein (CHOP/GADD153). *Molecular and cellular biology*, 16(8), pp.4273–80.

Wang, Y. et al., 2000. Activation of ATF6 and an ATF6 DNA binding site by the endoplasmic reticulum stress response. *The Journal of biological chemistry*, 275(35), pp.27013–20.

Watson, P. & Stephens, D.J., 2006. Microtubule plus-end loading of p150(Glued) is mediated by EB1 and CLIP-170 but is not required for intracellular membrane traffic in mammalian cells. *Journal of cell science*, 119(Pt 13), pp.2758–2767.

Werth, J.L. & Thayer, S. a, 1994. Mitochondria buffer physiological calcium loads in cultured rat dorsal root ganglion neurons. *The Journal of neuroscience : the official journal of the Society for Neuroscience*, pp.348–356.

Westhoff, B. et al., 2005. HSJ1 is a neuronal shuttling factor for the sorting of chaperone clients to the proteasome. *Current Biology*, 15(11), pp.1058–1064.

Wiedau-Pazos, M. et al., 1996. Altered reactivity of superoxide dismutase in familial amyotrophic lateral sclerosis. *Science*, 271(5248), pp.515–8.

Wilhelmus, M.M.M. et al., 2006. Small heat shock proteins inhibit amyloid-beta protein aggregation and cerebrovascular amyloid-beta protein toxicity. *Brain research*, 1089(1), pp.67–78.

Winton, M.J. et al., 2008. Disturbance of nuclear and cytoplasmic TAR DNA-binding protein (TDP-43) induces disease-like redistribution, sequestration, and aggregate formation. *Journal of Biological Chemistry*, 283(19), pp.13302–13309.

Witan, H. et al., 2009. Wild-type Cu/Zn superoxide dismutase (SOD1) does not facilitate, but impedes the formation of protein aggregates of amyotrophic lateral sclerosis causing mutant SOD1. *Neurobiology of Disease*, 36(2), pp.331–342.

Wood-Allum, C. & Shaw, P.J., 2010. Motor neurone disease: a practical update on diagnosis and management. *Clinical medicine (London, England)*, 10(3), pp.252–8.

Wood, J.D., Beaujeux, T.P. & Shaw, P.J., 2003. Protein aggregation in motor neurone disorders. *Neuropathology and Applied Neurobiology*, 29(6), pp.529–545.

Xiao, Q. et al., 2007. Mutant SOD1G93A microglia are more neurotoxic relative to wild-type microglia. *Journal of Neurochemistry*, 102(6), pp.2008–2019.

Xu, G. et al., 2014. Substantially elevating the levels of αb-crystallin in spinal motor neurons of mutant SOD1 mice does not significantly delay paralysis or attenuate mutant protein aggregation. *Journal of Neurochemistry*, 133(3), pp.452–464.

Xu, Y.-F. et al., 2010. Wild-type human TDP-43 expression causes TDP-43 phosphorylation, mitochondrial aggregation, motor deficits, and early mortality in transgenic mice. *The Journal of neuroscience : the official journal of the Society for Neuroscience*, 30(32), pp.10851–9.

Yamashita, H. et al., 2007. Heat-shock protein 105 interacts with and suppresses aggregation of mutant Cu/Zn superoxide dismutase: Clues to a possible strategy for treating ALS. *Journal of Neurochemistry*, 102(5), pp.1497–1505.

Yang, L. et al., 2007. A novel role for Bcl-2 associated-athanogene-1 (Bag-1) in regulation of the endoplasmic reticulum stress response in mammalian chondrocytes. *Journal of Cellular Biochemistry*, 102(3), pp.786–800.

Yang, Y. et al., 2009. Presynaptic Regulation of Astroglial Excitatory Neurotransmitter Transporter GLT1. *Neuron*, 61(6), pp.880–894.

Yang, Y. et al., 2001. The gene encoding alsin, a protein with three guanine-nucleotide exchange factor domains, is mutated in a form of recessive amyotrophic lateral sclerosis. *Nature genetics*, 29(2), pp.160–165.

Yerbury, J.J. et al., 2013. The small heat shock proteins αb-crystallin and Hsp27 suppress SOD1 aggregation in vitro. *Cell Stress and Chaperones*, 18(2), pp.251–257.

Yiwari, A. et al., 2009. Metal deficiency increases aberrant hydrophobicity of mutant superoxide dismutases that cause amyotrophic lateral sclerosis. *Journal of Biological Chemistry*, 284(40), pp.27746–27758.

Yoshida, H. et al., 2001. XBP1 mRNA is induced by ATF6 and spliced by IRE1 in response to ER stress to produce a highly active transcription factor. *Cell*, 107(7), pp.881–891.

Yoshida, T. et al., 2000. Targeted disruption of the mouse Sod I gene makes the hearts vulnerable to ischemic reperfusion injury. *Circulation research*, 86(3), pp.264–9.

Zaarur, N. et al., 2008. Triggering aggresome formation: Dissecting aggresome-targeting and aggregation signals in synphilin 1. *Journal of Biological Chemistry*, 283(41), pp.27575–27584.

Zakaryan, R.P. & Gehring, H., 2006. Identification and Characterization of the Nuclear Localization/Retention Signal in the EWS Proto-oncoprotein. *Journal of Molecular Biology*, 363(1), pp.27–38.

Zelko, I.N., Mariani, T.J. & Folz, R.J., 2002. Superoxide dismutase multigene family: A comparison of the CuZn-SOD (SOD1), Mn-SOD (SOD2), and EC-SOD (SOD3) gene structures, evolution, and expression. *Free Radical Biology and Medicine*, 33(3), pp.337–349.

Zhang, X. et al., 2011. Rapamycin treatment augments motor neuron degeneration in SOD1 G93A mouse model of amyotrophic lateral sclerosis. *Autophagy*, 7(4), pp.412–425.

Zhong, X. et al., 2004. AAA ATPase p97/valosin-containing protein interacts with gp78, a ubiquitin ligase for endoplasmic reticulum-associated degradation. *Journal of Biological Chemistry*, 279(44), pp.45676–45684.

Zhou, H. & Liu, R., 2014. ER stress and hepatic lipid metabolism. *Frontiers in Genetics*, 5(MAY).

Zhou, L. et al., 2014. P62/sequestosome 1 regulates aggresome formation of pathogenic ataxin-3 with expanded polyglutamine. *International Journal of Molecular Sciences*, 15(9), pp.14997–15010.

Appendix

Appendix (Chapter 2)

2.1 Cloning primers

Primers	Sequence (5'-3')
SOD1_F1	CAT ATG CTC GAG ATG GCG ACG AAG GCC GTG TGC NdeI XhoI SOD1 Forward
SOD1_R1	GGA TCC TTA TTG GGC GAT CCC AAT TAC ACC BamHI termination codon SOD1 Reverse
SOD1_F2	GGA TTC ATG GCG ACG AAG GCC GTG TGC BamHI SOD1 Forward
SOD1_R2	CTC GAG TTA TTG GGC GAT CCC AAT TAC ACC XhoI termination codon SOD1 Reverse

2.2 DNA expansion cycles

For SOD1 plasmid cloning:

Step	Temperature	Time	Cycles
Denaturation	94 ºC	2min	1
Denaturation	94 ºC	30s	15
Annealing	60 ºC	30s	
Extension	72 ºC	30s	
Extension	72 ºC	5min	1

For mCherry plasmid cloning:

Step	Temperature	Time	Cycles
Denaturation	94 ºC	2min	1
Denaturation	94 ºC	30s	15
Annealing	60 ºC	30s	
Extension	72 ºC	30s	
Extension	72 ºC	5min	1

2.3 Ethanol precipitation

1vol DNA sample

2.5vol 100% EtOH

0.1vol 3M NaAc

Centrifuge at highest speed for 30min after -80ºC 1h incubation.

Discard the supernatant.

Wash with 70% EtOH, centrifuge at highest speed for 10min.

Discard the supernatant.

Dry at 65 ºC for 5min.

Resuspend in ddH_2O or formamide (for sequencing).

2.4 Agarose gel loading dye (6X)

0.4% (w/v) Orange G

0.03% (w/v) Bromophenol Blue

0.03% (w/v) Xylene cyanol
15% (v/v) Ficoll 400
10 mM Tris-HCl (pH=7.5)
50 mM EDTA (pH=8.0)

2.5 Tris-acetate-EDTA Buffer (1X)

40mM Tris

20mM Acetic acid
1mM EDTA
pH=8.0

2.6 Ligation reaction

2.6.1 pGEM-T Easy ligation system

Inserts: vector=3:1
1ul T4 ligase
5ul 2X ligation buffer
1ul pGEM-T Easy vector (50ng)
3ul purified PCR products
Use ddH_2O to make the final volume as 10ul, 4ºC overnight or 3 hours at 22 ºC.

2.6.2 T4 ligation system

Inserts: vector=3:1
1ul T4 ligase
1ul 10X ligation buffer
100ng of vectors
30ng of inserts
Use ddH_2O to make the final volume as 10ul, 16ºC for 5h or 20 minutes at 22 ºC.

2.7 Bacterial culture medium

2.7.1 Luria-bertani broth

1% (w/v) Tryptone
0.5% (w/v) Yeast extract
1% (w/v) NaCl in ddH_2O, autoclaved

2.7.2 SOC medium

1% (w/v) Tryptone
0.5% (w/v) Yeast extract
1% (w/v) NaCl
2.5mM KCl
1% $MgCl_2$
1% $MgSO_4$
20% glucose in ddH_2O, autoclaved

2.7.3 M9 minimal medium

2.7.3.1 M9 salts

64g Na_2HPO_4-7H_2O

15g KH_2PO_4

2.5g NaCl in 1L ddH_2O, autoclaved.

2.7.3.2 M9 Medium

200ml M9 Salts

2ml of 1M $MgSO_4$ (autoclaved)

20 ml of 20% Glucose (filter sterilized)

5.0g NH_4Cl (filter sterilized)

100ul of 1M $CaCl_2$ (autoclaved)

Adjust to 1L with autoclaved ddH_2O

2.8 LB agar plate

2.8.1 LB agar

1% Tryptone (w/v)

0.5% Yeast extract (w/v)

1% NaCl (w/v)

1.5% Agar (w/v) in ddH_2O, autoclaved

2.8.2 Blue/white screening

2.8.2.1 IPTG stock

0.1M/L IPTG: 0.24g IPTG in ddH_2O to make the final volume as 10ml, filter sterilized and store at 4 °C fridge.

2.8.2.2 X-Gal stock

20mg/ml X-gal: 2g X-gal in 10ml N,N´-dimethylformamide (DMF), covered by aluminium foil and stored at -20℃ freezer.

100ul of IPTG stock, 200ul of X-gal and relevant anti-biotics were added into 100ml agar to make the plates for colour screening.

2.9 Antibiotics

2.9.1 Ampicillin

50mg/ml in ddH_2O, filter sterilized and stored at -20℃. 1:500 to 1:1000 dilution for use.

2.9.2 Kanamycin

20mg/ml in ddH_2O, filter sterilized and stored at -20℃. 1:1000 dilution for use.

2.9.3 Chloramphenicol

34mg/ml in 100% ethanol, filter sterilized and store at -20℃. 1:1000 dilution for use.

2.10Sequencing primers

Primer	Sequences (5'-3')
T7 Promoter Forward Primer	TAATACGACTCACTATAGGG
T7 Promoter Reverse Primer	GCTAGTTATTGCTCAGCGG
CMV Forward Primer	CGCAAATGGGCGGTAGGCGTG
SP6 Forward Primer	ATTTAGGTGACACTATAG
BGH Reverse Primer	TAGAAGGCACAGTCGAGG

2.11 Ni-NTA buffer

2.11.1 Native condition

Binding Buffer	Wash Buffer	Elute Buffer
50mM Na_2HPO_4	50mM Na_2HPO_4	50mM Na_2HPO_4
300mM NaCl	300mM NaCl	300mM NaCl
10mM Imidazole	100mM Imidazole	500mM Imidazole
5% Glycerol	5% Glycerol	5% Glycerol
0.2% Triton-100	----------	----------
pH=8	pH=8	pH=8

2.11.2 Denatured condition

Binding Buffer	Wash Buffer	Elute Buffer
100mM Na_2HPO_4	100mM Na_2HPO_4	100mM Na_2HPO_4
10mM Tris-base	10mM Tris-base	10mM Tris-base
7M Urea	7M Urea	8M Urea
pH=8	pH=6.3	pH=4.5

2.13 Ni-NTA resin regeneration

2vol regeneration buffer (6M GuHCl; 0.2M acetic acid)

5vol ddH_2O

3vol 2% SDS

1vol 25% EtOH

1vol 50% EtOH

1vol 75% EtOH

5vol 100% EtOH

1vol 75% EtOH

1vol 50% EtOH

1vol 25% EtOH

1vol ddH_2O

5vol 100mM EDTA pH=8

3vol ddH_2O

3vol 20% EtOH, store at 4ºC

Before reuse:

10vol ddH_2O

5vol 100mM NiSO4

2vol ddH_2O

2vol 1X Ni-NTA Bind Buffer

2.14 Dialysis buffer

Dialysis Buffer (Cu/Zn)	Dialysis Buffer (No Cu/Zn)
2.7mM KCl	2.7mM KCl
137mM NaCl	137mM NaCl
4.3mM Na_2HPO_4•$7H_2O$	4.3mM Na_2HPO_4•$7H_2O$
1.4mM KH_2PO_4	1.4mM KH_2PO_4
5% Glycerol	5% Glycerol

0.1mM $CuSO_4$/ $ZnSO_4$	----------

2.15 ATP regeneration system

2.15.1.1 10X Energy Mix

100mM Phosphocreatine

20mM ATP

10mM $MgCl_2$

2.16 Gateway T-Rex system

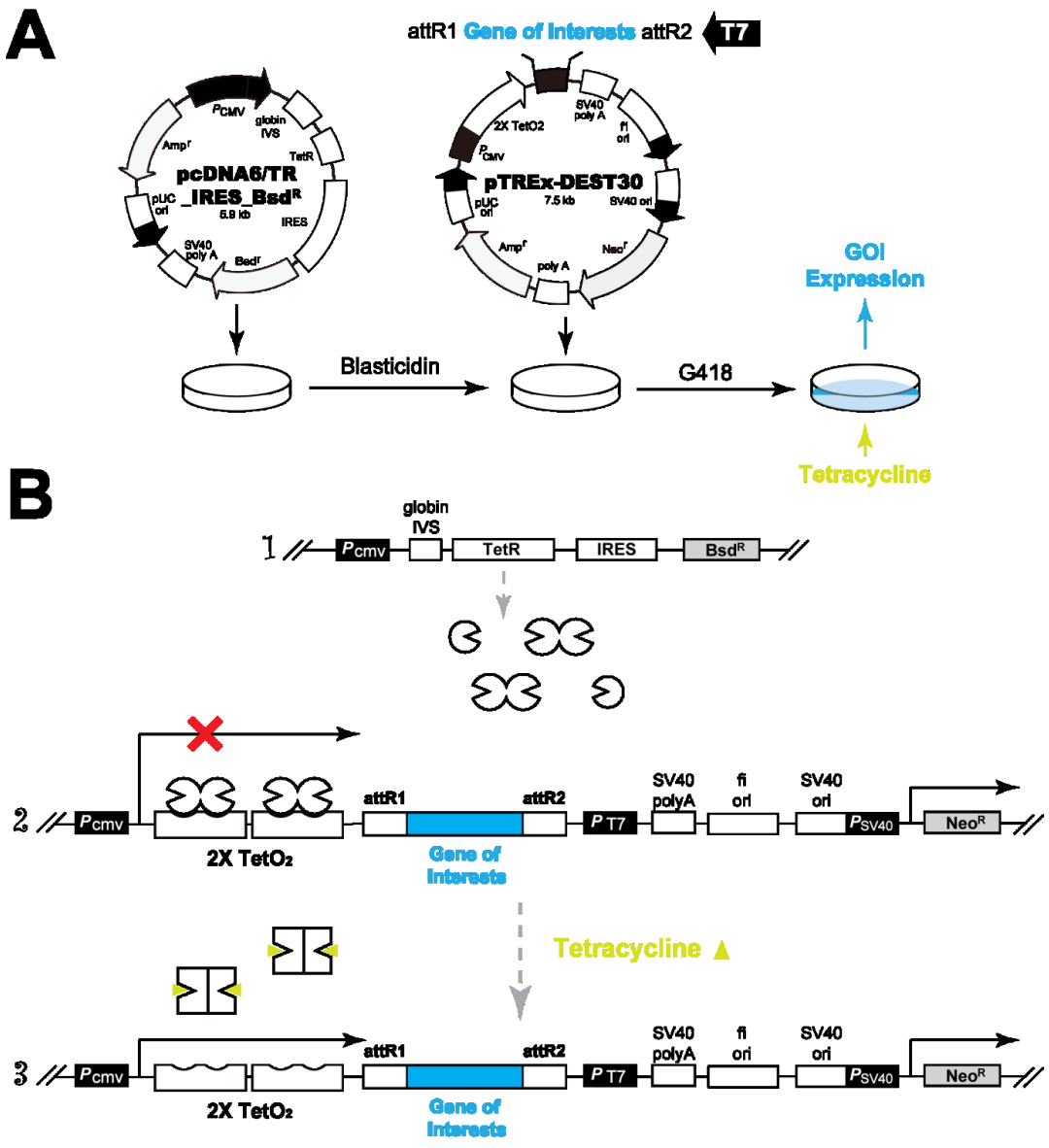

Figure 7.1 Gateway T-Rex inducible cell line generation using Bsd and G418. (A) Selection procedure of gateway T-Rex cell line; **(B)** Mechanism of Tet-regulated expression of gene of interests.

2.17 Anti-DNAJB2 antibody

Anti-DNAJB2 antibody is specially designed by Cheetham lab.

Target:EAAGKKPA

2.17.1 Anti-HSJ1a

Target:EAAGKKPADVP

2.17.2 Anti-HSJ1b

Target:EAAGKKPAGGREAQHRRQGRPKAQHQDPGLGGTQEGARGEATKRSPSPEE KASRCLIL

2.18 Cell lysis buffer

2.18.1.1 RIPA buffer

25mM Tris-HCl (pH=7.6)

150mM NaCl

1% (w/v) sodium deoxycholate

1% (v/v) Tergitol-type nonyl phenoxylpolyethoxylethanol (NP-40)

3% (v/v) PIC

0.1% (w/v) SDS

2.18.1.2 Co-IP lysis buffer

25mM Tris-HCl (pH=7.5)

50mM NaCl

0.25% sodium deoxycholate

1% NP-40

3% (v/v) PIC

1mM EDTA

2.19 Laemmli buffer (SDS loading buffer)

	2X	4X
Tris-HCl (pH=6.8)	120mM	240 mM
Glycerol	20%	40%
SDS	4%	8%
Bromophenol blue	0.02%	0.04%
β-mercaptoethanol	5%	10%

2.20 SDS-polyacrylamide gel

For 2 Gels	Resolving Gel			Stacking Gel
	10%	12%	15%	3%
1.5M Tris pH=8.8	2.5ml			
0.5M Tris pH=6.8				1.25ml
30% Acrylamide	3.3ml	4.0ml	5.0ml	0.65ml
ddH_2O	4.0ml	3.3ml	2.3ml	3.0ml
10% SDS	0.1ml			0.05ml
10% APS	0.1ml			0.05ml
TEMED	10ul			10ul

2.21 Coomassie staining

2.21.1 Coomassie staining solution

0.1% (w/v) Coomassie R250

40% (v/v) methanol

10% (v/v) acetic acid

50% (v/v) ddH_2O

2.21.2 Coomassie destaining solution

20% (v/v) methanol

10% (v/v) glacial acetic acid

70% (v/v) ddH_2O

2.22 Transfer buffer

20mM Tris-HCl

150mM Glycin

0.02% (w/v) SDS

20% (v/v) methanol

2.23 Ponceau S staining solution

2% acetic acid

0.5% Ponceau S in ddH_2O.

2.24 Blocking buffer

2.24.1 PBS-Tween buffer

1% (v/v) Tween in 1X PBS buffer

2.24.2 TBS-Tween buffer

1% (v/v) Tween in 1X TBS buffer

2.24.3 Blocking buffer (in PBS-Tween)

5% (w/v) non-fat dried milk in PBS-Tween buffer

2.24.4 Blocking buffer (in TBS-Tween)

5% (w/v) non-fat dried milk in TBS-Tween buffer

2.25 β-galactosidase assay buffer

2.25.1 Lysis buffer

250mM Tris Base (pH=8.0)

2.25.2 Cleavage buffer

600mM Na_2HPO_4-$7H_2O$

400mM NaH_2PO_4-H_2O

100mM KCl

10mM $MgSO_4$-$7H_2O$ (pH=7.0)

2.25.3 Stop buffer

1M Sodium Carbonate

Appendix (Chapter 4)

7.4.1 pmCherry-SOD1 cloning

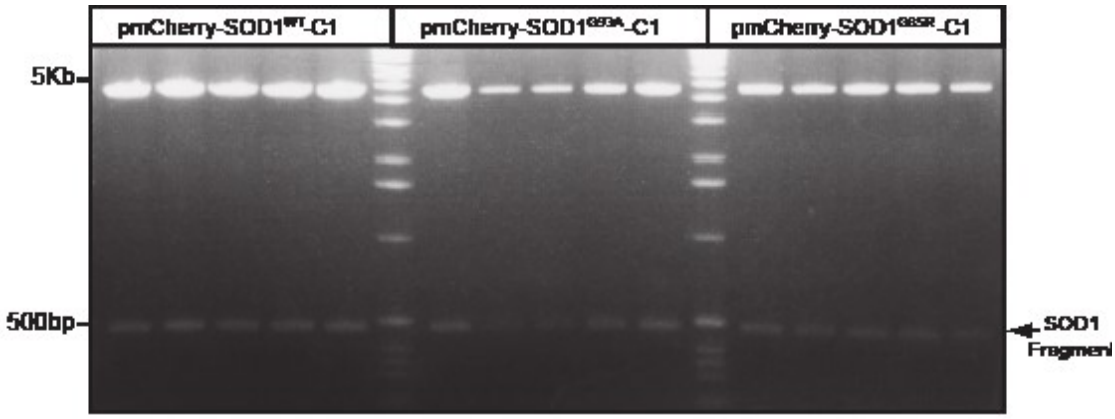

Figure 7.2 Digestion of pmCherry-SOD1 from ligation reaction. Plasmid extracted from individual colonies generated from pmCherry-SOD1 ligation reactions (WT, G93A & G85R) as indicated, digested at 37°C water bath for 2h using EcoRI-BamHI referred to Material and Methods. Digestion products were resolved by 1% agarose gel to detect the presences of SOD1 bands at 450bp.

7.4.2 pcDNA5/FRT/TO -V5-SOD1 cloning

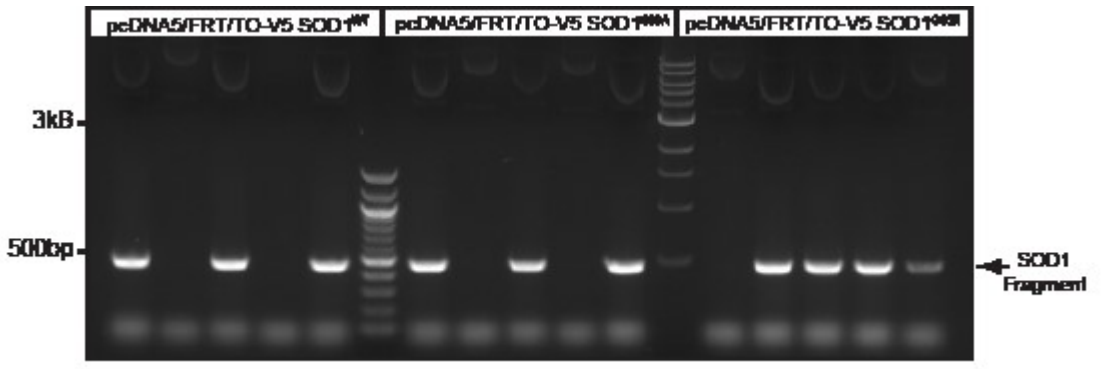

Figure 7.3 PCR screen of cloned inducible SOD1 constructs. PCR of colonies generated from pcDNA5/FRT/TO/V5-SOD1(WT, G93A & G85R) ligation reactions. Plasmid extracted from individual colonies as indicated, amplified using SOD1 primers and GoTaq enzyme referred to Material and Methods. PCR products were resolved by 1% agarose gel to detect the presences of amplified SOD1 bands at 450bp.

7.4.3 pcDNA5/FRT/TO -eGFP-SOD1 cloning

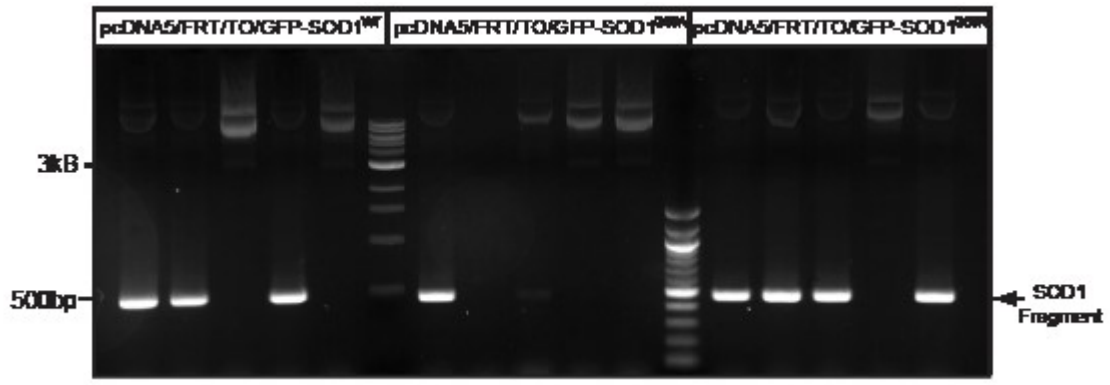

Figure 7.4 PCR screen of cloned inducible SOD1 constructs. PCR of colonies generated from pcDNA5/FRT/TO/eGFP-SOD1(WT, G93A & G85R) ligation reactions. Plasmid extracted from individual colonies as indicated, amplified using SOD1 primers and GoTaq enzyme referred to Material and Methods. PCR products were resolved by 1% agarose gel to detect the presences of amplified SOD1 bands at 450bp.

7.4.4 Flp-in T-Rex cell line generation

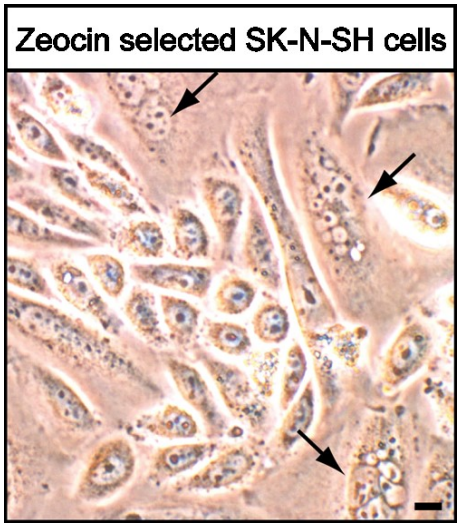

Figure 7.5 Zeocin selected SK-N-SH cells during the Flp-in host cell line generation. SK-N-SH cells were transfected with pFRT/lacZeo plasmid, and selected with 100ug/ml Zeocin in completed DMEM medium. Cells formed multiple nuclei (≥3) during the selection process were highlighted with arrow. Scale bar 10um.

7.4.5 RT-PCR performed in this chapter

7.4.5.1 Primers used in this chapter

All the primers used in this chapter to verify the expression of inducible cell line were listed below.

Primers	Sequence (5'-3')	Tm	Product Size
rtSOD1_F	GTGGGCCAAAGGATGAAGAGA	67.4	248bp (Exon 3-5)
rtSOD1_R	TTATTGGGCGATCCCAATTACACC	67.3	
β-actin_F	CTGGGACGACATGGAGAAAA	65	564bp
β-actin_R	AAGGAAGGCTGGAAGAGTGC	64.7	

7.4.5.2 RT-PCR expansion cycles

7.4.5.2.1 β-actin:

Step	Temperature	Time	Cycles
Denaturation	94 ºC	2min	1
Denaturation	94 ºC	30s	25
Annealing	59 ºC	30s	
Extension	74 ºC	40s	
Extension	74 ºC	5min	1

4.5.2.2 rtSOD1:

Step	Temperature	Time	Cycles
Denaturation	94 ºC	2min	1
Denaturation	94 ºC	30s	20
Annealing	58 ºC	30s	
Extension	74 ºC	30s	
Extension	74 ºC	5min	1

7.4.6 Effects of synthetic SOD1 aggregates on cells expressing SOD1

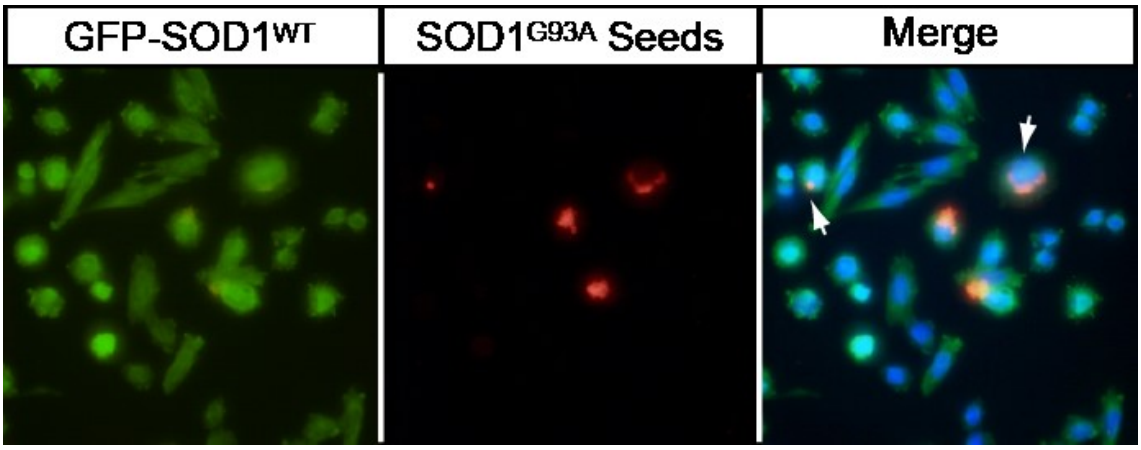

Figure 7.6 SOD1 cross-seeding assay. Purified 6XHis $SOD1^{G93A}$ protein samples were sedimentated by 5mM calcium/DTT, which was then fractionated at 17000g for 1h at 4 ˚C, washed by 1XPBS twice and then co-incubated with trypsin at 37˚C for 3mins. CHO cells expressing $SOD1^{WT}$ were co-incubated with the sedimented $SOD1^{G93A}$ in DMEM medium for 24hrs. Then cells were fixed, permeablised and immunostained with mouse anti-His (1:100) and mouse anti-Cy2 (1:100) as described in Materials and Methods.

Appendix (Chapter 5)

7.5.1 RT-PCR expansion cycles

7.5.1.1 tXBP-1:

Step	Temperature	Time	Cycles
Denaturation	94 ºC	2min	1
Denaturation	94 ºC	30s	30
Annealing	59 ºC	30s	
Extension	74 ºC	30s	
Extension	74 ºC	5min	1

7.5.1.2 eIF2α:

Step	Temperature	Time	Cycles
Denaturation	94 ºC	2min	1
Denaturation	94 ºC	30s	30
Annealing	55 ºC	30s	
Extension	74 ºC	30s	
Extension	74 ºC	5min	1

7.5.1.3 ATF4:

Step	Temperature	Time	Cycles
Denaturation	94 ºC	2min	1
Denaturation	94 ºC	30s	26
Annealing	60 ºC	30s	
Extension	74 ºC	30s	
Extension	74 ºC	5min	1

5.1.4 Chop:

Step	Temperature	Time	Cycles
Denaturation	94 ºC	2min	1
Denaturation	94 ºC	30s	27
Annealing	55 ºC	30s	
Extension	74 ºC	30s	
Extension	74 ºC	5min	1

7.5.1.5 PDI:

Step	Temperature	Time	Cycles
Denaturation	94 ºC	2min	1
Denaturation	94 ºC	30s	34
Annealing	56 ºC	30s	
Extension	74 ºC	30s	
Extension	74 ºC	5min	1

7.5.1.6 BiP:

Step	Temperature	Time	Cycles
Denaturation	94 ºC	2min	1
Denaturation	94 ºC	30s	27
Annealing	58 ºC	30s	
Extension	74 ºC	30s	
Extension	74 ºC	5min	1

7.5.1.7 BCL-2:

Step	Temperature	Time	Cycles
Denaturation	94 ºC	2min	1
Denaturation	94 ºC	30s	30
Annealing	54 ºC	30s	
Extension	74 ºC	40s	
Extension	74 ºC	5min	1

7.5.1.8 Derlin-1:

Step	Temperature	Time	Cycles
Denaturation	94 ºC	2min	1
Denaturation	94 ºC	30s	26
Annealing	56 ºC	30s	
Extension	74 ºC	40s	
Extension	74 ºC	5min	1

7.5.2 ANOVA analysis

SOD1 inclusion incidence

	Cell lines	DAY		*F*	p
SOD1^{WT}	**HSJ1a**	**Day 1**	Between groups Within groups	6.233	**0.047**
		Day 2	Between groups Within groups	15.965	**0.007**
	HSJ1b	**Day 1**	Between groups Within groups	4.666	**0.074**
		Day 2	Between groups Within groups	6.203	**0.047**
SOD1^{G93A}	**HSJ1a**	**Day 1**	Between groups Within groups	236.47	**<0.001**
		Day 2	Between groups Within groups	67.655	**<0.001**
	HSJ1b	**Day 1**	Between groups Within groups	144.14	**<0.001**
		Day 2	Between groups Within groups	110.43	**<0.001**
SOD1^{G85R}	**HSJ1a**	**Day 1**	Between groups Within groups	155.67	**<0.001**
		Day 2	Between groups Within groups	103.68	**<0.001**
	HSJ1b	**Day 1**	Between groups Within groups	93.186	**<0.001**
		Day 2	Between groups Within groups	60.91	**<0.001**

ANOVA. One-way ANOVA was carried out using SPSS to analyse SOD1 inclusion incidence between uninduced cells and cells expressing HSJ1 at different time points (Day 1 or Day2). Significant difference was set as $p<0.05$.

7.5.3 Test of homogeneity of variance

SOD1 inclusion incidence

	Cell lines	Levene	df1	df2	p value
$SOD1^{WT}$	**HSJ1a**	4.743	3	12	**0.021**
	HSJ1b	0.428	3	12	**0.736**
$SOD1^{G93A}$	**HSJ1a**	2.233	3	12	**0.137**
	HSJ1b	1.266	3	12	**0.33**
$SOD1^{G85R}$	**HSJ1a**	2.026	3	12	**0.164**
	HSJ1b	2.282	3	12	**0.131**

Test of homogeneity of variance. One-way ANOVA was carried out using SPSS to analyse SOD1 inclusion incidence within cells expressing HSJ1a or HSJ1b regardless of the Tet induction. Significant difference was set as $p<0.05$. $p<0.05$ suggested the variances were heterogeneous, and $p>0.05$ suggested the variances were homogeneous within each group. *Abbreviations*: df, degrees of freedom.

7.5.4 Multi group comparison

Dependent Variable: SOD1 inclusion incidence

	Method	Cell lines	DAY+Induction (I)	(J)	Sig. p value	95% Confidence Interval Lower	Upper
$SOD1^{WT}$	**Dunnett T3**	**HSJ1a**	1-	1+	**0.23**	-0.001425937	0.006043876
			1+	1-	**0.23**	-0.006043876	0.001425937
			2-	2+	**0.084**	-0.000456677	0.005136374
			2+	2-	**0.084**	-0.005136374	0.000456677
		HSJ1b	1-	1+	**0.317**	-0.001455871	0.005115501
			1+	1-	**0.317**	-0.005115501	0.001455871
			2-	2+	**0.222**	-0.001010327	0.004576087
			2+	2-	**0.222**	-0.004576087	0.001010327
$SOD1^{G93A}$	**Tukey HSD**	**HSJ1a**	1-	1+	**<0.001**	0.154645141	0.228899512
			1+	1-	**<0.001**	-0.228899512	-0.154645141
			2-	2+	**<0.001**	0.066016643	0.140271014
			2+	2-	**<0.001**	-0.140271014	-0.066016643
		HSJ1b	1-	1+	**<0.001**	0.125083363	0.184009515
			1+	1-	**<0.001**	-0.184009515	-0.125083363
			2-	2+	**<0.001**	0.029297888	0.08822404
			2+	2-	**<0.001**	-0.08822404	-0.029297888
$SOD1^{G85R}$	**Tukey HSD**	**HSJ1a**	1-	1+	**<0.001**	0.150272671	0.220030412
			1+	1-	**<0.001**	-0.220030412	-0.150272671
			2-	2+	**<0.001**	0.041204261	0.110962003
			2+	2-	**<0.001**	-0.110962003	-0.041204261
		HSJ1b	1-	1+	**<0.001**	0.110164737	0.183878572
			1+	1-	**<0.001**	-0.183878572	-0.110164737
			2-	2+	**0.001**	0.031302155	0.10501599
			2+	2-	**0.001**	-0.10501599	-0.031302155

Multi group comparison of cell lines transiently overexpressing SOD1. Multi group comparisons was performed by one-way ANOVA using SPSS with post-hoc analysis by Dunett T3 test when the variances are heterogeneous (WT) or by Tukey HSD test when the variances are homogeneous (G93A and G85R). Statistical significance was set at $p<0.05$.